SUCTION DRAIN AS A NOVEL LOW-CARBON GROUND IMPROVEMENT TECHNIQUE

Michela Martini

Thesis submitted to the Department of Civil and Environmental Engineering, University of Strathclyde, Glasgow, in fulfilment of the requirements for the degree of

Doctor of Philosophy

in

Civil and Environmental Engineering

December 2018,

Glasgow, UK

Declaration of authenticity and author's right

This thesis is the result of the author's original research. It has been composed by the author and has not been previously submitted for examination which has led to the award of a degree.

The copyright of this thesis belongs to the author under the terms of the United Kingdom Copyright Acts as qualified by University of Strathclyde Regulation 3.50. Due acknowledgement must always be made of the use of any material contained in, or derived from, this thesis.

Signed:

Date: 17 December 2018

ACKNOWLEDGMENTS

I would like to thank my supervisor Alessandro Tarantino for his guide throughout the PhD and for sharing his passion for the research.

I am grateful to Derek McNee, the other department technicians and my colleagues in the laboratory for their support and advices.

My thanks also to my examiners Alessio Ferrari and Stella Pytharouli for their time and their value comments.

Last but not the least, I would like to thank my family and my Glaswegian family for supporting me spiritually throughout this journey.

Table of contents

1 INTRODUCTION 9

2 BACKGROUND 12

2.1 Tunnelling and tunnelling mechanics 12

2.1.1 Tunnel construction techniques 12

2.1.1.1 Open face tunnelling 12

2.1.1.2 Close face tunnelling 14

2.1.2 Ground Improvement Techniques 16

2.1.2.1 Ground freezing 16

2.1.2.2 Lowering of the groundwater table 18

2.1.2.3 Grouting 19

2.1.3 Tunnel Face Stability 22

2.1.3.1 Face failure mechanism in cohesive soil 23

2.1.3.2 Propagation of movement towards the surface 24

2.1.3.3 Face stability in cohesive soils 26

2.1.3.4 The limit theorem of Davis et al. (1980) 28

2.1.3.5 Upper bound plane strain tunnel heading: inward collapse 31

2.1.3.6 Upper bound plane strain tunnel heading: local collapse 33

2.1.3.7 Upper bound plane strain tunnel heading: blow out 34

2.2 Moist air flow and evaporation 34

2.2.1 Moist air turbulent flow 34

2.2.1.1 Atmospheric Surface Layer 34

2.2.1.2 Theory of the mixing length model in turbulent flow 37

2.2.1.3 Logarithmic profile of the mean wind speed 38

2.2.1.4 Logarithmic profile of the mean specific humidity 41

2.2.1.5 Logarithmic profile of the mean wind temperature 42
2.2.2 Evaporation in open air 43
2.2.2.1 Equation of state of moist air 43
2.2.2.2 Mass balance at the soil-atmosphere interface 46
2.2.2.3 Energy balance at the soil-atmosphere interface 47
2.2.2.4 Potential evaporation from liquid surface or saturated soil 48

3 EVAPORATION-INDUCED SOIL WATER FLUX TO DESIGN SUCTION DRAIN FOR LOW-CARBON GROUND STABILISATION: EXPERIMENTAL INVESTIGATION AND MODELLING 55

3.1 Abstract 55

3.2 Introduction 56

3.3 Equipment 58
3.3.1 Long evaporation machine 58
3.3.2 Short evaporation machine 59
3.3.3 Control and measurement devices 60
3.3.3.1 RH/T sensors 60
3.3.3.2 Anemometer 64
3.3.3.3 Balances 65
3.3.3.4 Humid air injection system 67

3.4 Experimental procedure 69
3.4.1 Long evaporation machine with water 69
3.4.1.1 Initialisation of the test 69
3.4.1.2 Test procedure 70
3.4.2 Short evaporation machine with soil 72
3.4.2.1 Test procedure 72

3.5 Experimental results 73
3.5.1 Long evaporation machine with water 73
3.5.1.1 Control of air velocity, RH, and temperature 73

3.5.1.2 Individual evaporation test 76
3.5.1.3 Evaporation tests at different RHs and air velocities 80
3.5.2 Short evaporation machine with soil 85

3.6 Water evaporation model 86

3.6.1 Model calibration for water 89
3.6.2 Simulation of evaporation from water surface 91
3.6.3 Comparison between saturated soil and water surface 92

3.7 Discussion 93

3.7.1 Vapour transfer coefficient 93
3.7.2 Airflow relative humidity 97

3.8 Conclusions 99

4 SUCTION DRAIN AS A LOW CARBON GROUND IMPROVEMENT TECHNIQUE: PROOF-OF-CONCEPT AT THE LABORATORY SCALE 102

4.1 Abstract 102

4.2 Introduction 103

4.3 Suction drain concept 104

4.4 Material characterisation 105

4.4.1 Soil classification and index properties 105
4.4.2 Water retention behaviour 106
4.4.3 Hydraulic conductivity behaviour 111

4.5 Boundary condition characterisation 114

4.6 Suction drain mock-up scale test 117

4.6.1 Set-up 117

4.6.2 Experimental Procedure 119
4.6.3 Results 120

4.7 Suction drain modelling 123

4.7.1 Hydro-mechanical model 123
4.7.2 Numerical analysis and results 126

4.8 Effectiveness of suction drain in stabilising tunnel face 128

4.9 Conclusions 136

5 SUCTION DRAIN FOR GROUND IMPROVEMENT IN CLAY FORMATIONS: FIELD TRIAL 137

5.1 Abstract 137

5.2 Introduction 138

5.3 Site details 140

5.4 Material 140

5.4.1 BGLSoil classification and index properties 140
5.4.2 Compression behaviour 141
5.4.3 Water retention behaviour 143
5.4.4 Hydraulic conductivity behaviour 149

5.5 Field method 151

5.5.1 Field installation 151
5.5.2 Field test procedure 153
5.5.3 Data sampling 155

5.6 Experimental results 157

5.6.1 Measurement of relative humidity and temperature of the airflow 157

5.6.2 Measurement of soil undrained shear strength in the site 160
5.6.3 Measurement of soil water content 162

5.7 Discussion 167

5.7.1 Numerical modelling of the suction drain..... 167
5.7.2 Scenario of the horizontal natural suction drain 172

5.8 Conclusions 175

6 CONCLUSION 177

7 REFERENCES 181

8 LIST OF CAPTIONS FOR FIGURES 187

9 LIST OF CAPTIONS FOR TABLES 192

10 APPENDIX A.1- EXPERIMENTAL INVESTIGATION OF THE EVAPORATION-INDUCED SOIL WATER FLUX 193

1 INTRODUCTION

The undrained shear strength is the most important parameter in the analysis of tunnel face stability in clayey soils. Soft clays possess very low undrained shear strength and ground improvement techniques need to be implemented prior to tunnel excavation. Jet grouting and fiberglass reinforcement are the most common soil reinforcement methods used in tunnelling to ensure stability. Ground freezing is also used as temporary structural support and/or to exclude groundwater from the excavation until construction of the final lining provides permanent support. These techniques leave chemical residues and spoils into the soil or into the groundwater, slow down construction process due to the need of cleaning up the soil after construction, and have high costs of implementation. Cristelo et al., (2015) show that around 80% of the carbon dioxide emissions of cement-based mixtures for jet grouting is generated by the material used. The technology hereafter conceptualised and studied, the suction drain, utilises compressed air in lieu of cement-based mixture into the ground, hence it has a high margin for reducing the carbon dioxide footprint to the current ground stability techniques.

This study presents the suction drain as an innovative and low-carbon technique for temporary stabilisation of geo structures in soft clayey soils. Based on suction generated into the ground by the evaporation from pre-drilled holes, this technique aims to enhance the undrained shear strength in soft clayey by reducing the soil water content. The goal of this study is to investigate the capability of the suction drain in enhancing the undrained shear strength of clayey soils.

The objectives of this study are:

1. Understanding and modelling the evaporation-induced water flow that is generated by a tangential airflow in a confined space (as occurs in the suction drain);
2. Testing and validating the suction drain at mock-up laboratory scale level;
3. Investigating the capability of the suction drain to reduce soil water content via field trial.

This thesis is structured in papers and includes four chapters as follows:

Chapter 2 illustrates the background in tunnelling and water evaporation. The ground improvement techniques currently used in tunnelling, the tunnelling construction techniques, and the theoretical and empirical approaches used to evaluate the tunnel face stability are summarised in this chapter. An insight into moist air turbulent flow and of evaporation in open air is also presented.

Chapter 3 focuses on the development of a model that allows estimating the water evaporation rate of the soil exposed to a tangential airflow in a confined space. An evaporation model is required to prescribe the air flow characteristics in terms of air velocity and relative humidity in the implementation of the suction drain.

Chapter 4 investigates the suction drain model at mock-up laboratory scale level. An experimental investigation at laboratory scale was conducted to assess the capability of the suction drain in reducing soil water content of the surrounding soil. A numerical application of the suction drain is finally presented to appreciate the enhancement of tunnel face stability that can be potentially achieved following the decrease of soil water content generated by the suction drain.

Chapter 5 deals with the validation of the suction drain at the field scale. The field installation and the field procedure are described in this chapter. Numerical analyses based on

the hydro-mechanical characterisation of the soil material were carried out to interpret the experimental field data and to validate the field test.

Appendix A.1 shows the results of the experimental investigation that was carried out for developing the model described in Chapter 2.

2 BACKGROUND

2.1 Tunnelling and tunnelling mechanics

2.1.1 Tunnel construction techniques

The following Section deals with advance tunnelling technique about “bored” tunnel construction in soft ground. Referring to any kind of mined tunnel, as distinct from cut-and-cover, Mair and Taylor classified the tunnelling technique according to open face and close face tunnelling, considering the first one the case where there is an easy access to the tunnel face in contrast with the second one (Chapman et al., 2017).

2.1.1.1 Open face tunnelling

The most common tunnelling technique is the New Australian Tunnelling Method usually denoted as NATM. This technique includes the use of sprayed concrete lining as a temporary support although several years may be required before the permanent lining is installed. However according to advance tunnelling technique composite sprayed concrete lining can be applied both as temporary support at first and as permanent subsequently. In general this technique is adopted for relative short tunnel and non circular cross sections. Since this technique involves an excavation sequence through different faces as shown in Figure 2-1

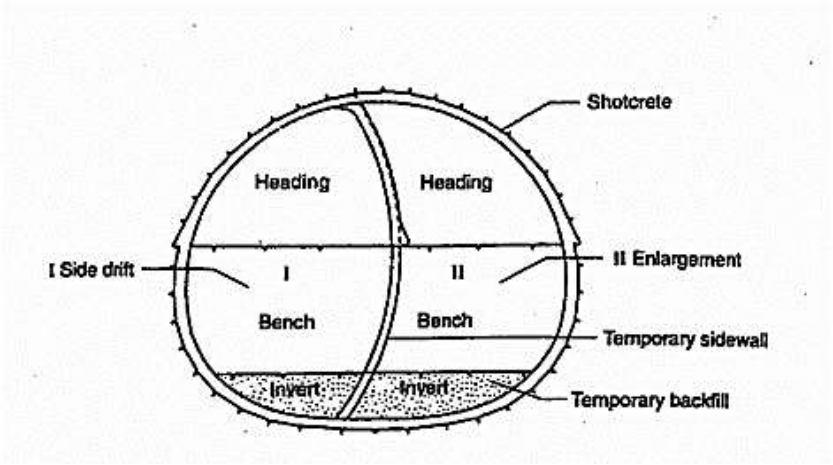

Figure 2-1: Example of divided tunnel face using sprayed concrete linings (Mair & Taylor, 1997)

Ground treatment is more easily undertaken from within tunnels with open faces (Figure 2-2). Reinforcement of the soil ahead of the face are required in order to improve stability and to control ground movements, whereas improvement in jet grouting techniques are being made to form umbrella arches as a prelining in difficult ground conditions. An extension of the concept of the umbrella-arch is sometimes referred to as mechanical pre-cutting method. This involves the cutting of the overlapping slots around the tunnel periphery in advance of the excavation, and filling them by means of sprayed concrete. The technique is always used in conjunction with face reinforcement and other forms of ground treatment.

a) Face reinforcement

b) Jet Grouting "Umbrella arches"

c) Pre-vault (pre-cutting)

*Figure 2-2: Ground treatment and prelining techniq*ue (Mair & Taylor, 1997)

2.1.1.2 Close face tunnelling

Mair & Taylor (1997) claim that considerable advance have been made in the use of sophisticated closed face tunnelling machines which operate in the principle of a pressurized face. These machines are used in unstable ground conditions where the face requires support at all times; this principally applies to permeable ground below the water table or soft clays. The slurry shield machine (Figure 2-3) is most commonly used in water bearing granular soils. The face is supported by a pressurized bentonite or polymer based slurry, which is circulated so that it and the excavated soil are removed to a separation plant.

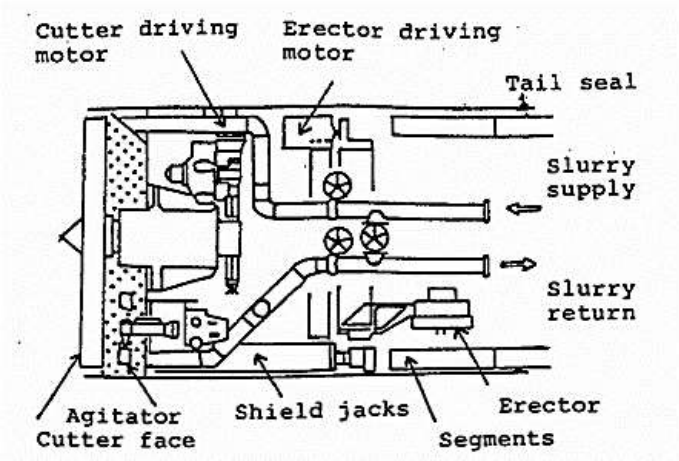

Figure 2-3: Principle of the slurry shield machine (Mair & Taylor, 1997)

Earth Pressure balance (EPB) machines are being used more universally for all types of unstable ground; the principle is shown in Figure 2-4. By controlling the entry of soil and water through the cutter face by means of earth pressure balance doors, and by conditioning the spoil so that it can easily be removed through a screw conveyor. It is possible to control the pressure of the excavated soil in the chamber to balance the earth and water pressures in the ground. In addition recent developments have centred on the injection of special slurries, foam and other materials in EPB machines to improve the properties of the excavated soil and facilitate the proper control of the pressure in the chamber.

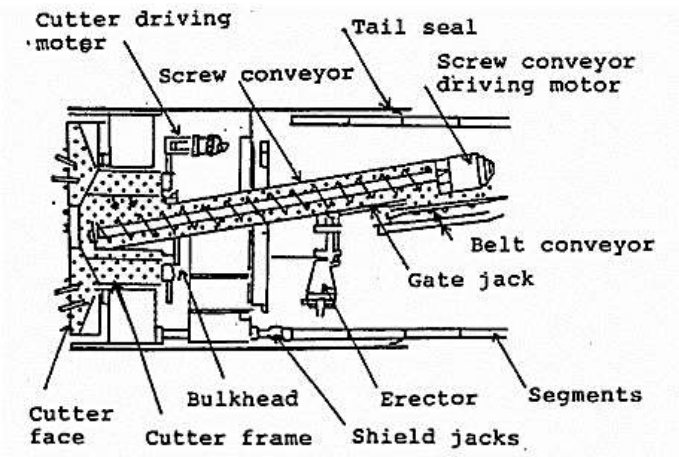

Figure 2-4: Principle of the earth pressure balance machine (Mair & Taylor, 1997)

2.1.2 Ground Improvement Techniques

This section describes the most common ground improvement measures currently used in tunnelling to improve soil stability and to reduce/control ground displacement. These techniques aid the tunnel construction and mitigate the effect of tunnelling on adjacent existing structures such as shallower tunnels and services. Many of the techniques described in this section can generally be applied either from the ground surface or from within the tunnel during construction.

2.1.2.1 Ground freezing

The principle of this technique is to use a refrigerant to convert in situ pore water into a frostwall, with the ice bonding the soil particles together. Freezing can be carried out from the surface or from the working face. If used from within the tunnel, freezing lances are installed from the tunnel in the direction of the tunnel excavation as the frozen ground should create an arching mechanism. The lances are situated in the crown, and if necessary, at the springline. In order to create a closed frozen body, the distance between the lances is usually about 1m and lances are 20m or more long. This allows the overlap of the frozen areas and provides an impermeable barrier. Cooling fluid is pumped through the freezing lances. For application from the ground surface, a freeze wall is formed around the periphery of the planned excavation or a layer above the tunnel crown is frozen, as frequently occurs in shallow tunnelling (Chapman et al., 2017). In this case, the refrigerant pipes are equally spaced at approximately 1m apart in order to ensure a continuous freeze wall.

Cooling materials that are used are brine with a temperature of -50˚C to -20˚C or liquid nitrogen which evaporates at -196˚C. The liquid nitrogen is injected into the ground via a direct process. It is the only effective method in fine grained soils and is good for short-term or

emergency projects. The brine is generally applied via the two phase method that uses a primary refrigerant like ammonia or freon to cool the brine.

The main advantages of this technique includes the possibility to increase the strength of the ground. It can be applied to the whole range of ground types and its application depends on the ground water flow. It is non-toxic and noiseless and it is totally removable, although some adverse reaction may occur in some soils.

The main difficulties lie both in the control of drilling deviations during the installation of the freezing pipes (which length is limited to 50 m) and of the circulation of large quantities of underground water. Ground to freeze may require weeks depending on the ground and on the groundwater conditions. Also, flowing water can cause heat drain and can prevent ground freezing, depending on the flow rate and on the type of the freezing used. (Leca & New, 2007) highlights that one of the main limitations of this technique in fine grained soils is the potential of the ground to heave during the freezing process and subsequent settlement at the end of the freezing process. Ground heave is related to the frost susceptibility of the ground. The lower is the permeability of the soil, the slower the water drains during the freezing process and greater is the heave. However, ground heave can be limited by controlling the speed of the freezing process. A careful monitoring of the ground temperature, refrigerant temperature and groundwater is also crucial throughout the freezing operation to ensure the formation of the frozen ring around the excavation face. Figure 2-5 shows the application of the ground freezing from within the tunnel to extend the flow path for water. In this case the freezing process is conducted from the crown to the tunnel springline (or above) and it is combined with the pressurised tunnelling.

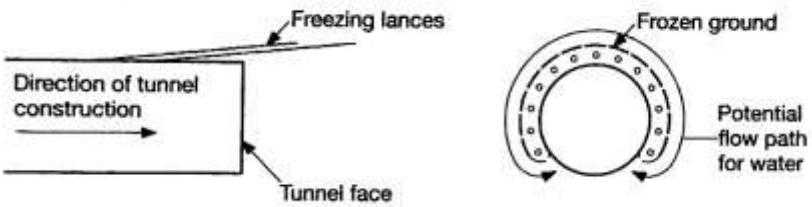

Figure 2-5: Ground freezing from within the tunnel (after Chapman et al., 2017)

2.1.2.2 Lowering of the groundwater table

This technique consists of pumping water from wellpoints or from deep filter wells to lower the groundwater table. Used for dewatering soil strata with high permeability, (generally greater than 10^{-5} m/s) or for lowering the groundwater level below a less permeable strata, this technique is widely used in open excavations, shallow tunnels and cut-and-cover tunnels.

Wellpoints limit the dewatering to a depth of 6 m as a consequence of the effective vacuum lift of the pump. They can be used from ground level or from inside the tunnel. They are installed at between 1-3 m intervals by wash boring and their spacing depends on the permeability of the ground. Deep walls are used instead to dewater to greater depths. These consist of 300 mm or greater well sunk at an average spacing of 3 m to below the level required for the dewatering. A filter is used at the base of the well around perforated suction pipes, above which a submersible pump is located.

This technique allows to achieve significant improvement of the ground properties, however it should not be used in settlement-critical inner city areas, in areas where there may be an influence on existing water supply aquifers or in area where there could be a potential adverse effect on the flora. Drawdown of the groundwater level can cause consolidation settlement in the surrounding ground and hence affect adjacent structures. An accurate monitoring during the operation is required. Also an intensive installations for holding the extracted water and treating it before it can be disposed of are required.

2.1.2.3 Grouting

Grouting consists of injecting a material into the ground to reduce the permeability of the ground and to strengthen and stabilise the ground.

Grouting operation can be carried out from the ground surface, from within an adjacent shaft to the tunnel operation or from within the tunnel construction itself. The grouting holes are drilled ahead of the advancing tunnel in a pattern of diverging holes at an acute angle to the tunnel axis to form overlapping cones of treated ground. For drill and blast tunnels the holes can be drilled at the face (Wood, 2002). For Tunnel Boring Machines (TBMs) the holes are drilled in the rear of the machine towards the advancing excavation or directly from the face through the cutter wheel.

Percussion and rotary drilling are used to install the grout tubes. The grouting tubes may be simple open-ended tubes, possible fitted with an expandable tip to prevent blockage during installation, or perforated tubes which allow grout to be injected over a specific length. Tube a manchettes or sleeved tubes (TAM) make successive injections at specific location possible. TAM includes an external tube that has perforations at appropriate intervals which are covered by an external elastic sleeve. These sleeves open by the internal pressure of the grout. A separate movable tube inside the case deliver the grout to the injection point. The grout is contained within the location of the perforation using seals either side of the end of this internal tube.

There are several types of grouting technique that can be classified as: permeation grouting, jet grouting and compaction grouting.

Permeation Grouting

This technique aims to fill the voids with either chemical or cement binders without disturbing the fabric of the ground. The range of particles sizes over which it can be applied is from sands (0.06mm) to coarse gravel (60mm).

Jet Grouting

This technique uses high pressure jets to break up the soil and replace it with a mixture of excavated soils and cement. The application of this technique is extended to a wider range of soils, from clays (<0.002 mm) to fine gravels (10 mm). Jet grouting can be used in pre drilled holes or in self-drilled jets. Once the jet has reached the required depth, it is rotated and the jetting fluids are pumped at high pressure to the jetting tip while the system is withdrawn from the hole at a controlled rate to form an in situ column. If it is not rotated then more of a "panel" shape is produced rather than a column.

The diameter of the column varies in the range 0.30–1.20 m depending on the technique used and the consistency and nature of the ground. Ground treatment can be performed through vertical, inclined or sub-horizontal borings. The last option can be implemented from the tunnel face. Particular attention must be paid, when using this approach in fine soil grounds, to potential adverse effects associated with unexpected pressure build up within the ground being excavated at the face (sudden fracture and large heave). The efficiency of this technique is well proven, and can lead, when used with a fine drilling mesh, to total ground substitution. There are, however, a number of implementation constraints (power consumption, spoil pro- cessing and removal, instantaneous loss of bearing capacity before the grout has set) which require a thorough evaluation to be made before this technique is used.

Compaction grouting

Compaction grouting consists of injecting a slow dump of grout such as an expanding bulb forms at a certain depth. The expansion causes deformation and densification in the surrounding soil and ultimately an improvement of the ground. The range of applicable soils for this method goes from sands (0.06 mm) to medium gravel (30 mm).

Suspension grouts and chemical solution grouts are the two main categories of grout type. Suspension grout consists of cement slurry with cement/water ratio of approximately 0.1 to 0.4 and an optional clay components. The purpose of the clay is to reduce cement consumption and to improve the stability and viscosity of the suspension. Sand can be added to grout suspension when large fissures are to be injected. Additives can be used in suspension grouts to prevent the clay particles flocculating. Suspension grout are best suited to injection into fissured rocks and granular media with large voids and porosity. Chemical grout consists of solutions and resins which form gels. They reduce the permeability by void filling and strengthen the ground. These grouts can be injected into very fine grained soils since some liquid grout such as resin types, have viscosities approaching that of water. The strength of chemical grouts is generally low compared to cement grouts.

In terms of basic properties, the following requirements should be met by the grout (Whittaker & Frith, 1990):

- Stability: grout should remain stable during the mixing and injection processes and not separate prematurely in the case of suspension grouts, or set prematurely if it is a liquid grout;
- Particle size: for a suspension grout this set the lower limit of the grain size of the soil that it can penetrate;
- Viscosity: this is a measure of its ability to penetrate soils. Other flow properties and the gelling time determine the maximum injection radius;
- Strength when set or gel strength: this depends on whether the grout is being used to strengthen the ground or reduce its permeability;
- Permanence/durability: the grout, when set, should resist chemical attack and erosion by groundwater.

Further details on grouting technique and grouting materials can be found in (Xanthakos et al., 1994) and (Moseley, M. P. & Kirsch, K., 2004).

2.1.3 Tunnel Face Stability

Adequate stability during construction is clearly of prime importance and particularly within urban environments where the consequence of major tunnel collapse can be catastrophic. The following section provides an insight of the tunnel face failure mechanism in cohesive soil and presents experimental and theoretical studies that evaluate the tunnel face stability in cohesive soil.

Stability of tunnel heading is particularly critical and referring to a circular cross-section, it may be considered in terms of idealized geometry shown in Figure 2-6. The heading can be supported by a fluid pressure σ_T such as compressed air or pressurized slurry (in case of slurry shield). It may be excavated in free air in face mode, in which case σ_T=0. The dimension P represents the distance from the face to the point where stiff support is provided; in the absence of a tunnelling shield, this is the distance from the face to the lining. In most cases, especially in ground of low permeability, when a tunnelling shield is in use the ground is in contact with the shield and therefore P can be taken to zero. An exception is when a shield is being used in ground of higher stability, such as stiff clays. In this case there is often an oversized cutting edge at the front of the shield. Therefore, determination of P then requires some judgements.

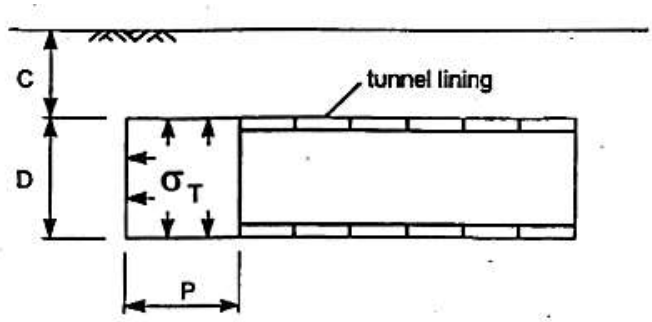

Figure 2-6: Tunnel heading in soft ground (Mair, Taylor 1997)

The issue of weather undrained of drained conditions are more applicable to the tunnel stability problem depends principally on the permeability of the soil, the excavation advance rate, and the size of the tunnel. Based on parametric study of seepage flow into tunnel excavations, (Anagnostou & Kovari, 1996) concluded that for most tunnels drained conditions are to be expected when the soil permeability is higher than 10^{-7} to 10^{-6} m/s and the excavation advance rate is 0.1-1m/h or less. Hence, in a predominately sandy soil, drained stability should be considered. In low permeability clayey soils undrained stability is of more importance during tunnel excavation.

2.1.3.1 Face failure mechanism in cohesive soil

In the case of cohesive soils face failure involves a large volume of ground ahead of the working front (Figure 2-7). This mechanism leads to the formation of a sinkhole at the ground surface with a width larger than one tunnel diameter (Leca & New, 2007).

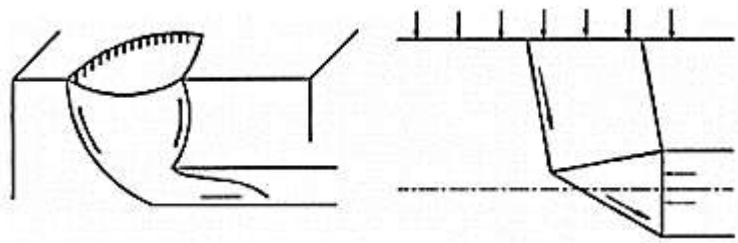

Figure 2-7: Face collapse: basic diagram in cohesive ground soils (Leca & New, 2007)

The same mechanism is presented in theoretical studies (Leca, E. & Dormieux, L., 1990) and it is also consistent with the observed failure mechanism based on centrifuge model tests (Mair, 1978) on tunnel headings in clays, where the mechanism propagates upwards and outwards from the tunnel invert becoming significantly wider than the tunnel diameter (Figure 2-8).

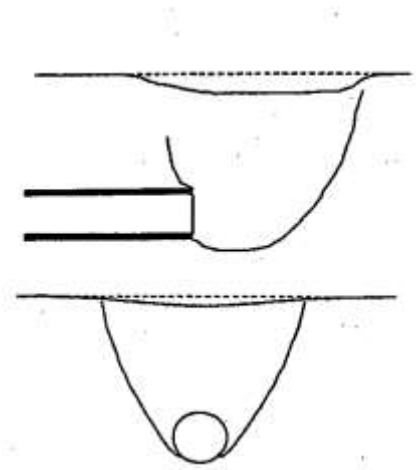

Figure 2-8: Observed failure mechanism based on centrifuge model test (Mair,1978)

2.1.3.2 Propagation of movement towards the surface

Ground movements initiated at the tunnel opening will tend to propagate towards the ground surface. The extent and time scale of this phenomenon typically is dependent on the geotechnical and geometrical conditions, as well as construction methods used on the site. Leca & New (2007) identified two propagation modes, based on the conclusions of in situ measurements and observations. These modes are referred to as primary mode and secondary mode.

The primary mode (Figure 2-9) occurs as ground stresses are released at the face. It is characterised by the formation of a zone of loosened ground above the excavation. The height of this zone is typically 1–1.5 times the tunnel diameter and about one diameter wide. Two compression zones develop laterally along the vertical direction (Leca & New, 2007).

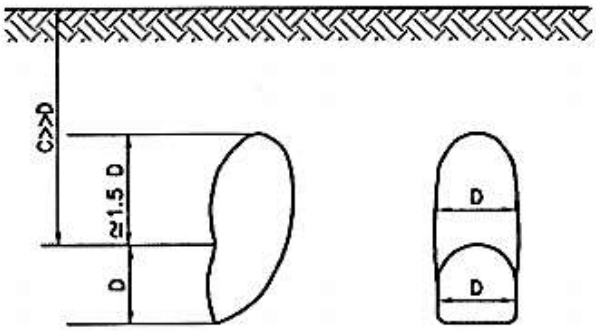

Figure 2-9: Primary mode: basic transverse cross section (Leca & New, 2007)

The secondary mode (Figure 2-10) may occur subsequently, when the tunnel is located close to the surface (*C/D* < 2.5) and insufficient confining support exists. These conditions result in the formation of a 'rigid' ground block, bounded by two single or multiple shear planes extending from the tunnel to the surface. Displacements at the ground surface above the opening are of the same order of magnitude as those generated at the opening.

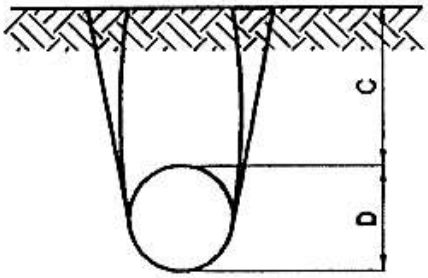

Figure 2-10: Secondary mode: basic transverse cross section (Leca & New, 2007)

These ground response mechanisms typically lead to vertical and horizontal displacements that tend to develop at the ground surface as excavation proceeds; this results in what is referred to as the settlement trough (Figure 2-11).

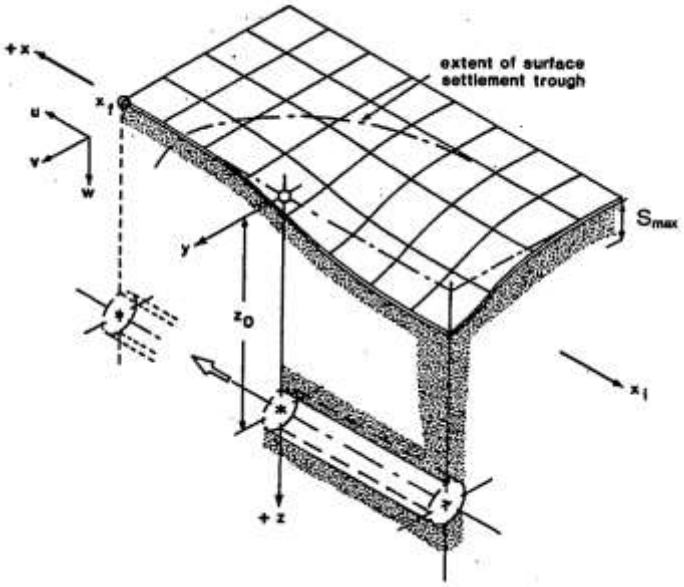

Figure 2-11: Three dimension settlement through

For practical purposes, the observed three-dimensional trough is conventionally characterised by means of a transverse trough and a longitudinal trough along the tunnel centre-plane.

2.1.3.3 Face stability in cohesive soils

The stability of the front of a tunnel driven in cohesive material was studied by several Authors since the paper by (Broms & Bennermark, 1967) on a stability criterion based on laboratory extrusion tests and field observations. The undrained stability for a homogeneous soil was defined in terms of stability ratio N equals to the overburden stress divided by the undrained shear strength:

$$N = \frac{\gamma H}{C_u}. \tag{2.1}$$

Where γ is the bulk unit weight of the soil, H is the depth to the tunnel axis $(C + D/2)$, and C_u is the undrained shear strength at tunnel axis level.

In the more general case where there is a surcharge at the ground surface and a support pressure is used at the face, for example as applied via an earth pressure balance machine (EPBM), the stability ratio *N* can be expressed as the difference between the total overburden stress in the ground at the axis of the tunnel (before the tunnel is constructed) and the tunnel pressure divided by the undrained shear strength:

$$N = \frac{\sigma_s + \gamma H - \sigma_T}{C_u} \tag{2.2}$$

Where σ_s is the surface surcharge pressure (if any) and σ_T is the tunnel support pressure (if any). They concluded that if *N* is less than 6 then the opening will be stable.

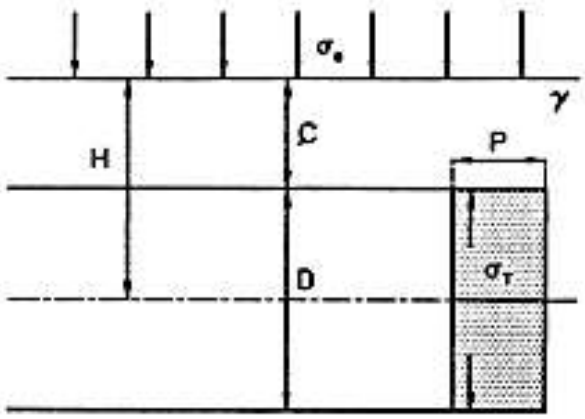

Figure 2-12: Stability parameters (Leca & New, 2007)

Similar conclusions, based on field observations, were presented by (Peck, 1969) who claimed that *N* values ranging from 5 to 7 typically result in tunnelling difficulties and may cause tunnel face instability. Furthermore, based on findings from centrifuge testing (Leca & New, 2007)has suggested the following typical values:

- when N≤3 : the overall stability of the tunnel face is usually ensured;
- when 3<N≥6: special consideration must be taken of the evaluation of the settlement risk, with large amounts of ground losses being expected to occur at the face when N≥5;

- when *N*>6: the face is unstable.

Other three parameters are involved in the stability of the opening during construction:

- *C/D* which controls the effect of depth on the stability condition;
- $\frac{\gamma D}{c_u}$ which account for the possibility of localized failures occurring at the face;
- *P/D* which account for the distance behind the face until the lining is installed.

With respect to the first ratio it can be considered that if C/D <2 a detailed analysis of the face stability is required. This criterion is in accordance with the definition of shallow tunnel where the ground above the tunnel crown is assumed to have no bearing capacity. With reference to the second parameter it should be taken into account that for $\frac{\gamma D}{c_u} > 4$ localised failure can occur at the face. In addition the effect of P/D on the critical stability ratio (Nc) is shown in Figure 2-13 using data from centrifuge test.

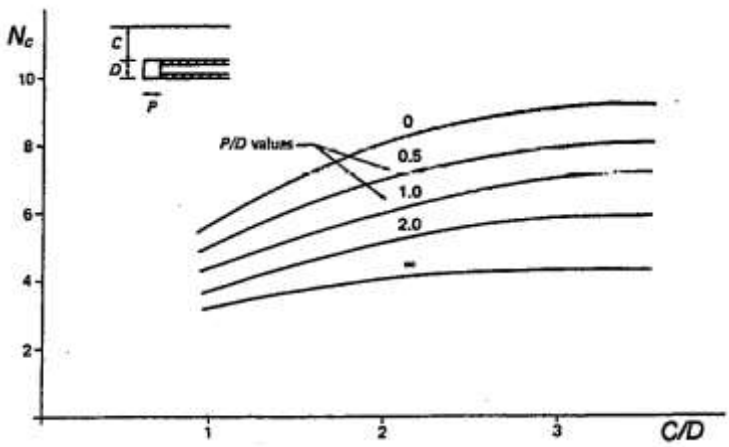

Figure 2-13: Critical stability ratio Nc (Mair & Taylor, 1997)

2.1.3.4 <u>The limit theorem of Davis et al. (1980)</u>

With reference to Equation (2.2) a more theoretical approach was proposed by Davis et al., (1980) which is derived from the limit state design concept. According to the definition of stability factor *N*, one possible approach to maintain stability would be to set the tunnel support

pressure equal to the overburden stress (i.e. N=0). The problem with this approach is its expense and also the health risks for tunnellers working at high air pressures. In practice, the air pressure in a tunnel is often given as the value to ensure that there is no flow of water into the tunnel. This is achieved by applying a tunnel pressure greater than the pore water pressure at the tunnel invert. However Davis et al., (1980) investigated which tunnel pressure σ_T is required in order to maintain the stability of the heading for different values of the parameters that were mentioned above ($D, C, P, \gamma, \sigma_S$) and the undrained shear strength of the ground.

Three different cases were taken into account separately and the analyses were carried out studying the value of $(\sigma_S - \sigma_T)/C_u$ for limiting stability once the values of independent parameters C/D, P/D, and $\gamma D/C_u$ were fixed. In particular the first cases are both problems of plane strain; whereas the first is referred to the radial pressure in unlined cylindrical tunnel (P/D large), the second one concerns the "plane strain tunnel heading" when the excavated volume is not cylindrical but instead similar to a long wall mining excavation. The third case is a three-dimensional problem referring as "circular tunnel heading" with the geometry shown in Figure 2-14 when P/D=0. It is worth mentioning that in their analysis they assumed Cu constant with depth although the variation of undrained cohesion with depth depends on the history of the soils. However the Authors claimed that this method can be extended to cases where there is an arbitrary distribution of Cu with depth.

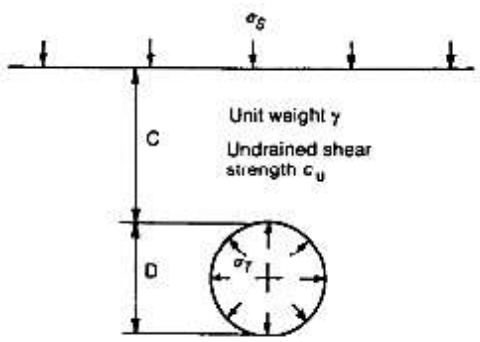

Figure 2-14: The plane strain unlined circular tunnel (Davis et al., 1980)

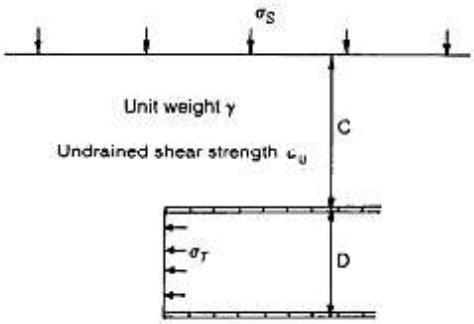

Figure 2-15: The plane strain tunnel heading (Davis et al., 1980)

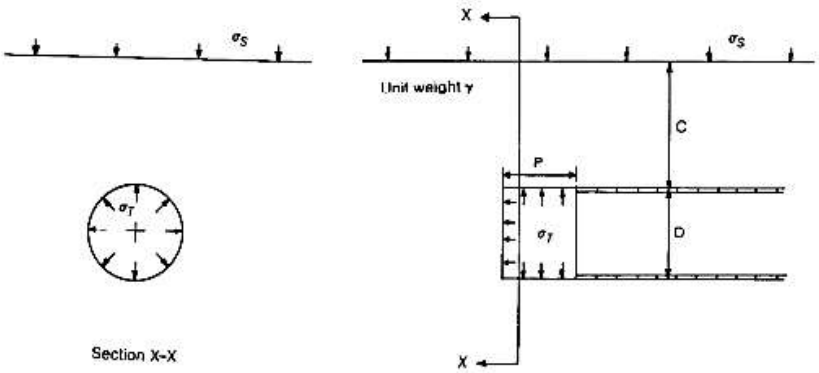

Figure 2-16: The circular tunnel heading (Davis et al., 1980)

Based on considerable experimental evidences, the soil was idealised as an elastic, perfectly plastic material with cohesion equal to *Cu.* According to the theory of plasticity the collapse load for a particular configuration of loading on a perfectly plastic body is unique. The lower bound theorem claims that if any stress field can be found which supports the loads, and is everywhere in equilibrium without yield being exceed, then the loads are lower than (or equal to) those for collapse. On the other hand the upper bound theorem states that if a work calculation is performed for a kinematically admissible collapse mechanism then the loads thus deduced will be higher (or equal to) those for collapse. As a result the lower bound theorem provides a safe estimate of the tunnel pressure necessary to maintain stability (i.e. higher or

equal to that actually required) whereas the upper bound theorem furnishes an unsafe estimate (Davis et al., 1980).

2.1.3.5 Upper bound plane strain tunnel heading: inward collapse

Referring to the case of the "plane strain heading", the upper bound failure mechanism illustrated in Figure 2-15 is consistent with the observed failure mechanism based on centrifuge model test for cohesive soils.

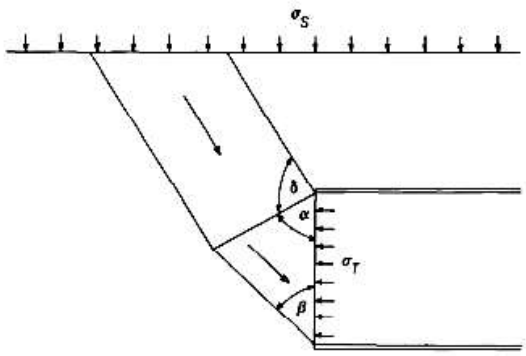

Figure 2-17: Upper bound mechanism for the plane strain heading (Davis et al,1980)

Davis et al., (1980) optimized the geometry of the model in terms of variable angles in order to find the critical collapse load. Thus with $tan\alpha = tan\beta = 2\sqrt{C/D + 1/4}$ and δ=π/2 the collapse load was found to be:

$$\frac{\sigma_s - \sigma_T}{c_u} = 4\sqrt{\frac{C}{D} + 1/4} \tag{2.3}$$

Considering the self-weight of the soil ($\gamma D/Cu$>0) in the work calculation for the mechanism shown in Figure 2-17, the equation above was written as:

$$\frac{\sigma_s - \sigma_T}{C_u} + \frac{\gamma D}{C_u}\left(\frac{C}{D} + \frac{1}{2}\right) = 4\sqrt{\frac{C}{D} + 1/4} \tag{2.4}$$

Referring to the expression on the left-hand side of the Equation (2.4) it is possible to identify the first term with the net work done by the pressures, the second term with the work done by the self-weight of the soil and the third term with the plastic work dissipated on the sliding surfaces. Referring to the second member as *Ncr*, the Equation (2.4) can be written as:

$$\frac{\sigma_s - \sigma_T}{C_u} + \frac{\gamma D}{C_u}\left(\frac{C}{D} + \frac{1}{2}\right) = N_{cr} = f(C/D) \tag{2.5}$$

The solution of the numerical computation was plotted in terms of *Ncr* against *C/D* for all values of *γD/Cu* since the latter parameter was found to have a negligible influence on this failure mechanism (Figure 2-18).

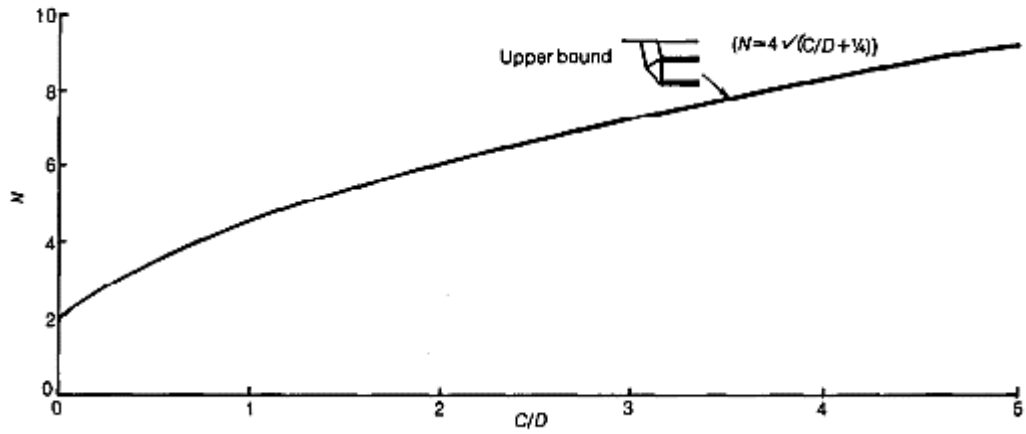

Figure 2-18: Upper bound stability solution for plane strain heading (Davis et al., 1980)

With reference to the Equation (2.4) since *C+D/2* is equal to *H* by definition, it is easy to demonstrate that the expression on the left-hand side corresponds to the stability ratio *N* proposed by Broms & Bennermark, (1967). As a result it can be written as:

$$\frac{\sigma_s - \sigma_T + \gamma H}{C_u} = 4\sqrt{\frac{C}{D} + 1/4} \tag{2.6}$$

The experimental critical value of the stability ratio *N* suggested by Broms & Bennermark, (1967), Peck, (1969) and Leca & New, (2007) are consistent with the Equation

(2.4). It follows that a theoretical explanation can be associated to the benchmarks used in practice. In particular it is made evident that the critical value of N=6 can be obtained by the Equation (2.6) for C/D=2. Leca & New, (2007) suggest that a detailed analysis of the face stability is required if C/D<2. This benchmark is also in accordance with the definition of shallow tunnels (C/D<2) for which the ground above the tunnel crown is assumed to have no bearing capacity (Chapman et al., 2017).

2.1.3.6 Upper bound plane strain tunnel heading: local collapse

Although $\gamma D/Cu$ does not affect the collapse in failure mechanism, it was evaluated greatly relevant in term of local collapse (2.25). In particular Davis et al. (1980) found that the critical value, over which the collapse will take place independently from the value of the uniform tunnel pressure, is 8.28 for an upper bound plane strain tunnel heading. On the other hand for $\gamma D/Cu$<4 there is no possibility for the local collapse to occur with a uniform tunnel pressure equals to ($\sigma_S+\gamma(C+D/2)$) since it corresponds to N=0 (Equation (2.4)). Even though this mechanism involves no immediate subsidence of the ground surface, it is likely that this would be the first step of a progressive failure which would eventually propagate to the soil. Since for a given site the value of γ/Cu would be predetermined, the limiting value of $\gamma D/Cu$ can be seen as specifying the maximum height of a tunnel heading which can be constructed under uniform tunnel pressure (Davis et al., 1980).

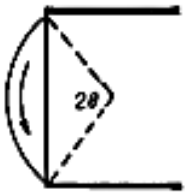

Figure 2-19: Local collapse for plane strain tunnel heading (Davis et al,1980)

2.1.3.7 Upper bound plane strain tunnel heading: blow out

The blow out is a failure mechanism caused by an excessive tunnel pressure. With reference to the Equation (2.5) when $\sigma_T > \sigma_S$ the direction of the motion is reversed and it becomes:

$$\frac{\sigma_T - \sigma_S}{C_u} + \frac{\gamma D}{C_u}\left(\frac{C}{D} + \frac{1}{2}\right) = -N = -f(C/D) \tag{2.7}$$

Thus a high estimate of tunnel pressure to cause blow-out can be evaluated by reversing the sign of the stability ratio for inward collapse.

2.2 Moist air flow and evaporation

This Section provides an insight of the moist air turbulent flow and of the evaporation in open air, focusing on the derivation of Penman equation for the potential evaporation from liquid surfaces or saturated soil (Tarantino, (in prep.)).

2.2.1 Moist air turbulent flow

2.2.1.1 Atmospheric Surface Layer

In the atmosphere, the largest changes in wind velocity, temperature and humidity usually occur in the vertical direction and in proximity of the surface. For this reason the air close to the surface is regarded as a boundary layer, as a concept set forth by Prandtl for the momentum transport in the neighbourhood of a solid wall (Brutsaert, 1982). Accordingly, the horizontal scales of most problems are much larger than the vertical, so that the horizontal gradients and the vertical velocities are negligible as compared to the vertical gradients and the horizontal velocities.

The atmospheric boundary layer (ABL) can be defined as the lower part of the atmosphere where the nature and properties of the surface affect the turbulence directly. Under stable condition the thickness of the boundary layer may range from only a few tens of meters to about 500 m. As shown in Figure 2-20 the ABL includes a interfacial sublayer which is the closest region to the surface, the inner region and the outer region. In the outer region the flow is nearly indipendent of the nature of the surface and mainly determined by the free-stream velocity, whereas in the inner region, also called wall, Prandtl or surface layer, the flow is strongly affected by the nature of the surface. Between the outer and the inner region, it is assumed a region of overlap. The inner region is defined as a fully turbolent region where the vertical turbulent fluxes do not change appreciably from their value at the surface. The lower part of the inner region is referred to as dynamic sublayer, in which the Carolis forces due to the rotation of the earth are negligible. In this layer, according to Prandtl (1904) the vertical scales of the problem are much smaller than the horizontal and hence, the vertical gradients are much larger than the horizontal. The effects of density stratification resulting from humidity and temperature gradients are also negligible. Finally, in the closest region to the surface, the turbolence is strongly affected by the structure of the roughness elements. Thus the nature of the roughness elements must be considered. This region is referred to as interfacial sublayer and its thickness is of the order of the mean height of the roughness obstacles h_0. In the case of smooth flow it is often referred to as the viscous sublayer and its thickness is of the order of $30\ \nu/u_*$, where ν is the dynamic viscosity and u_* is the friction velocity (Brutsaert, 1982).

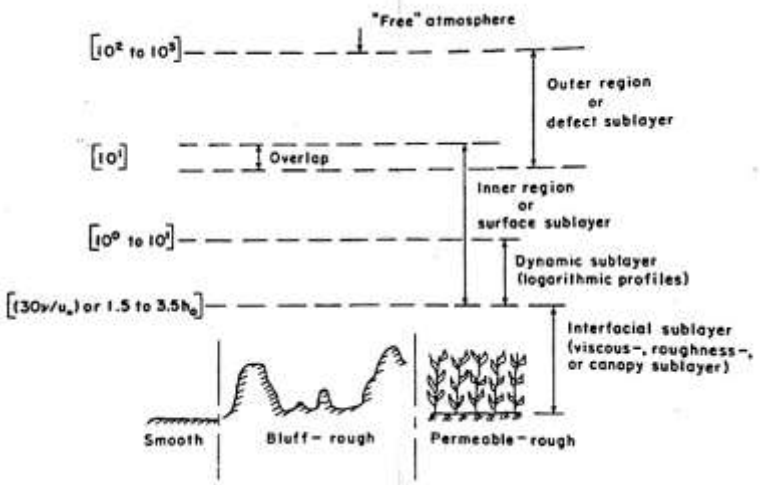

Figure 2-20: Schematic of the sublayers of the atmospheric boundary layer ABL (Brutsaert, 1982)

The study of transport of energy and transport of water vapour in the Atmospheric Boundery Layer (ABL) generally takes into account the following assumptions:

- The dynamic viscosity ν and the molecolar thermal conductivity k_T are constant;
- The work dissipated by the viscous shear stresses is negligible;
- The mix of dry air and water vapour is assumed to be incompressible;
- The density of the fluid is not function of the pressure (Boussinesq hypotheis);
- In the dynamic sublayer, the Reynolds number is generally high (Re~10^7) and the turbolent terms in the equations of conservations are several orders of magnitude greater than the molecolar terms, which are generally neglected.

If it is assumed that the transport of air is stationary the equations of conservation of vapour mass, of momentum in x direction and of energy become, respectively:

$$\frac{\partial}{\partial z}\left(\rho\overline{q_h' \, v_z'}\right) = 0 \tag{2.8}$$

$$\frac{\partial}{\partial x}\left(\rho\overline{v_x' \, v_z'}\right) = 0 \tag{2.9}$$

$$\frac{\partial}{\partial z}\left(\rho c_p \overline{T' v_z'}\right) = 0 \tag{2.10}$$

Where the air temperature *T*, the air velocity *v* and the specific humidity q_h are expresssed as the sum of the mean term and of the fluctuating term ($T = \overline{T} + T', v_i = \overline{v_i} + v_i'$, $q_i = \overline{q_i} + q_i'$), ρ is the density of the the mix of dry air and water vapour and c_p is the specific heat of air. By indicating *E* as the flux of mass of vapour, *H* as the flux of sensible heat and τ as the turbolent shear stress or Reynolds shear stress, it follows:

$$E = -\rho \overline{q_h' v_z'} = const \tag{2.11}$$

$$\tau = \rho \overline{v_x' \, v_z'} = \tau_0 = const \tag{2.12}$$

$$H = -\rho c_p \overline{T' v_z'} = const \tag{2.13}$$

In order to define the flux of vapour mass, momentum (tangential stress) and sensible heat is necessary identifying the mean value at the second term of equations (2.11), (2.12) and (2.13) . This problem is known as the *problem of closure* and it is generally solved by identifying semi-empirical relationship between the average values of the fluctuation terms at the second term of the equations and the mean components of velocity, specific humidity and temperature.

2.2.1.2 Theory of the mixing length model in turbulent flow

Prandtl (1904) has proposed the theory of the mixing length model in the turbolent flow as a method for the problem of closure. The turbolent flow is studied as a sequence of eddies that moves air particles for a short period before they mix with the surrounding air. These eddies transfer momentum, sensible heat and mass from one point to another one, in accordance with the molecolar transport of gas. If an air particle at height z is considered to mix with the surrounding air at *z+l'*, the fluctuating velocity v_x' can be expressed as follows:

$$v_x' = \overline{v_x}\,(z + l') - \overline{v_x}(z) \cong l'\,\frac{d\overline{v_x}}{dz} \tag{2.14}$$

where l' is the fluctuating distance, which can be assumed proportional to the distance z from the surface as:

$$l' = kz \tag{2.15}$$

It follows that the fluctuating velocity v_x' can be written as:

$$v_x' = kz\,\frac{d\overline{v_x}}{dz} \tag{2.16}$$

2.2.1.3 Logarithmic profile of the mean wind speed

It has been well verified experimentally, and it is therefore almost accepted by definition, that in the dynamic sublayer the profiles of the mean wind speed, mean temperature and mean specific humidity are all logarithmic function of *z*. The logarithmic relationship was first established for the mean wind (Brutsaert, 1982).

Assuming that $v_x' \cong v_z'$ equation (2.12) becomes:

$$\tau_0 = \rho k^2 z^2 \left(\frac{d\overline{v_x}}{dz}\right)^2 = const \tag{2.17}$$

Defining the friction velocity *u** as:

$$u^* = \sqrt{\frac{\tau_0}{\rho}} \tag{2.18}$$

it follows that:

$$\frac{u^*}{z\,\frac{d\overline{v_x}}{dz}} = k \tag{2.19}$$

where *k* is the von Kármán's constant and it is equal to *k*=0.41, based on experimental observations (Brutsaert, 1982). Equation (2.19) can be integrated as follows:

$$\frac{\overline{v_x}}{u^*} = \frac{1}{k}\ln\left(\frac{z}{z_{0m}}\right) \qquad z \gg z_{0m} \tag{2.20}$$

where z_{0m} is an integration constant whose dimesions are length; herein it is referred to as the momentum roughness parameter. It is worth to stress that this velocity profile has been obtained assuming that the viscous tangential stress is negligible in the Navier-Stoke turbolent equations for incompressible fluids . Therefore it is valid only in the fully turbulent region and it cannot be extended to the proximity of surface (viscous sublayer). Experimental results (Brutsaert, 1982) show that, in case of smooth surface, the turbulent region develops at a distance z from the surface equals to $\delta_l = 30\ \nu/v^*_x$,where ν is the kinematic viscosity. The term δ_l represents the distance from which equation (2.20) is valid.

The logarithmic profile is shown in Figure 2-21. The dotted line represents the extension of the logarithmic profile of the velocity in the viscous sublayer. It is possible to see that the paramenter z_{0m} represents the height at which the logarithmic profile intercept the vertical axis. This parameter depends on the nature of the surface.

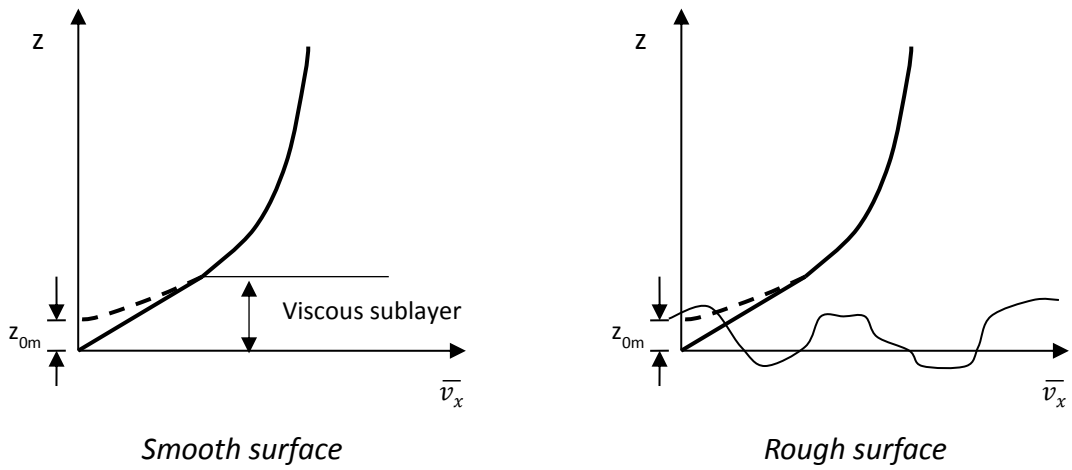

Figure 2-21. Logarithmic profile of the air velocity in the proximity of a smooth surface and a rough surface.

In the case of rough surfaces, with the average height or size of the roughness elements much larger than ν/v^*_x, the surface is called dynamically rough and the viscous sublayer is

absent. For a rough surface the momentum roughness z_{0m} is referred to as surface roughness length. Typical values of z_{0m} are listed in Table 2-1.

Table 2-1:Values of the surface roughness length z_{0m} for different types of surface (after (Trombetti & Tagliazucca, 1994)

Surface	**z_0 (m)**
Flat desert	0.0005
Mown grass, few trees in winter time	0.006-0.01
Uncut grass, isolated trees, airport runway	0.02
Wheat stubble plain (h_0=18 cm)	0.025
Long grass, crops, farmland, rocky ground (h_0=60 cm)	0.05
Many hedges	0.08
Many trees	0.15-0.3
High vegetation (h_0=1-2 m)	0.2
Trees (h_0=10-15 m)	0.4-0.7
Forests	0.7-1.2

In the case of rough surfaces there is some uncertainties concerning the reference level z=0 to be used in the equations (2.19) and (2.20). For very sparsely placed roughness elements this level can be taken at the base of the roughnesses; on the other hand, for extremely densely placed elements, z=0 should refer to the level of top of the elements. Hence, in most situations the zero level reference should be located at a height somewhere between the tops and the bases of the roughness obstacles. To minimise this difficulty, it is common practice to define z=0 as the level of the bases of the roughness elements, and to allow for a shift in reference level for the coordinate used in equations (2.19) and (2.20):

$$\frac{u^*}{(z-d_0)\,\frac{d\overline{v_x}}{dz}} = k \tag{2.21}$$

$$\frac{\overline{v_x}}{u^*} = \frac{1}{k}\ln\left(\frac{z-d_0}{z_{0m}}\right) \qquad z \gg z_{0m} \tag{2.22}$$

where d_0 is called the zero-plan displacement height.

2.2.1.4 Logarithmic profile of the mean specific humidity

In a similar way to equation (2.16), the the fluctuating velocity v_z' and the fluctuating specific humidity q_h' can be written as:

$$v_z' = kz\frac{d\overline{v_x}}{dz} \tag{2.23}$$

$$q_h' = k_v z\frac{d\overline{q_h}}{dz} \tag{2.24}$$

Where k_v is the von Kármán constant for the water vapour. By substituing equations (2.23) and (2.24) in equation (2.11) can be obtained:

$$E = -\rho k k_v z^2 \frac{d\overline{v_x}}{dz}\frac{d\overline{q_h}}{dz} \tag{2.25}$$

Substituing equation (2.18) in equation (2.25) it follows that:

$$E = -\rho k_v z u^* \frac{d\overline{q_h}}{dz} \tag{2.26}$$

This equation can be integrated as follows:

$$(\overline{q_{hs}} - \overline{q_h}) = \frac{E}{k_v \rho u^*}\ln\left(\frac{z}{z_{0v}}\right) \qquad z \gg z_{0v} \tag{2.27}$$

where $\overline{q_{hs}}$ is the specific humidity at the surface and z_{0v} is the water vapour roughness length. This latter parameter represents the height at which $\overline{q_{hs}}$ becomes equal to $\overline{q_h}$ if the logarithmic profile was extrapolated downward outside its actual range of validity. By substituting equation (2.20) in equation (2.27) it follows that:

$$E = \frac{k_v k \rho \overline{v_x}(z)}{ln\left(\frac{z}{z_{0m}}\right) ln\left(\frac{z}{z_{0v}}\right)}\,[\overline{q_{hs}} - \overline{q_h}(z)] \tag{2.28}$$

In general , it is reasonable to assume that $k=k_v$ (Brutsaert, 1982). In addition, by assuming that $z_{0v}=z_{0m}$, although this assumption can result in considerable error (Brutsaert, 1982), it is obtained the following expression for the flux of mass of water vapour:

$$E = \frac{k^2 \rho \overline{v_x}(z)}{\left[ln\left(\frac{z}{z_{0m}}\right)\right]^2} \left[\overline{q_{hs}} - \overline{q_h}(z)\right] \tag{2.29}$$

In the case of rough surfaces, equations (2.27), (2.28) and (2.29) are modified as follows:

$$(\overline{q_{hs}} - \overline{q_h}) = \frac{E}{k_v \rho u^*} \ln\left(\frac{z - d_0}{z_{0v}}\right) \qquad z \gg z_{0v} \tag{2.30}$$

$$E = \frac{k_v k \rho \overline{v_x}(z)}{ln\left(\frac{z-d_0}{z_{0m}}\right) ln\left(\frac{z-d_0}{z_{0v}}\right)} \left[\overline{q_{hs}} - \overline{q_h}(z)\right] \tag{2.31}$$

$$E = \frac{k^2 \rho \overline{v_x}(z)}{\left[ln\left(\frac{z-d_0}{z_{0m}}\right)\right]^2} \left[\overline{q_{hs}} - \overline{q_h}(z)\right] \tag{2.32}$$

2.2.1.5 Logarithmic profile of the mean wind temperature

In a similar way to equation (2.16), the fluctuating air temperature T' can be written as:

$$T' = k_h z \frac{d\overline{T}}{dz} \tag{2.33}$$

where k_h is the von Kármán constant for the temperature. By substituing equtions (2.23) and (2.33) in equation (2.13) it is obtained:

$$H = -\rho c_p k k_h z^2 \frac{d\overline{v_x}}{dz} \frac{d\overline{T}}{dz} \tag{2.34}$$

By substituing equation (2.19) in equation (2.34) it follows:

$$H = -\rho c_p k_h z u^* \frac{d\overline{T}}{dz} \tag{2.35}$$

This equation can be integrated as follows:

$$(\overline{T_s} - \overline{T_h}) = \frac{H}{k_v \rho c_p u^*} \ln\left(\frac{z}{z_{0h}}\right) \qquad z \gg z_{0h} \tag{2.36}$$

where z_{0h} is the temperature roughness length and $\overline{T_s}$ is the specific humidity at the surface. The parameter z_{0h} represnts the heigth at which $\overline{T}$ would be equal to the value at the

surface $\overline{T_s}$ if the logarithmic profile was extrapolated downward outside its actual range of validity. By substituting equation (2.20) in equation (2.36) it follows that:

$$H = \frac{k_v k \rho c_p \overline{v_x}(z)}{ln\left(\frac{z}{z_{0m}}\right) ln\left(\frac{z}{z_{0h}}\right)} [\overline{T_s} - \overline{T}(z)] \tag{2.37}$$

In general, it is reasonable assuming $k=k_h$ (Brutsaert, 1982). In addition, by assuming that $z_{0h}=z_{0m}$, although this assumption can result in considerable error (Brutsaert, 1982), the following expression of the flux of the sensible heat energy can be achieved:

$$H = \frac{k^2 \rho c_p \overline{v_x}(z)}{\left[ln\left(\frac{z}{z_{0m}}\right)\right]^2} [\overline{T_s} - \overline{T}(z)] \tag{2.38}$$

In the case of rough surfaces, the equations (2.36), (2.37) and (2.38) are modified accordingly as follows:

$$(\overline{T_s} - \overline{T_h}) = \frac{H}{k_v \rho c_p u^*} \ln\left(\frac{z - d_0}{z_{0h}}\right) \qquad z \gg z_{0h} \tag{2.39}$$

$$H = \frac{k_v k \rho c_p \overline{v_x}(z)}{ln\left(\frac{z-d_0}{z_{0m}}\right) ln\left(\frac{z-d_0}{z_{0h}}\right)} [\overline{T_s} - \overline{T}(z)] \tag{2.40}$$

$$H = \frac{k^2 \rho c_p \overline{v_x}(z)}{ln\left(\frac{z-d_0}{z_{0m}}\right) ln\left(\frac{z-d_0}{z_{0h}}\right)} [\overline{T_s} - \overline{T}(z)] \tag{2.41}$$

2.2.2 Evaporation in open air

2.2.2.1 Equation of state of moist air

For many practical purposes the moist air is considered as a mixture of the dry air and the water vapour. In the literature, both gases are studied as perfect gases by means of the ideal gas laws. The total pressure of the moist air is calculated by using Dalton's law as the sum of the partial pressure of each component of the moist air.

The *density of the water vapour* ρ_v is defined as the ratio between the mass of the water vapour m_v and the total volume of the moist air V:

$$\rho_v = \frac{m_v}{V} \tag{2.42}$$

Similarly, the *density of the dry air* ρ_d is defined as the ratio between the mass of the dry air m_d and the total volume of the moist air:

$$\rho_d = \frac{m_d}{V} \tag{2.43}$$

The *specific humidity* q is defined as the mass of water vapour m_v per unit mass of moist air and is expressed as follows:

$$q = \frac{m_v}{m_d + m_v} = \frac{\rho_v}{\rho} \tag{2.44}$$

According to Dalton's law, the total pressure in a mixture of perfect gases equals the sum of the partial pressures of each component gas. This allows to express the total pressure of the moist air p as the sum of the pressure of the dry air p_d and the pressure of the water vapour p_v:

$$p = p_d + p_v \tag{2.45}$$

Each gas component of the mixture obeys to its own equation of state, thus the density of the dry air ρ_d is

$$\rho_d = \frac{m_d}{V} = \frac{n_d M_d}{V} = \frac{p_d}{(R/M_d)T} = \frac{p - p_v}{R_d T} \tag{2.46}$$

where n_d is the number of moles of dry air, V is the volume of the gas, M_d is the molecular weight of the dry air ($M_d = 28.966\ g\ mol^{-1}$), R is the universal gas constant ($R = 8.314\ J\ K^{-1}\ mol^{-1}$), R_d is the gas constant of dry air ($R_d = 287.04\ J\ K^{-1}\ kg^{-1}$) and T is the absolute temperature. Similarly, the density of water vapour is

$$\rho_v = \frac{m_w}{V} = \frac{n_w M_w}{V} = \frac{p_v}{(R/M_w)T} = \frac{p_v}{R_w T} \tag{2.47}$$

where n_w is the number of moles of water, V is the volume of the gas, M_w is the molecular weight of the water vapour ($M_w = 18.016\ g\ mol^{-1}$), R_w is the gas constant of water vapour ($R_w = 461.50\ J\ K^{-1}\ kg^{-1}$). The density of water vapour can also be expressed in terms of R_d as follows:

$$\rho_v = \frac{p_v}{R_w T} = \frac{p_v}{R_d(R_w/R_d)T} = 0.622\ \frac{p_v}{R_d T} \tag{2.48}$$

Combining equations (2.46) and (2.48) the equation of state of moist air is obtained:

$$\rho = \rho_d + \rho_v = \frac{p}{R_d T}\left(1 - 0.378\frac{p_v}{p}\right) \tag{2.49}$$

This equation shows that the density of the water vapour is smaller than that of the dry air at pressure p. Considering the definition of the specific humidity q as

$$q = \frac{\rho_v}{\rho} \tag{2.50}$$

and combining equations (2.47) and (2.48), the equation of state of moist air can also be expressed without the term p_v as follows:

$$p = \rho R_d T(1 + 0.61q) \tag{2.51}$$

Often it is also expressed as

$$p = \rho R_d T_V \tag{2.52}$$

where T_V is the virtual temperature defined by:

$$T_V = T(1 + 0.61q) \tag{2.53}$$

and it represents the temperature that the dry air should have in order to have the same density as moist air with given q, T and p.

From equations (2.48) and (2.51) the specific humidity can be written as:

$$q = \frac{\rho_v}{\rho} = 0.622 \frac{1}{\left({}^{p}/_{p_v} - 0.378\right)} \tag{2.54}$$

In saturated conditions, the pressure of the water vapour at the temperature of 20°C is $p_v = 2.337\ kPa$. Considering the atmospheric pressure $p = 101.325\ kPa$, the maximum value of the specific humidity q at the temperature of 20°C is:

$$(q)_{\max} = 0.0145 \tag{2.55}$$

2.2.2.2 Mass balance at the soil-atmosphere interface

The soil atmosphere interface is assumed to be infinitesimally small, hence with no storing capacity of mass. For this reason the equation of the water mass balance can be written as:

$$q_m = q_{ml} + q_{mv} = \rho_w (E^* - P^*) \tag{2.56}$$

where q_{ml} and q_{mv} are the water fluxes exiting the soil in liquid and vapour phase respectively, ρ_w is the density of water, E^* is the evaporation rate and P^* is the precipitation. The mass fluxes at the interface are summarised in Figure 2-22 . The black arrows indicate the flows related to the liquid water whereas the empty arrow indicate the flows related to water vapour.

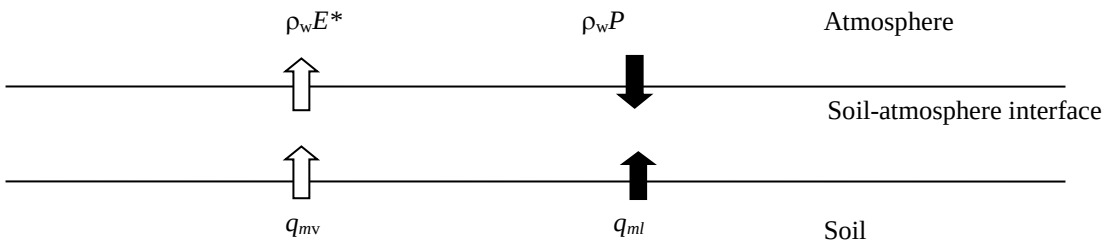

Figure 2-22: The mass fluxes at the interface soil-atmosphere

2.2.2.3 Energy balance at the soil-atmosphere interface

The energy balance equation at the soil atmosphere interface can be obtained from the first principle of the thermodynamics for an open system:

$$q + h_v(T_s)q_{mv} + h_l(T_s)q_{ml} = -R_n + H + h_v(T_s)(\rho_l E^*) - h_l(T_a)(\rho_w P^*) \qquad (2.57)$$

where q is the heat flux by conduction exiting the soil, $h_v(T_s)$ is the specific enthalpy of the water vapour at the interface at the temperature T_s, $h_l(T_s)$ is the specific enthalpy of the water at the interface at the temperature T_s, q_{mv} is the flux of the mass of water vapour exiting the soil, q_{ml} is the flux of the mass of liquid water exiting the soil, R_n is the net radiation, H is the turbulent diffusion of sensible enthalpy into the atmosphere and $h_l(T_a)$ is the enthalpy of water (precipitation) at the air temperature T_a.

Figure 2-23 shows the energy fluxes at the soil atmosphere interface.

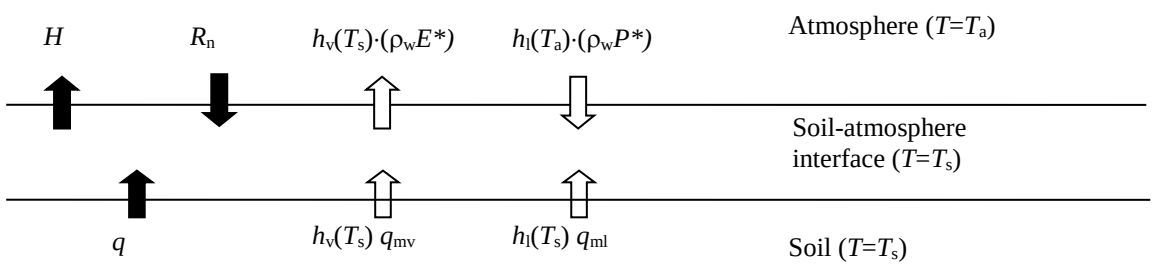

Figure 2-23: The energy fluxes at the interface soil-atmosphere

The soil transfers energy to the interface via conduction q and via convection associated with the mass flux in liquid and vapour phase are $h_l(T_s)q_{ml}$ and $h_v(T_s)q_{mv}$, respectively. At the top boundary, the energy flux occurs via a convective mechanism associated with air turbulence (H) and a radiation mechanism associated solar radiation and the emissivity of the atmosphere and the earth surface. These fluxes are lumped together in the net radiation R_n.

2.2.2.4 Potential evaporation from liquid surface or saturated soil

The equation proposed by Penman (1948) for the evaporation from saturated surface was derived by introducing simplifying assumptions in the mass and energy balance equations. The vapour flux exiting the soil is assumed to be equal to zero:

$$q_{mv} = 0 \tag{2.58}$$

In the absence of precipitation (P=0), the mass balance equation becomes:

$$q_{ml} = E = \rho_l E^* \tag{2.59}$$

The energy balance equation is simplified by assuming that the heat flux by conduction exiting the soil is also equal to negligible:

$$q = 0 \tag{2.60}$$

The energy balance equation therefore becomes:

$$h_l(T_s)q_{ml} = -R_n + H + h_v(T_s)E \tag{2.61}$$

By combining Equations (2.59) and (2.61) for the mass and energy balance respectively, and considering that the latent heat of evaporation L can be written by considering the enthalpy differential associated with the phase change:

$$L(T_s) = h_v(T_s) - h_l(T_s) \tag{2.62}$$

It follows that:

$$R_n = H + L(T_s)E \tag{2.63}$$

By introducing the following ratio:

$$Bo = \frac{H}{L(T_s)E} \tag{2.64}$$

referred to as Bowen ratio, the energy balance equation can then be written as follows:

$$R_n = (1 + Bo)L(T_s)E \tag{2.65}$$

which provides a simplified equation (2.63) for the evaporation once the Bowen ratio, *Bo*, is characterised.

In the dynamic sublayer, conditions of statically neutral equilibrium can be assumed. This means that velocities in horizontal direction are negligible with respect to velocities in vertical direction. In addition, i) molecular diffusion of mass and energy are negligible with respect to turbulent transport and ii) viscous shear stresses are negligible with respect to turbulent shear stresses.

Under such conditions, the profile of the wind velocity and air humidity is logarithmic. It can be demonstrated that the evaporation *E* and the sensible heat *H* can be written as follows (Brutsaert, 1982):

$$E = \rho_l E^* = \frac{0.622}{R_d T(z)} \frac{k^2 v_x(z)}{\left[\frac{\ln(z-d_0)}{z_{0m}}\right]^2} [p_{vs} - p_v(z)] \tag{2.66}$$

$$H = \frac{k^2 \rho_a c_p v_x(z)}{\left[\frac{\ln(z-d_0)}{z_{0m}}\right]^2} [p_{vs} - p_v(z)] \tag{2.67}$$

where *E* is the outward mass flux per unit time and unit surface, E^* is the outward volume flux per unit time and unit surface, ρ_l is the density of the liquid, *k* is the von Karman's constant (*k*=0.41), ρ_a is the air density, $v_x(z)$ is the wind speed at height *z*, d_0 is zero plane displacement height, and z_{0m} is the roughness length for the momentum, q_{hs} is the specific humidity at the soil-atmosphere interface, $q_h(z)$ the specific humidity at height *z*, T_s is the temperature at the soil-atmosphere interface, $T_s(z)$ the temperature at height *z*, c_p is the specific heat of air, and R_d is the gas constant for dry air (R_d =287.0 J K^{-1} kg^{-1}). The Bowen ratio can therefore be written as:

$$Bo = \frac{c_p}{L(T_s)} \left(\frac{\rho_a R_d T}{0.622}\right) \frac{T_s - T(z)}{p_{vs} - p_v(z)} \tag{2.68}$$

Since (Brutsaert, 1982)

$$\rho_a = \frac{p}{R_d T}\left(1 - 0.378\frac{p_v}{p}\right) \tag{2.69}$$

and assuming

$$1 - 0.378\frac{p_v}{p} \cong 1 \tag{2.70}$$

the Bowen ratio in Equation (2.68) can be expressed as follows:

$$Bo = \frac{c_p p}{0.622\, L(T_s)} \frac{T_s - T(z)}{p_{vs} - p_v(z)} \tag{2.71}$$

By introducing the psychrometric constant γ:

$$\gamma = \frac{c_p p}{0.622\, L(T_s)} \quad \left[\frac{Pa}{K}\right] \tag{2.72}$$

it is obtained:

$$Bo = \gamma \frac{T_s - T(z)}{p_{vs} - p_v(z)} \tag{2.73}$$

Equation (2.73) shows that the determination of *Bo* requires the estimation of the temperature T_s and vapour pressure p_{vs} at the soil-atmosphere interface. Penman (1948) resolves this problem by assuming that the vapour pressure at the interface is equal to the saturated vapour pressure. This assumption is acceptable for evaporation occurring from a liquid or a saturated soil but it would not be appropriate for evaporation occurring from an unsaturated soil.

$$p_{vs} = p_{v0s} \tag{2.74}$$

In addition, Penman (1948) assumes that the saturated vapour pressure at the interface p_{v0s} is linked to the temperature T_s via a linear relationship derived from the slope Δ of the curve

of saturated vapour pressure versus, calculated by considering the air temperature T(z) as a reference:

$$\Delta = \frac{p_{v0s} - p_{v0}(z)}{(T_s) - T(z)} \quad \left[\frac{Pa}{K}\right] \tag{2.75}$$

By replacing Equations (2.74) and (2.75) into (2.73) it is obtained:

$$Bo = \frac{\gamma}{\Delta}\frac{p_{v0s} - p_{v0}(z)}{p_{vs} - p_v(z)} = \frac{\gamma}{\Delta}\frac{p_{v0s} - p_{v0}(z) - p_v(z) + p_v(z)}{p_{vs} - p_v(z)} =$$

$$= \frac{\gamma}{\Delta}\left[\frac{p_{v0s} - p_v(z)}{p_{vs} - p_v(z)} - \frac{p_{v0}(z) - p_v(z)}{p_{vs} - p_v(z)}\right] = \tag{2.76}$$

$$= \frac{\gamma}{\Delta}\left(1 - \frac{p_{v0}(z) - p_v(z)}{p_{vs} - p_v(z)}\right)$$

By replacing the Bowen ratio given by Equation (2.76) in the energy balance equation in Equation (2.65) it is obtained:

$$Rn = \left(1 + \frac{\gamma}{\Delta}\right) L(T_s)E - \frac{\gamma}{\Delta}\frac{p_{v0}(z) - p_v(z)}{p_{vs} - p_v(z)}\, L(T_s)E \quad \left[\frac{Pa}{K}\right] \tag{2.77}$$

If evaporation E is expressed in the general form:

$$E = f[v_x(z)][p_{vs} - p_v(z)] \tag{2.78}$$

where $f\,[v_x(z)]$ is the wind function, Eq. (2.77) becomes:

$$R_n = \left(1 + \frac{\gamma}{\Delta}\right) L(T_s)E - \frac{\gamma}{\Delta} L(T_s) f[v_x(z)][p_{v0}(z) - p_v(z)] \tag{2.79}$$

By assuming:

$$L(T_s) \cong L[T(z)] \tag{2.80}$$

and extracting E from Equation (2.79), it is obtained the *Penman's* equation for the estimation of evaporation:

$$E = \frac{\Delta}{\Delta + \gamma}\frac{R_n}{L[T(z)]} + \frac{\gamma}{\Delta + \gamma} f[v_x(z)]p_{v0}(z)[1 - RH] \qquad \left[RH = \frac{p_v(z)}{p_{v0}(z)}\right] \tag{2.81}$$

The advantage of this relationship is that the measurement of wind speed $v_x(z)$, temperature T and vapour pressure $p_v(z)$ are carried out at a single elevation z above ground surface. The simplifying assumptions introduced to derive the Penman's equation (2.81) are summarised hereafter:

- Water vapour flux from the soil assumed to be equal to zero (q_{mv}=0)
- Heat flux by conduction from the soil assumed to be equal to zero (q=0)
- Partial vapour pressure of the vapour p_v negligible with respect to the portal pressure of the vapour-air mixture;
- Linear relationship between temperature and vapour pressure;
- The vapour pressure at the soil-atmosphere interface is saturated, i.e. the soil suction is equal to zero or, practically, limited to a few hundredths of kPa.

The Penman's equation (2.81) is generally presented in a slightly different form which is derived hereafter. The wind function $f\,[v_x(z)]$ can be extracted from Equation (2.76), which is valid under conditions of neutral stability:

$$f[v_x(z)] = \frac{0.622}{R_d T(z)} \frac{k^2 \overline{v_x}(z)}{\left[\frac{\ln(z-d_0)}{z_{0m}}\right]^2} \tag{2.82}$$

This relationship is acceptable for the estimation of the evaporation over periods of one or more days but is generally inadequate for the estimation of hourly evaporation because stability conditions of the atmosphere vary significantly during the day.

By introducing the aerodynamic resistance r_a:

$$r_a = \frac{\left[\frac{\ln(z-d_0)}{z_{0m}}\right]^2}{k^2 v_x(z)} \tag{2.83}$$

and considering that, by combining Equations (2.69), (2.71) and (2.72) it can be written:

$$\frac{0.622}{R_d T(z)} = 0.622\frac{\rho_a}{p} = \frac{0.622\rho_a(c_p)}{\gamma\ 0.622\ L[T(z)]} = \frac{\rho_a(c_p)}{\gamma\ L[T(z)]} \tag{2.84}$$

the Equation (2.82) for the wind function can be written as follows:

$$f[v_x(z)] = \frac{\rho_a(c_p)}{\gamma\ L[T(z)]}\frac{1}{r_a} \tag{2.85}$$

Finally, by substituting Equation (2.85) into Equation (2.81), it follows:

$$E = \frac{1}{L[T(z)]}\frac{\Delta R_n + \rho_a c_p p_{v0}(z)[1 - RH]/r_a}{\Delta + \gamma} \qquad \left[RH = \frac{p_v(z)}{p_{v0}(z)}\right] \tag{2.86}$$

which is the Penman's equation as reformulated by Monteith (1965).

Various empirical equations have been proposed in the literature for the aerodynamic resistance:

$$r_a = \frac{250}{1 + 0.54\ v_x(z = 2m)} \qquad \left[\frac{s}{m} \cong \frac{mm}{sPa}\right] \quad \text{(Penman, 1948)} \tag{2.87}$$

$$r_a = \frac{250}{0.5 + 0.54\ v_x(z = 2m)} \qquad \left[\frac{s}{m} \cong \frac{mm}{sPa}\right] \quad \text{(Penman, 1956)} \tag{2.88}$$

$$r_a = \frac{250}{1 + 0.86\ v_x(z = 2m)} \qquad \left[\frac{s}{m} \cong \frac{mm}{sPa}\right] \quad \text{(Doorenbos and Pruitt, 1975)} \tag{2.89}$$

where v_x is the wind velocity in ms^{-1} at a distance of 2 m from the ground surface. These relationships are commonly used for water surfaces of bare soils (2.87), for mown grass (2.88), and irrigated crops (2.89) respectively. These relationships are clearly not accurate for wind velocities close to 0 *m/s* as they return a finite value for the aerodynamic resistance r_a rather than an infinite value.

A comparison between Equations (2.87), (2.88) and (2.89), and Equation (2.83) for two different values of z_0 (assuming d_0=0) is presented in Figure 2-24.

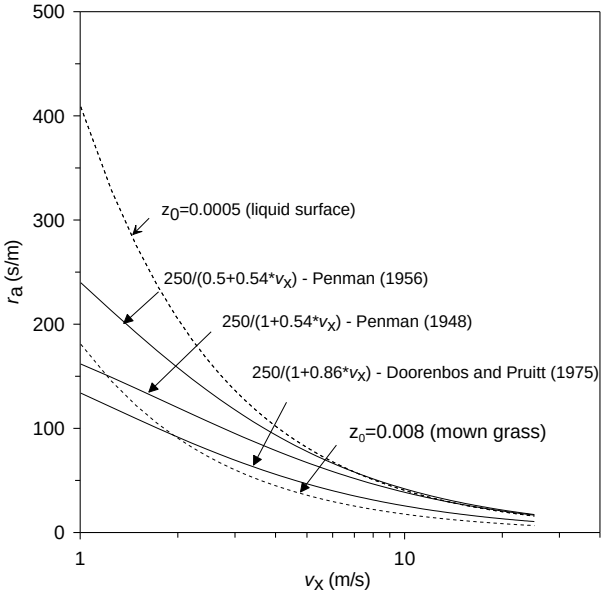

Figure 2-24. Comparison between different relationships used to estimate the aerodynamic resistance r_a.

3 EVAPORATION-INDUCED SOIL WATER FLUX TO DESIGN SUCTION DRAIN FOR LOW-CARBON GROUND STABILISATION: EXPERIMENTAL INVESTIGATION AND MODELLING

3.1 Abstract

The suction drain is a novel concept for low-carbon temporary ground stabilisation in clayey soils alternative to jet grouting and ground freezing. Boreholes are drilled into the ground and air is injected to the borehole end through a delivery pipe. The air flowing through the gap between the pipe and the borehole surface backward towards the borehole entry removes water by evaporation and, hence, increases the undrained shear strength of the soil surrounding the drain. There are no studies that allow quantifying soil water evaporation generated by tangential airflow in a confined space. This paper first presents an experimental investigation on - water evaporation induced by air flow. A 3 m long wet surface was subjected to tangential air flow into a 40 mm gap. Tests were carried out by considering different air velocities and inlet air relative humidity. A model was then formulated to quantify the water evaporation rate for any length of the wet surface. The model parameters were calibrated against one experimental dataset and the model was then validated against an independent dataset. Finally, an empirical equation is proposed to estimate model parameters without the need of carrying out experimental tests. This is based on the vapour transfer coefficient established empirically for evaporation from open water, which was found to remain valid for confined evaporation. The

paper therefore provides a tool to estimate airflow-induced evaporation to successfully design the suction drains.

3.2 Introduction

The suction drain is an innovative concept for temporary stabilisation of tunnels and excavations in clays. The soil is exposed to the air flowing tangentially to the surface of a drilled borehole, which generates water removal by evaporation. This concept was developed in Martini et al, (2018-submitted) and is based on the principle that undrained shear strength is enhanced by decreasing soil water content.

The concept of the suction drain is shown in Figure 3-1. A borehole is drilled into the ground and a centralised air delivery tube is positioned into the borehole. This is used to inject compressed air to the end of the borehole. The air flows from the end of the borehole to its entry through the gap between the centralised air delivery tube and the inner surface of the borehole. The air that flows tangentially to the inner surface of the drilled borehole exposes the soil to evaporation. Water flows towards the borehole therefore reducing the water content of the surrounding soil and increasing the soil shear strength. The key of this technique is therefore the water outflow generated by air-flow.

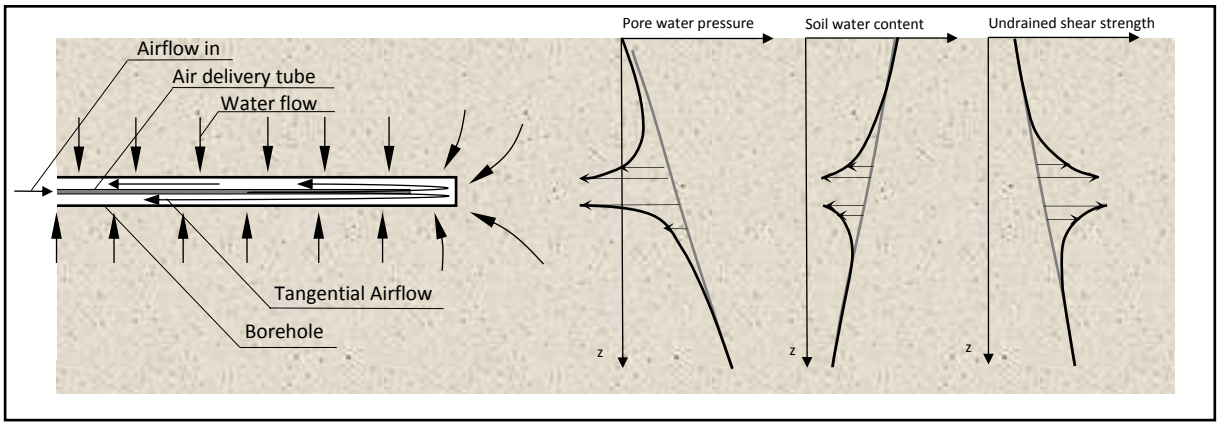

Figure 3-1: Concept of the suction drain (not in scale)

Several studies have been carried out to investigate the correlation between relative humidity and velocity of the airflow and the evaporation rate from soil (Leighly, 1937; Thornthwaite & Holzman, 1939; Penman, 1946; Chu, Li, Chen, & Kuo, 2010; Lim et al., 2012; Brutsaert, 2013). However, these refer to evaporation from open surfaces and there is a lack of understanding of the processes occurring under confined air flow as occurs in the suction drain. To design the suction drain, tools are required to estimate the airflow-induced evaporation under confined air flow.

This paper first presents an apparatus designed to mimic the evaporation process occurring in the suction drain. The ‘evaporation machine’ allows the injection of airflow over a 3m-long evaporation surface under confined airflow. The air is injected at different velocities and relative humidities. The total water mass loss (evaporation) and the air relative humidity along the evaporation surface are measured.

The experimental results aim to lead to an ‘accessible’ model to estimate airflow-induced evaporation for any length of the evaporation surface, i.e. different from the length investigated experimentally. This model would be the key to design the air flow characteristics in terms of air velocity and relative humidity.

3.3 Equipment

3.3.1 Long evaporation machine

The long evaporation machine was designed to investigate the correlation between the characteristics of confined airflow and the evaporation rate from a wet surface subjected to tangential airflow. As illustrated in Figure 3-2 the device is composed of a 4 m long upper air channel above a 3 m long container. The air channel inlet is connected to the air injection system as described in the next section and the air channel outlet is open to atmosphere.

The upper channel is designed to allow the air to flow tangentially over the evaporating surface of liquid or soil placed in the lower container. The air channel is 40 mm high and 30 mm wide and the container is 100 mm high and 30 mm wide. The lid of the channel is removable to ease the filling or emptying of the lower container. Once in place, the lid is sealed using silicon grease. The upper air channel and the lower container were manufactured by assembling Perspex acrylic extruded sheets 8mm thick joined together using epoxy resin.

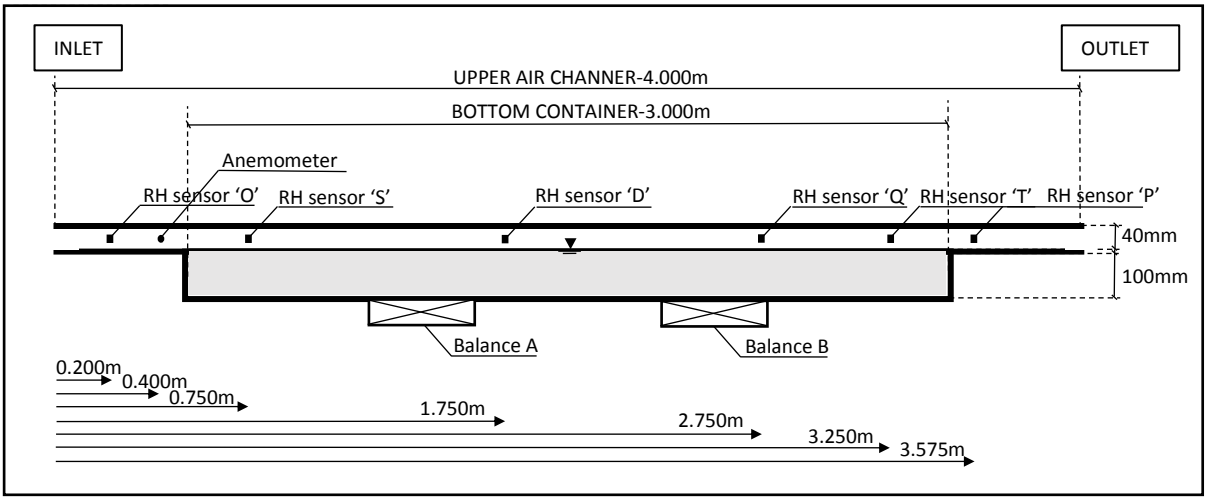

Figure 3-2: Layout of the long evaporation machine (not in scale)

Six sensors were placed in the upper air channel to measure temperature and relative humidity (Sensirion Kit EK-H5 sensors SHT21) as shown in Figure 3-2. Holes were drilled into the lid to allow the cables of the RH/T sensors to pass through. These holes were sealed once the RH/T sensors were located mid-height and mid-width of the upper air channel with the RH/T sensing elements frontal to the airflow.

An anemometer (OMEGA FMA1006R-V2-S) was used to measure the airflow velocity. The anemometer was installed through the side wall of the channel at 0.4 m from the inlet of the channel. The RH/T device measuring velocity and the temperature of air was located normal to the airflow mid-height and mid-width of the upper air channel.

The evaporation machine was placed on two balances (ADAM CBK-32 and ADAM CBK-48) positioned 1.5 m rightward from the inlet and 1.5 m leftward from the outlet respectively (Figure 3-2). Balance readings were acquired at regular time lapse.

3.3.2 Short evaporation machine

The short evaporation machine was designed to assess the evaporation rate of water from a saturated soil sample exposed to tangential airflow. As anticipated by the name, this device is the short version of the long evaporation machine composed of 1.50 m long upper air channel and 0.5 m long bottom container (Figure 3-3). The dimensions of the cross section of both the upper air channel and of the bottom container are the same of those in the long evaporation machine. Also the lid of the upper air channel is removable as the lid in the long evaporation machine to ease the filling or emptying of the lower container and once in place, is sealed using silicon grease. The air channel inlet is connected to the air injection system with the bypass for dry air as described in the next section. The air channel outlet is open to atmosphere.

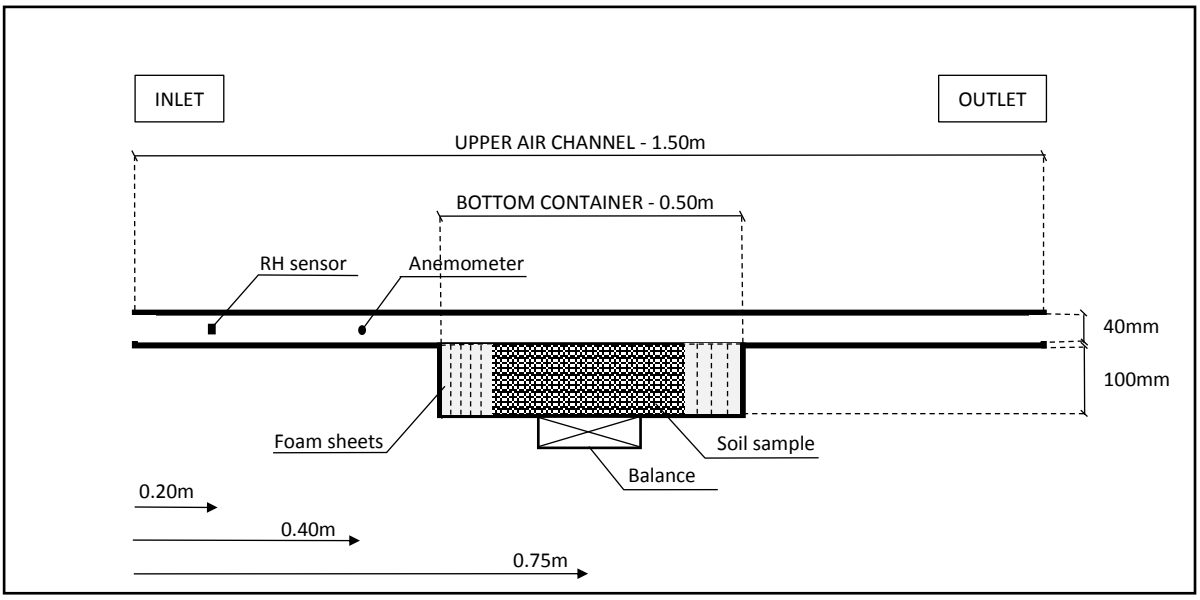

Figure 3-3: Layout of the short evaporation machine (not in scale)

The anemometer OMEGA FMA1006R-V2-S was used to measure the airflow velocity and it was installed through the side wall of the channel at 0.4 m from the inlet of the channel. The RH/T device measuring velocity and temperature of the air was located normal to the airflow mid-height and mid-width of the upper air channel. The short evaporation machine was placed on one balance with higher resolution (ADAM PGW6002e) positioned at the centre of the bottom container (Figure 3-3). Balance readings were acquired at regular time lapse.

3.3.3 Control and measurement devices

3.3.3.1 RH/T sensors

The RH/T sensors installed in the long evaporation machine are Sensirion Kit EK-H5 sensors SHT21. The specifications of the RH/T sensors are listed in Table 3-1.

Table 3-1: Manufacturer's specification of the RH/T sensors

Sensor size	3 x 3 x 1.1 mm
RH sensing element	Capacitive-type
RH operating range	0 - 100% RH
RH accuracy	±2% (20%-80% RH) ±3% (0-20% RH – 80%-100% RH)
T sensing element	Band-gap
T operating range	-40 to +125°C
T accuracy	±0.3°C

The relative humidity sensors were calibrated prior to be installed in the evaporation machines using the fixed-point humidity systems. According to (de Métrologie Légale, 1996), the fixed point method is inexpensive, accurate, and easily reproducible in a research laboratory.

Relative humidity fixed points (HFP) were imposed via six saturated salt solutions and dry silica gel. The saturated salt solutions are listed in Table 3-2 together with the associated values of relative humidity and their uncertainty (3 times the standard deviation) according to (Greenspan, 1977). The aqueous saturated solutions were prepared according to (de Métrologie Légale, 1996). Demineralised water with electrical conductivity no greater than 5.5 μS/m was used to prepare the aqueous saturated solutions. The amount of salt mixed with the demineralised water was about twice the value corresponding to the saturated conditions to ensure that precipitated salt remained clearly visible.

The aqueous solutions were prepared in six separated containers 48 hours prior to the RH measurement to allow the thermodynamic equilibrium between the solid (salt precipitation) the liquid (solution). The containers were filled with the same amount of aqueous solution to leave a headspace between the water level and the rim of the container equal to 30 mm. Each

container was closed with an air-tight lid and placed in water bath in a temperature-controlled room (20±0.5°C).

An additional container was filled with silica gel to leave the same headspace and placed in the same water bath.

Table 3-2: The saturated salt solution and its standard relative humidity value for the calibration of humidity sensors at 20°C

List of salt solutions		Standard relative humidity (%)	Uncertainty (%)
1	$MgCl_2$	33.07	±0.18
2	K_2CO_3	43.16	±0.33
3	KI	69.90	±0.26
4	NaCl	75.47	±0.14
5	KCl	85.11	±0.29
6	$CuSO_4$	98.00	N/A

Source: All values from (Greenspan, 1977) except $CuSO_4$ from (Winston & Bates, 1960)

The electrical parts of the RH/T sensors were spray-coated with Servisol Plastic Seal 60 Protective Insulator to protect from oxidation. Parafilm was used to cover the connection between the sensor and the electrical cable. A single extra lid was drilled with six small holes and the sensor cables were passed through them. The cables were sealed with silicone and the sensors were connected to the cables on the inner side of the lid. The sensors were all hanging from the lid at the same height in the container headspace.

The lid carrying the six RH/T sensors was placed onto the container with the lower relative humidity fixed point (silica gel). The sensors remained in each container for 24h, a time sufficient for the sensor readings to stabilise. The lid was then removed and placed on the

following container. The RH was increased from 0% to 98% and then decreased to 0% according to the list of saturated salt solutions specified in Table 3-2.

The calibration curve was derived by establishing a correlation between the RH imposed and the sensor output. The sensor output consisted in a nominal RH based on manufacturer calibration. The calibration curve is linear in the range 0-70% with negligible hysteresis (Figure 3-4). The calibration curve was derived in this range only, which encompasses the values measured in the tests in this experimental programme.

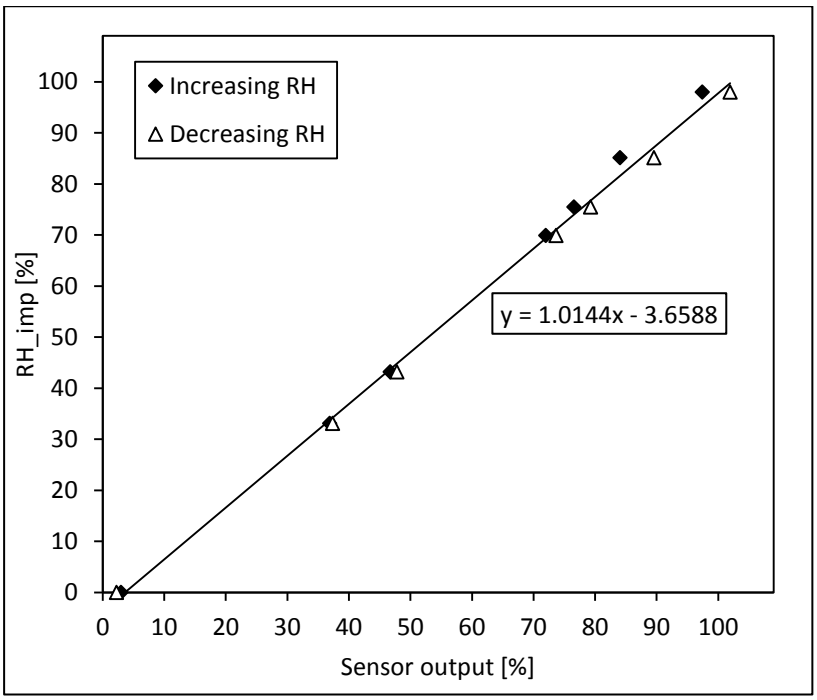

Figure 3-4: Typical calibration curve of the RH/T sensor

The RH/T sensors were not calibrated with respect to temperature. However, the temperature returned by the sensors based on manufacturer calibration was checked by comparison with a high-precision reference temperature sensors (Fluke 5641-P Thermistor Probe). The RH/T sensors were wrapped together with the high precision reference temperature sensors in foam sheet and discrepancies were found to be lower than ±0.2°C. This accuracy was considered acceptable for the purpose of this study.

3.3.3.2 Anemometer

The anemometer used in both the short and the long evaporation machine to monitor the airflow velocity was OMEGA FMA1006R-V2-S. The sensor design is based on three RTD elements, one measures the air temperature and the other two measure the air velocity. The air velocity is measured based on the heat loss from the RTD velocity sensor as it cools down by the air flow (Omega Engineering, 2018). The specification of the velocity sensor are summarised in Table 3-3.

Table 3-3: Specification of the anemometer

Range Air velocity	0-60.96 m/s
Accuracy air velocity	1.5% Full scale range
Display resolution air velocity	0.01m/s
Sensor probe	6.3 OD x 95 mm- 304 Stainless steel
Response time	250 msec default
Operating Relative Humidity	0 to 95% RH without condensation

The anemometer returns an output directly in engineering units, i.e. m/s, based on a manufacturer's calibration. To assess the accuracy of the anemometer measurements, the verification of the manufacture's calibration was carried out. The anemometer was installed in a wind-tunnel normal to the airflow and firmly connected to a support to prevent vibration at high velocity. Air velocity was increased from 3 m/s to 8 m/s in steps then decreased to 3 m/s. The air velocity measured by the anemometer was benchmarked against a Pitot tube. For each step, the measurement of air velocity from both anemometer and Pitot tube was taken once the air velocity stabilised (typically in less than 2 min). At relatively low air velocity (<2-3 m/s),

Pitot tubes are not sensitive enough (Comtebellot, 1976), thus 3 m/s was the lowest air velocity imposed in the wind-tunnel. The tests were carried out at a temperature of 20°C ± 0.5°C.

The measurements by the anemometer are compared with the measurement by the Pitot tube in Figure 3-5. There is no apparent hysteresis and the standard deviation of the error is less than 0.13 m/s. The response of the anemometer in the range was taken as an evidence of satisfactory performance of the anemometer. It was therefore assumed the measurements were accurate also in the range 0-3 m/s.

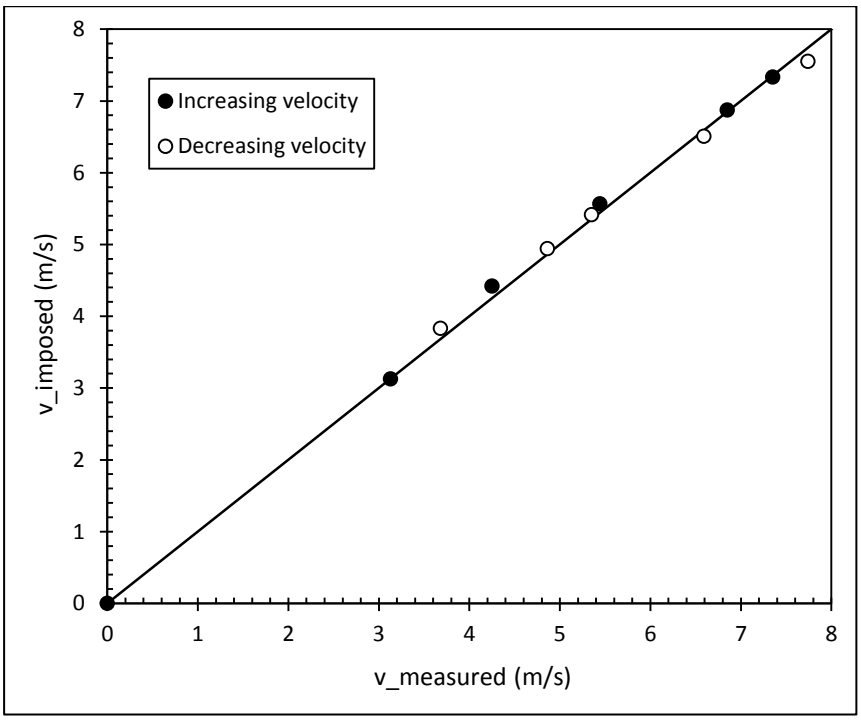

Figure 3-5: Calibration curve of the anemometer

3.3.3.3 Balances

The balances used in the long evaporation were ADAM CBK-32 and ADAM CBK-48 with the maximum capacity equals to 32 kg and 48 kg and accuracy according to manufacturer's specifications equal to 1 g and 2 g, respectively. The balance used in the small evaporation machine was ADAM PGW6002e with the maximum capacity equals to 6 kg and the accuracy according to manufacturer's specifications equal to 0.1 g. The balances return an output directly

in engineering units, i.e. grams, based on a manufacturer's calibration. To assess the accuracy of the balance measurements, a weight equal to 11110 g was placed on the balances used in the long evaporation machine to mimic the weight of half of the long evaporation machine. Similarly, a weight equals to 6110 g was placed on the balance used in the short evaporation machine to mimic the weight of the short evaporation machine. Weights were added to the balances in the sequence 1g, 2g, 2g, 5g, 10g, 20g, 20g, 50g, 100g, 200g, 200g, 500g, 1000g, 2000g, 2000g, 5000g and then removed by inverting the sequence to mimic the variation of water mass occurring in the evaporation machines. The incremental measurements by the balances are compared with the incremental weights in Figure 3-6. There is no apparent hysteresis and the standard deviation of the error is less than 1.3 g for the balances used for the long evaporation machine and less than 0.3 g for the balance used for the short evaporation machine.

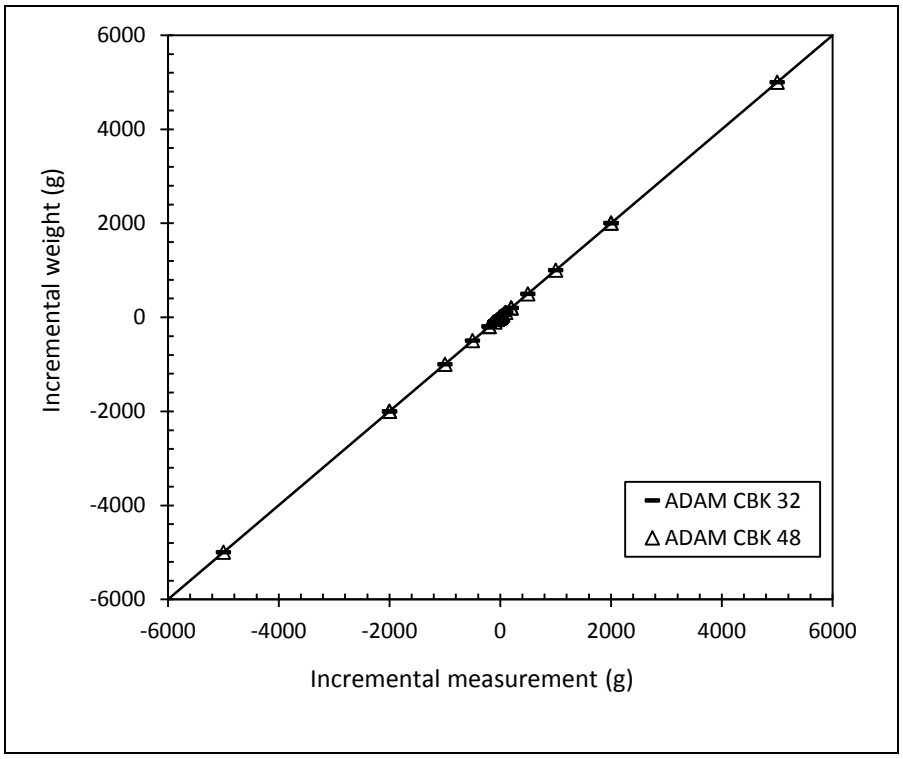

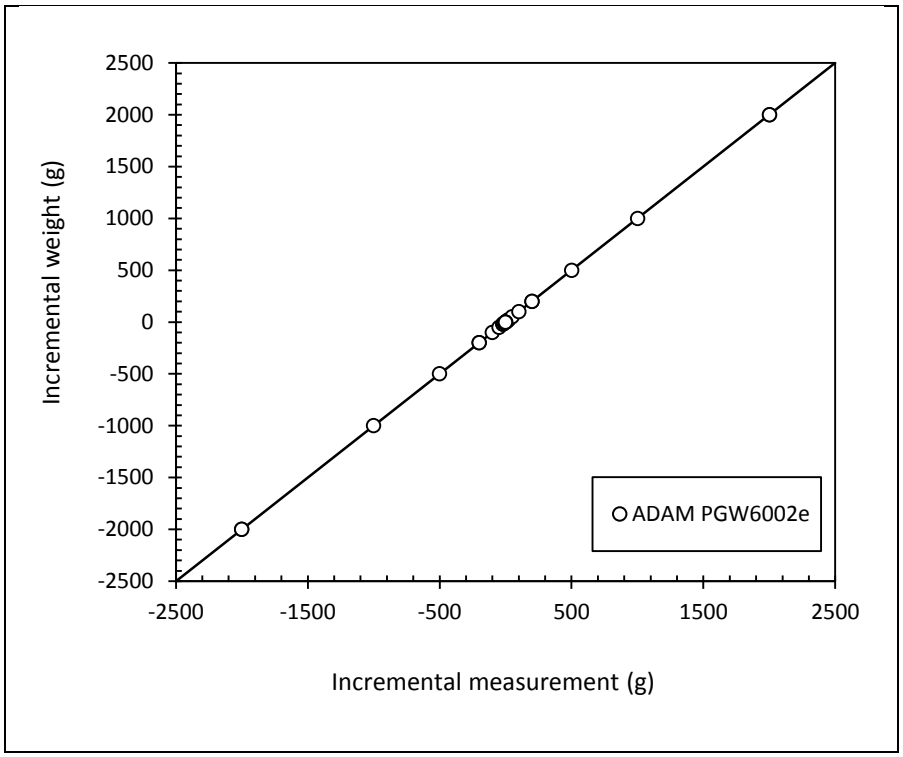

Figure 3-6: Calibration curves of the balances

3.3.3.4 Humid air injection system

An air injection system was developed with the purpose of controlling the velocity and the relative humidity of the air entering the upper air channel.

As shown in Figure 3-7, air was supplied to the humid air injection system from the compressed air system of the laboratory. Two air lines were derived from the ring main distribution system and each line was regulated by a laboratory tap. The two lines were connected in parallel via a T connection to ensure the delivery of the highest target air velocity. A pressure regulator was installed downstream the T connection to adjust the velocity of the airflow.

When the relative humidity of the airflow required to be increased prior to be injected into the evaporation machine, the airflow was forced to pass through the humidification

chamber and the intermediate chamber before reaching the upper air channel via the divergent duct.

The humidification chamber consists of 1L capacity graduated glass cylinder containing water and sealed on top with a rubber bung. Two holes were drilled through the rubber bung to allow the inlet tube and the outlet tube to pass through. The inlet tube could be positioned at different heights into the glass cylinder (by forcing it to slide through the rubber bung) whereas the outlet tube was fixed in place in the rubber bung.

The mixing of the dry air supplied by the compressed air system with the saturated vapour above the free water inside the cylinder allowed the airflow to increase its relative humidity. The desired relative humidity was achieved by i) adding a pre-determined volume of water inside the glass cylinder (depending on the target air velocity) and ii) adjusting the vertical position of the inlet pipe with respect to the water surface (at the beginning and during the test).

The glass cylinder was half-immersed into a water bath (10L) to mitigate the drop in temperature inside the glass cylinder due to evaporation. The volume of water inside the bath was not sufficient to maintain a constant temperature (as measured by laboratory glass thermometer immersed in the water bath). Water temperature in the bath was maintained constant by periodically replacing cooling water in the bath with water at relatively high temperature.

The flow from the glass cylinder was conducted to an intermediate chamber to separate water droplets from the humid air (droplets were captured by gravity at the bottom of the intermediate chamber).

A divergent duct 100 mm long with a gradually lofted transition between the 16 mm diameter air delivery tube and the 46x46 mm rectangular cross-section of the evaporation machine was installed at the inlet of the evaporation machine to reduce the turbulence of the

airflow due to the enlargement of the section. The taper angle 'θ' of the duct was designed to 7° to reduce the effects of boundary layer separation across the connection according to (Chandavari, V., & Palekar, 2014). The duct was designed and manufactured by utilising a 3D printer (Simpson, 2017).

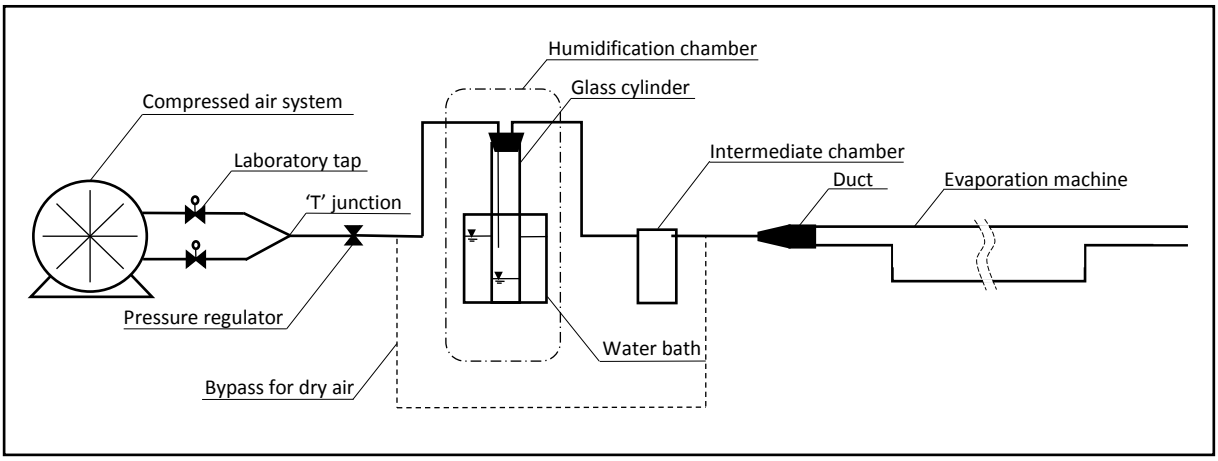

Figure 3-7: Layout of the air injection system (not in scale)

3.4 Experimental procedure

3.4.1 Long evaporation machine with water

3.4.1.1 Initialisation of the test

The initial condition of each test consisted in establishing saturated vapour conditions in the upper air channel. This was aimed at double-checking the readings from the RH sensors before each test. To this end, the bottom container was filled with demineralised water until the water surface was lined up the base of the upper air channel. The inlet and the outlet of the upper air channel were sealed for approximately 10 h using parafilm and silicon grease and the relative humidity and the temperature were recorded continuously. It was then checked that the

RH sensors were recording the same values within the accuracy expected at values of RH close to saturation.

3.4.1.2 Test procedure

Two sets of tests are presented in the paper characterised by a relative humidity at the inlet of the upper air channel equal to RH=0% and RH=30% respectively. The experimental procedure is first discussed for the test at RH=30%. Tests were run in a temperature controlled laboratory (T=20±0.5°C).

a) Before starting the air injection, the glass cylinder was filled with a pre-determined volume of water and the position of the inner air delivery tube inside the cylinder were adjusted to a pre-determined distance from the water level according to Table 3-4. These distances were determined by trial and error until a target relative humidity of RH=30% at the inlet of the upper air channel could be achieved. These distances were found to depend on the air velocities, which was ranged from 1 to 4 m/s. Airflow was not pointed directly to the water surface in the glass cylinder because this would have increased turbulence and caused significant amount of water droplets to be carried forward into the evaporation machine. The inner air delivery tube was therefore pointed towards the inner wall of the cylinder to break the air flow.

Table 3-4: Specifications of the test procedure in the long evaporation machine

Nominal air velocity (m/s)	Initial volume of water (ml)	Distance of the air delivery tube from the free water level (mm)	Target temperature of the water bath (°C)
1	300	114	25
2	180	160	28

3	150	171	35
4	100	190	40

b) Laboratory taps were open and the pressure regulator was adjusted until the air velocity measured by anemometer attained the target air velocity with a maximum tolerance of ±0.05 m/s.

c) All the RH/T sensors were switched on and the readings from the sensor at the inlet of the upper air channel (RH/T Sensor 'O') was initially monitored. The position of the inner air delivery tube inside the cylinder was then fine adjusted until the RH was stable at 30%.

d) The water bath was filled with water prepared at the pre-determined temperature specified in Table 3-4. Again these values were determined in preliminary tests by trial and error until a target temperature of 20°C at the inlet of the upper air channel could be achieved (with a tolerance of ±2°C).

e) The air velocity, the temperature, and the relative humidity at the inlet of the evaporation machine were monitored until stable values were reached. This phase typically took ~5-10 min. The RH sensors, the anemometer, and the balances were then logged as the test was assumed to start at this stage.

f) During the test the level of water inside the cylinder dropped as a result of evaporation. In turn, this caused the RH at the inlet of the upper air channel to drop. When the RH recorded by the sensor 'O' decreased from 30% to 25%, the inner air delivery tube was pushed downward into the cylinder until the RH recorded by sensor 'O' increased to 35%. In this way, the relative humidity at the inlet was maintained at 30% with a tolerance of ±5%.

g) During the test, the temperature of the water bath was monitored by using a glass laboratory thermometer immersed into the water bath. When the temperature of the water bath dropped by 2°C from the target temperature specified in Table 3-4, part of water in the bath was

replaced with water at higher temperature until the temperature of the water bath regained the target value.

h) The test was run for 2 h and this time was sufficient for all the sensors to attain stable values indicating that the system had reached a steady-state.

For the test involving injection of air in the upper air channel at RH=0%, the humidification chamber and the intermediate chamber were by-passed as shown in Figure 3-7. In this case, the procedure only included steps b) and e).

3.4.2 Short evaporation machine with soil

3.4.2.1 Test procedure

A core of soil between 3 m and 4 m from the ground level was sampled at the Bothkennar research Station in Falkirk by using the Terrier driller rig. After the sampling the core was stored in the plastic liner that was sealed at the two extremes to preserve the natural water content of the soil.

In the laboratory part of the soil from the core was used for the soil classification and the determination of index properties. The limit liquid assessed by fall cone test was LL=0.72 and the thread-rolling plastic limit was 0.30. The specific gravity was 2.64. The initial water content of the soil was measured equal to w=50% and the initial soil suction was measured via the high-capacity tensiometer equal to s=35kPa. Under these conditions the soil sample was saturated. A rectangular undisturbed soil sample 118 mm long, 17 mm wide and 100 mm high was trimmed from the core at the depth of 3.5 m from the ground level.

The bottom and lateral surfaces of the cuboidal soil sample were covered by silica grease and parafilm to make them impermeable. The sample was placed at the centre of the bottom

container as shown in Figure 3-3 and the empty space around the soil sample was filled with foam sheets to prevent eddies of air around the soil sample and to ensure that the air would flow tangentially over the top surface of the soil sample.

The small evaporation machine was connected to the air injection system that included the bypass for dry air explained in Section 3.3.3.4. The laboratory valves were opened until the velocity of the air, measured by the anemometer at the inlet of the upper air channel, was equal to v=4m/s. The airflow at RHinlet=0% and air velocity v=4m/s was flowing in the upper air channel for the time enough to ensure that the constant rate period of drying was achieved. This is generally associated to the soil sample that remains saturated. Hypothesis of steady state condition is assumed to be valid in transient process. The loss of mass of water from the top surface of the soil sample was recorded via the balance every 15 min.

3.5 Experimental results

3.5.1 Long evaporation machine with water

3.5.1.1 Control of air velocity, RH, and temperature

Figure 3-8 shows the air velocity measured via the anemometer at the inlet of the upper air channel during each test. It can be observed that the air velocities were maintained constant to the nominal values specified in Table 3-4 throughout the duration of the tests with a standard deviation of fluctuation σ that varies between ±0.02 m/s (at lower air velocities) and ± 0.17 m/s (at higher air velocities). The control of the air velocity was considered satisfactory for the purpose of this study.

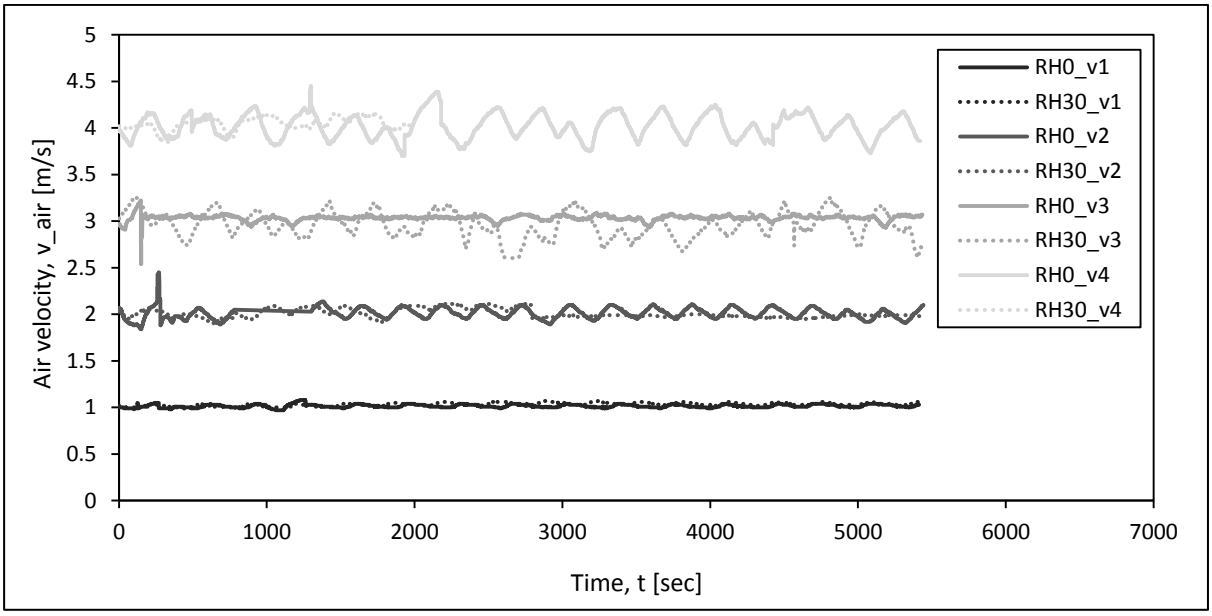

Figure 3-8: Air velocity recorded via the anemometer during the tests

Figure 3-9 shows the *RH* of the airflow at the inlet of the upper air channel measured by sensor 'O' during the tests with RH_{inlet}=30% and air velocities from v_{air}=1m/s to v_{air}=4m/s. The graph confirms the effectiveness of the humidification chamber to maintain the average *RH* of the airflow at the inlet of the upper air channel equal to RH_{inlet}=30% with a maximum standard deviation of the fluctuation equals σ=±1.9%. The control of the relative humidity of the airflow at the inlet was considered satisfactory for the purpose of this study.

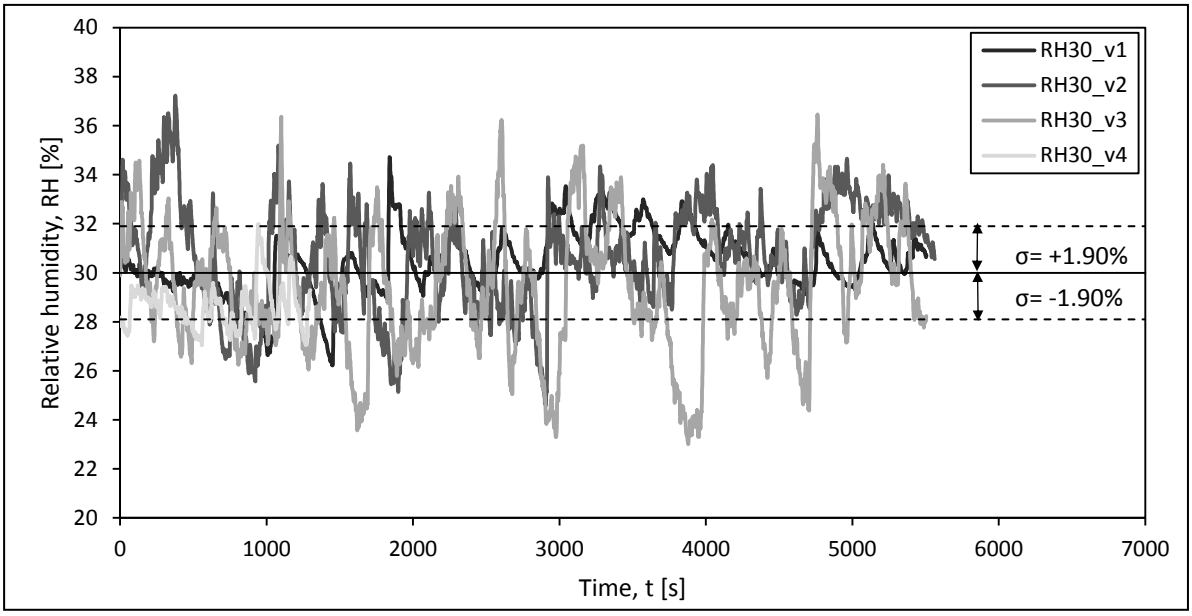

Figure 3-9: RH of the airflow at the inlet of the upper air channel recorded by the sensor 'O' during the tests with RH_{inlet}=30%

Figure 3-10 shows the temperature of the airflow at the inlet of the upper air channel measured by sensor 'O' during the tests with RH_{inlet}=30% and air velocities from v_{air}=1m/s to v_{air}=4m/s. As described in the procedure, the temperature of the airflow at the inlet of the upper air channel was controlled by the temperature of the water bath in the humidification chamber. The graph shows the effectiveness of the method used for maintaining the temperature of the airflow at the inlet of the upper air channel constant to 20°C with a maximum standard deviation of the fluctuation equals σ=±0.93% throughout the duration of each test. The control of the temperature of the airflow at the inlet was considered satisfactory for the purpose of this study.

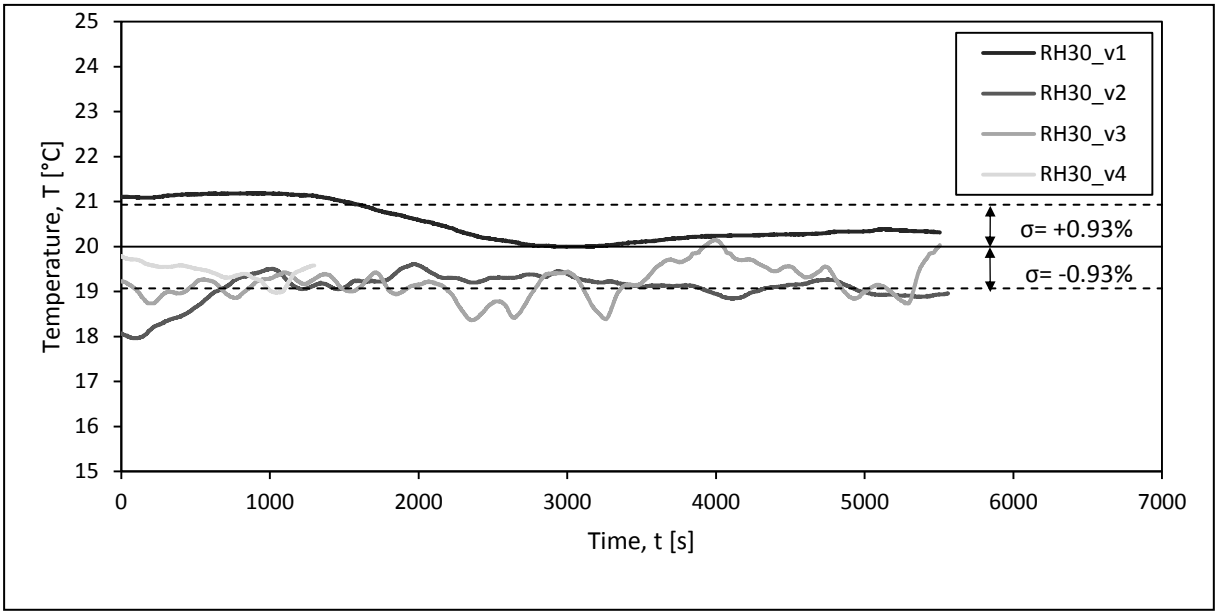

Figure 3-10: Temperature of the airflow at the inlet of the upper air channel recorded by the sensor 'O' during the tests with RH_{inlet}=30%

3.5.1.2 Individual evaporation test

Figure 3-11 shows the typical relative humidity and temperature of the airflow recorded by the *RH/T* sensors over time along the upper air channel during one of the tests with RH_{inlet}=30%. With reference to the relative humidity of the airflow it can be observed that the *RH* measured by each sensor is fairly stable throughout the duration of the test and that the responses of the sensors are in phase with each other. These findings suggest that the fluctuation recorded by each sensor is generated by the fluctuation of the relative humidity of the airflow imposed at the inlet of the upper air channel. It is also possible to see that the *RH* of the airflow progressively increases from the inlet to the outlet of the upper air channel showing the lowest value at the inlet (sensor O) and the highest value at the outlet (sensor P). This is clearly expected. The temperature of the airflow remains fairly constant at 20±1˚C over time along the upper air channel. Interestingly, the first two sensors at the inlet of the upper air channel give the same values of relative humidity and temperature of the airflow. The temperature of the

airflow recorded by sensor O and sensor S is slightly lower than the temperature of the airflow recorded by the other sensors. This suggests that both the temperature and the relative humidity of the first two sensors are controlled by the humidification chamber, whereas the relative humidity and the temperature measured by the other sensors is also influenced by the water in the bottom container. Similar results were obtained in the other tests and are shown in the Appendix.

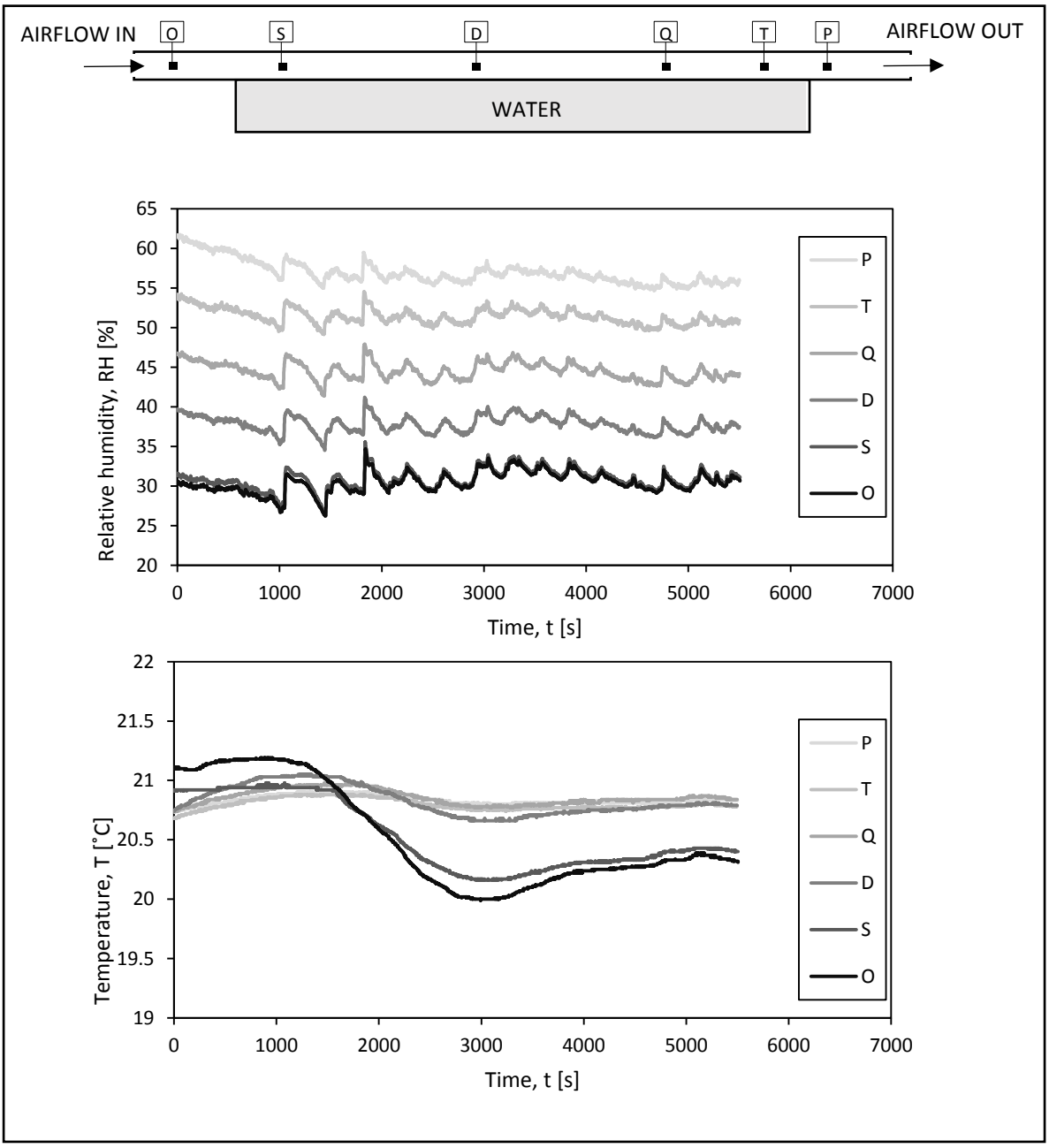

Figure 3-11: Typical reading of the relative humidity of the airflow during the test with RH_{inlet}=30% and v_{air}=1m/s

Figure 3-12 shows the criteria used for identifying the phase of steady state of each test for the computation of the relative humidity and the temperature of the airflow and the evaporation rate of water from the bottom container. Figure 3-12 refers to the test with RH_{inlet}=30% and v_{air}=1m/s; however similar results were obtained in the other tests (see Appendix). The first graph of Figure 3-12 shows the difference between the *RH* measured by each sensor and the *RH* measured by sensor O at the same time is plotted versus the time t (s). The second graph shows the data in terms of temperature processed in similar way. It can be observed that the difference of relative humidity and temperature between each sensor and sensor O decreases over time and reaches the phase of steady state after approximately 4000 seconds since the start of the test. The reading of the mass of the system versus time plotted in the third graph does not show a significant transition between the transient phase and the steady state phase in contrast with the relative humidity. This indicates that the fluctuation of the *RH* and the *T* of the airflow between the transient and the steady state do not effect significantly the evaporation rate. For the purpose of this study, the values of relative humidity and temperature of the airflow measured by each sensor and the evaporation rate measured in each test will refer to the average values of relative humidity, temperature and evaporation rate calculated in the steady state phase of each test highlighted in the figure with a dotted window.

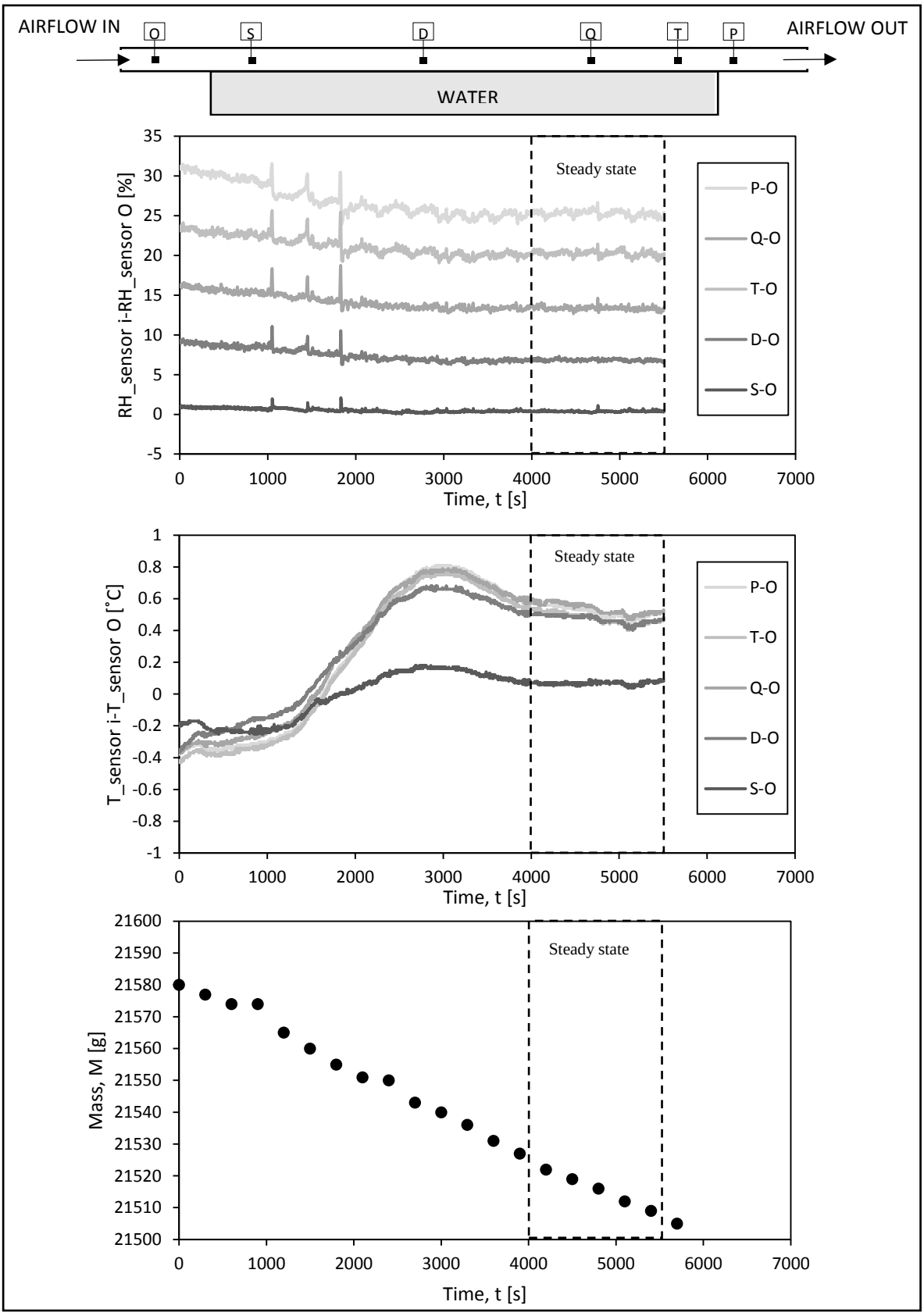

Figure 3-12: Steady state phase of the test with RH_{inlet}=30% and v_{air}=1m/s

3.5.1.3 Evaporation tests at different RHs and air velocities

The graphs in Figure 3-13 show the steady state *RH* of the airflow recorded by each *RH/T* sensor inside the upper air channel in the tests at air velocity from v_{air}=1m/s to v_{air}=4m/s and relative humidity of the airflow equals to RH_{inlet}=0% and RH_{inlet}=30% for Figure 3-13a and Figure 3-13b, respectively. The two dotted vertical lines represent the boundaries of the bottom water-filled container, sensor O provides the *RH* of the airflow at the inlet and sensor P provides the RH of the airflow at the outlet. Figure 3-13 shows that *RH* increases almost linearly with distance from the inlet. It can be observed that in each test the RH of the airflow measured by sensor S is approximately equal to the RHinlet recorded by sensor O. A closer inspection to the RH profile also shows that an accumulation of the *RH* of the air flow is present at the outlet of the upper air channel with the airflow at v_{air}=1m/s. This boundary effect was probably due to some air stagnation for which the reason is not clear. It is also worth noticing that the RH of the airflow at the outlet of the upper air channel is greater when the airflow has a lower air velocity. This can be explained by the fact that high air velocity sweeps away evaporating water more efficiently, preventing the boundary layer to enrich its vapour content and maintaining lower *RH* in the boundary layer.

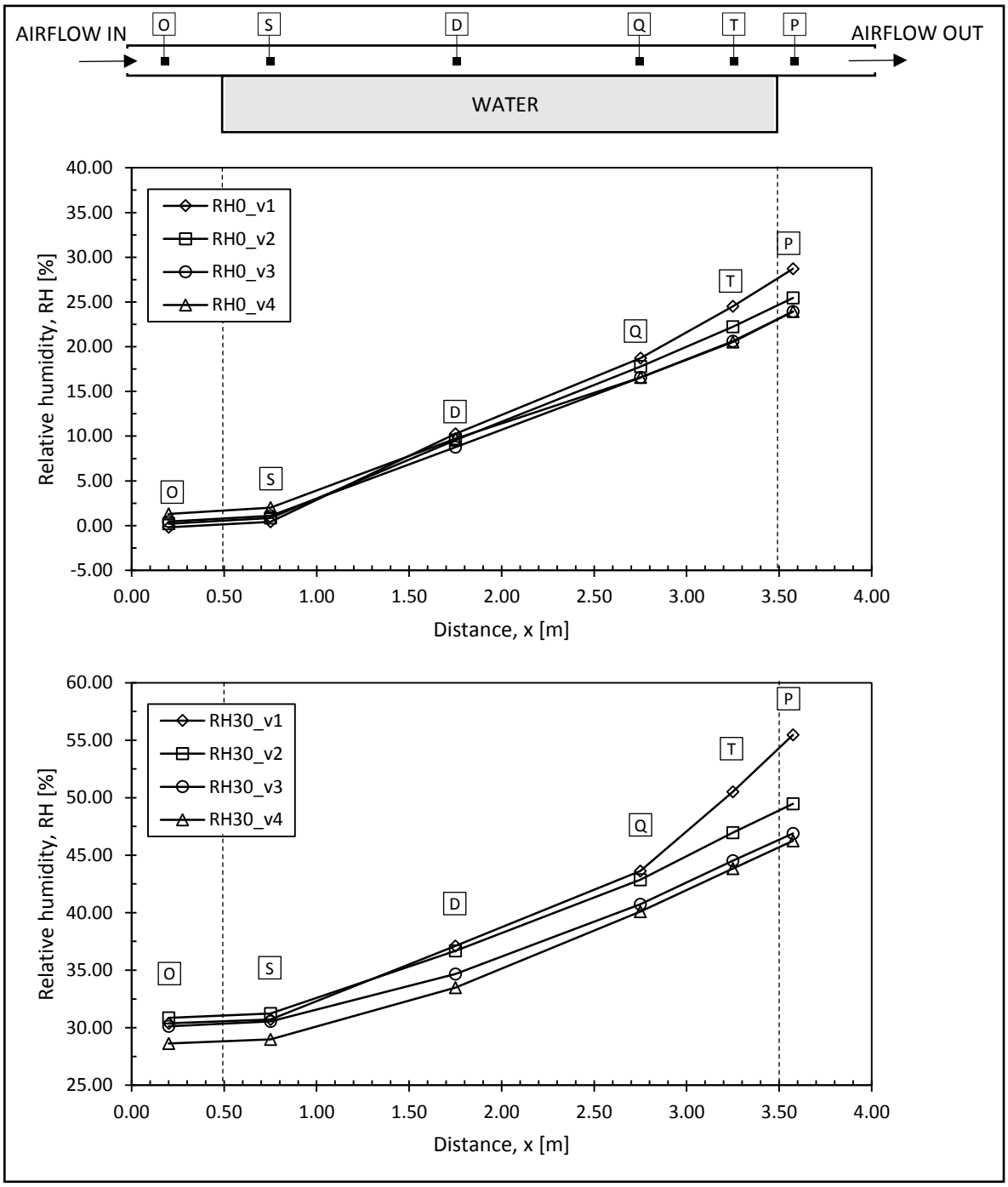

Figure 3-13: Relative humidity of the airflow measured via the RH/T sensors along the upper air channel-comparison for tests with the airflow at the same RH_{inlet} and different air velocity.

Figure 3-14 shows the comparison of the steady state *RH* of the airflow in the tests with the airflow at air velocity equals to v_{air}=1m/s for the *RH* at the inlet equal to RH_{inlet}=0% and RH_{inlet}=30%, respectively. It can be observed that the *RH* of the airflow increases almost linearly along the upper air channel in both tests. It is worth noticing that the increase of *RH* of

the airflow between the inlet and the outlet of the upper air channel in the test with RH_{inlet}= 0% is greater than the increase of *RH* of the airflow in the test with RH_{inlet} =30% at the same air velocity. This finding is consistent with the fact that the lower is the *RH* of the airflow, the higher is the evaporation rate of the water from the wet surface. With high evaporation rate, the amount of water vapour carried by the tangential airflow above the wet surface increases, hence the *RH* of the airflow also increases.

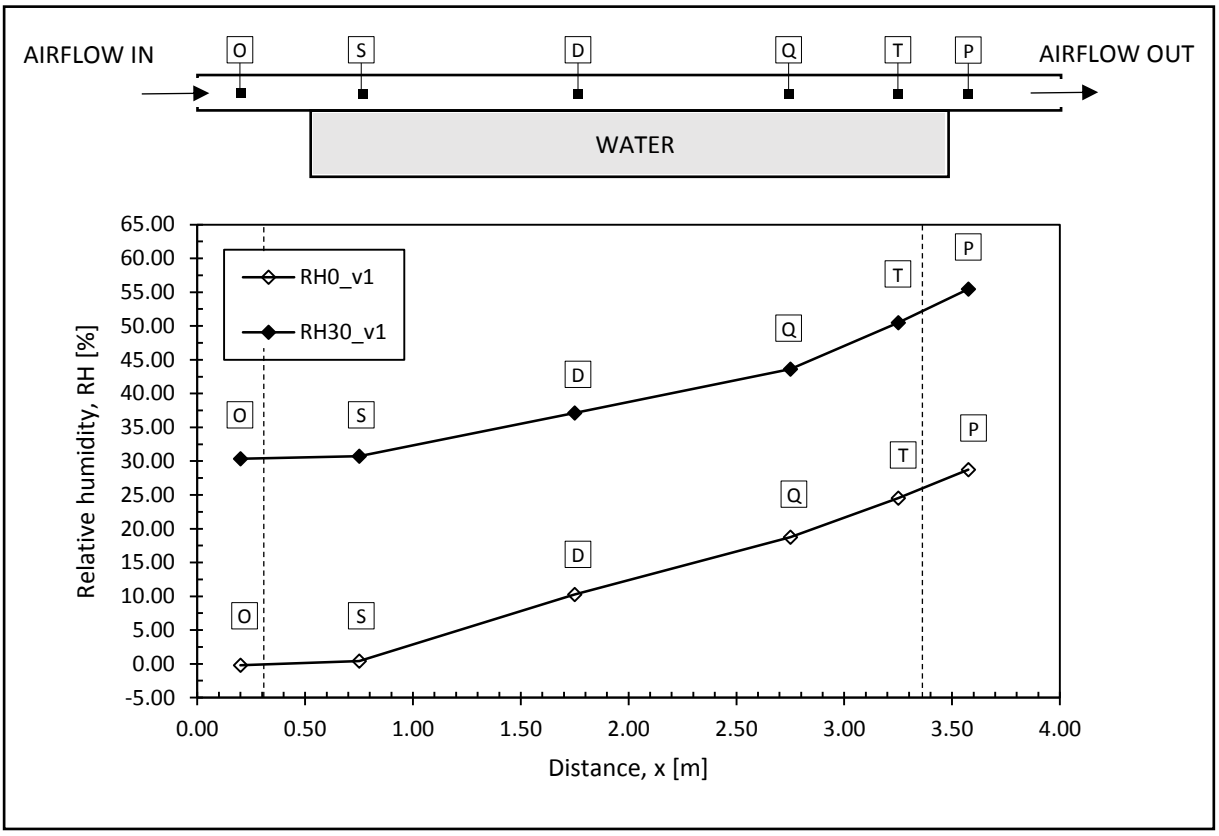

Figure 3-14: Relative humidity of the airflow measured via the RH/T sensors along the upper air channel-comparison for tests with the airflow at the same air velocity and different RH_{inlet}

The graphs in Figure 3-15 show the steady state temperature of the airflow recorded by each RH/T sensor at air velocity from v_{air}=1m/s to v_{air}=4m/s and relative humidity equal to RH_{inlet}=0% and RH_{inlet} =30% in Figure 3-15a and Figure 3-15b respectively. It can be observed that the temperature of the airflow at the inlet could be maintained at 20±2˚C. In the tests with RH_{inlet} =0% the temperature of the airflow at the inlet was imposed by the compressed air

system, whereas in the tests with RH_{inlet} =30% the temperature of the airflow was controlled by the temperature of the water bath in the humidification chamber. It is also possible to see that the temperature of the airflow remains fairly constant along the upper air channel.

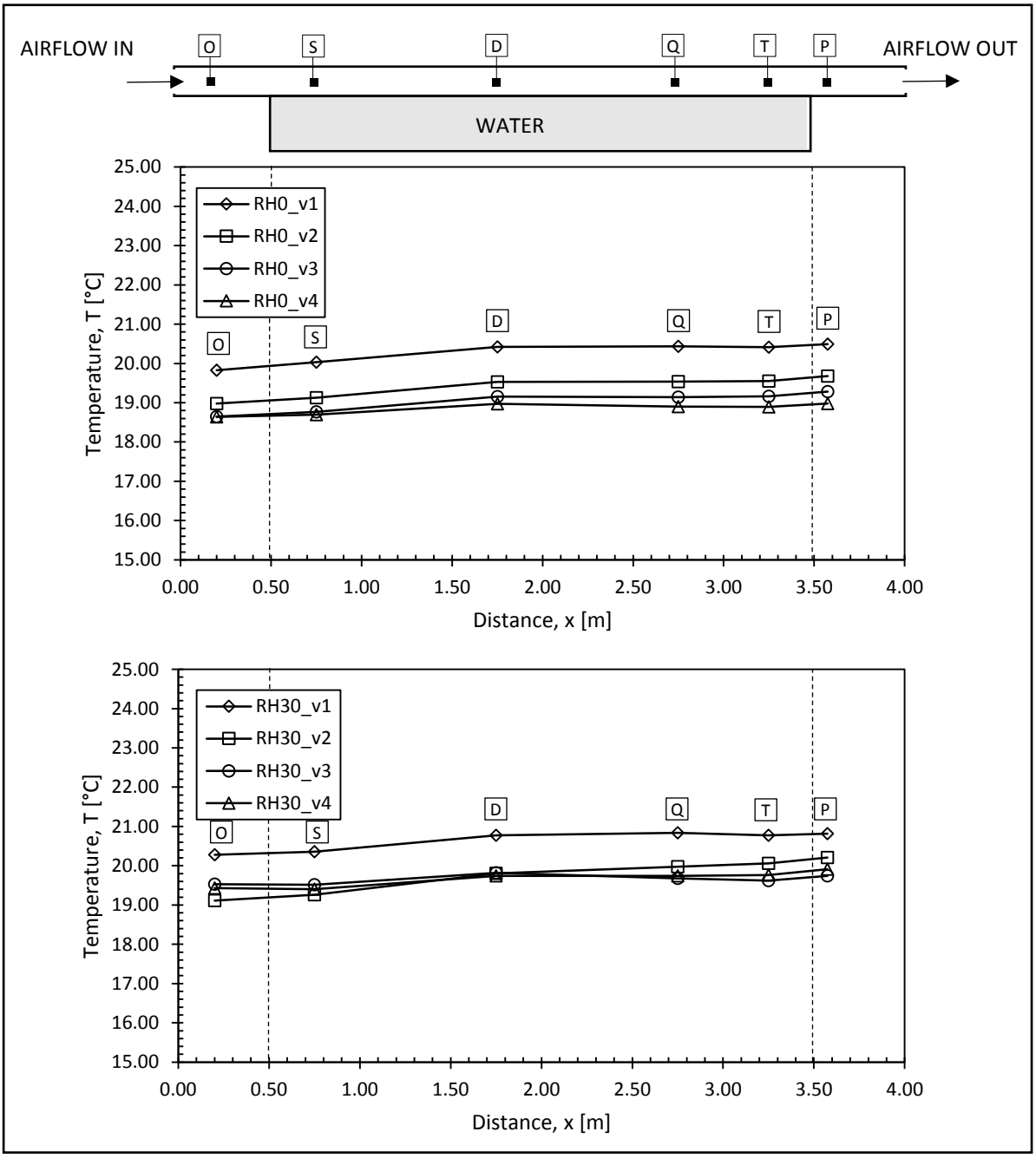

Figure 3-15: Temperature of the airflow measured via the RH/T sensors during the tests at varies air velocities and RH_{inlet} =0% and RH_{inlet} =30%

A closer inspection to the temperature profile reveals that the temperature of the airflow slightly increases between sensor O and sensor D and remains constant above the bottom container to slightly increases at the outlet between sensor T and sensor P. This suggests that the temperature of the airflow is controlled by the external boundary conditions at the inlet and at the outlet of the upper air channel whereas the temperature above the wet surface is slightly affected by the evaporation of the water from the bottom container.

The water flux q (volume of water per unit time and unit area) measured during the steady state of each test is plotted versus the tangential air velocity v_{air} (m/s) in Figure 3-16. As one would expect the evaporation rate increases with air velocity and the evaporation rate is lower at high *RH*.

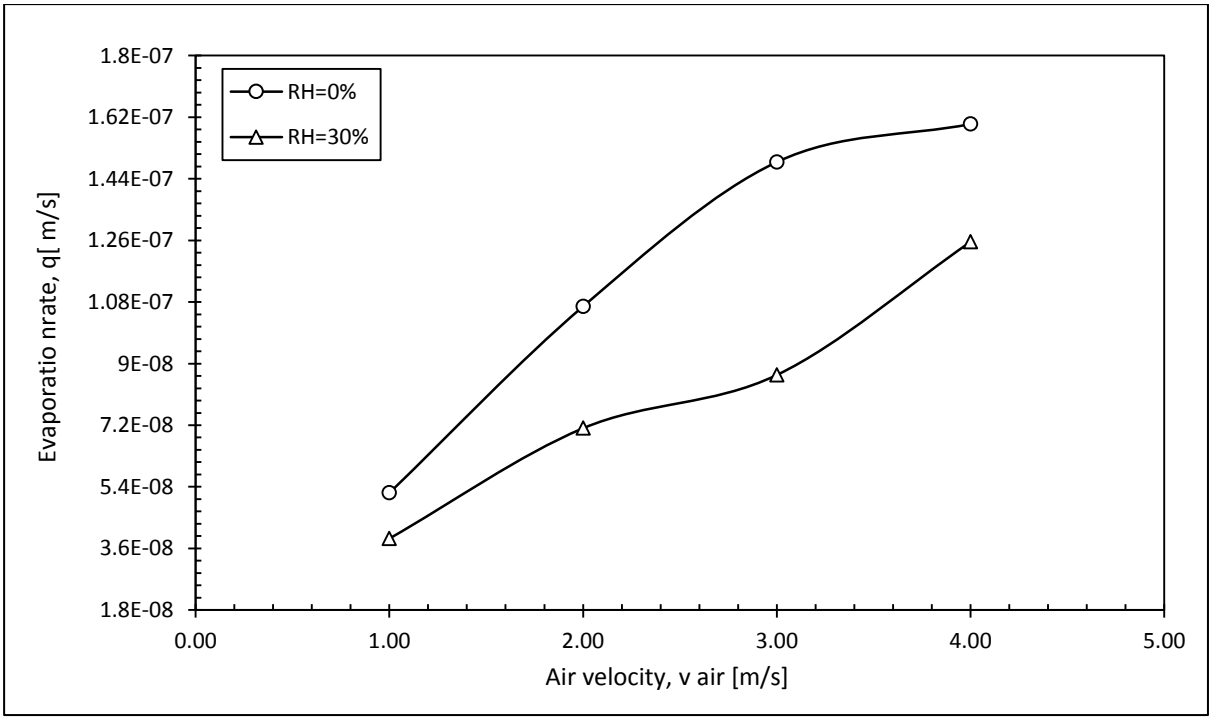

Figure 3-16: Experimental evaporation rate of water versus air velocity in the tests with RHinlet=0% and RHinlet=30%

The evaporation of water from a wet surface occurs due to the difference of *RH* between the *RH* of the wet surface (*RH*=100%) and the RH of the boundary layer above the wet surface.

The higher is the RH differential, the higher is the evaporation rate according to equation (3.7) shown later on in this Chapter (Section 3.6). On the other hand, higher tangential airflow velocity maintains lower *RH* in the boundary layer and hence, higher *RH* differential between the wet surface and the boundary layer. As a result, the evaporation increases with air velocity. It is also worth noticing that the two curves tend to converge at low air velocity, where the mechanism of evaporation by diffusion has a tendency to prevail.

3.5.2 Short evaporation machine with soil

The loss of mass of water from the soil sample exposed to a tangential airflow with RH_{inlet}=0% and air velocity equals to v_{air}=4m/s in the short evaporation machine is plotted in Figure 3-17. It can be observed that the constant rate period of drying ends after approximately 3.5 hours from the start of the test. This stage can be associated with the saturated stage of the soil sample (Tarantino, A., et al., 2010).

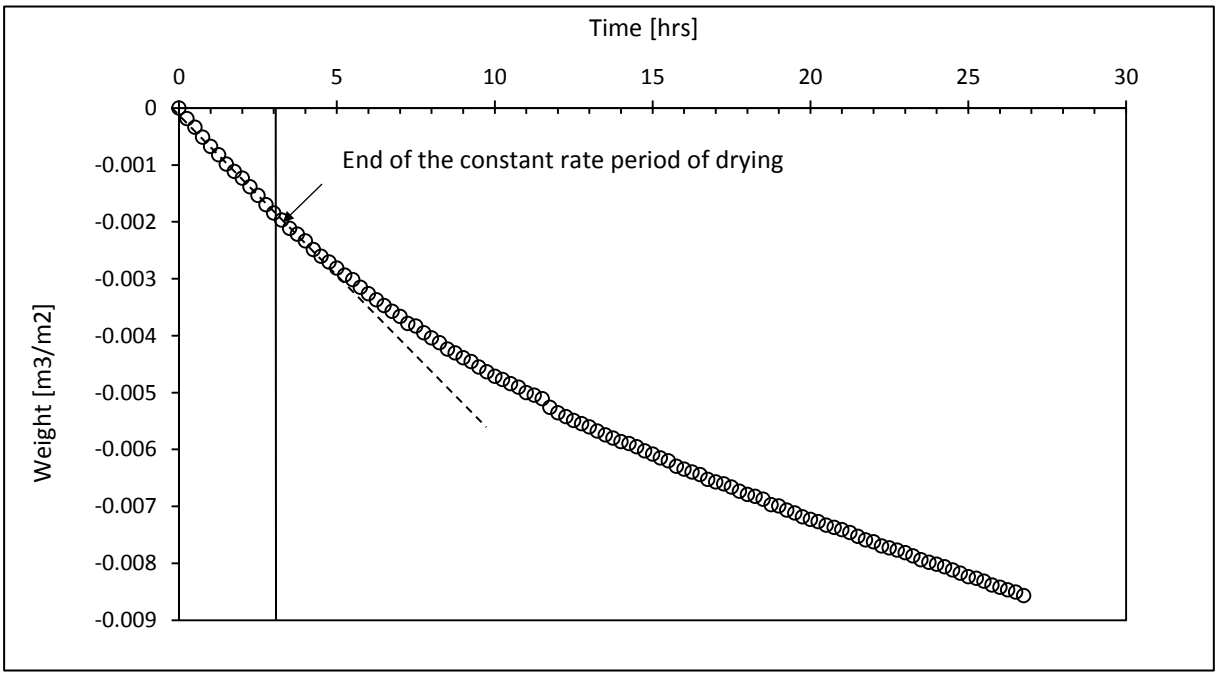

Figure 3-17: Loss of mass of water per unit area from the saturated soil sample over time

3.6 Water evaporation model

A model was developed to extend the results of the evaporation machine to suction drains that are longer and/or have airflow at the inlet with different relative humidity. The model was built for stationary conditions by discretising the upper air channel above the bottom water-filled container into elements 0.05 m wide. For each element the following balance equation holds:

$$m_{in(i)} + m_{ev(i)} = m_{out(i)} = m_{in(i+1)} \tag{3.1}$$

where $m_{in(i)}$ is the mass of water vapour carried by the airflow at the inlet of the element *(i)*, $m_{ev(i)}$ is the mass of water that evaporates from the water surface at the bottom of the element *(i)*, $m_{out(i)}$ is the mass of water vapour carried by the airflow at the outlet of each element *(i)*, and $m_{in(i+1)}$ is the mass of water vapour carried by the airflow at the inlet of the element *(i+1)*.

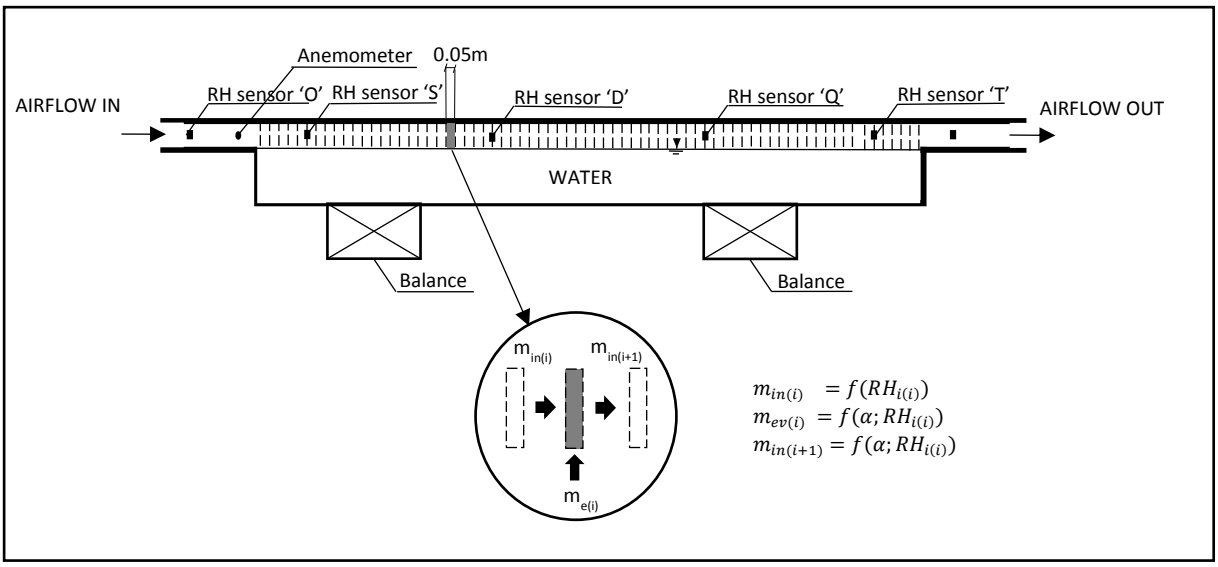

Figure 3-18: Graphical representation of the mass balance in the long evaporation machine for detecting the vapour transfer coefficient α

The mass of the water vapour at the inlet of each element $m_{in(i)}$ is expressed as:

$$m_{in(i)} = \rho_{v,i(i)} \cdot v_{air} \cdot \Delta t \cdot A_c \tag{3.2}$$

where $\rho_{v,i}$ is the density of the water vapour at the inlet of the element *(i)*, v_{air} is the velocity of the airflow measured via the anemometer at the inlet of the upper air channel, Δt is the time interval, and A_c is the cross sectional area of the upper air channel. In turn, the density of the water vapour at the inlet of the element $\rho_{v,in(i)}$ is a function of the relative humidity of the airflow at the inlet of the element (i), $RH_{in}(i)$. In turn, $RH_{in}(i)$ can be calculated as follows:

$$\rho_{v,in\,(i)} = \frac{p_{vo}\, RH_{in(i)}}{R_w T} \tag{3.3}$$

where p_{vo} is the equilibrium vapour pressure at saturation as a function of the temperature of the airflow, R_w is the gas constant of water vapour ($R_w = 461.50\, J\, K^{-1}\, kg^{-1}$) and *T* is the absolute temperature. By combining equations (3.2) and (3.3), the mass of the water vapour at the inlet $m_{in(i)}$ can be derived from the relative humidity at the inlet $RH_{in}(i)$ as follows:

$$m_{in(i)} = \frac{p_{vo}\, RH_{in(i)}}{R_w T} \cdot v_{air} \cdot \Delta t \cdot A_c \tag{3.4}$$

By similarity the mass of water vapour at the inlet of the element *(i+1)* can be derived from the relative humidity at the inlet $RH_{in(i+1)}$ as:

$$m_{in(i+1)} = \frac{p_{vo}\, RH_{in(i+1)}}{R_w T} \cdot v_{air} \cdot \Delta t \cdot A_c \tag{3.5}$$

The mass of water that evaporates from the water surface at the bottom of each element $m_{ev(i)}$ is described as follows:

$$m_{ev(i)} = q_{(i)} \cdot A_{ev} \cdot \Delta t \cdot \rho_w \tag{3.6}$$

where $q_{(i)}$ is the evaporation rate (water volume per unit area and unit time) in the element *(i)*, A_{ev} is the area of the water surface exposed to evaporation at the bottom of each element *(i)*, Δt is the time interval, and ρ_w is the density of liquid water. The evaporation rate of water per unit area and unit time $q_{(i)}$ under isothermal conditions is given by Dalton equation:

$$q_{(i)} = \alpha(v_{air}) \cdot p_{vo} \cdot \left(1 - RH_{in(i)}\right) \tag{3.7}$$

where $\alpha(v_{air})$ is the vapour transfer coefficient , which is a function of the horizontal air velocity, p_{vo} is the equilibrium vapour pressure at saturation, $RH_{in(i)}$ is the relative humidity of the airflow at the inlet of the element *(i)*. By combining equations (3.6) and (3.7) the mass of the water that evaporates from the water surface at the bottom of each element *(i)* can be written as a function of α and $RH_{in(i)}$ as follows:

$$m_{ev(i)} = \alpha(v_{air}) \cdot p_{vo} \cdot (1 - RH_{in(i)}) \cdot A_{ev} \cdot \Delta t \cdot \rho_w \tag{3.8}$$

The unknown of the model is the relative humidity of the airflow at the inlet of the element *(i)*, $RH_{in(i)}$ and the only parameter of the model to be calibrated is the vapour transfer coefficient $\alpha(v_{air})$. It is worth mentioning that both the relative humidity and the velocity of the airflow are assumed to be uniform within the cross section of the upper air channel. The relative humidity of the airflow is assumed to be equal to RH=100% in contact with the wet surface and to decrease sharply towards a constant value with height. Similarly, the air velocity is assumed to be v_{air} =0m/s in contact with the top and the bottom of the upper air channel and to increase sharply to a uniform value within the upper air channel as shown in Figure 3-19. The values of the uniform relative humidity and velocity of the air flow in the upper air channel are assumed to be equal to the values of relative humidity and air velocity measured experimentally via the RH/T sensors and the anemometer at 20 mm height from the wet surface.

The temperature profile (not shown in the figure) was assumed to be uniform across the upper air channel.

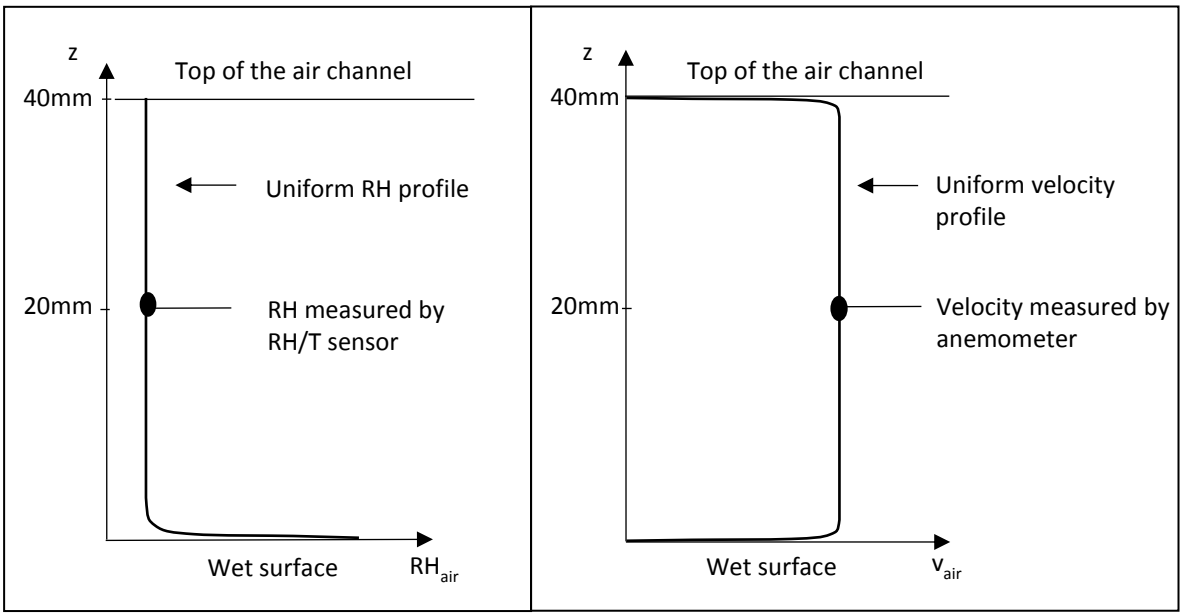

Figure 3-19: Uniform RH and velocity profile of the airflow in the upper air channel assumed in the model

3.6.1 Model calibration for water

The vapour transfer coefficient α model parameter was calibrated against the experimental results of the tests with the RH_{inlet}=0% and the air velocity varying from v_{air}=1m/s to v_{air}=4m/s. As shown in

Figure 3-18, the part of the upper air channel above the bottom container was divided into elements 0.05 m wide. The *RH* of the airflow at the inlet of the upper air channel was assumed to be equal to the value measured by the sensor 'O' and was used as model input.

The vapour transfer coefficient α was calculated by imposing that:

$$q_{model} = \frac{\sum_1^n q_{(i),model} \cdot \Delta l_i}{\sum_1^n \Delta l_i} = q_{experimental} \tag{3.9}$$

where q_{model} is the overall evaporation rate returned by the model, $q_{(i),model}$ is the evaporation rate associated with the element i, Δl_i is the width of the element i, and $q_{experimental}$ is the overall evaporation rate measured via the balances in the tests with RH_{inlet}=0% and air velocity varying from v_{air}=1m/s to v_{air} =4m/s.

The evaporation rate (water volume per unit area and unit time) of each element i, $q_{(i),model}$, is a function of the vapour transfer coefficient α (the model parameter to be calibrated) and the relative humidity at the inlet of the element i $RH_{in(i)}$ derived from equation (3.7).

By combining equations (3.1), (3.4), (3.5), and (3.8) the relative humidity at the inlet of each element can be expressed as a function of the vapour transfer coefficient α. By imposing $RH_{in(1)} = RH_{sensor'O'}$ the RH profile can be derived by using the forward integration:

$$RH_{in(i+1)} = \left(RH_{in(i)} \cdot v_{air} \cdot A_c + \alpha \cdot p_{vo} \cdot \left(1 - RH_{in(i)}\right) \cdot A_{ev} \cdot \rho_w \cdot R_w \cdot T\right) \cdot \frac{\Delta t}{v_{air} \cdot A_c} \tag{3.10}$$

Once the $RH_{in(i)}$ is determined for each element, the water flow $q_{(i),model}$ for each element can be estimated via equation (3.7) and, hence, the overall evaporation rate, q_{model}. The vapour transfer coefficient α at given velocity v_{air} is then determined by imposing the equality given by equation (3.9) for each of the velocities varying from v_{air}=1m/s to v_{air} =4m/s. The Generalised Reduced Gradient (GRG) Nonlinear algorithm was used to solve the iteration. The parameters used for the model are listed in Table 3-5 and the values of the vapour transfer coefficient α derived from the calibration are shown in Table 3-6.

Table 3-5: Parameters of the model

T_0 (K)	$p_{v0}(T_0)$ (Pa)	R_w (J K^{-1} kg^{-1})	Δt (sec)	A_c (m^2)	A_{ev} (m^2)	ρ_w (kg/m^3)

293.16	2333.44	461.9	1	0.0012	0.0015	998.2

Table 3-6: Values of the vapour transfer coefficients derived from calibration

v_{air}	1 m/s	2 m/s	3 m/s	4 m/s
$\alpha(v_{air})$	2.43×10^{-11}	5.02×10^{-11}	6.94×10^{-11}	7.37×10^{-11}

3.6.2 Simulation of evaporation from water surface

Figure 3-20 shows the simulation of the test at *RH*=30%. The evaporation rate per unit time and unit area, q_{model} obtained from the model simulation (solid triangles) based on the calibration of the vapour transfer coefficient α against an independent test (*RH*=0%) is compared with the evaporation rate $q_{experimental}$ obtained experimentally in the long evaporation machine (open triangles) for airflow at RH_{inlet}=30% and air velocities varying from v_{air}=1m/s to v_{air} =4m/s. The evaporation rate from the model was calculated by using equation (3.7) with the vapour transfer coefficients α derived from the calibration discussed in Section 3.6.1. The comparison shows that the data from the simulation and experimental data overlap at low air velocity, whereas scatter slightly increases at high air velocity. This difference might be due to the fact that v_{air}=3m/s and v_{air}=4m/s had a greater fluctuations during the experiments than v_{air}=1m/s and v_{air}=2m/s, resulting in slightly effecting the evaporation rate. Overall the model simulates satisfactorily the experimental results and it can therefore be considered an adequate tool to design the suction drain, i.e. to estimate the evaporation rate from the inner surface of the borehole exposed to a tangential airflow at a known air velocity.

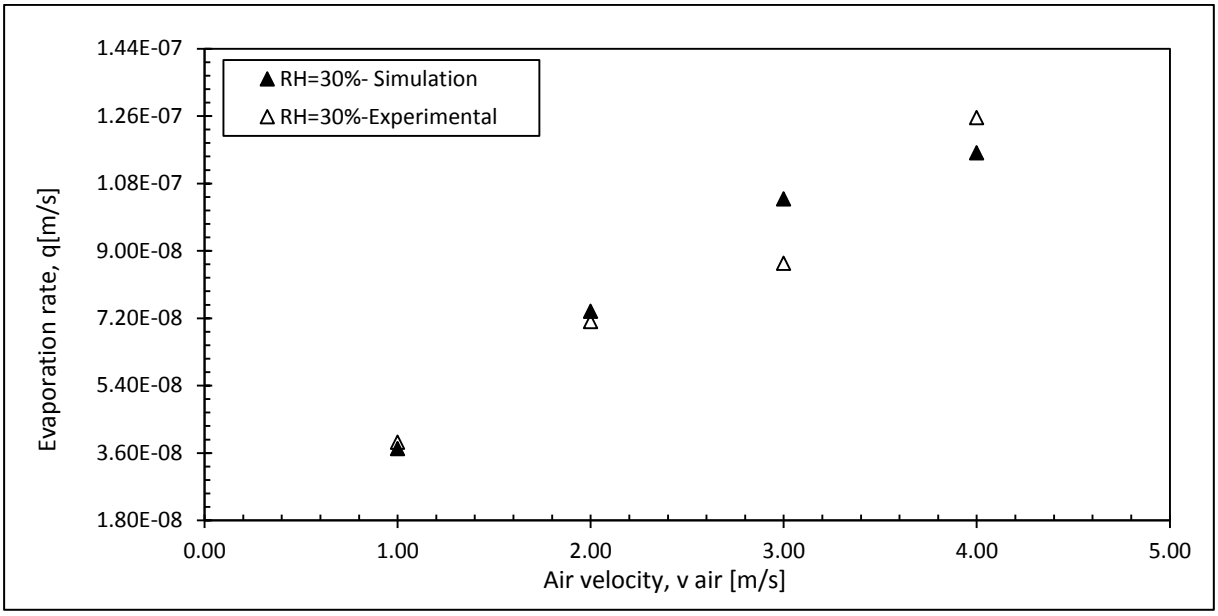

Figure 3-20: Comparison of the evaporation rate of water estimated via the model and obtained experimentally

3.6.3 Comparison between saturated soil and water surface

Figure 3-21 shows the comparison between the evaporation of water from the saturated soil surface in the short evaporation machine and the evaporation of water from the water surface in the long evaporation machine over time. The comparison is carried out in terms of the loss of water volume ΔV_{water} per unit area A normalised to the relative humidity differential ΔRH, i.e. the difference between the relative humidity at the evaporating surface (RH=100%) and the average relative humidity of the airflow in the upper air channel above the evaporating surface ($RH_{average}$=0% for the soil sample in the short evaporation machine and $RH_{average}$=12% for the water surface in the long evaporation machine). The slope of the curves in Figure 3-21 actually represents the vapour transfer coefficient α.

The tests are compared for the airflow having RH_{inlet}=0% and air velocity v_{air}=4m/s. The normalised water volume loss for soil and water compares favourably as shown in Figure 3-21. This suggests that the vapour transfer coefficient α derived from evaporation from water surface

also holds for saturated soil sample. As a result, the outcomes of evaporation tests involving a wet surface water surface can be extrapolated to evaporation involving saturated soil surfaces.

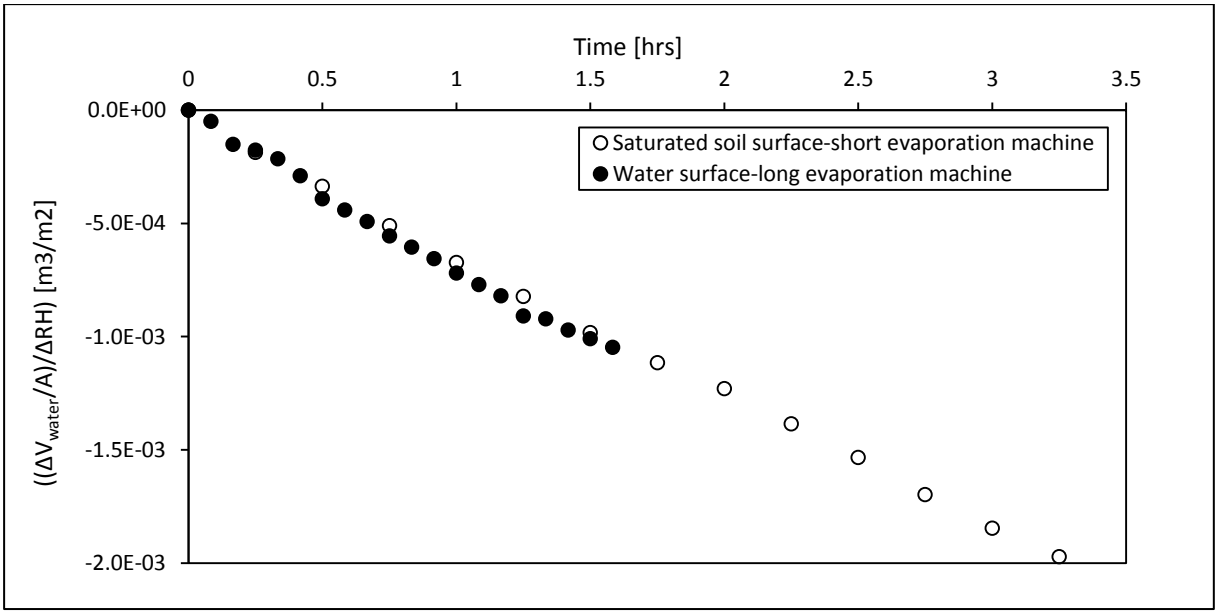

Figure 3-21: Evaporation rate of water from the saturated soil sample and from the water surface in tests with airflow at v_{air}=4m/s and RH_{inlet}=0%

3.7 Discussion

3.7.1 Vapour transfer coefficient

The key of the model is the vapour transfer coefficient α in equation (3.7). In Section 3.6.1, the coefficient α was calibrated for tangential airflow injected through a gap of 40 mm. A different clearance between the inner surfaces of the borehole and the inner air delivery tube in the suction drain would require in principle the design of a new evaporation machine with different height of the upper air channel. This approach would not be suitable for practical applications. A semi-empirical relationship to estimate α without the need of developing a different evaporation machine was therefore sought.

Penman (1948) provides a theoretical equation for the estimation of the evaporation rate from open water surface by using the standard meteorological data at the reference height z=2m from the wet surface. Penman equation was then probed to estimate the evaporation rate in the evaporation machine, i.e. the evaporation rate occurring from a wet surface exposed to a tangential airflow in a confined space. The relative humidity and the air velocity at z=20mm above the wet surface were used in place of the relative humidity and the air velocity at z=2m as per the original Penman's equation.

The evaporation rate of water E from a wet surface suggested by Penman (1948) can be written as follows (Brutsaert, 1982):

$$E = \frac{0.622}{\rho_w R_d T(z)\, r_a} \cdot p_{v0}\,(1 - RH(z)) \tag{3.11}$$

where 0.622=(18.016/28.966) is the ratio of the molecular weights of water and dry air, ρ_w is the density of water, R_d is the gas constant of dry air ($R_d = 287.04\, J\, K^{-1}\, kg^{-1}$) and *T(z)* is the absolute temperature at the reference height z from the wet surface, p_{vo} is the equilibrium vapour pressure at saturation, $RH(z)$ is the relative humidity of the airflow at the reference height z from the wet surface and r_a is the aerodynamic resistance that was expressed by Penman, (1956) as follows (Brutsaert, 1982, Thom & Oliver, 1977):

$$r_a = \frac{250}{0.5 + 0.54 \cdot v_{air}(z)} \quad \left[\frac{s}{m}\right] \tag{3.12}$$

where $v_{air}(z)$ is the air velocity measured at reference height z=2m from the wet surface.

By combining equation (3.11) and (3.12) the evaporation rate E (m/s) (volume of water per unit time and unit area) can be calculated as follows according to Penman:

$$E = \frac{0.622}{\rho_w R_d T(z)} \cdot \frac{250}{0.5 + 0.54 \cdot v_{air}(z)} \cdot\, p_{v0}\,(1 - RH(z)) \tag{3.13}$$

where the reference height z for the purpose of this study is z=20mm from the wet surface.

By defining α_{Penman} as:

$$\alpha_{Penman} = \frac{0.622}{\rho_w R_d T(z)} \cdot \frac{250}{0.5 + 0.54 \cdot v_{air}(z)} \tag{3.14}$$

the volume of water per unit time and unit area E (m/s) that evaporates from the bottom container in the long evaporation machine by means of Penman equation can finally be written as:

$$E = \alpha_{Penman} \cdot p_{v0} \, (1 - RH(z)) \tag{3.15}$$

Figure 3-22 shows the values of $\alpha_{Experimental}$ obtained from direct calibration (Section 3.6.1) against the values α_{Penman} obtained from equation (3.14) as a function of the air velocity v_{air} (m/s). It can be observed that $\alpha_{Experimental}$ and α_{Penman} compare fairly well.

The equation of Penman (3.13) is generally used for estimating the evaporation from wet surface in open space by using the measurement of the air velocity at 2 m height from the wet surface. This result suggests that Penman equation (3.13) estimates with good approximation also the evaporation of water from a wet surface that is exposed to a confined airflow by using the RH and air velocity of the airflow at 20mm height from the wet surface.

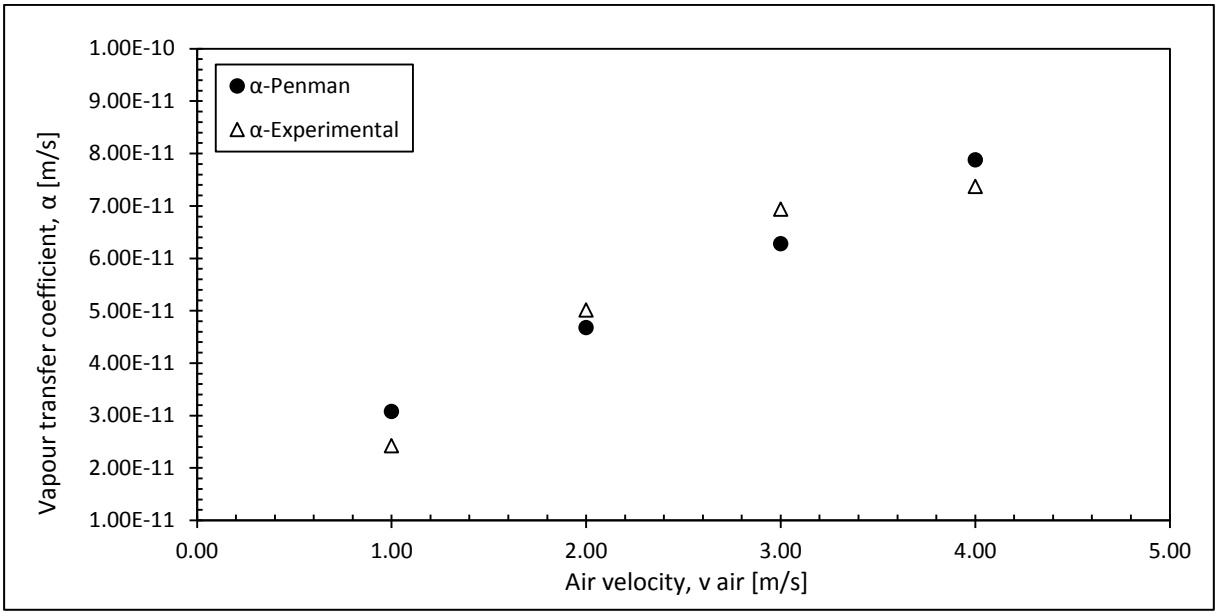

Figure 3-22: Comparison between α-Penman and α-Experimental

The relatively accurate estimation of the vapour transfer coefficient using Penman's equation suggests that the assumptions behind Penman's equation also hold for the airflow in a confined space. Figure 3-23 shows the profile of the mean wind speed above the evaporating surface and it is possible to see that only above the interfacial sublayer the logarithmic profile is fully developed. The interfacial sublayer is the region where the turbulence is strongly affected by the structure of the roughness element or it is greatly damped by viscous effects. Brutsaert (1982) suggests that the interfacial sublayer is 1.5 to 3.5 times the height h_0 of the roughness obstacles. In the evaporation machine the surface exposed to evaporation is a smooth surface with virtually zero roughness. The interfacial sublayer is therefore expected to be very small so that the anemometer at 20 mm from the evaporating surface measures air velocity in the fully developed logarithmic profile.

This also implies that Penman equation (3.13) could be used in the design of the suction drain as long as the roughness of the inner surface of the borehole is of the order of a few millimetres. This would generate a thickness of the interfacial sublayer significantly smaller

than the gap between the inner surface of the borehole and the centralised air delivery tube at air velocity. The profiles of air relative humidity and velocity would be quasi-uniform, which is the assumption behind the simple model put forward in this paper.

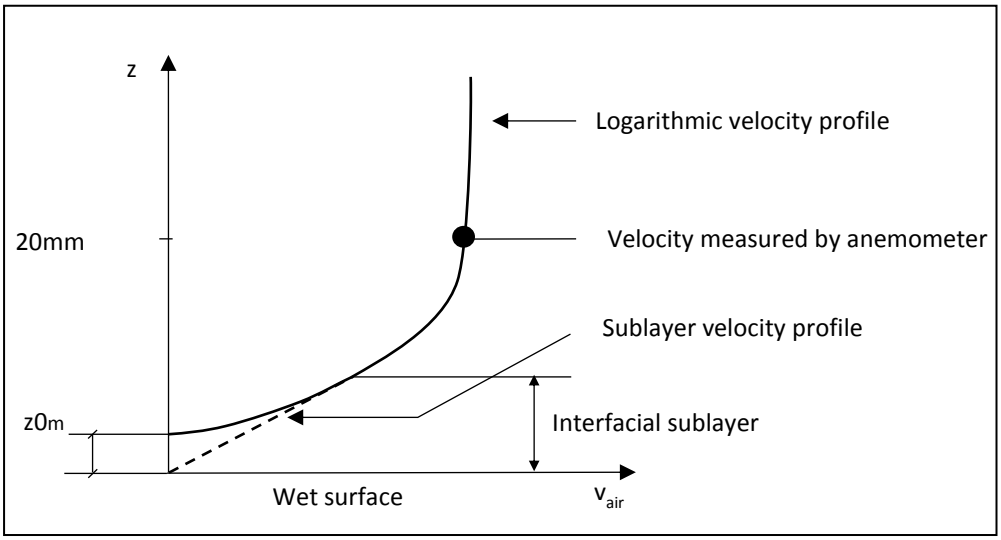

Figure 3-23: Air velocity profile

Ultimately, the findings of Figure 3-22 suggests that: i) the assumptions behind Penman equation are also valid for the evaporation machine, ii) the semi-empirical approach proposed by Penman provides a valid tool for estimating the evaporation rate in a confined space. The second point becomes important in the practical design of the suction drain because it will allow the water flux to be estimated without the need to develop a purposely designed evaporation machine.

3.7.2 Airflow relative humidity

Figure 3-24a and Figure 3-24b show the comparison between the RH of the airflow above the wet surface measured experimentally via the RH/T sensors ($RH_{experimental}$), the RH of the airflow predicted by the model based on the vapour transfer coefficient calibrated experimentally, $RH_{calibration}$ (see Section 3.6.1), and the RH of the airflow predicted by the model

based on the vapour transfer coefficient estimated by using Penman's equation, RH_{Penman} (see Section 3.7.1) for the tests with the airflow at v_{air}=2m/s and RH_{inlet}=0% and RH_{inlet}=30% respectively. The RH of the airflow predicted by the model was based on equation (3.10).

It can be observed that there is a fair agreement between the values derived from the model ($RH_{calibration}$ and RH_{Penman}) and the experimental values $RH_{experimental}$. The very basic model for water evaporation along a wet surface put forward in this paper can therefore be considered adequate for practical applications despite the simplifications introduced in the model including the assumptions on the air velocity and RH profiles.

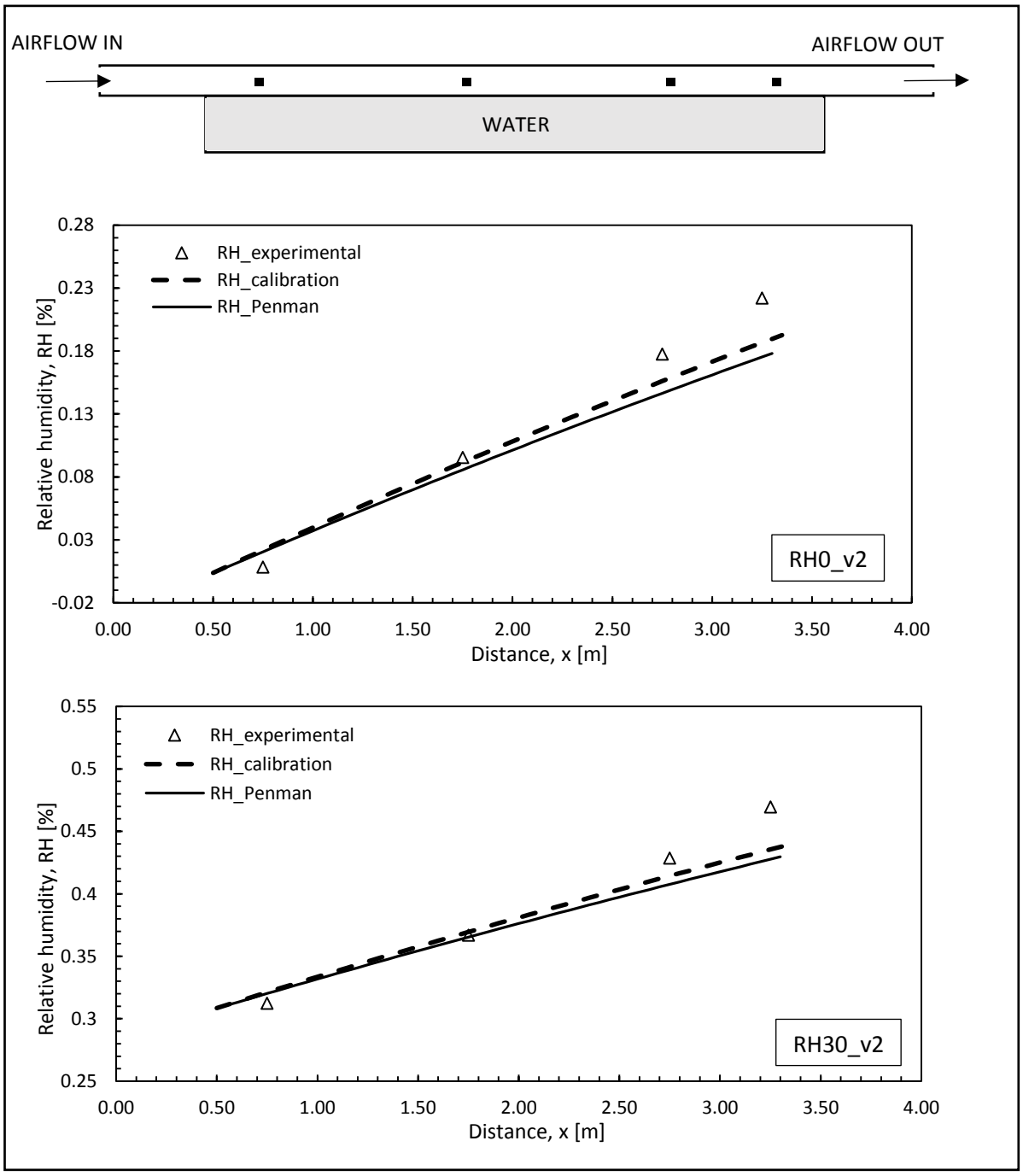

Figure 3-24: Relative humidity of the airflow measured experimentally, estimated via α-model and estimated via α-Penman for v_{air}=2m/s.

3.8 Conclusions

The paper has presented an experimental investigation of the evaporation from water and soil surfaces induced by tangential air flow through a confined space. This study was aimed

to support the design of suction drains, a technique for low-carbon temporary stabilisation of tunnels and excavations in clays.

An apparatus was developed to measure water evaporation from a 3 m long wet surface subjected to a tangential airflow through a 40 mm gap. Tests have explored different air velocities (1 to 4 m/s) and relative humidity at the inlet (RH=0% and RH=30%). As expected, experimental results showed that i) evaporation rate increased with air velocity, ii) evaporation rate decreased with RH at the inlet of the airflow, and iii) relative humidity increased along the wet surface, i.e. the airflow progressively enriched with water vapour.

The relationship derived experimentally between the evaporation rate along a 3 m wet surface and the air velocity and relative humidity of the airflow cannot be applied straightway to longer or shorter evaporation surfaces. For this reason, a simple evaporation model was developed based on the assumption that relative humidity and velocity of airflow are uniform in the confined space.

The key parameter of the model is the vapour transfer coefficient α, which controls the linear dependency of the evaporation rate on the relative humidity differential between the wet surface and the airflow. The vapour transfer coefficient α was calibrated against the tests with relative humidity at the inlet RH_{inlet}=0% and this allowed probing the model against the tests with relative humidity at the inlet RH_{inlet}=30%. The model was found to perform satisfactorily showing that the simple assumption of uniform relative humidity and velocity does not represent a significant limitation of the model.

The vapour transfer coefficient α detected in the test on water surface was then found to be the same as the vapour transfer coefficient for saturated soil exposed to the airflow. As a result, findings from tests on water surfaces can be extrapolated to soil surfaces.

The values of vapour transfer coefficient derived from the empirical relationship derived by Penman (1948, 1956) for open water was therefore benchmarked against the values derived experimentally for confined airflow. The good matching between the two sets of values indicates that Penman's relationship can be used successfully for a first estimation of the vapour transfer coefficient for confined airflow. At a more fundamental level, the matching between the vapour transfer coefficients for open airflow and confined airflow seems to suggest that the assumptions behind Penman's formulation for open water also hold for confined airflow. In particular, the logarithmic profile would fully develop in the confined air flow due to the reduced thickness of the interfacial sublayer.

For the case of the suction drain, the roughness of the inner surface of the borehole would be of the order of a few millimetres. This would generate a thickness of the interfacial sublayer significantly smaller than the gap between the inner surface of the borehole and the centralised air delivery tube. In turn, this would produce quasi-uniform velocity and relative humidity profiles across the gap, which is the basic assumption behind the evaporation model proposed in this paper.

4 SUCTION DRAIN AS A LOW CARBON GROUND IMPROVEMENT TECHNIQUE: PROOF-OF-CONCEPT AT THE LABORATORY SCALE

4.1 Abstract

The most common soil reinforcement method used in tunnelling, such as jet grouting, fiberglass reinforcement and ground freezing, leave spoils into the ground and have high costs of implementation. On the other hand, preloading methods for soils improvement require long construction periods and limit the enhancement of the undrained shear strength to the applied surcharge load or vacuum load. This paper presents the concept of suction drain as an innovative technique for temporary stabilisation of geo structures in soft clayey soils, which overcomes the inconvenience of current soil reinforcement techniques and the limitation of the preloading. Based on suction generated into the ground by the evaporation from pre-drilled holes, the suction drain enables the enhancement of the undrained shear strength in soft clayey. The concept and its validation at mock-up scale level are presented in this study. The experimental investigation assessed the capacity of the suction drain to reduce the soil water content via soil water evaporation induced by forced ventilation. The mock-up scale test was then validated numerically via FEM modelling. Finally, the suction drain modelling was extended to an ideal case of tunnelling for assessing the potential impact of the suction drain on undrained shear strength and, hence, on tunnel face stability.

4.2 Introduction

Soft clays possess very low undrained shear strength and ground improvement techniques need to be implemented prior to construction to ensure tunnel stability. The enhancement of soils shear strength is achieved by either soil reinforcement technique or preloading.

Jet grouting and fiberglass reinforcement are the most common soil reinforcement methods used in tunnelling to ensure stability. Ground freezing is also used as temporary structural support and/or to exclude groundwater from the excavation until construction of the final lining provides permanent support. These techniques leave chemical residues and spoils into the soil or into the groundwater, slow down construction process due to the need of cleaning up the soil after construction, and have high costs of implementation.

On the other hand, preloading methods apply the surcharge effective stress to the soft clayey soils either via the self-weight of a fill material (i.e. embankment) and/or by the vacuum pressure. Under fill surcharge, the excess pore water pressure first build up from its initial (normally hydrostatic) state and then dissipate gradually. The soil undergoes consolidation and soil water content decreases, which generates higher undrained shear strength. Under vacuum pressure, the pore-water pressure in the soil instead reduces from its initial (normally hydrostatic) state by the same amount as the applied vacuum pressure. Again, the soil undergoes consolidation and the undrained shear strength increases. In both cases, the enhancement of undrained shear strength is limited to the applied surcharge load or vacuum load (generally smaller than 100kPa). Heavy machinery and long construction periods are also required for the fill surcharge preloading technique.

This paper explores the potential of the suction drain as an innovative technique for temporary stability of geo structures in soft clayey soils. Based on suction generated into the

ground by evaporation from pre-drilled holes, this technique enables the enhancement of the undrained shear strength in soft clayey. No expensive equipment is required for its implementation and no spoils are left into the ground after its application. The suction drain overcomes the inconvenience of the soil reinforcement technique and the limitation of the preloading technique. The concept of the suction drain and its validation at mock-up scale level are presented in this study together with examples of its application to tunnel face stability.

4.3 Suction drain concept

The suction drain is conceived as a ground improvement technique to ensure temporary stability of open face tunnels and open excavations. The goal of the technique is to enhance the undrained shear strength of the soil by reducing its water content via evaporation-induced water flow.

In the proposed technique boreholes are drilled into the ground and compressed air is injected through a delivery pipe. The soil around the borehole is exposed to a continuous and constant tangential air flow at the soil interface. This generates evaporation, hence pore water pressure is depleted at the soil interface and eventually becomes negative (suction). A hydraulic head differential is generated and water flow is triggered towards the borehole. As suction propagates from the borehole and consolidation takes place, water content in the surrounding soil reduces and undrained shear strength increases accordingly (Figure 4-1).

The sequence of operations related to the technology would consist in i) drilling a cased borehole to the required distance from the tunnel face by means of a dry drilling technique, ii) uncasing the borehole and installing an inner slotted case, and iii) installing an air delivery pipe coaxially into the borehole down to its end. Air is injected at the end of the borehole and circulates from the end to the entry of the borehole through the gap between the air delivery

tube and the inner surface of the borehole. The continuous airflow generates evaporation-induced soil water flux on the soil interface. When the water content is decreased adequately, the excavation face is advanced.

Stability is therefore insured by the suction drain-enhanced undrained shear strenght, assuming that clayey deformations at the onset of failure occurs rapidly with little or no dissipation of excess pore-water pressure due to low permeability of the clayey soil (Mair & Taylor, 1997).

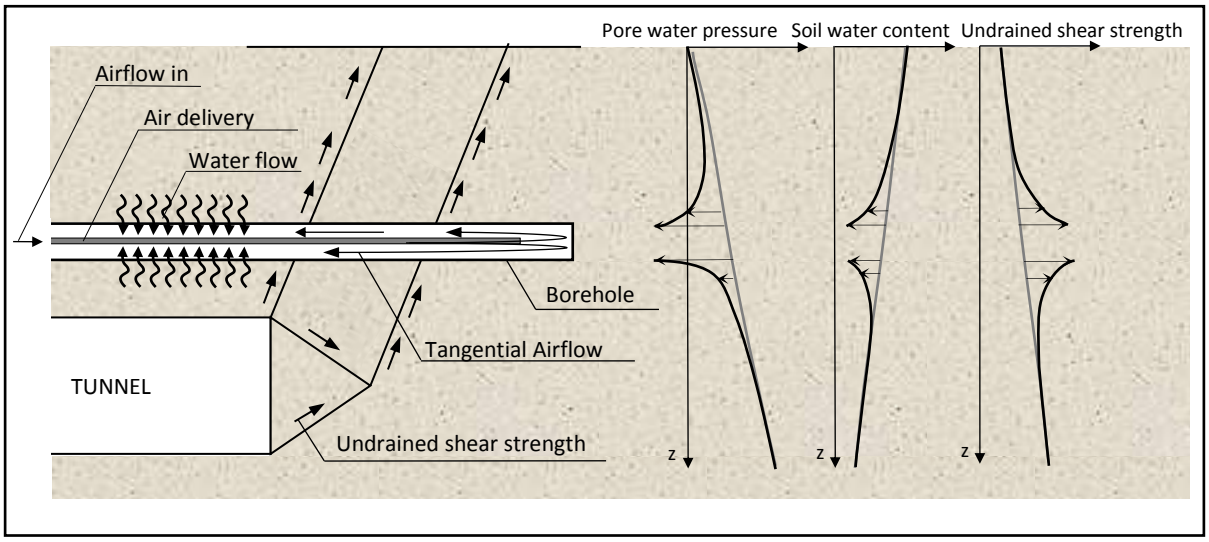

Figure 4-1: Concept of the suction drain (not in scale)

4.4 Material characterisation

4.4.1 Soil classification and index properties

A block sample of natural soil was taken from a working site located off Newton Farm Road in the north eastern outskirts of Newton, Cambuslang. The soil was as soft mottled orange sandy clay with bands of mottled orange sandy silt. A block sample was taken at 2.2 m below ground level and it was wrapped with Parafilm ® and silicon grease on site to preserve the

natural soil water content. In the laboratory part of the soil from the block sample was used for soil classification and the determination of index properties. The grain size distribution, obtained via wet sieving and sedimentation showed it to have 33% clay, 64% silt and 3% sand. The limit liquid assessed by fall cone test was LL=0.47 and the thread-rolling plastic limit was PL= 0.23. According to the plasticity chart of Casagrande the clay is classified as inorganic clay with intermediate plasticity (PI=0.24). The soil is also classified as inactive clay with the activity A=0.73. The specific gravity is G_s= 2.66. All testing was carried out in accordance with BS1377:1190.

4.4.2 Water retention behaviour

A 50 mm diameter metallic cutting ring was used to cut soil specimens from the block sample. The specimen were air-dried to target water contents then wrapped within a waterproof layer of Parafilm ® and silicon grease and stored for 24 hrs to ensure the equilibrium of the water content throughout the soil. High-capacity tensiometers (HCT) (Tarantino, 2009) were used to measure the soil suction *s* in the range 0-2000 kPa. Two holes were cut through the waterproof layer of the specimen and two high-capacity tensiometers were placed in contact with the surface of the specimen. A Parafilm® cover was placed around the tensiometers during the measurement to avoid water evaporation occurring from the holes. After the measurement, the sample was placed into the oven at 105˚C for 24 hrs to obtain the moisture content related to the matric suction.

A dew point water potentiometer (WP4C) was also used to measure suction *s* in the range 100-5000 kPa. The calibration curve of the device was verified by using sodium chloride solutions with known water potentials at 20˚C with a measured standard deviation in accuracy of ±30 kPa. Specimens of approximately 1 cm^3 were cut from the 50 mm diameter soil sample

and were placed into the WP4C. At the end of the suction measurement the specimens were placed into the oven at 105°C for 24 hrs to obtain the moisture content related to the total suction.

The measurement of total suction (WPC4) and matric suction (HCT) versus water ratio, e_w are plotted in Figure 4-2a. The overlap of total suction and matric suction data in the range 100kPa-2000kPa shows that the osmotic suction is negligible.

The relationship between the soil void ratio, e and the soil water ratio, e_w was assessed independently. A 16 mm diameter and 12.5 mm high cutting ring was used to cut small specimens from the 50mm diameter soil samples after they were air-dried to target water content. The cutting ring was pushed into the sample slowly using a loading frame to prevent soil cracking. The top and bottom of the specimen were trimmed to give the specimen the same volume as the inner volume of the cutting ring, which allowed for the calculation of the void ratio. The specimen was then placed into the oven at 105°C for 24 hrs to obtain the soil water content. The void ratio, e, versus water ratio, e_w, is shown in Figure 4-2b. Data were fitted by using the following equations (Tarantino A. et al., 2010):

$$e = w \cdot Gs = e_w \qquad (w > w_{AE}) \tag{4.1a}$$

$$e = e_{res} + \frac{e_{AE} - e_{res}}{exp[b\,(w_{AE} - w)]} \qquad (w < w_{AE}) \tag{4.1b}$$

where w_{AE} is the gravimetric water content at air entry, G_s is the specific gravity of the soil, e_{res} is the residual void ratio, e_{AE} is the void ratio at air entry, and b is a fitting parameter. It is possible to see that upon drying, the void ratio decreases to $e = 0.53$ in the saturated range then remains constant when the soil desaturates.

The drying curve in terms of degree of saturation, S_r versus soil suction, s, is shown in Figure 4-2c. For each data point of known water ratio, e_w, and soil suction, s, the degree of

saturation S_r was calculated as per the ratio of water ratio to void ratio ($S_r = e_w/e$) with void ratio e obtained from Equation (4.1). Experimental data of the degree of saturation, S_r versus soil suction, s, were fitted by using Van Genuchten's function (Van Genuchten, 1980):

$$S_r = \left(\frac{1}{1 + (\alpha s)^n}\right)^m \tag{4.2}$$

where α, n and m are fitting parameters.

The relationship of void ratio, e versus soil suction, s is shown in Figure 4-2d. Experimental data were fitted by using the following equations:

$$e = e_k - k \cdot ln(s) \qquad (s < s_p) \tag{4.3a}$$

$$e = N - \lambda \cdot ln(s) \qquad (s_p < s < s_{AE}) \tag{4.3b}$$

$$e = e_{res} + \frac{e_{AE} - e_{res}}{exp(a\,(s - s_{AE}))} \qquad (s > s_{AE}) \tag{4.3c}$$

where s_p is the suction associated with the preconsolidation effective stress, s_{AE} is the suction at air entry, e_k, k, N, λ and a are fitting parameters. From Figure 4-2d it is possible to see that the soil is over consolidated for soil suction lower than s_p=177kPa, normally consolidated at suctions between s_p=177kPa and s_{AE}=420kPa, and it desaturates at soil suction greater than s_{AE}=420kPa.

Ultimately, the water retention behaviour in terms of volumetric water content, θ, was defined by the product of the porosity, n to the degree of saturation, S_r ($\theta = n \cdot S_r$). The values of the parameters used for defining the water retention behaviour of the soil are given in Table 4-1.

Table 4-1: Parameters for the water retention behaviour

w_{AE} [-]	e_{res} [-]	e_{AE} [-]	b [-]	α [kPa]$^{-1}$	n [-]	m [-]
0.205	0.531	0.545	186.593	0.00199	9.748	0.0279
s_p [kPa]	s_{AE} [kPa]	e_k [-]	k [-]	N [-]	λ [-]	a [kPa]$^{-1}$
177.417	419.679	0.796	0.034	1.065	0.086	0.0144

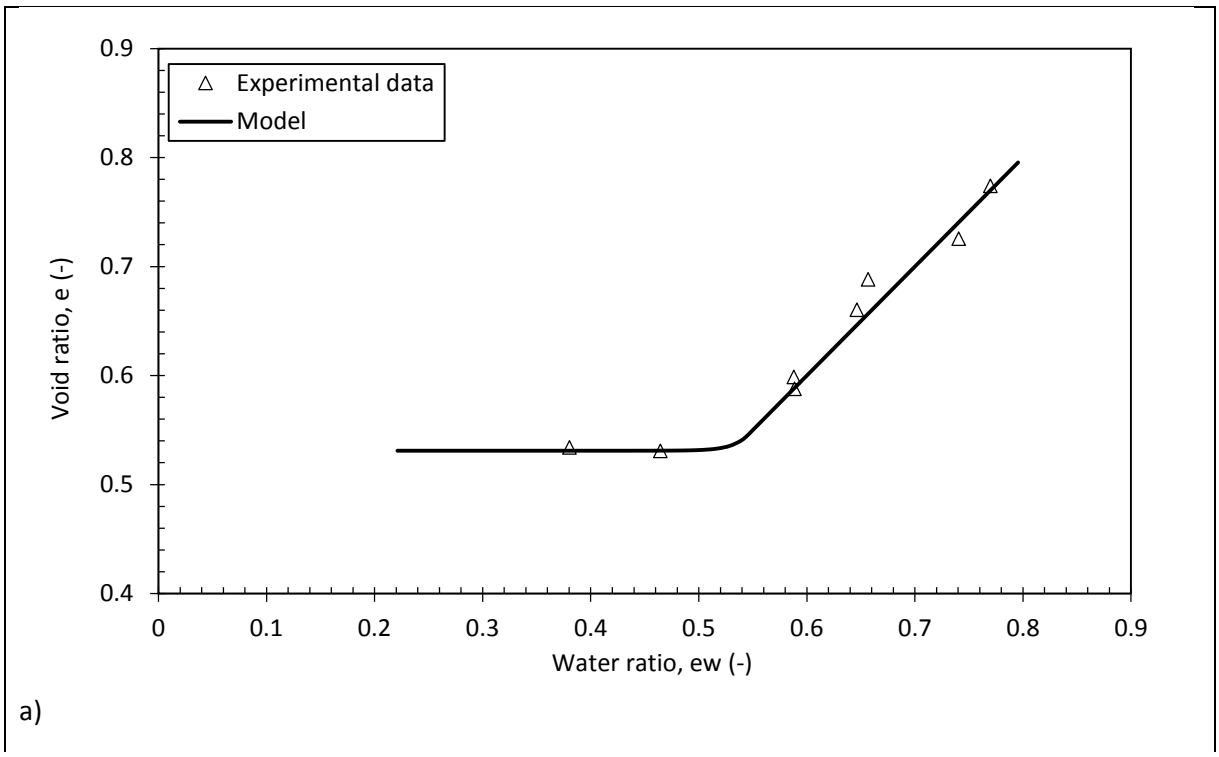

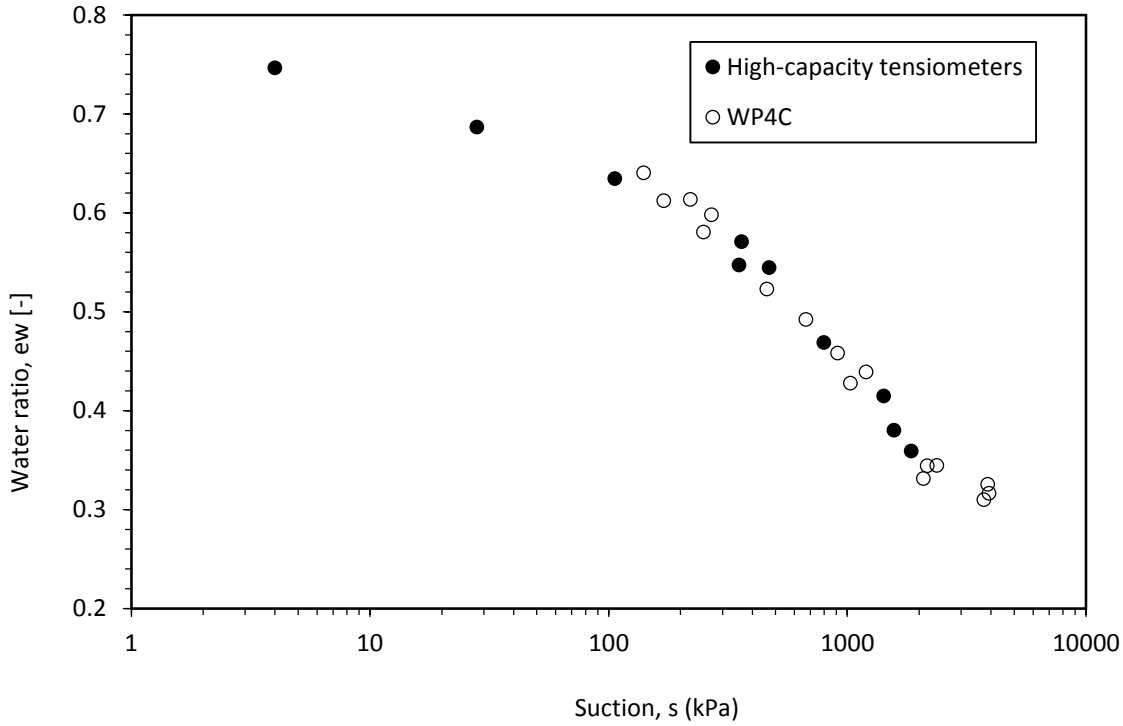
0.8
0.7
0.6
0.5
0.4
0.3
0.2
Water ratio, ew [-]
1
10
100
1000
10000
Suction, s (kPa)
High-capacity tensiometers
WP4C

b)

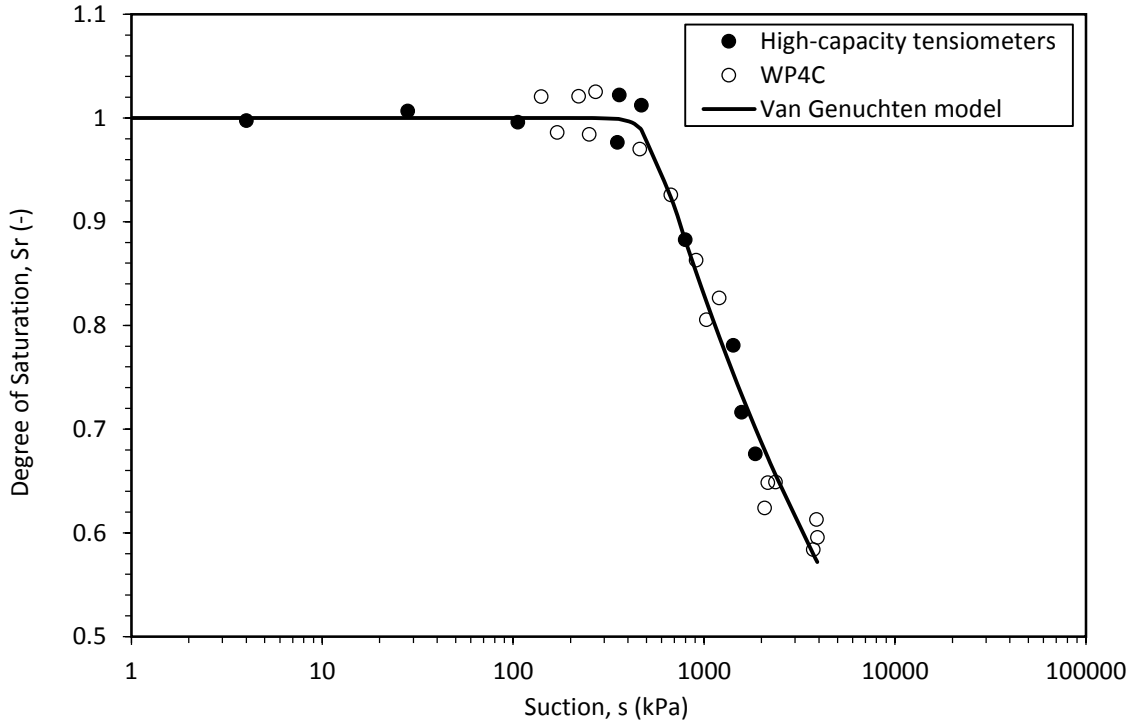
1.1
1
0.9
0.8
0.7
0.6
0.5
Degree of Saturation, Sr (-)
1
10
100
1000
10000
100000
Suction, s (kPa)
High-capacity tensiometers
WP4C
Van Genuchten model

c)

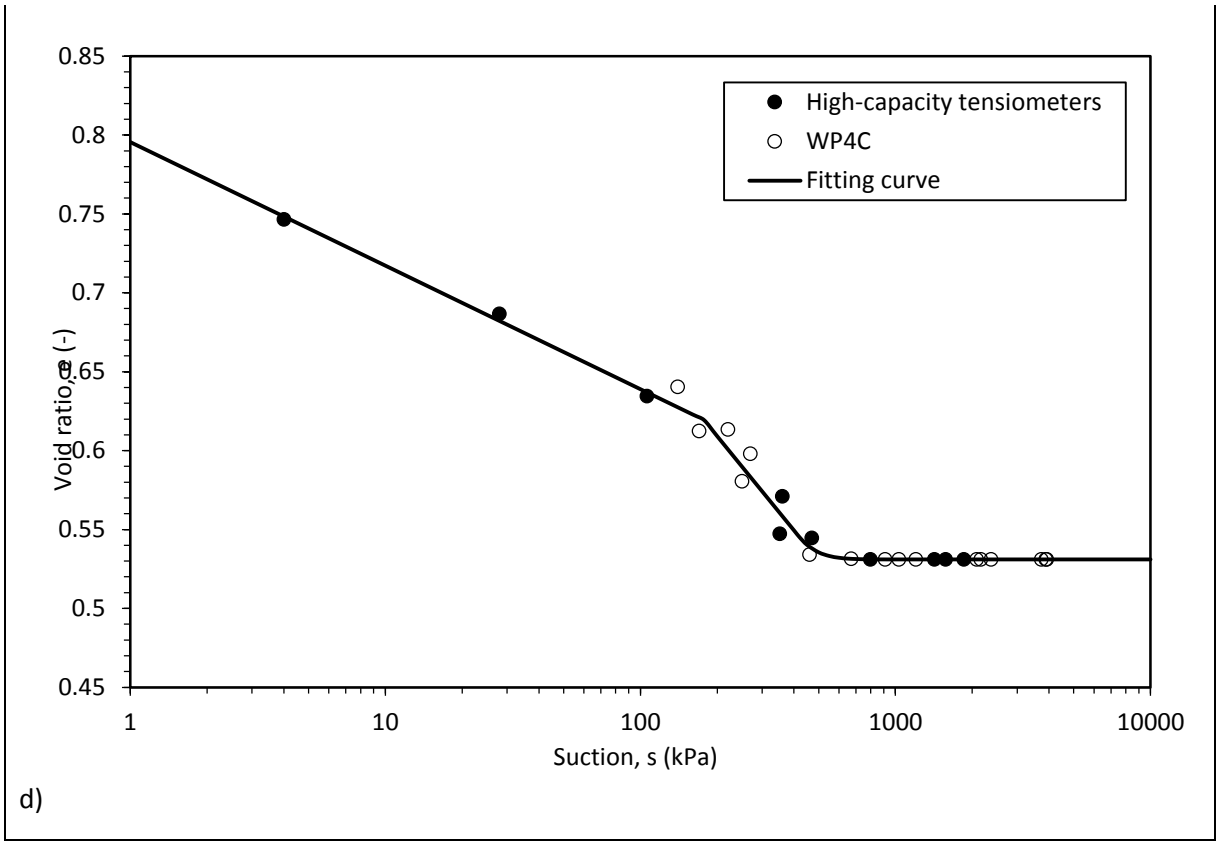

Figure 4-2: Water retention behaviour of the soil material used for the mock-up scale test

4.4.3 Hydraulic conductivity behaviour

The Kozeny-Carman equation suggested by Tarantino et al., (2010) was used to model the hydraulic conductivity:

$$k = k_{sat}\left(\frac{e}{e_0}\right)^3\left(\frac{1+e_0}{1+e}\right)S_r^3 \tag{4.4}$$

where k_{sat} is the saturated hydraulic conductivity associated to the reference soil void ratio e_0, e is the void ratio and S_r is the degree of saturation. The void ratio e and the degree of saturation S_r were obtained from Equation (4.3) and Equation (4.2), respectively. The hydraulic conductivity curve is shown in Figure 4-3.

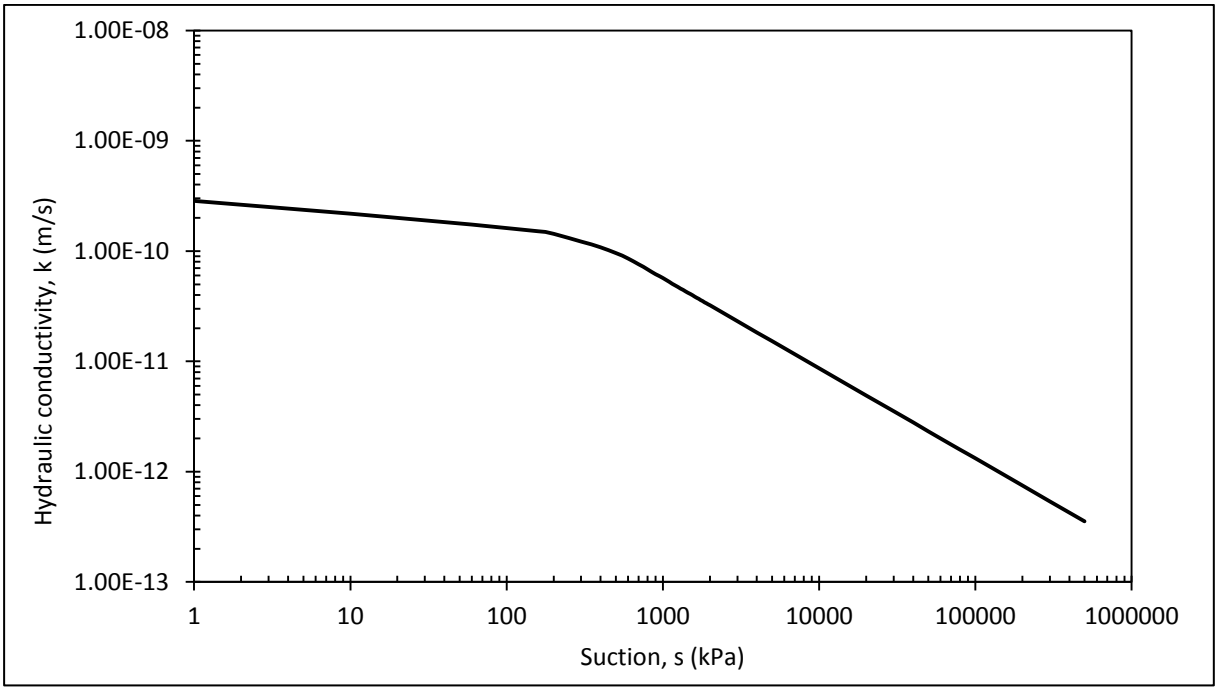

Figure 4-3: Hydraulic conductivity model of the soil material used for the mock-up scale test

The saturated hydraulic conductivity k_{sat} was assessed experimentally via a constant head hydraulic permeability test carried out in a modified oedemeter cell. A 75 mm diameter, 20 mm high soil specimen was cut from the block sample by using the oedometer cutting ring. The specimen was placed into the oedometer, covered with water, and loaded in steps to a maximum vertical stress of $\sigma_v = 1428\text{kPa}$. The oedometer cell was connected to a reservoir of water located at *H*=1.062m above the water level of the oedometer. At the end of the primary consolidation of selected loading step, the valve connecting the base of the oedometer to the reservoir was open and the water was allowed to flow upwards through the specimen. The amount of water passing through the specimen was measured by the balance underneath the water reservoir, accounting for the loss of mass of water due to the evaporation from the water reservoir. Three permeability tests were carried out at vertical stress of $\sigma_{v1} = 90\text{kPa}, \sigma_{v2} = 179\text{kPa}$ and $\sigma_{v3} = 357\text{kPa}$, associated with void ratios of $e_1 = 0.70$, $e_2 = 0.67$ and $e_3 = 0.62$, respectively (Figure 4-4). The hydraulic conductivity k_{sat} was calculated by means of Darcy's law.

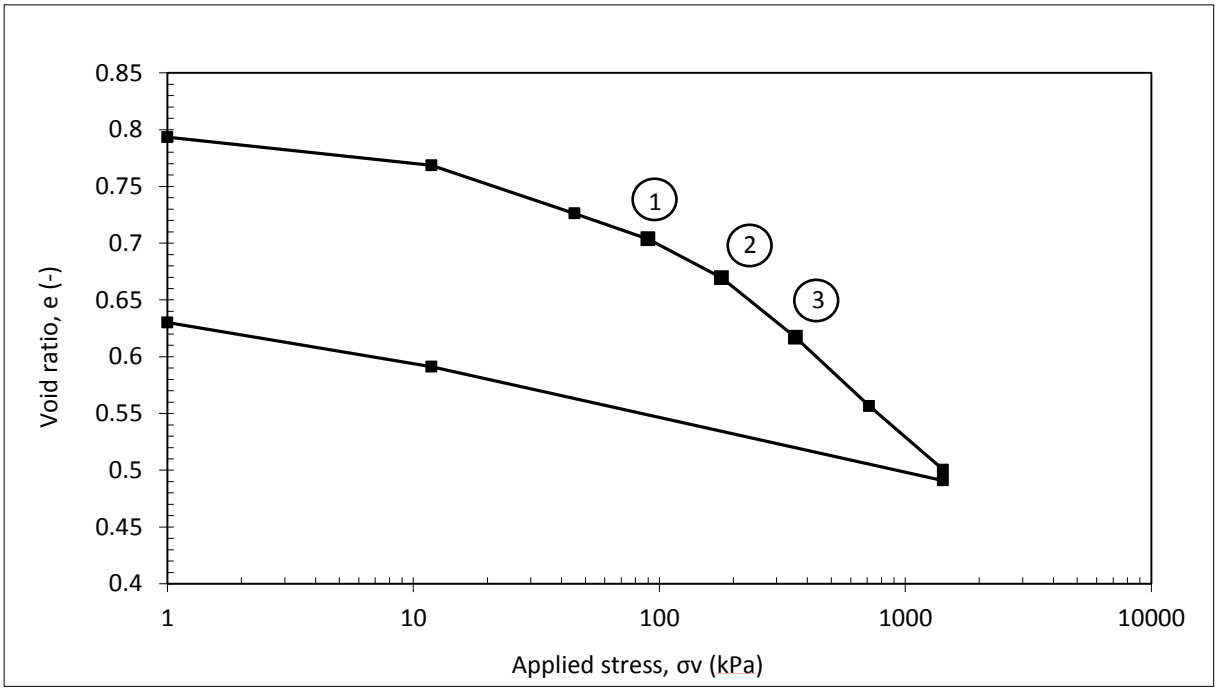

Figure 4-4: Compressibility curve of the soil and indication of the loading steps where the permeability tests were carried out

Direct measurements of k_{sat} versus $e^3/(1+e)$ are shown in comparison with the values of k_{sat} derived from the Terzaghi's consolidation theory in Figure 4-5. The experimental k_{sat} and k_{sat} from the consolidation theory are within the same order of magnitude and vary linearly with $e^3/(1+e)$. The linear relationship is supported by the Kozeny-Carman model (Mitchell & Soga, 2005) and it was used as a check of the quality of the permeability tests (Chapuis & Aubertin, 2003). The offset between the two series of data might be explained by the fact that the Terzaghi's theory of consolidation assumes the soil to be linearly elastic and k_{sat} to remain constant throughout the consolidation process.

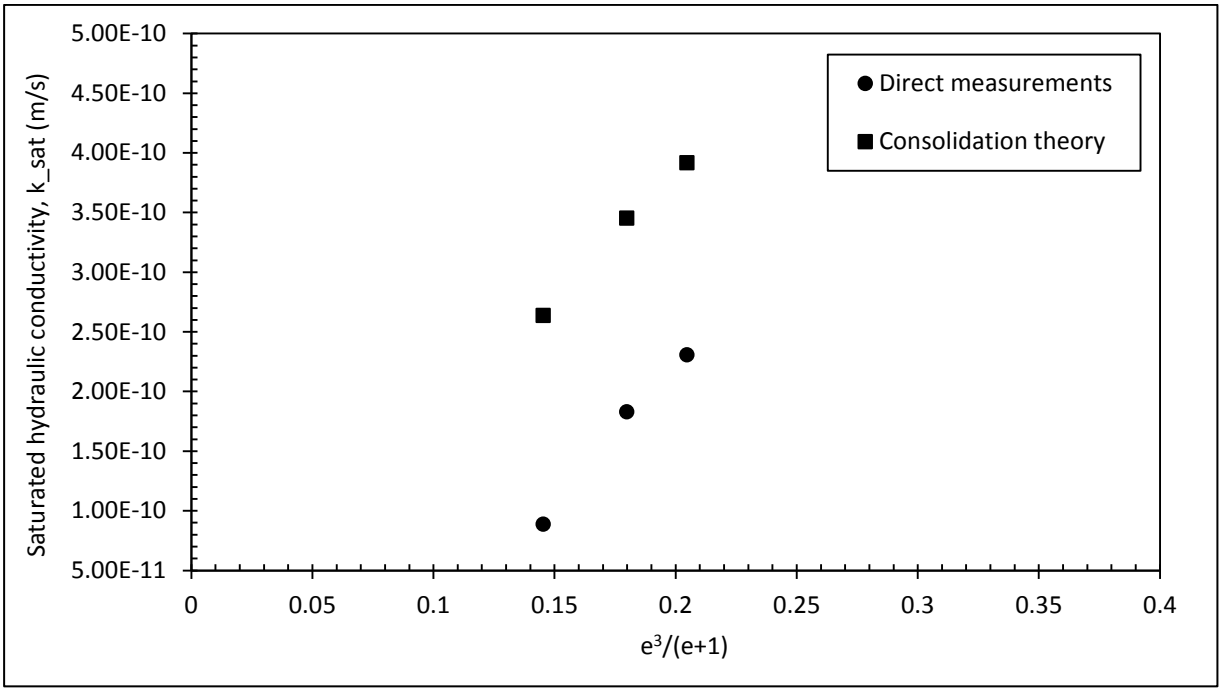

Figure 4-5: Saturated hydraulic conductivity of the soil material used for the mock-up scale test

4.5 Boundary condition characterisation

An independent study was carried out to quantify the water evaporation from the inner surfaces of the suction drain that are exposed to a tangential airflow of a known air velocity and relative humidity in a confined space (Martini & Tarantino, 2018-submitted). To this end, the apparatus shown in Figure 4-6 was designed in the laboratory with an upper air channel of similar dimension to the confined space in the suction drain and a bottom container that simulates the inner surface of the suction drain. Compressed air was injected through the upper air channel and the airflow circulated tangentially to the wet surface of the water-filled container. Tests were carried out by considering different air velocities and relative humidity (*RH*) of the airflow at the inlet. The relative humidity at the inlet RH_{inlet} and the velocity of the airflow were measured via the RH/T sensor (Sensirion Kit EK-H5 sensors SHT21) and the anemometer (OMEGA FMA1006R-V2-S) installed at the inlet of the upper air channel

respectively. The average water evaporation rate was measured over time by the two balances installed at the bottom of the water-filled container.

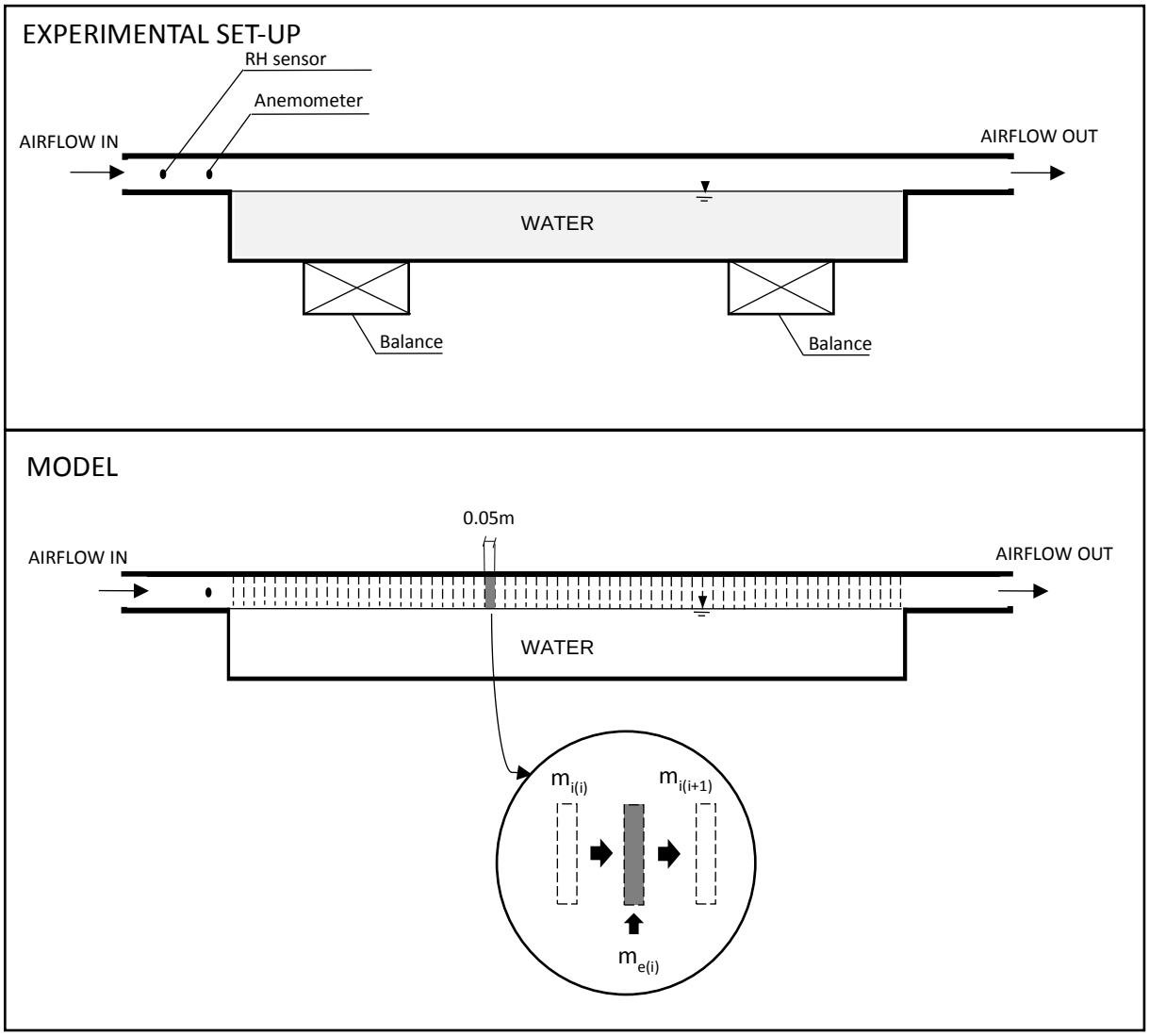

Figure 4-6: Experimental set-up and model for detecting the boundary condition in terms of water flow per unit area and unit time, q (m/s)

A model was formulated to quantify the water evaporation rate for any length of the wet surface. The upper air channel above the evaporating surface was divided into 0.05 m wide elements as shown in Figure 4-6. In each element the water mass balance was calculated as follows:

$$m_{in(i)} + m_{ev(i)} = m_{out(i)} = m_{in(i+1)} \tag{4.5}$$

where $m_{in(i)}$ is the mass of water vapour carried by the airflow at the inlet of each element *i*, $m_{ev(i)}$ is the mass of water that evaporates from the water surface at the bottom of each element *i* and it is a function of the water evaporation rate $q_{(i)}$, $m_{out(i)}$ is the mass of water vapour carried by the airflow at the outlet of each element *i* and $m_{in(i+1)}$ is the mass of water vapour carried by the airflow at the inlet of the element *i+1*. The water evaporation rate $q_{(i)}$ at the bottom of each element *i* was calculated by using of the following equation:

$$\mathrm{q_{(i),model}} = \alpha[\mathrm{v_{air}}(z)] \cdot \mathrm{p_{vo}} \cdot (1 - \mathrm{RH_{in(i)}}) \tag{4.6}$$

where $\alpha[v_{air}(z)]$ is the vapour transfer coefficient and function of the air velocity, p_{vo} is the equilibrium vapour pressure at saturation and function of the temperature of the airflow, and $RH_{in(i)}$ is the relative humidity of the airflow at the inlet of the element *i*. The vapour transfer coefficient α is the sole parameter of the model and was calibrated by imposing that:

$$\mathrm{q_{model}} = \frac{\sum_1^{\mathrm{n}} \mathrm{q_{(i),model}} \cdot \Delta l_i}{\sum_1^{\mathrm{n}} \Delta l_i} = \mathrm{q_{experimental}} \tag{4.7}$$

where q_{model} is the average evaporation rate, $q_{(i),model}$ is the local evaporation rate associated with the *i-th* element, Δl_i is the width of the *i-th* element, and $q_{experimental}$ is the average evaporation rate measured via the balances in the tests where the *RH* of the airflow at the inlet was equal to RH_{inlet}=0% and air velocity varied from v_{air}=1m/s to v_{air}=4m/s. The model was then validated in the tests with airflow at different inlet relative humidity.

It is worth to stress that the vapour transfer coefficient α was detected in steady-state conditions and that the hypothesis of steady state condition is assumed to be valid in transient process.

The vapour transfer coefficient α that was detected in the test with airflow at v_{air}=4m/s on water surface was found to be the same α for water evaporation on saturated soil exposed to the airflow at the same air velocity.

The values of the vapour transfer coefficient α against the air velocity are shown in Figure 4-7. These values of α allowed estimating the boundary conditions in terms of water evaporation rate (Equation (4.6)) for the suction drain model.

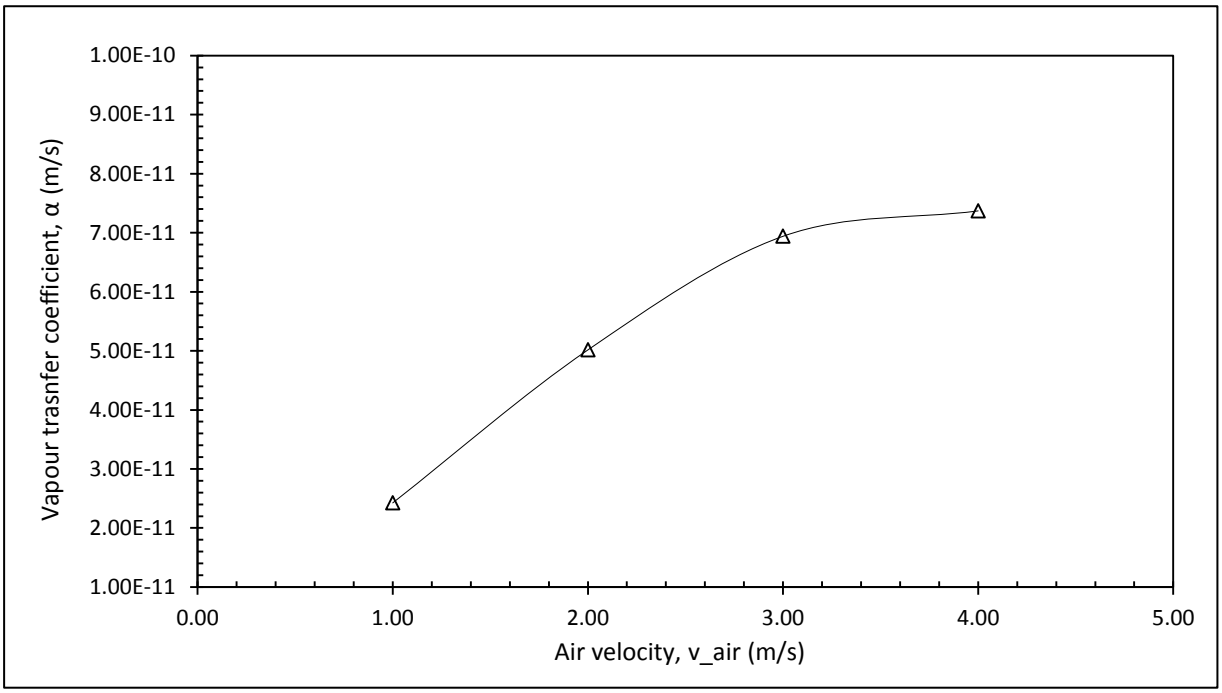

Figure 4-7: Experimental vapour transfer coefficient, α versus the velocity of the airflow, v_{air}

4.6 Suction drain mock-up scale test

4.6.1 Set-up

A mock-up scale test was designed to verify the technique of the suction drain at laboratory scale (Figure 4-8). A cylindrical specimen 300 mm diameter and 150 mm high was

cut from the block sample taken on the site. The external surface of the specimen was made waterproof by using a layer of silicon grease and Parafilm® to prevent water evaporation. A central borehole 70 mm diameter was drilled through the specimen. A metal air delivery tube 700 mm long, 15 mm OD was placed centrally into the borehole and was kept suspended at 25 mm distance from the bottom of the soil sample to allow the airflow to circulate from the bottom to the top through the gap between the delivery tube and the borehole. A 500 mm high and 80 mm diameter plastic case was placed at the entry of the borehole to isolate the air flow from the environment. Air from the laboratory compressed air system was injected through the air delivery tube to the bottom of the borehole 24/7 for 6 days.

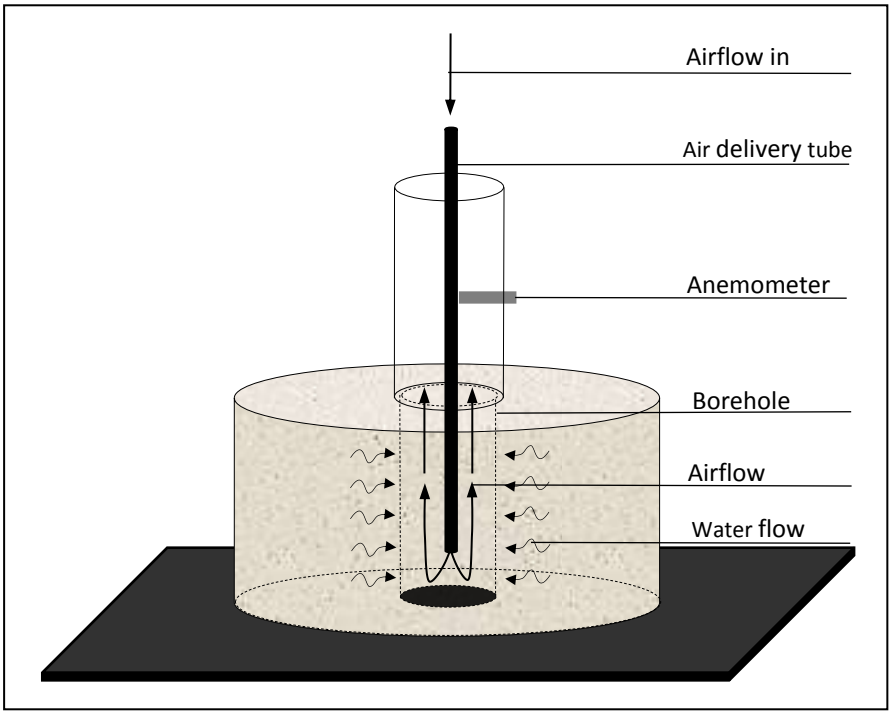

Figure 4-8: Schematic layout of the mock-up scale test

Air velocity and temperature of the airflow were measured via the anemometer (OMEGA FMA1006R-V2-S) which was placed perpendicular to the airflow at the inlet of the air delivery tube. The sensor design of the anemometer is based on three RTD elements; one measures the air temperature and the other two sensors measure the air velocity. The

measurement of the air velocity is based on the heat loss from the RTD velocity sensor as it cools down by the air flow (Omega Engineering, 2018). The specification of the velocity sensor are summarised in Table 4-2. The manufacture's calibration of the anemometer was checked against the measurement from a Pitot tube in a wind-tunnel.

Table 4-2: Specification of the anemometer

Range Air velocity	0-60.96 m/s
Accuracy air velocity	1.5% Full scale range
Display resolution air velocity	0.01m/s
Sensor probe	6.3 OD x 95 mm- 304 Stainless steel
Response time	250 msec default
Operating Relative Humidity	0 to 95% RH without condensation

4.6.2 Experimental Procedure

A continuous airflow was injected inside the borehole through the inner delivery tube 24/7 for 6 days at the air velocity v_{air}=2m/s and air temperature T=20°C.

The variation of the soil water content was monitored over time at different distances from the central borehole. Four 150 mm long and 15 mm diameter samples were sampled every day for measuring the water content according to the scheme shown in Figure 4-9. Two samples were taken at 35 mm from the central borehole (solid line) and two samples were taken at 70 mm from the central borehole (broken line). Each sample was divided in three parts 50 mm long each (top, middle and bottom) and each part was placed in the oven at 105˚C for 24 hours to measure the gravimetric water content. After each sampling, the hole was sealed with silicon grease and Parafilm ® in order to avoid extra evaporation occurring from the sampling hole.

Since the cylindrical specimen was assumed to have homogeneous initial water content and the evaporation-induced soil water flux was asymmetric, samples were taken from a different portion each day as shown in Figure 4-9. By using this scheme, the sampling of the previous days did not interfere with the sampling of the following days.

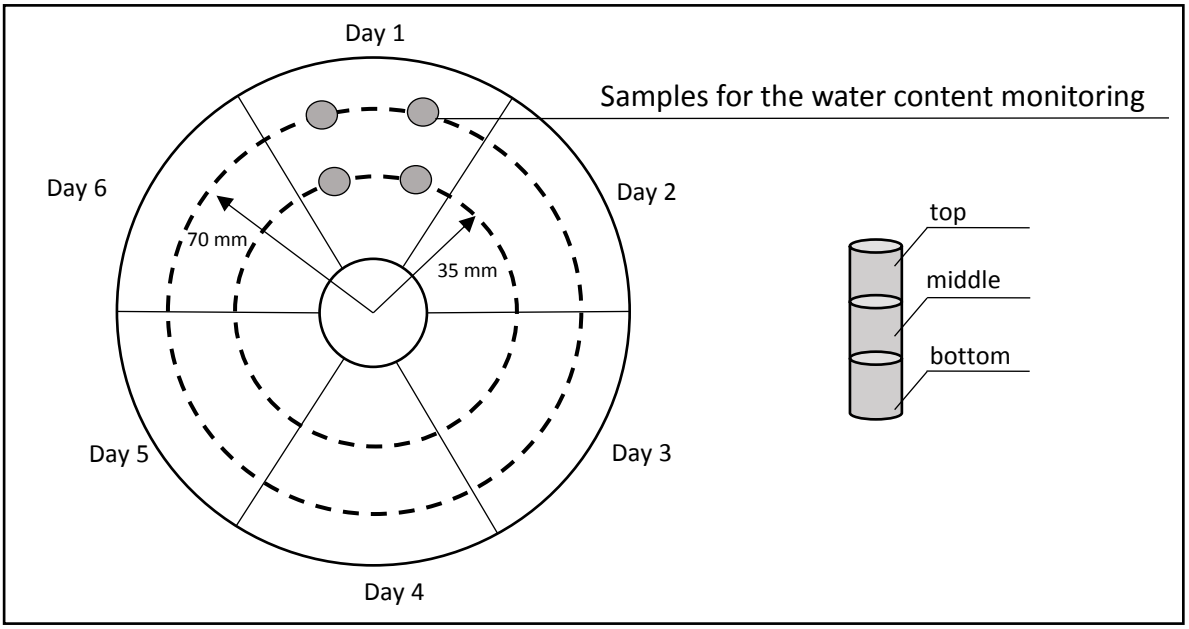

Figure 4-9: Schematic layout of the soil sampling in the mock-up scale test for monitoring the soil water content

4.6.3 Results

The results from the mock-up test are presented in Figure 4-10. The gravimetric water content, *w* of each soil sample at 35 mm and at 70 mm from the central borehole is plotted versus the time, *t*.

The soil water content decreases over time from the initial value w=0.29 to the final values w=0.16 and w=0.11 for samples at 70 mm and 35 mm from the borehole, respectively. In Figure 4-10 can be seen that when the soils desaturates (w<0.18), soil water content decreases at a slower rate. As expected, the soil water content recorded at 35 mm decreases faster than soil water content at 70 mm since the soil samples are closer to the central borehole where

evaporation occurred. The average water content of the soil samples at 35 mm is about 0.03-0.05 smaller than the average water content of the soil samples at 70 mm over the duration of the experiment.

It can also be observed that the soil water content of the top, middle and bottom parts of each soil sample differ of 0.02-0.04 to each other without a consistent pattern. A possible explanation for this is the fact that the tested soil is sandy clay and the presence of sand lenses in the soil sample can lead to scattering in the soil water content.

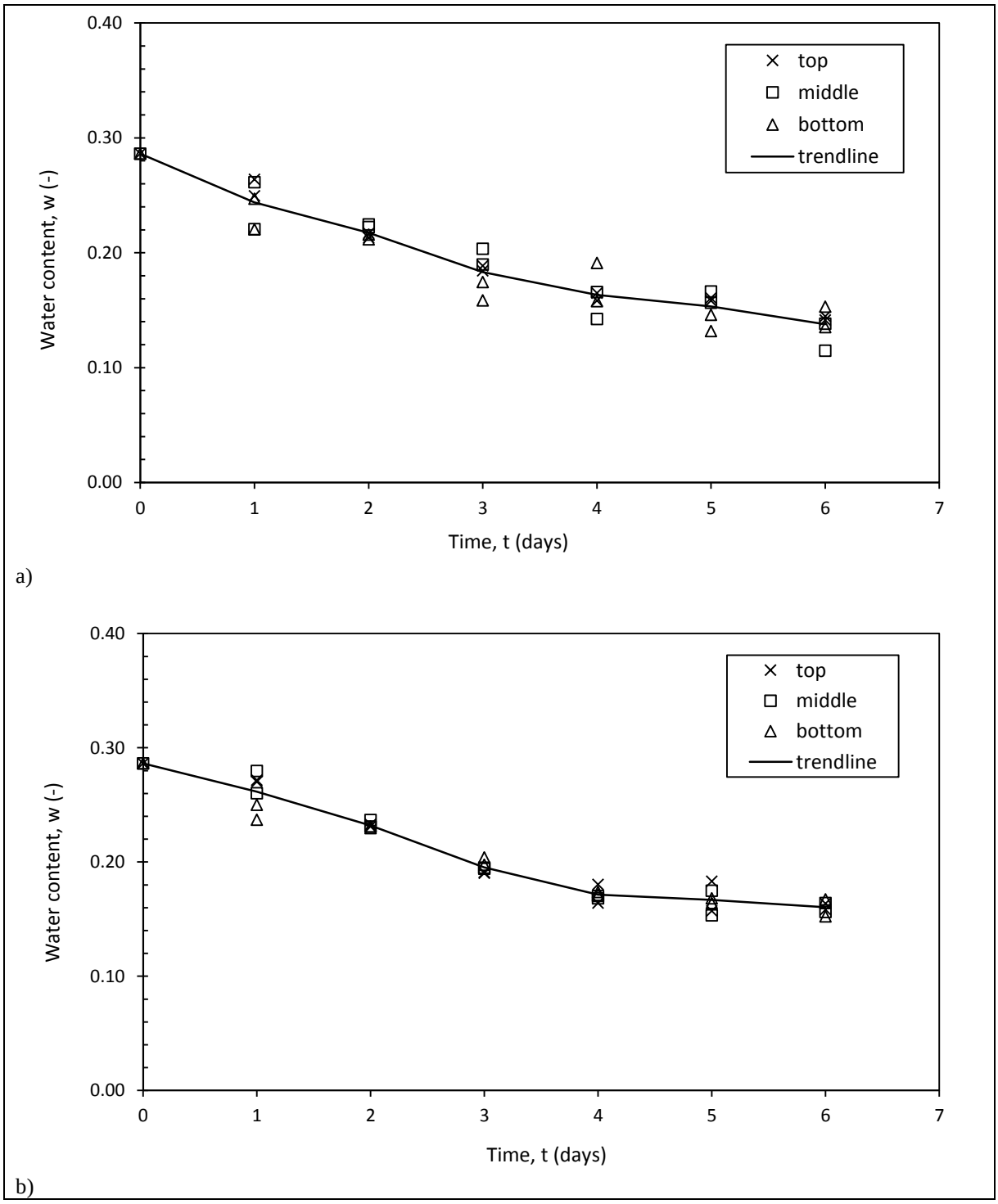

Figure 4-10: Experimental soil water content in the mock-up scale test: a) at 35mm from the central borehole; b) at 70mm from the central borehole

4.7 Suction drain modelling

The suction drain modelling aims to reproduce the evaporation-induced water flow that was generated into the block of natural soil during the mock-up test. An axisymmetric finite element analysis was conducted to simulate the water content of the soil around the borehole in the mock-up test.

4.7.1 Hydro-mechanical model

The hydro-mechanical model that simulates water flow generated by tangential airflow in the suction drain was derived from Tarantino et al., 2010. Water evaporation at the borehole surface generates a gradient in pore-water pressure which, in turn, generates a water flow towards the inner surface of the borehole. In an initially saturated soil, changes in pore-water pressure cause mechanical deformation of the clay skeleton that affects its water storage capacity. Hence, the evaporation-induced water flow is a hydro mechanical coupled process and water mass balance and momentum balance equations are required to be solved simultaneously in principle.

The water mass balance can be written as follows:

$$div(\vec{v}) = \frac{\partial \theta}{\partial t} \tag{4.8}$$

where $\vec{v}$ is the flow velocity, θ is the volumetric water content (volume of water per total volume), and t is the time. In Equation (4.8), the flow velocity is given by the Darcy-Buckingam law (Fredlund & Rahardjo, 1993) (Lu & Likos, 2004):

$$\vec{v} = -k\,(e, Sr)\; grad\left(\frac{u_w}{\gamma_w} + z\right) \tag{4.9}$$

where u_w is the pore-water pressure, z is the vertical coordinate increasing upward, γ_w is the specific weight of water, and k is the hydraulic conductivity, which depends on void ratio e and degree of saturation Sr (Mitchell & Soga, 2005). Equation (4.9) neglects diffusive and advective transport of water vapour and this assumption is corroborated by numerical simulation of isothermal drying in low-permeability materials (Baroghel-Bouny, et al., 2001; Coussy, 2004). The volumetric water content can be expressed as a function of Sr and e as follows:

$$\theta = \frac{e(\sigma_{ij}, u_w)}{1 + e(\sigma_{ij}, u_w)} \cdot Sr(u_w) \tag{4.10}$$

where the void ratio e and, hence, the volumetric water content θ, depend on the pore water pressure and on the total stress tensor σ_{ij}. It follows that the second term of Equation (4.8) becomes:

$$\frac{\partial \theta}{\partial t} = \frac{\partial \theta}{\partial \sigma} \cdot \frac{\partial \sigma}{\partial t} + \frac{\partial \theta}{\partial u_w} \cdot \frac{\partial u_w}{\partial t} \tag{4.11}$$

Since the total stress at the boundaries of the mock-up scale test is σ=0kPa, the variation of the total stress $\partial\sigma/\partial t$ can be assumed to be negligible in comparison to the variation of the pore water pressure $\partial u_w/\partial t$. In this case the volumetric water content only depends on u_w (Equation (4.10)) and Equation (4.8) simplifies to a single-variable partial differential equation as follows:

$$\frac{\partial}{\partial x}\left[k \cdot \frac{\partial}{\partial x}\left(\frac{u_w}{\gamma_w}\right)\right] = \frac{\partial \theta(u_w)}{\partial u_w} \frac{\partial u_w}{\partial t} \tag{4.12}$$

With the following boundary conditions:

$$q(l, t) = \alpha(v_{air}) \cdot p_{v0}(T_{air}) \cdot (RH_{soil} - RH_{air}) \tag{4.13}$$

$$q\ (L, t) = 0 \tag{4.14}$$

and initial conditions:

$$u_w(x,0) = u_{w0} \tag{4.15}$$

where x=l coincides with the inner surface of the borehole and x=L coincides with the external surface of the block of soil. The term q is the water evaporation rate, α is the vapour transfer coefficient that is a function of the air velocity, p_{v0} is the saturated vapour pressure that is a function of the temperature of the airflow, RH_{soil} is the relative humidity at the inner surfaces of the borehole, and RH_{air} is the relative humidity of the airflow. The vapour transfer coefficient $\alpha(v_{air})$ was determined experimentally as illustrated in Section 4.5. The relative humidity at the clay surface RH_{soil} is related to the soil suction by the psychrometric law:

$$RH_{soil} = exp\left[\frac{v_w s}{RT}\right] \tag{4.16}$$

where v_w is the molar volume of liquid water, s is the soil suction, R is the universal constant of gas, and T is the absolute temperature.

Equation (4.12) together with the boundary conditions and the initial conditions given by Equations (4.13), (4.14) and (4.15) was solved via finite element analysis by using SEEP-W. Non-linear mechanical and hydraulic constitutive functions were considered. The hydraulic conductivity k was modelled by using the Kozeny-Carman model (Equation (4.4)). The function $\theta = \theta(u_w)$ was derived from the void ratio e and the degree of saturation Sr, as follows:

$$\theta = \frac{e(u_w)}{1 + e(u_w)}\, Sr\,(u_w) \tag{4.17}$$

where the void ratio $e(u_w)$ is defined by Equation (4.3) and the degree of saturation $Sr\,(u_w)$ is defined by Equation (4.2) .

4.7.2 Numerical analysis and results

The finite element mesh is shown in Figure 4-11 represents a radiant section of the mock-up test with the vertical axis of the model coinciding with the axis of symmetry. Initial conditions are specified in terms of pore water pressure that enables the water content of the soil to be equal to the soil water content measured experimentally before the test (w=0.29). Boundary conditions were specified in terms of water flow. This was set equal to q=0 m/s at the top, bottom and outer surface of the model, and was given by Equation (4.13) at the inner surface of the model. The vapour transfer coefficient α was derived from Figure 4-7 as a function of the air velocity ($\alpha = 5.02 \text{ x } 10^{-11} \text{m/s for } \text{v}_{\text{air}} = 2\text{m/s}$), the saturated vapour pressure was set equal to $p_{v0}(20°\text{C}) = 2.34 \text{ kPa}$, and the average relative humidity of the airflow along the borehole was set equal to $RH_{air} = 0\%$. The value RH_{air} was consistent with the relative humidity of the airflow from the compressed air system measured via the RH/T sensor placed at the outlet of the air delivery tube. The relatively short length of 150 mm of the borehole allowed assuming that the relative humidity of the airflow remains constant along the borehole. This assumption is based on previous experimental observation (Martini & Tarantino, 2019). Parameters used for the psychrometric law are presented in Table 4-3.

Table 4-3: Parameters for Psychrometric Law

$\mathbf{v_w}$ [m^3/mol]	**R** [J (K mol)$^{-1}$]	**T** [K]	$\mathbf{p_{v0}}$ **at T= 20·C** [kPa]
18 x 10^{-6}	8.314	293	2.34

The water retention curve and the hydraulic conductivity curve measured experimentally (Figure 4-2 and Figure 4-3) were used to model the soil in the numerical analysis. The analysis was run for 6 days and adaptive time steps were used to optimise the convergence.

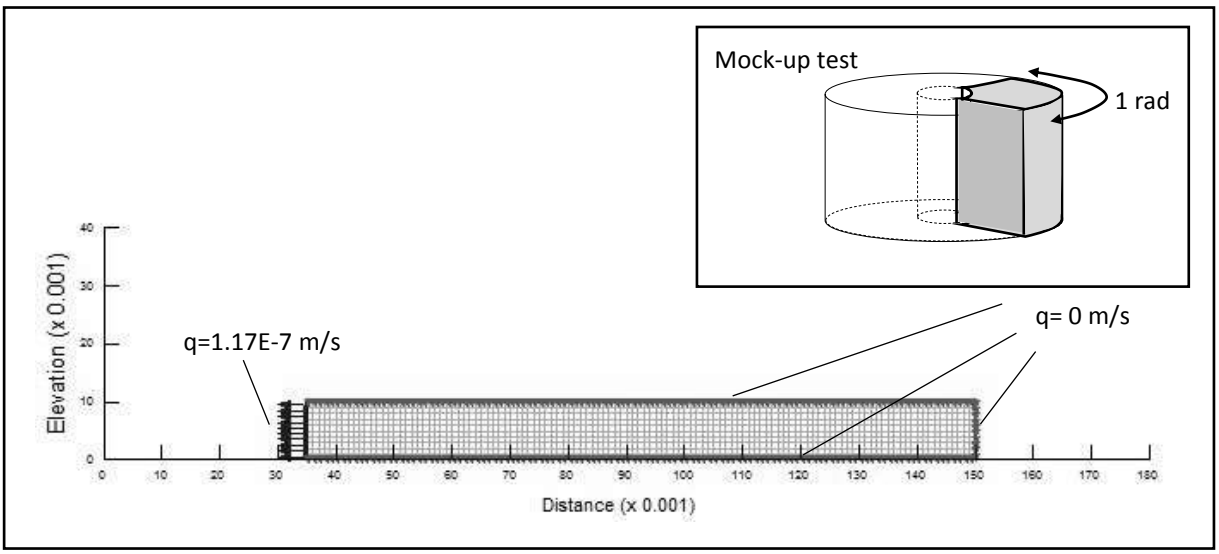

Figure 4-11: Numerical modelling for the validation of the mock-up scale test (axisymmetric conditions)

Simulated soil water content at 35 mm and 70 mm from the central borehole are compared with the average experimental soil water content measured at the same distances in the mock-up test over time in Figure 4-12. It can be seen that the numerical results are in fair agreement with the experimental data. This indicates that the suction drain model represents with good approximation the evaporation-induced water flow generated in the clay sample.

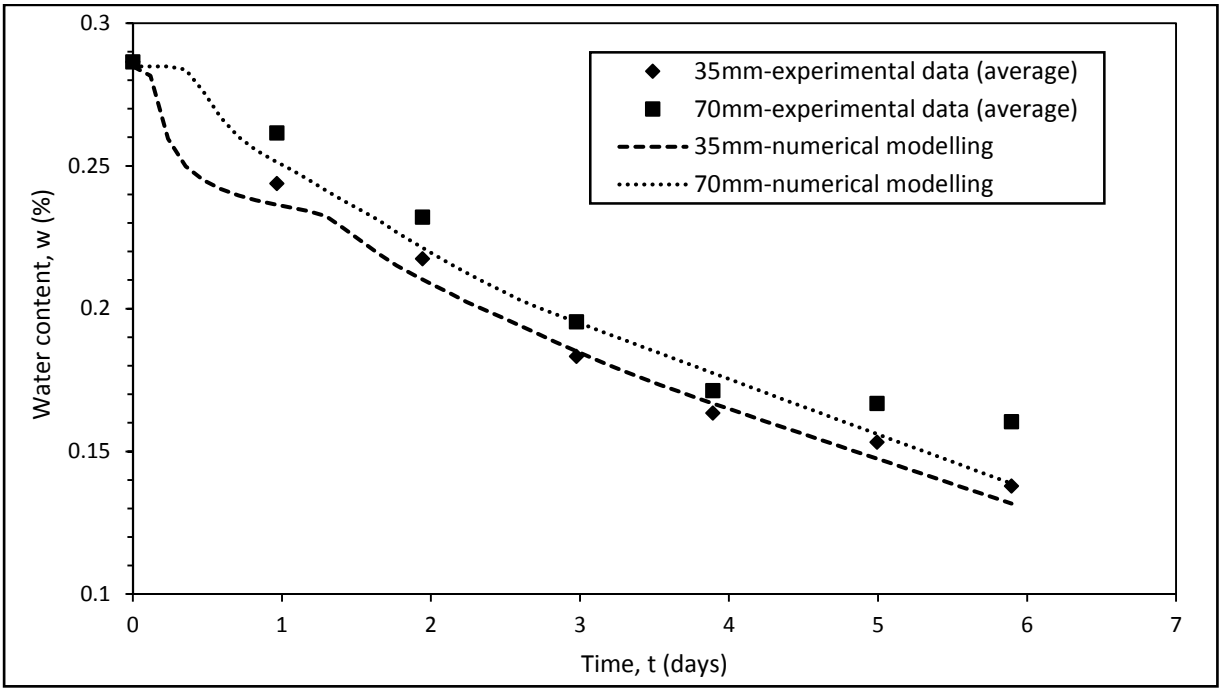

Figure 4-12: Comparison between the experimental and the numerical soil water content, w versus time, t

4.8 Effectiveness of suction drain in stabilising tunnel face

This section explores the beneficial effects of the suction drain in stabilising tunnel face. The suction drain reduces the water content of the surrounding soil and, hence, increases its undrained shear strength. The undrained shear strength of the soil provides the soil resistance to collapse to the tunnel. When the tunnel is excavated, the overburden applies an inward pressure to the front of the tunnel and the undrained shear strength of the soil mobilised along the failure mechanism provides the soil resistance to the collapse (Leca & New, 2007). The stability of the front of a tunnel is expressed by the stability factor N that is defined by the following Equation (Broms & Bennermark, 1967):

$$N = \frac{\gamma \cdot H}{Cu} \tag{4.18}$$

where γ is bulk unit weight of the soil, H is the depth to the tunnel axis, Cu is the undrained shear strength of the overburden. An increase of the undrained shear strength of the overburden results in increased stability of the tunnel face and, hence, in a decrease of the stability factor *N*.

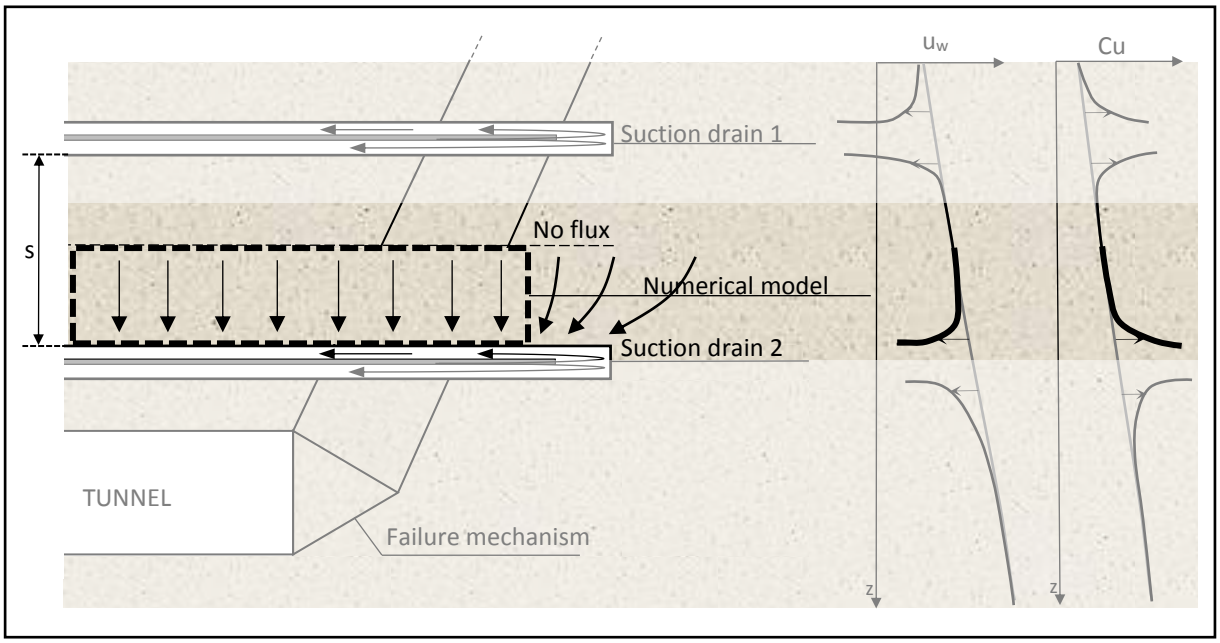

Figure 4-13: Numerical model of the suction drain in tunnelling

The design of the suction drains would include drilling the boreholes in an umbrella arch configuration above the crown of the tunnel. Boreholes are drilled from the crown of the excavation face of the tunnel or from a higher vertical wall prior the excavation of the tunnel (i.e. shaft, bigger diameter tunnel normal to the tunnel in excavation). For the sake of this exercise a simplified configuration of the excavation of the suction drains is considered. Suction drains are excavated every 2 m in the overburden of the tunnel with the excavation axis parallel to the axis of the tunnel. The tunnel is excavated at 14 m below ground level.

Figure 4-13 presents the numerical model. The three-dimensional (3D) problem of the evaporation-induced water flow at the inner surface of the borehole is studied as a two-dimensional (2D) problem. Suction drains are modelled as planes, having an infinitive depth in

the dimension out of page. Under these conditions, the flow net is expected to be 2D at the entry and at the end of the borehole, and essentially 1D along the length of the borehole far-off from the ends. The flow is symmetric between two suction drains and the line 'No Flux' indicates the mid-plane between two drains. A column of soil that extends from the surface of the suction drain to the mid-plane was modelled to investigate the evaporation-induced water flow between two suction drains (Figure 4-14)

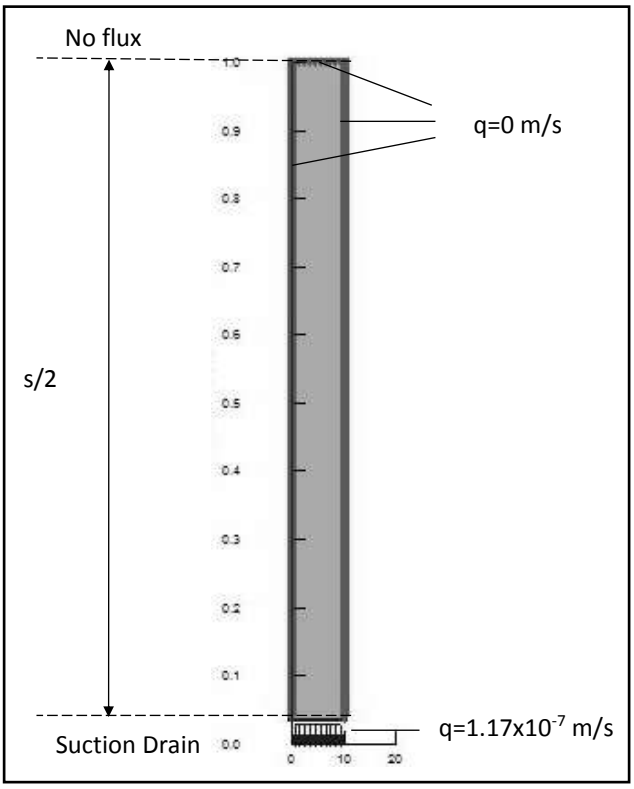

Figure 4-14: 1D finite element mesh and boundary conditions of the numerical model

Initial and boundary conditions of the model were defined in terms of pore water pressure and water evaporation rate, respectively. The initial pore water pressure was assumed to be hydrostatic and equal to 50kPa at the base of the column. The evaporative water flux at the bottom surface of the column, which coincides with the inner surface of the borehole of the suction drain, was defined via Equation (4.13) with the vapour transfer coefficient equal to the one derived for the mock-up scale test ($q = 1.17\text{x}10^{-7}\text{m/s}$ for RH_{soil}=100%).

The water retention behaviour of the soil in the unsaturated range was described by the water retention curve versus suction used for the mock-up test with the following changes: i) the soil was assumed to be normal consolidated; ii) the total stress equal to $\sigma_v = 45$ kPa was taken into account; iii) the air entry value was assumed to remain constant with depth. The water retention behaviour of the soil in the saturated range ($Sr = 1$) was instead expressed by the coefficient of the volumetric compressibility m_v:

$$\frac{\partial \theta}{\partial t} = -m_v \cdot \frac{\partial \sigma'_v}{\partial t} \tag{4.19}$$

The hydraulic conductivity behaviour was expressed by the Kozeny-Carman equation (Equation (4.4)) with $k_{sat} = 1.83\text{x}10^{-10}$ m/s and $e_0 = 0.67$, equal to the saturated hydraulic conductivity of the soil in the mock-up scale test.

Numerical results in terms of soil suction, *s* versus distance from the suction drain, *z* are shown in Figure 4-15. The soil suction at the inner surface of the borehole increases progressively from a negative value (positive pore=-water pressure) at day 0 to $s = 15152$ kPa at day 10 of evaporation. The soil suction decreases with distance from the inner surface of the suction drain as expected.

Figure 4-16 shows the soil water content, *w*, plotted versus distance from the suction drain, *z*. The soil water content decreases over time at the interface with the suction drain and it increases with distance from the surface of the suction drain. These results are consistent with the results in terms of suction.

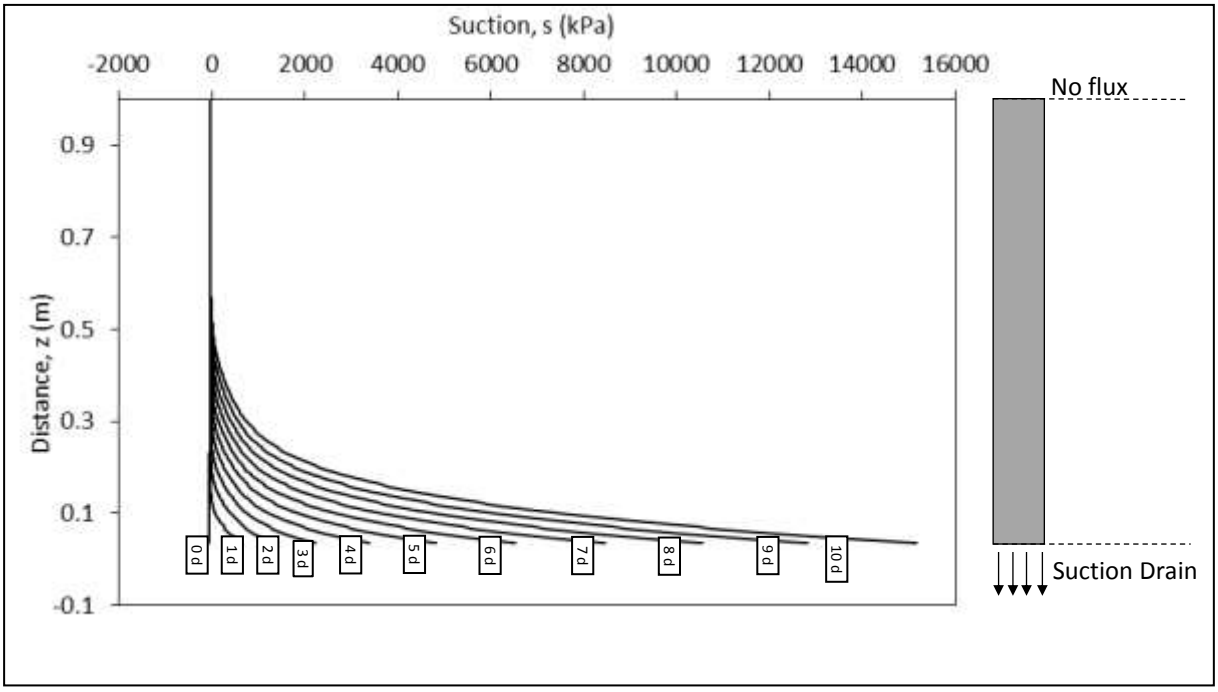

Figure 4-15: Distribution of the suction, s versus distance from the borehole, z at different time steps

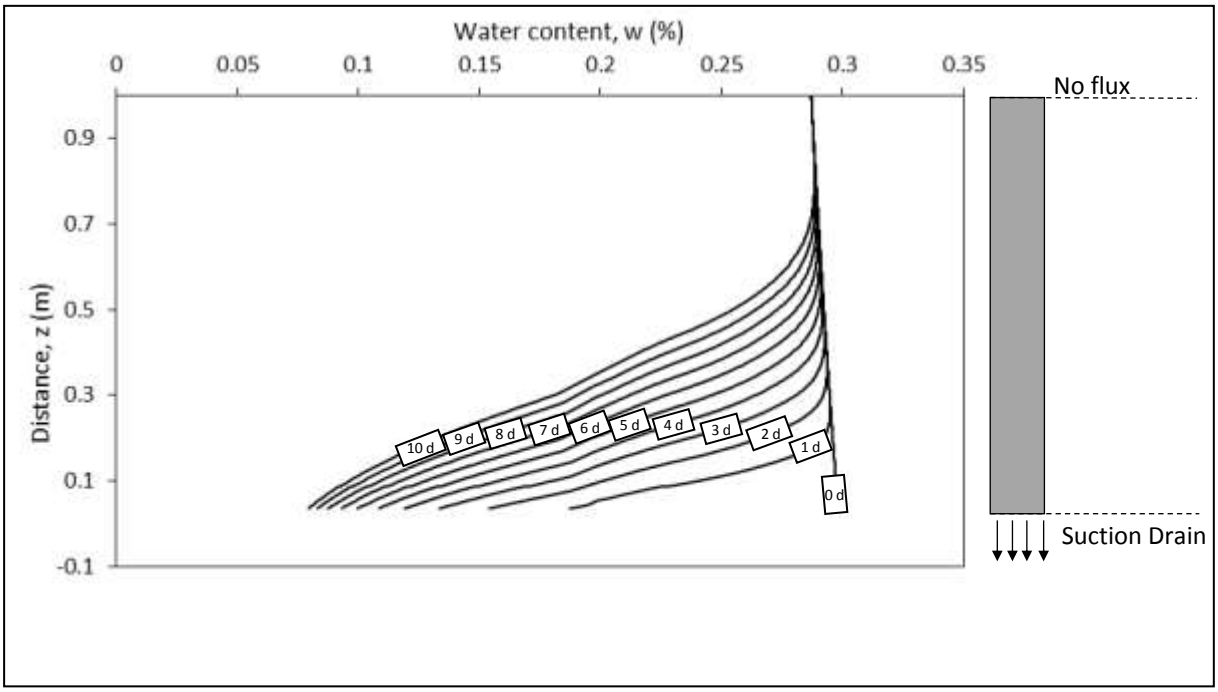

Figure 4-16: Distribution of the soil water content, w versus distance from the borehole, z at different time steps

The undrained shear strength of soil was calculated as a function of the soil water content by using the equation proposed by (Wroth & Wood, 1978):

$$Cu = 170e^{-4.6I_L} = 1.7 \cdot 10^{2(1-I_L)} \qquad (kPa) \tag{4.20}$$

where I_L is the liquidity index and it is defined as:

$$\mathrm{I_L} = \frac{\mathrm{w} - \mathrm{w_P}}{\mathrm{w_L} - \mathrm{w_P}} \tag{4.21}$$

where w is the soil water content, w_P is the plastic limit and w_L is the liquid limit. Equation (4.20) implies that the undrained shear strength of soil is 1.7 kPa at the limit liquid and 170 kPa at the plastic limit. For the sake of this exercise when the water content drops below the plastic limit $w<w_P$ the undrained shear strength Cu is assumed to remain constant and equal to 170 kPa. This is a conservative assumption.

Figure 4-17 shows the undrained shear strength, Cu versus distance z from the suction drain at different time steps. It is possible to see that after 1day of evaporation Cu is equal to Cu=170kPa at the interface with the suction drain and it decreases with distance from the suction drain. The longer is the time that the soil is exposed to the evaporation, the more the undrained shear strength Cu increases. At a certain distance from the suction drain, the undrained shear strength recovers the far field profile.

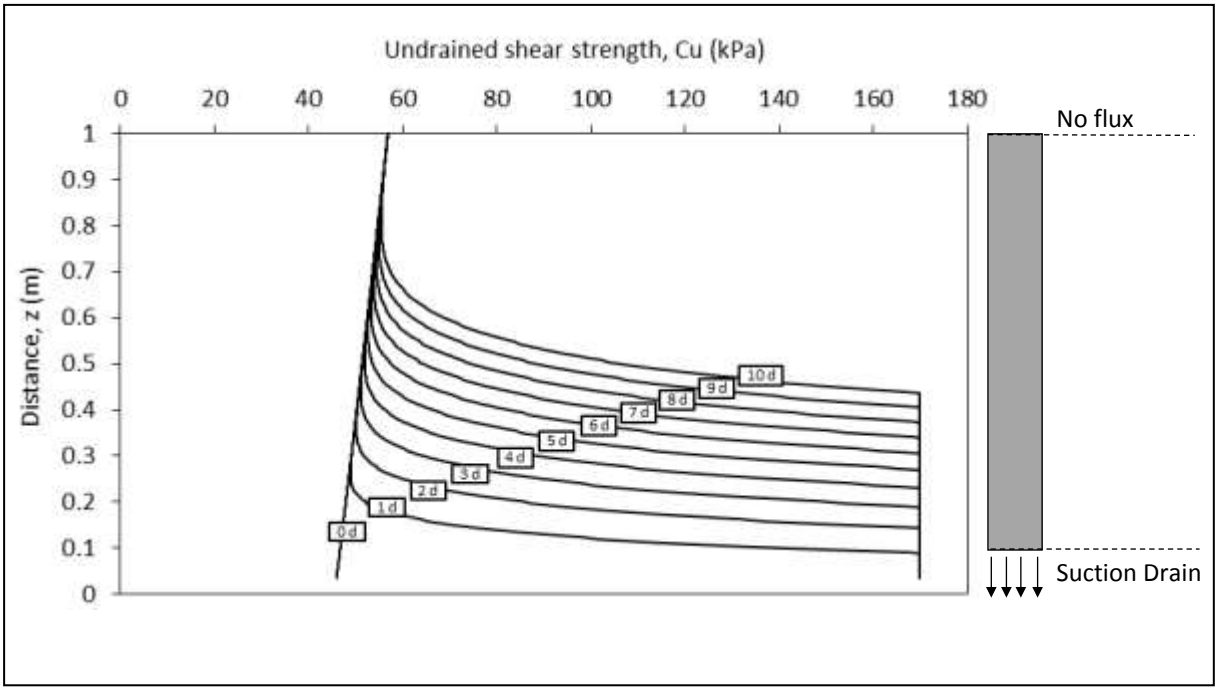

Figure 4-17: Distribution of the soil undrained shear strength, Cu versus the distance from the borehole, z at different time steps

In order to measure the tunnel face stability by means of Equation (4.18), a unique value of undrained shear strength representative of the 'average' undrained cohesion of the overburden is required. To this end, the average undrained shear strength $C_{u,av}$ of the overburden was calculated as shown in the window of Figure 4-18.

The average undrained shear strength versus time, t is plotted in Figure 4-19. It is possible to see that the average undrained shear strength of the overburden at the time t=0 day is $C_{u,av}$=51.50kPa and it is more than double at t=10days.

Ultimately, the stability factor N was calculated at different time steps by means of Equation (4.18) with a bulk weight of soil taken equal to $\gamma = 20\ \mathrm{KN/m^3}$, the depth to the tunnel axis equal to $H = 14\mathrm{m}$, and the undrained shear strength over time given by $C_{u,av}$ in Figure 4-18. The stability factor N over the 10 days of evaporation is shown in Figure 4-19. The stability factor N decreases from N=5.44 at t=0 day to N=2.50 at t=10 days. Based on the guidelines provided by centrifuge testing (Leca & New, 2007), these results suggest that the

tunnel face stability moves from a condition of nearly instability, with ground losses being expected to occur, to a condition of overall ensured stability.

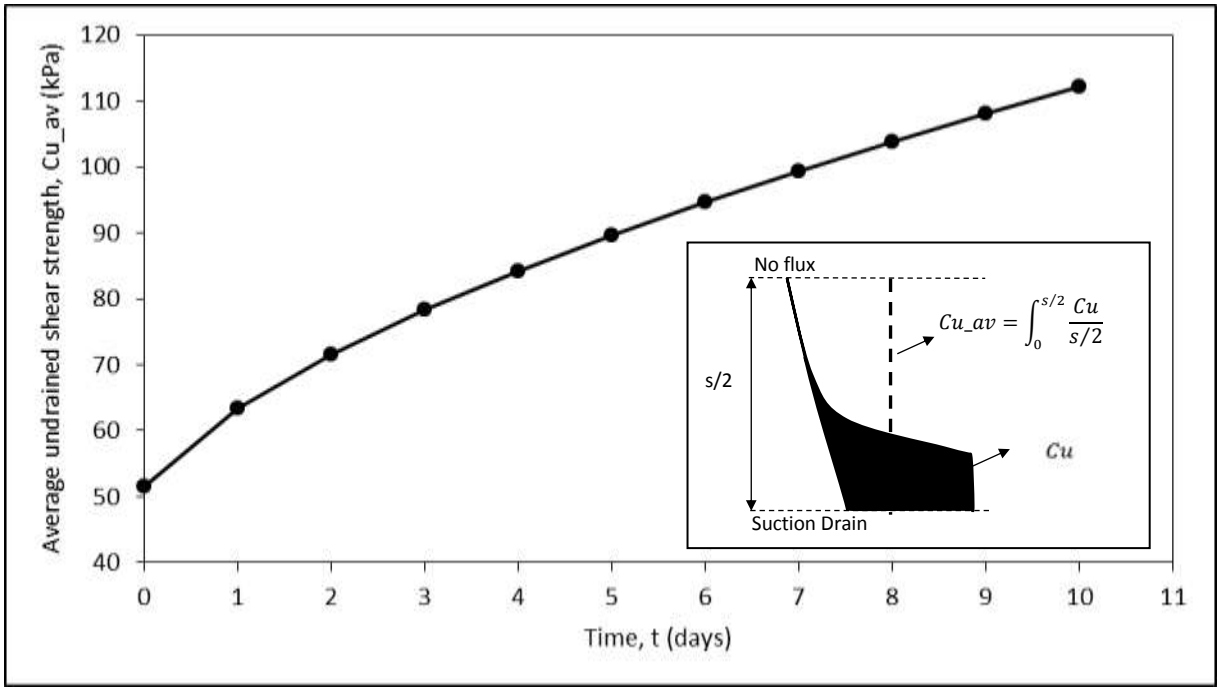

Figure 4-18: Average undrained shear strength of the overburden, Cu_av versus time, t

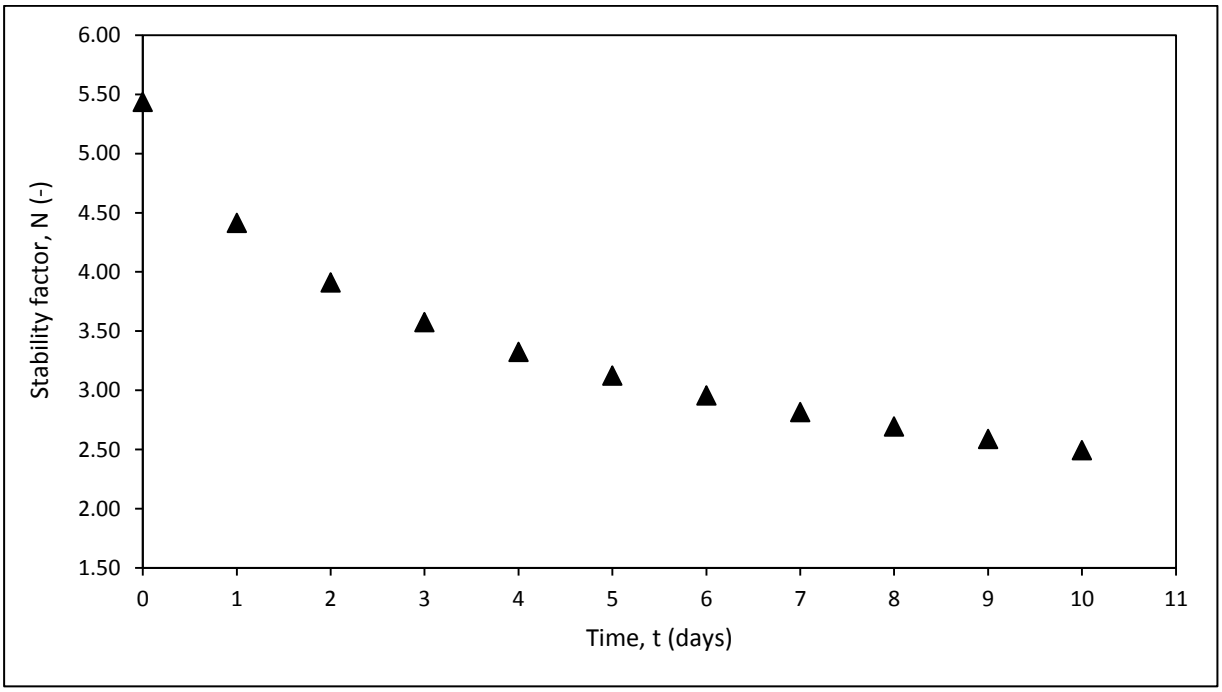

Figure 4-19: Stability factor, N versus the time of evaporation from the suction drain, t

4.9 Conclusions

This paper has presented the concept of the suction drain as an innovative technique for temporary stabilisation of geo structures in clayey soils. The concept is validated at laboratory mock-up scale level. A borehole was drilled into a block sample and air was injected to the bottom of the borehole. Airflow circulated from the bottom to the top of the borehole tangentially to the inner surface of the borehole. Experimental results show that the water content of the soil around the borehole decreased significantly. This demonstrated the capacity of the tangential airflow to remove water via evaporation from the soil. The numerical modelling of the mock-up scale test was carried out via a finite element analysis. The agreement between the numerical and the experimental results validated the numerical model as a tool to design suction drain. The suction drain was applied to an ideal case study to demonstrate its effectiveness in enhancing the undrained shear strength and, hence, the tunnel face stability.

The suction drain therefore represents a viable technique for ground improvement that enables the enhancement of the undrained shear strength of clayey soils without using expensive equipment and without leaving spoils into the ground after its application.

5 SUCTION DRAIN FOR GROUND IMPROVEMENT IN CLAY FORMATIONS: FIELD TRIAL

5.1 Abstract

The suction drain is an innovative concept for ground improvement in clayey soils. This technique is based on the depletion of water content generated by the evaporation induced by forced ventilation into a borehole. The decrease in water content generates an increase in undrained shear strength and, hence, the stability of the geostructure. This paper presents a field trial of the suction drain. A 5 m deep borehole was drilled into the ground and compressed air was injected at the borehole end through a delivery pipe for 4 days. The air flowing back through the gap between the borehole and the pipe was expected to generate evaporation at the borehole interface and, hence, water flow towards the drain. The air velocity and the relative humidity of the airflow was controlled. The water content of the soil around the borehole was measured at different distances from the borehole and at different times from the start of the experiment. Experimental results showed that the water content of the soil around the borehole decreased significantly after 1 day of 'forced' ventilation showing that the trial was successful in demonstrating the effectiveness of the suction drain. A 2D finite element analysis was conducted to simulate the evaporation-induced water flow that occurred in the soil around the borehole. A possible scenario of the water flow generated during the field trial is discussed.

5.2 Introduction

The suction drain is an innovative concept for temporary stabilisation of tunnels and excavations in clay formations. The concept is based on the principle of water flow induced by evaporation that reduces the water content of the soil and, hence, increases its undrained shear strength. The concept of the suction drain, first presented by Martini et al., (2018-submitted) is summarised in Figure 5-1. The technique consists of drilling a borehole into the ground and installing a centralised air delivery tube inside the borehole. Air is injected at the end of the borehole through the tube, then flows back from the end to the entry of the borehole through the gap between the tube and the inner surfaces of the borehole. The air, which flows tangentially to the inner surface of the borehole, exposes the soil to evaporation. Water therefore flows towards the borehole reducing the water content of the surrounding soil and increasing its undrained shear strength.

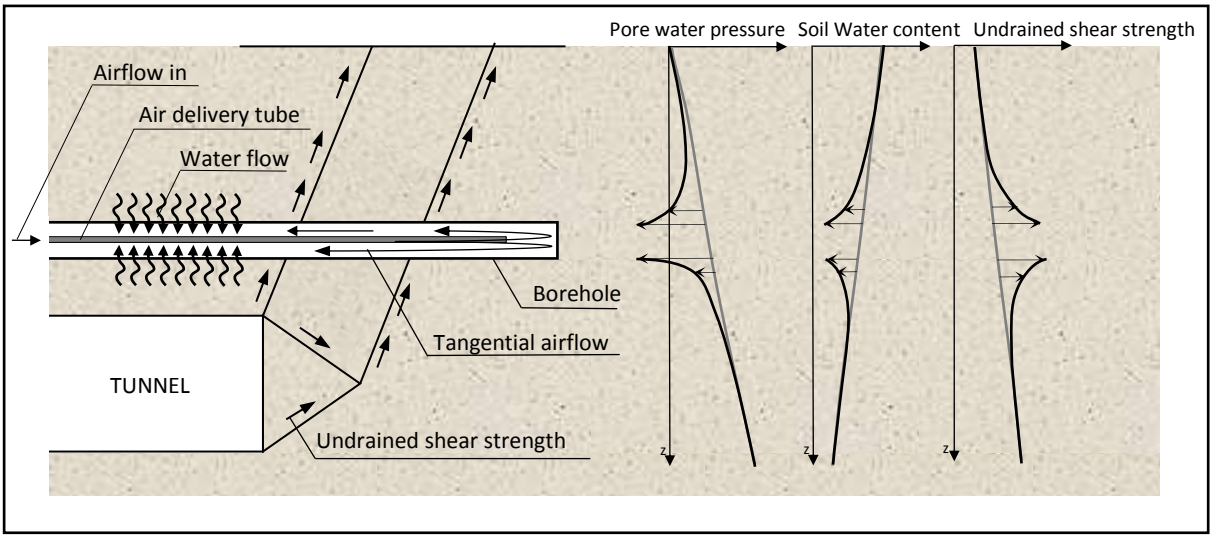

Figure 5-1: Application of the suction drain for temporary soil stabilisation in tunnelling

One of the key aspects of this technique is the water flow generated by the tangential air-flow. Martini & Tarantino, (2018-submitted) developed a model for estimating the water

evaporation rate from a wet surface that is exposed to a tangential airflow in a confined space. The model allows quantifying the water flow from the inner surfaces of the borehole as a function of the air velocity and the relative humidity of the airflow inside the borehole.

The suction drain was also tested in the laboratory in a block of natural soil. The proof of concept of the suction drain at mock-up scale was presented in Martini et al., (2018-submitted). Air was injected through a pre-drilled borehole at the centre of the block of soil and the water content of the soil around the borehole was monitored over time and distance. The evaporation-induced water flow in the soil was modelled in a 2D analysis. The proof of concept was achieved by matching the experimental and the numerical water content of the soil around the borehole.

This study aims to verify the concept of the suction drain at the field scale. A 5 m deep borehole was drilled in a silty clay deposit in Newton (Scotland) and air was injected at the end of the borehole for 4 days. The water content of the soil was measured at different distances from the borehole and at different time from the start of the airflow-induced evaporation. The field installation, the field procedure and the data sampling of the field test are described in this paper.

Numerical analyses were then conducted to simulate the evaporation-induced water flow in the soil around the borehole. To this end, a hydro-mechanical characterisation of the soil was carried out. The water content simulated numerically was finally compared with the water content measured experimentally in the field to analyse the processes occurred in the field.

5.3 Site details

The site is located off Newton Farm Road in the north eastern outskirts of Newton, Cambuslang. It was part of the working site dedicated to the construction of the Newton Farm Primary School in Cambuslang. A conventional site investigation carried out by BAM Ritchies for the construction of the school showed the presence of clay/ silty clay in the north-west corner of the working site. This part of the site was selected for carrying out the field test of the suction drain in clay formations. The national grid reference of the centre of the site is NS 66694 61415 (Easting: 266693.713, Northing: 661414.926).

5.4 Material

The material used for the characterisation of the soil in the laboratory was obtained from the U86 soil samples of borehole BH01 (see Figure 5-8) between 3mBGL and 5mBGL. Borehole BH01 was drilled by using the continuous percussion boring Terrier technique.

5.4.1 BGLSoil classification and index properties

Soil samples from the depth intervals of 3.00-3.30m and 4.25-4.50m were used for the soil classification and for assessing of the soil index properties. Moisture content tests, Atterberg Limit tests, particle density tests by the small pycnometer method and particle size distribution including sedimentation tests were carried out in accordance with BS1377:1190.

The average moisture content of the soil between 3mBGL and 5mBGL was w=0.40. The limit liquid assessed by fall cone test was LL=0.55 and the thread-rolling plastic limit was PL=0.27. According to the plasticity chart of Casagrande the clay is classified as inorganic clay

with high plasticity (PI=0.28). The soil material is an inactive clay with the activity A=0.56. The specific gravity was Gs= 2.750.

The particle size distribution of the two soil samples taken at 3.00-3.30mBGL and two soil samples taken at 4.25-4.50mBGL is shown in Figure 5-2. Each curve was obtained via wet sieving and sedimentation. The four curves show similar grain size distributions: 42% to 51% is clay fraction (<2μm), 56% to 47% is silt fraction (2-75μm) and 2% is sand fraction. The grain size distribution of the soil between 3mBGL and 5mBGL was considered to be homogeneous.

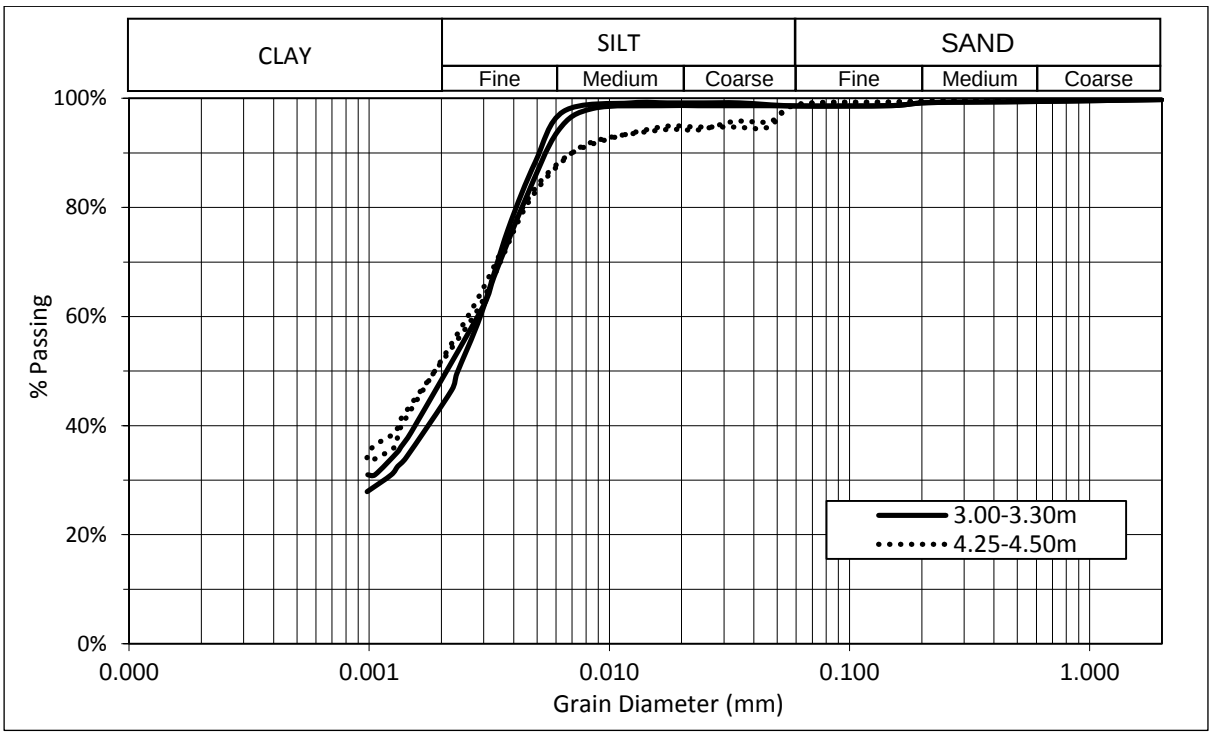

Figure 5-2: Particle size distribution of the soil at the site

5.4.2 Compression behaviour

Figure 5-3 shows five one-dimensional (oedometer) compression tests that were performed on soil specimens taken at 3.00-3.30mBGL, 4.00-4.15mBGL and 4.25-4.50mBGL from borehole BH01. A 75mm diameter and 20mm high steel cutting ring was used to cut the

specimen from the U86 soil samples. The excess clay was trimmed to obtain the specimen of equal dimension to the cutting ring.

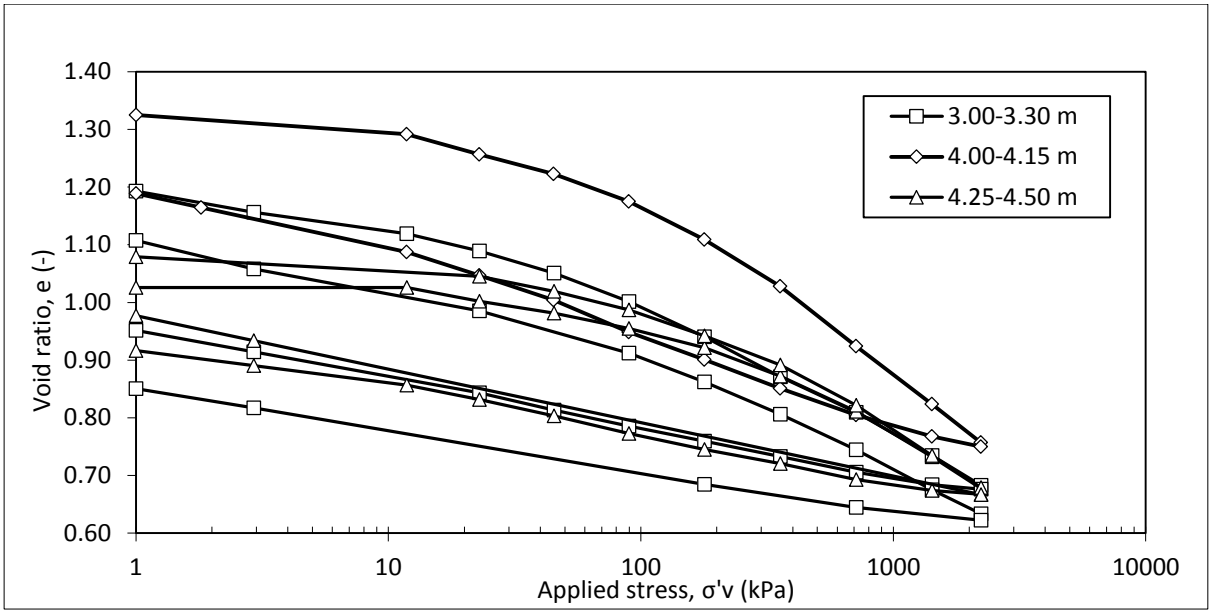

Figure 5-3: Results of one-dimensional compression tests in terms of void ratio e versus vertical effective stress σ'v of the soil in situ

The specimen was placed into the oedometer cell and the water reservoir was filled with water to saturate the specimen before to start the test. The specimen was loaded in steps to the final vertical stresses of 2230 kPa and then unloaded by reversing the loading cycle. Each applied vertical stress was maintained for sufficient time to allow for equalisation of vertical displacement. The change in thickness of the specimen versus time was recorded at each loading step via a displacement transducer.

The void ratio *e* is plotted versus the vertical effective stress *σ'v*. The variable *e* was calculated backwards from the final water content and the volume changes recorded at each step. At the end of each loading step, the pore water pressure was assumed to be equal to zero and therefore *σ'v=σv*. The vertical total stress was calculated by dividing the vertical load by the specimen area.

It is possible to observe that the compressibility curves of the specimens at 3.00-3.30mBGL and at 4.25-4.50mBGL present parallel normal consolidation lines and rebound lines, whereas the specimen at 4.00-4.15mBGL has a different normal consolidation line and rebound line. These observations are consistent with the visual examination of the soil in the site between 3mBGL and 5mBGL that presents a homogeneous clay matrix and sparse bands of clayey sandy silt and lenses of sand. It is also visible that for the same depths the specimens at 3.00-3.30mBGL have different initial void ratio. This suggests that the clay matrix may be composed of clay with different porosity and/or density.

5.4.3 Water retention behaviour

The water retention behaviour was derived by assessing experimentally i) the void ratio e versus the water ratio e_w, and ii) the water ratio e_w versus the soil suction s. This allowed defining the water retention behaviour in terms of the degree of saturation S_r versus suction s and void ratio e versus the suction s.

A 50mm diameter metallic cutting ring was used to cut soil specimens between 4.70mBGL and 4.90mBGL from the U86 soil samples of borehole BH01. The soil specimens were air-dried to target water contents and afterwards enclosed in a waterproof layer of Parafilm® and silicon grease for 24hrs for water content equilibration.

Measurement of suction

High-capacity tensiometers (Tarantino & Mongiovì, 2002) were used to measure the soil suction in the range 0-2000 kPa. They consist of a water reservoir, a high air-entry ceramic disk (1.5 MPa) and a strain-gauged diaphragm. A review of this measurement technique can be found in Tarantino, (2004) and Marinho et al., (2008). The tensiometers were calibrated in the

positive range 0-1500 kPa with a measure standard deviation accuracy of ±1.5 kPa. The calibration was extrapolated to the negative range of pore water pressure according to Tarantino & Mongiovì, (2002).Two tensiometers were used simultaneously to measure the soil suction in each specimen. Two holes of the size of the tensiometer porous ceramic were cut on the layer of Parafilm® and the tensiometers were placed into the holes with the porous ceramics in contact with the soil. An additional layer of Parafilm® and silicon grease was placed around the connection of the tensiometer and the specimen to prevent water evaporation occurring from the hole during the measurement. Once the tensiometers recorded a stable value of suction, the specimen was placed into the oven at 105°C for 24hrs to obtain the moisture content related to the matric suction.

The dew point water potentiometer only (WP4C) was used for suction measurement in the range 300-200,000 kPa. The calibration curve of the device was verified by using sodium chloride solutions with known water potentials at 20˚C with a measured standard deviation in accuracy of ±30 kPa. Further information on the use of the WP4C can be found in Decagon Devices (2014). Specimens of approximately 1 cm^3 were cut from the 50 mm diameter soil sample and were placed into the WP4. At the end of the pore water pressure measurement the specimen was placed into the oven at 105°C for 24hrs to obtain the moisture content related to the total suction.

The WP4C and the high-capacity tensiometer measurements overlapped the range 300-2000 kPa.

Measurement of void ratio

The relationship between the void ratio, e and the water ratio, e_w was assessed independently. A 16mm diameter, 12.5 mm high cutting ring was used to cut small specimens

from the 50 mm diameter soil samples that were air-dried to target water content. The cutting ring was pushed into the sample slowly using a loading frame to prevent soil cracking. The top and bottom of the specimen were trimmed to give the specimen the same height of the cutting ring. The inner volume of the cutting ring allowed the calculation of the void ratio. The specimen was then placed into the oven at 105°C for 24hrs to obtain the soil water content.

Water retention curve

The experimental data of water ratio e_w versus the soil suction s is shown in Figure 5-4a. It is possible to see that the suction measurements obtained via the tensiometers define a clear trend whereas the suction measurements obtained via the WP4C appear to be more scattered. This scatter might be linked to the accuracy of the WP4C and to the fact that the tested soil is a natural soil. Despite the dispersion of the WP4C data, there seems to be continuity between total suction and matric suction data, i.e. the osmotic component of suction appears to be negligible.

The void ratio e versus water ratio e_w is shown in Figure 5-4b. The experimental data were fitted by using two distinctive functions for the saturated and unsaturated range, respectively (Tarantino A. et al., 2010):

$$e = w \cdot Gs = e_w \qquad (w > w_{AE}) \qquad (5.1a)$$

$$e = e_{res} + \frac{e_{AE} - e_{res}}{\exp\big(b\,(w_{AE} - w)\big)} \qquad (w < w_{AE}) \qquad (5.1a)b)$$

where w_{AE} is the gravimetric water content at air entry, Gs is the specific gravity of the soil, e_{res} is the residual void ratio, e_{AE} is the void ratio at air entry, and b is a fitting parameter. It is possible to see that upon drying, the void ratio decreases to $e = 0.8$ in the saturated range then remains constant when the soil desaturates.

The drying curve in terms of degree of saturation S_r versus soil suction s is shown in Figure 5-4c. Per each data point of a known water ratio, e_w and soil suction s, the degree of saturation Sr was calculated as the ratio of water ratio to void ratio ($Sr = e_w/e$) with void ratio e obtained from Equation (5.1a). Experimental data of the degree of saturation Sr versus soil suction s were fitted by using Van Genuchten's function (Van Genuchten, 1980)):

$$S_r = \left(\frac{1}{1+(\alpha s)^n}\right)^m \tag{5.2}$$

where α, n and m are soil parameters and were derived by best-fitting using the least-square method (Table 5-1).

Finally, the relationship of void ratio e versus soil suction s is shown in Figure 5-4d. Two distinctive functions were used to model the void ratio e versus the suction s in the saturated and unsaturated range, respectively as follows (Tarantino, A., 2010):

$$\mathrm{e} = N - \lambda \cdot \ln(s) \qquad (s < s_{AE}) \tag{5.3a}$$

$$e = e_{res} + \frac{e_{AE} - e_{res}}{\exp\left(a\ (\mathrm{s} - s_{AE})\right)} \qquad (s > s_{AE}) \tag{4.3b}$$

where s_{AE} is the suction at air entry, N, λ and a are fitting parameters (Table 5-1).

The water retention behaviour of the soil was defined by the volumetric water content θ (volume of water per total volume) versus the soil suction s. The volumetric water content θ was calculated as the product of the porosity n to the degree of saturation Sr. The values of the parameters used for defining the water retention behaviour of the soil are given in Table 5-1 .

Table 5-1: Parameters for the water retention behaviour

w_{AE} [-]	e_{res} [-]	e_{AE} [-]	b [-]	α [kPa]$^{-1}$	n [-]	m [-]	s_{AE} [kPa]	N [-]	λ [-]	a [kPa]$^{-1}$
0.29	0.794	0.798	728.170	0.002	58.289	0.007	500.971	1.406	0.098	0.052

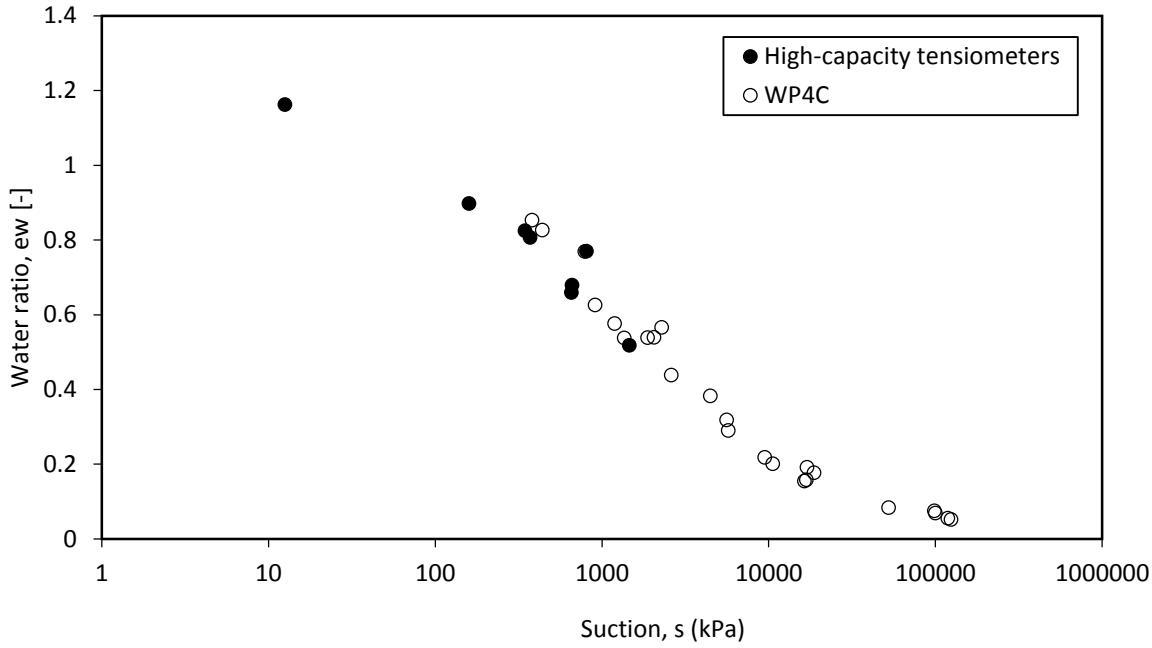
High-capacity tensiometers
WP4C
Water ratio, ew [-]
Suction, s (kPa)
1.4
1.2
1
0.8
0.6
0.4
0.2
0
1
10
100
1000
10000
100000
1000000

a)

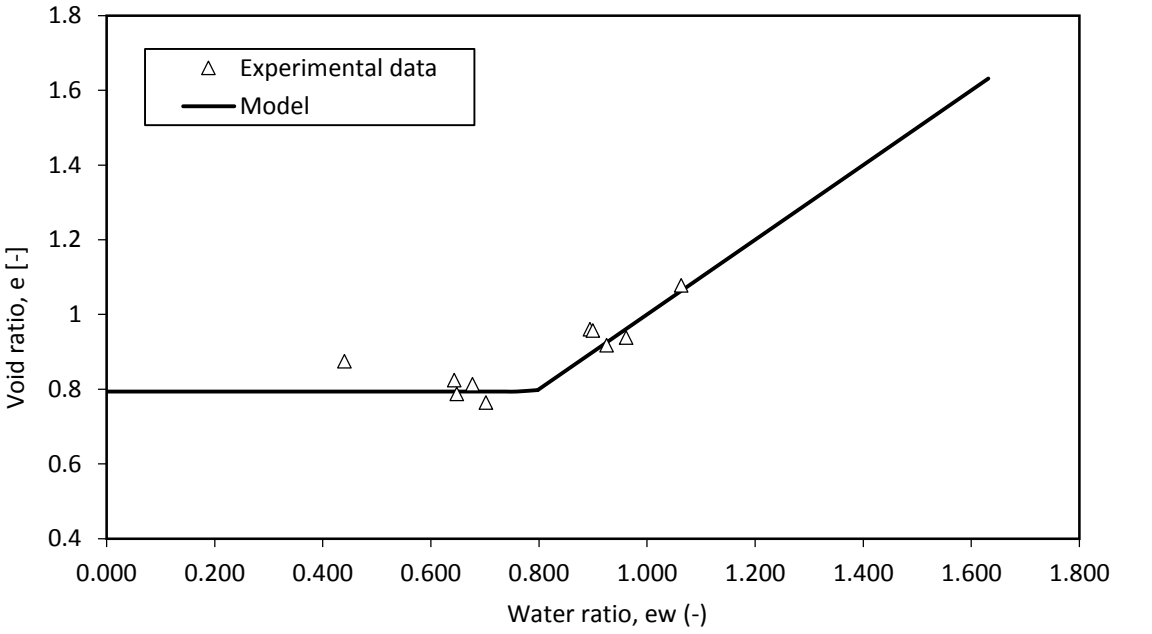
Experimental data
Model
Void ratio, e [-]
Water ratio, ew (-)
1.8
1.6
1.4
1.2
1
0.8
0.6
0.4
0.000
0.200
0.400
0.600
0.800
1.000
1.200
1.400
1.600
1.800

b)

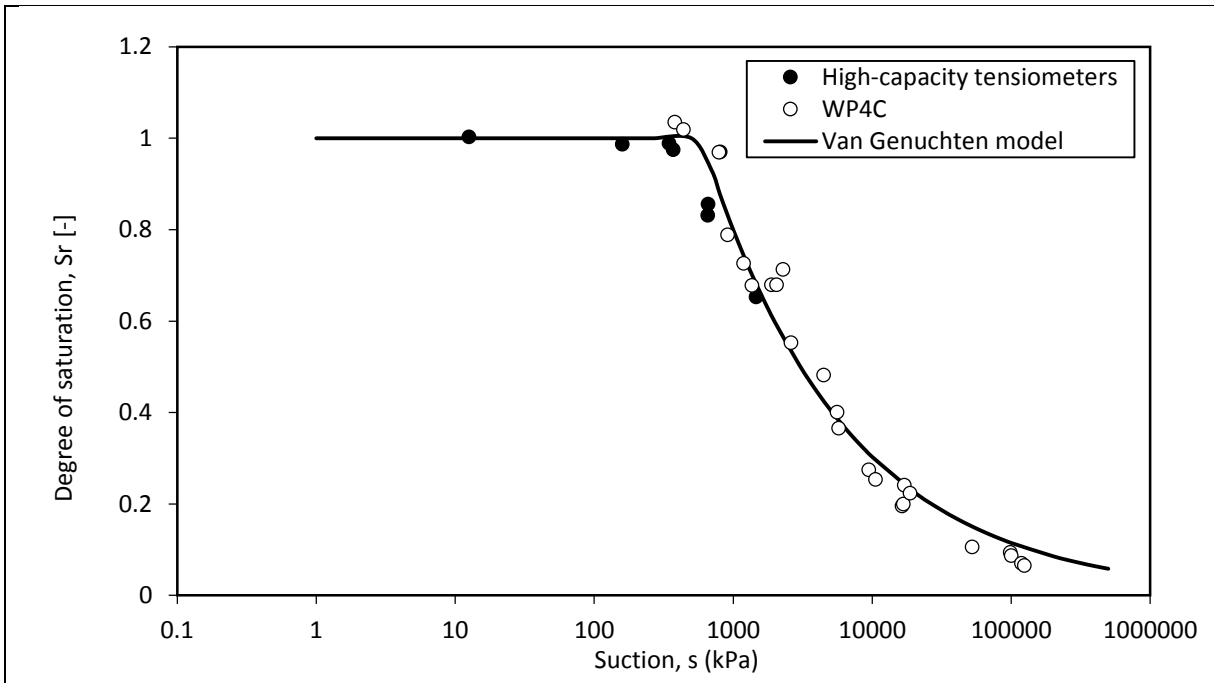

c)

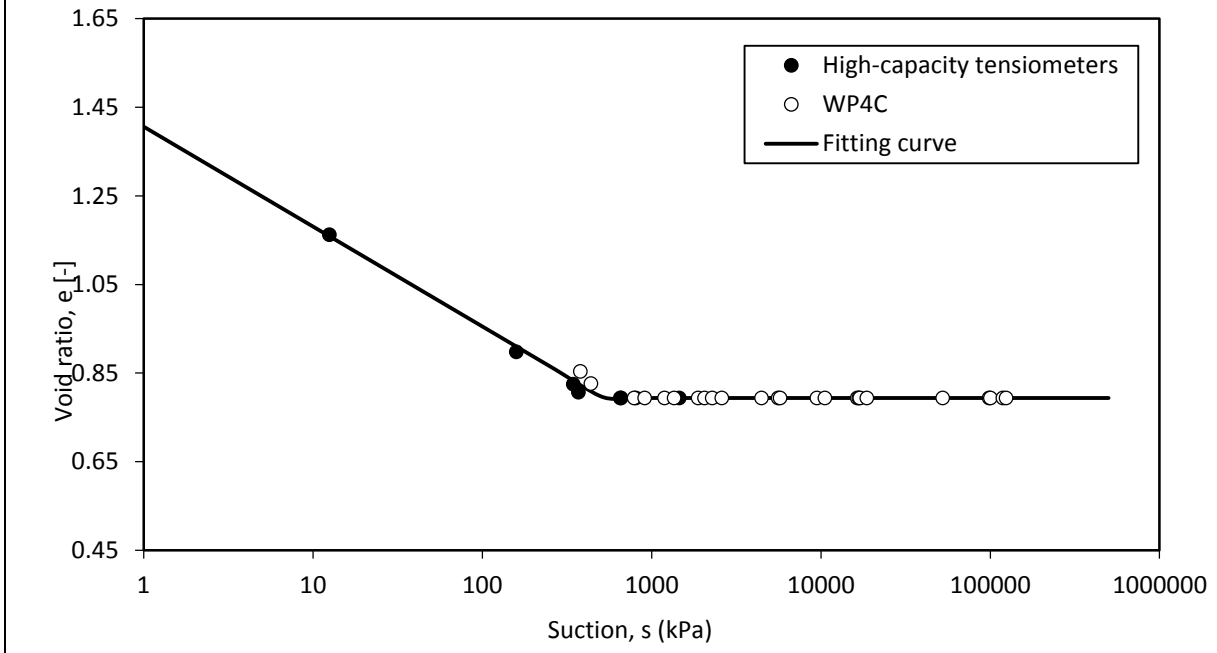

d)

Figure 5-4: Water retention behaviour of the soil in situ

5.4.4 Hydraulic conductivity behaviour

The hydraulic conductivity k was modelled via the Kozeny-Carman equation (Chapuis & Aubertin, 2003):

$$k = k_{sat0}\left(\frac{e}{e_0}\right)^3\left(\frac{1+e_0}{1+e}\right)S_r^3 \tag{5.4}$$

where k_{sat0} is the saturated hydraulic conductivity associated to the reference soil void ratio e_0, e is the void ratio and Sr is the degree of saturation. The void ratio e and the degree of saturation Sr are defined by Equations (5.3a) and (5.2). The saturated hydraulic conductivity k_{sat0} is obtained at the reference void ratio e_0 from the constant head hydraulic conductivity test in a modified oedometer cell as explained later in this section. The hydraulic conductivity k versus the soil suction s is shown in Figure 5-5.

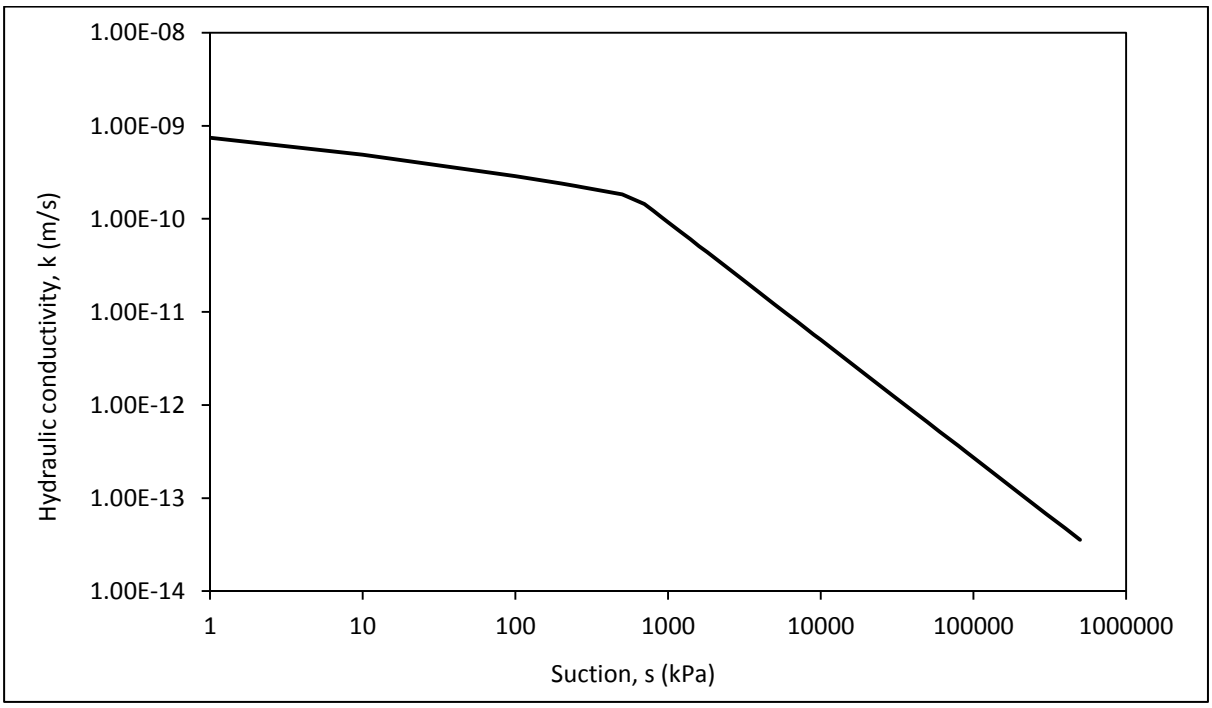

Figure 5-5: Hydraulic conductivity curve of the soil in the site

Saturated hydraulic conductivity

The saturated hydraulic conductivity was assessed experimentally via constant head hydraulic conductivity tests carried out in a modified oedometer cell. The soil specimens were cut from the U86 samples of borehole BH01 at the depth of 3.00 mBGL, 4.00 mBGL and 4.25 mBGL by using the sampling technique described in Section 5.4.2. The specimens were placed into the oedometer and the cell was covered with water. The specimens were loaded in steps, as per standard oedometer test, to a vertical pressure of 2230 kPa. The oedomter cell was connected to a water reservoir located at 1.062 m height from the oedometer cell. At the end of the primary consolidation of selected loading steps, the valve was open and the water was able to flow through the specimen thanks to the hydraulic head differential *H* between the top and the bottom of the specimen. The quantity of mass of water passing through the sample was measured by the balance underneath the water reservoir, taking into account the water evaporation rate from the reservoir.

Direct measurements of k_{sat} versus $e^3/(1+e)$ are shown in Figure 5-6 for the three soil specimens taken at 3.00 mBGL, 4.00 mBGL and 4.25 mBGL. It is possible to see that the values of the saturated hydraulic conductivity k_{sat} for the three specimen are within the same order of magnitude and are characterised by a linear trend with $e^3/(1+e)$. The linear trend is supported by the Kozeny-Carman model (Mitchell & Soga, 2005) and it was used as a check of the quality of the permeability tests (Chapuis & Aubertin, 2003). The value of the saturated hydraulic conductivity k_{sat0} at a reference void ratio $e_0 = 0.89$ was selected with reference to the sample at 4.25-4.50 m ($k_{sat0} = 2.4\ 10^{-10}\ m/s$).

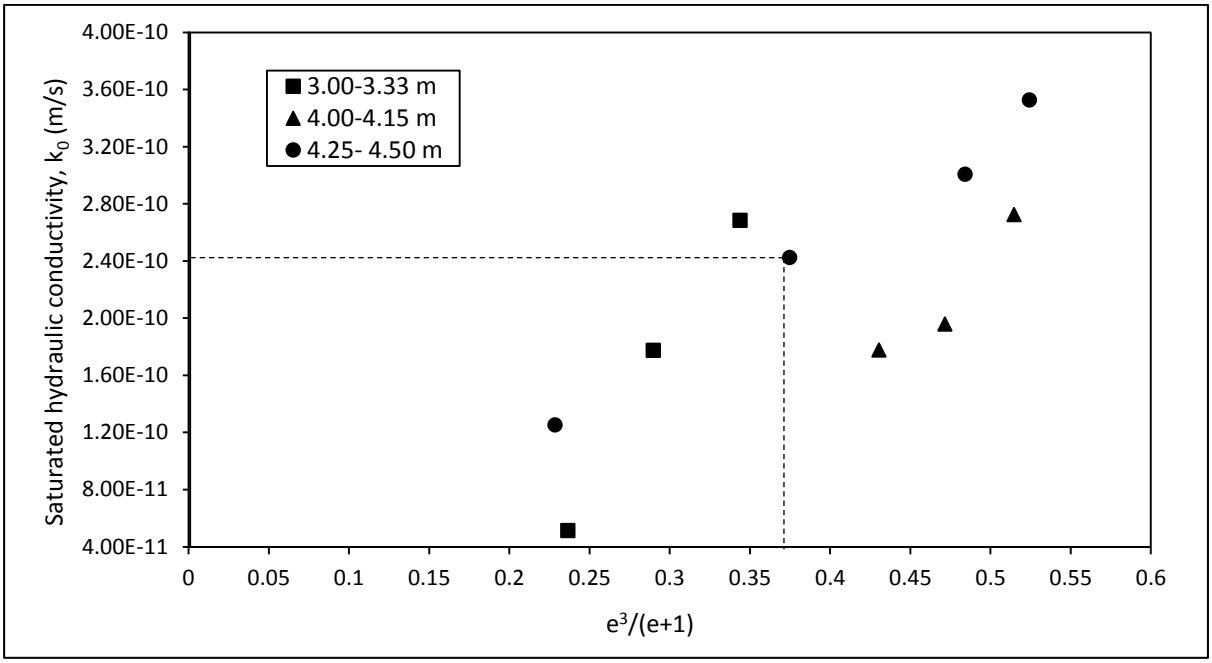

Figure 5-6: Saturated hydraulic conductivity

5.5 Field method

5.5.1 Field installation

Figure 5-7 shows a schematic of the suction drain. A perforated case was installed to support the borehole and, at the same time, to allow the soil water to evaporate into the borehole once air was injected at the end of the delivery pipe.

The perforated case was manufactured in the laboratory and assembled on site. It consisted of five sheets of metallic net with 11mm x 11mm aperture folded into a 1 m long and 80 mm diameter tubular cases and joined together to form the 5 m long perforated case. Four additional tubular cases with a smaller diameter were installed in correspondence of the joints to strengthen the outer perforated case. A solid plastic cup was placed at the end of the perforated case. Four circular spacers equipped with a central hole were fixed to the perforated case every 1 m. A 5 m long and 26 mm outer diameter plastic tube was installed inside the case

through the holes in the spacers. The plastic tube protruded 0.5 m above the ground level and its end was located at 4.5 m from ground level inside the borehole. Three RH/T sensors (Sensirion Kit EK-H5 sensors SHT21) were attached to the outer perforated case at 0.3 m, 2.15 m and 3.35 m from the entry of the case with the measuring sensor facing the soil. One RH/T sensor was installed at ground level, outside of the borehole, to record the temperature and the relative humidity of the air in the environment. The electrical parts of the RH/T sensors were spray-coated with Servisol Plastic Seal 60 Protective Insulator to protect them from oxidation. The measuring sensors were also encapsulated through a filter cup to protect them from long exposure to moisture, chemical corrosion as well as mechanical shocks (Yang, W. et al., 2015). Sensors were calibrated after the field test using the fixed-point humidity systems (de Métrologie Légale, 1996). The specifications of the RH/T sensors are listed in Table 5-2.

Table 5-2: Manufacturer's specification of the RH/T sensors

Sensor size	3 x 3 x 1.1 mm
RH sensing element	Capacitive-type
RH operating range	0 - 100% RH
RH accuracy	±2% (20%-80% RH) ±3% (0-20% RH – 80%-100% RH)
T sensing element	Band-gap
T operating range	-40 to +125°C
T accuracy	±0.3°C

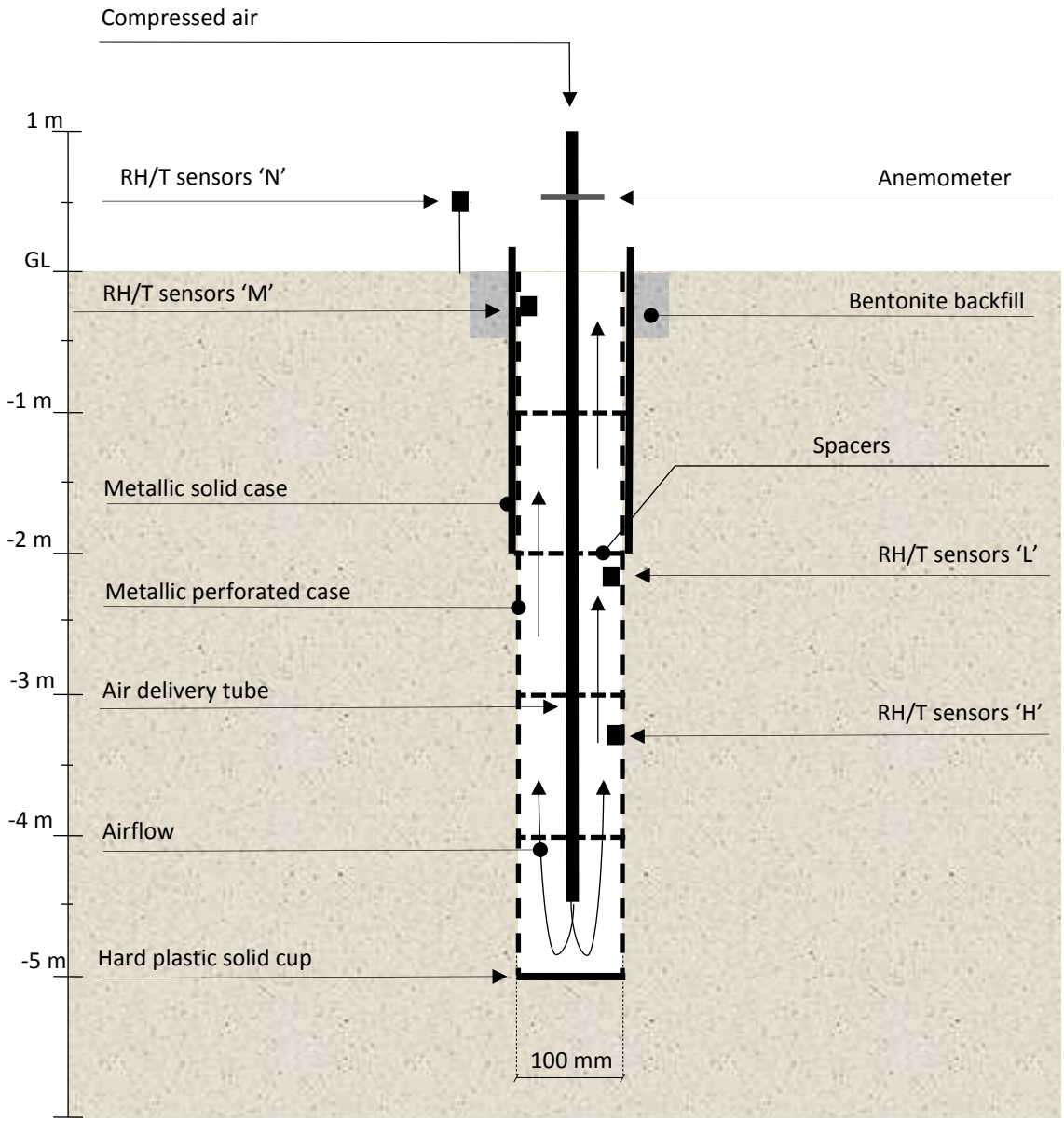

Figure 5-7: The suction drain cage and its installation in the site

5.5.2 Field test procedure

A non-invasive inspection was conducted at ground level in the area of the field test to ensure that no pipes and electrical cables were present underground. A 500 mm diameter and 300 mm deep hole was excavated at ground level where the central borehole was planned to be excavated to carry out the service check.

A 100 mm diameter and 5 m deep borehole was then drilled via continuous percussion boring technique (Terrier). No drilling mud was used during the drilling to avoid the alteration of the natural water content of the soil. Solid case was temporarily installed inside the borehole during the drilling to ensure its stability.

The perforated case was lowered to the end of the borehole. The solid case was then partially withdrawn to leave clear space between 2mBGL and 5mBGL. Bentonite was used to backfill the hole at the ground level and to prevent water infiltration from ground level around the borehole.

The hose from a compressor was connected to the inlet of the air delivery tube inside the borehole. The air, supplied by a compressor at 280 kPa, was injected to the end of the borehole 24/7 for 4 days.

Air velocity was measured at the entry of the air delivery tube via the anemometer (OMEGA FMA1006R-V2-S) at regular intervals. The air velocity was v=10m/s. The specification of the velocity sensor are summarised in Table 5-3. The RH/T sensors inside the borehole were connected to the laptop to record the relative humidity and the temperature of the air inside the borehole during working hours on site.

Table 5-3: Specification of the anemometer

Range Air velocity	0-60.96 m/s
Accuracy air velocity	1.5% Full scale range
Display resolution air velocity	0.01m/s
Sensor probe	6.3 OD x 95 mm- 304 Stainless steel
Response time	250 msec default
Operating Relative Humidity	0 to 95% RH without condensation

5.5.3 Data sampling

Figure 5-8 shows a schematic layout of the data sampling that was undertaken on site for monitoring the gravimetric water content and the soil strength before and during airflow-induced evaporation.

The initial water content of the soil on site was obtained from soil samples of the borehole BH01. Radial boreholes were drilled at 0.3 m and 0.7 m from borehole BH01 at day 1, day 2, day 3 and day 4 of evaporation. One additional borehole at 1.5 m from BH01 was drilled at day 1 and day 2 of evaporation. Boreholes were drilled via the continuous percussion (Terrier) technique from ground level to 5mBGL and U86 samples were taken every 1 m. Soil specimens were cut from the U86 samples approximately every 0.3 m to measure the gravimetric water content. The gravimetric water content was measured at different depths between ground level and 5mBGL, at different distance from the evaporating surface and at different time from the start of the evaporation as shown in

.

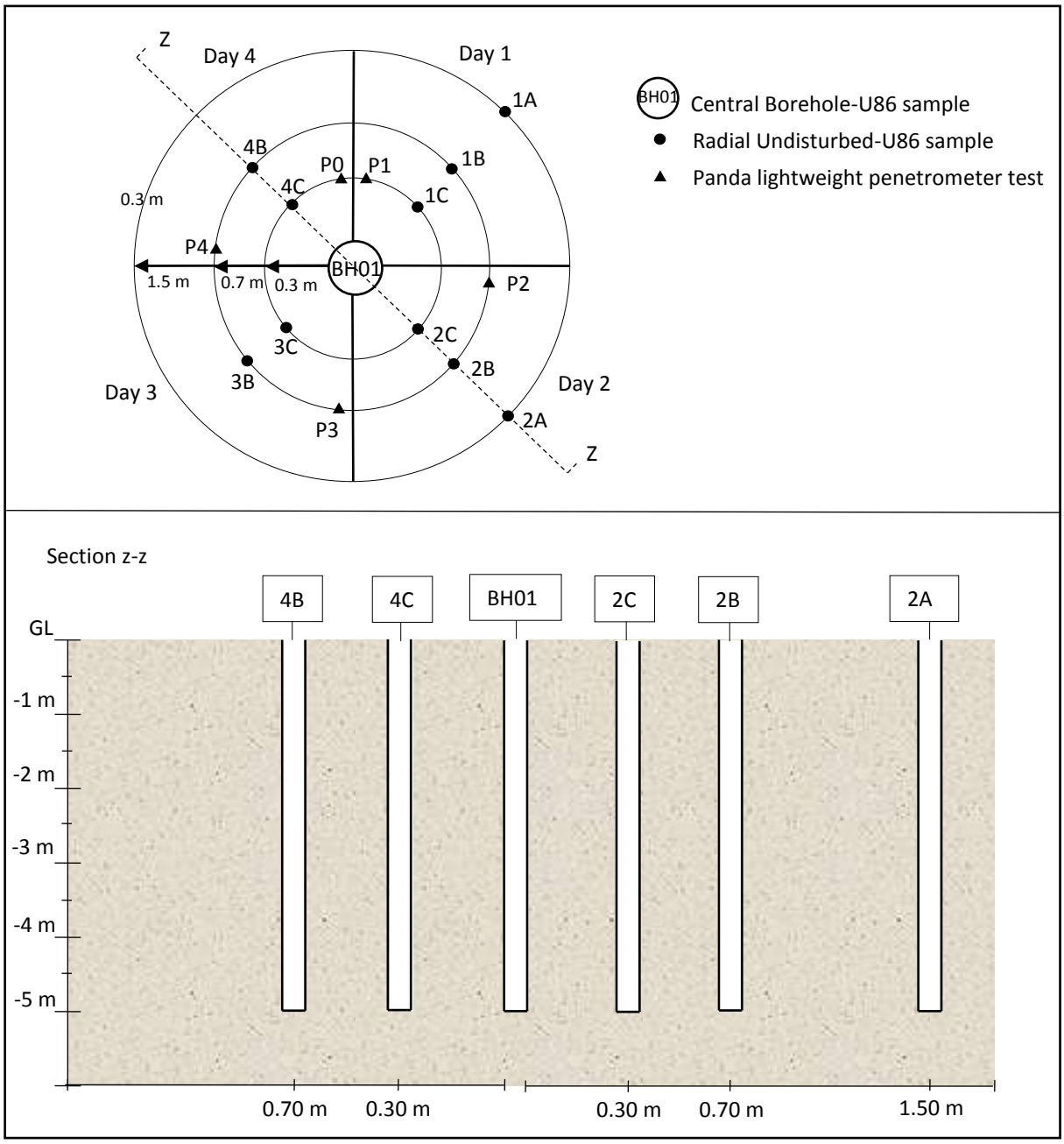

Figure 5-8: Mapping of data sampling

It can be observed that the radial boreholes were drilled each day in different quarter of the circular area around the central borehole. This scheme was thought to limit the interference between boreholes drilled at different days. Radial boreholes were also backfilled with bentonite after sampling to avoid evaporation occurring from there.

Panda lightweight penetrometer tests measured the dynamic penetration resistance of the soil. The objective was to correlate the penetration resistance to the undrained shear strength of the soil via available correlations in the literature (Butcher A. P. et al., 1995; DD Langton, 1999). A Panda test was carried out before to start the evaporation (P0) and at every day of evaporation (P1, P2, P3 and P4). Test P1 was carried out at 0.3 m from the central borehole and tests P2, P3 and P4 were carried out at 0.7 m from the central borehole. It is possible to see that also the Panda tests were carried out each day in a different quarter of the circular area around the central borehole.

The data sampling scheme shown in Figure 5-8 is supported by the following assumptions: i) the evaporation-induced water content change is axisymmetric from the central borehole; ii) the water content and the dynamic penetration resistance of the soil measured before the start the test was homogeneous in the 1.5 m radius circular area around the central borehole BH01.

5.6 Experimental results

5.6.1 Measurement of relative humidity and temperature of the airflow

Figure 5-9 shows the relative humidity and the temperature of the airflow that circulates in the central borehole BH01 through the gap between the air delivery tube and the surfaces of the borehole over time. The relative humidity and the temperature of the airflow were measured via the RH/T sensors H, L and M that were installed inside the borehole at 3.35mBGL, 2.15mBGL and 0.3mBGL, respectively. The relative humidity and the temperature of the air in the environment were also measured via the RH/T sensor N at 0.5m above ground level (Figure 5-7).

The sensor at 0.3mBGL (M) essentially measures the ambient RH whereas the lower sensor at 3.35mBGL (H) and the intermediate sensor at 2.15mBGL (L) are exposed to the evaporating surface of the borehole. Because the ground surrounding the borehole in its bottom part is saturated, one would expect the relative humidity in the borehole to be close to 100% if air was stagnant. The air flow on days 0 to 1 actually depletes the relative humidity to about 85% for the sensors H and L. It can then be noticed that the relative humidity then tends to increase steadily on days 2 to 4 for the sensors H and L as if the air injected at the bottom of the borehole does not effectively move back upward through the gap between the borehole and the air delivery tube.

The temperature of the airflow inside the borehole (sensors H and L) remains fairly constant, lower that air temperature above ground and generally oscillating in phase with the temperature above ground (sensor N).

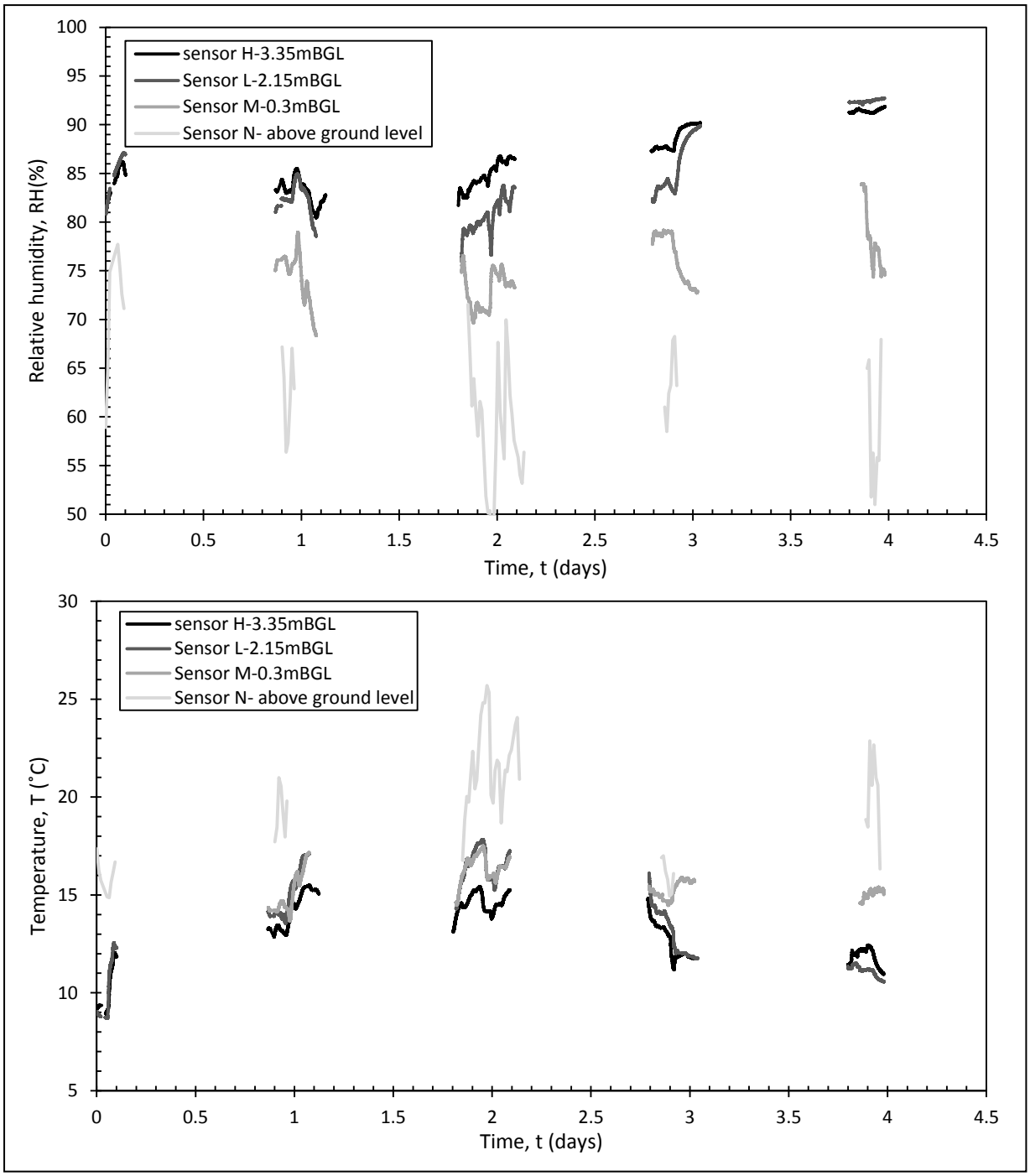

Figure 5-9: Relative humidity and temperature of the airflow inside the borehole BH01 measured via the RH/T sensors from the start of the evaporation versus the time, t

5.6.2 Measurement of soil undrained shear strength in the site

Figure 5-10 shows the dynamic penetration resistance of the soil versus depth that was measured via the Panda test. Penetration tests started at ground level on day 0 and 1, and started at 2mBGL on days 2, 3, and 4. The tests were interrupted at about 3.8mBGL when the critical rod friction was reached.

Comparison between the dynamic cone resistance *qd* at day 0 (P0) and at day 1 (P1) shows that the penetration resistance of the soil after 24hrs of evaporation remains approximately the same. Also, the dynamic cone resistance between 2m and 4mBGL does not appear to change significantly on days 2 to 4 (data are quite dispersed but there does not seem to be any temporal trend in the dynamic cone resistance data).

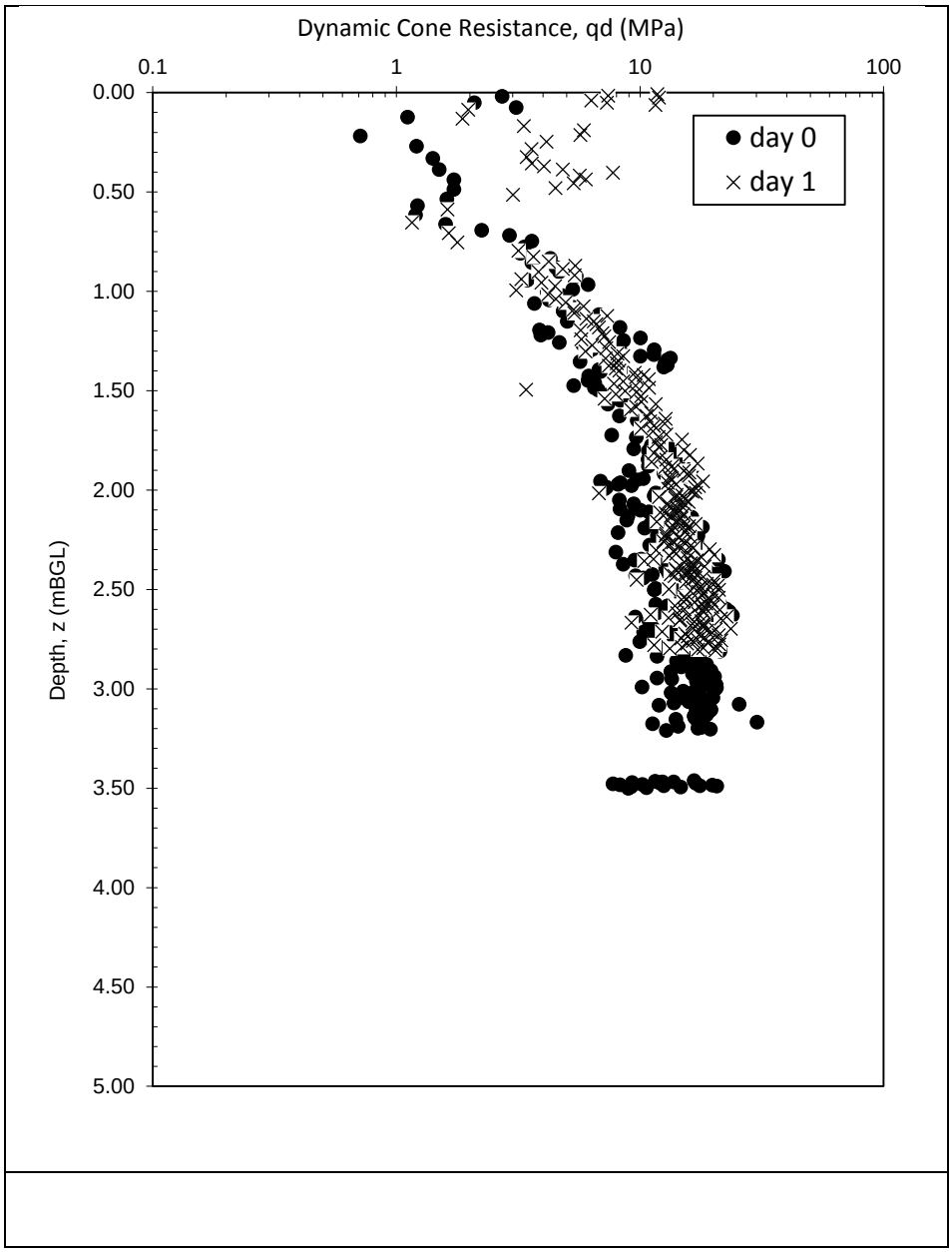
Dynamic Cone Resistance, qd (MPa)
0.1
1
10
100
0.00
0.50
1.00
1.50
2.00
2.50
3.00
3.50
4.00
4.50
5.00
Depth, z (mBGL)
day 0
day 1

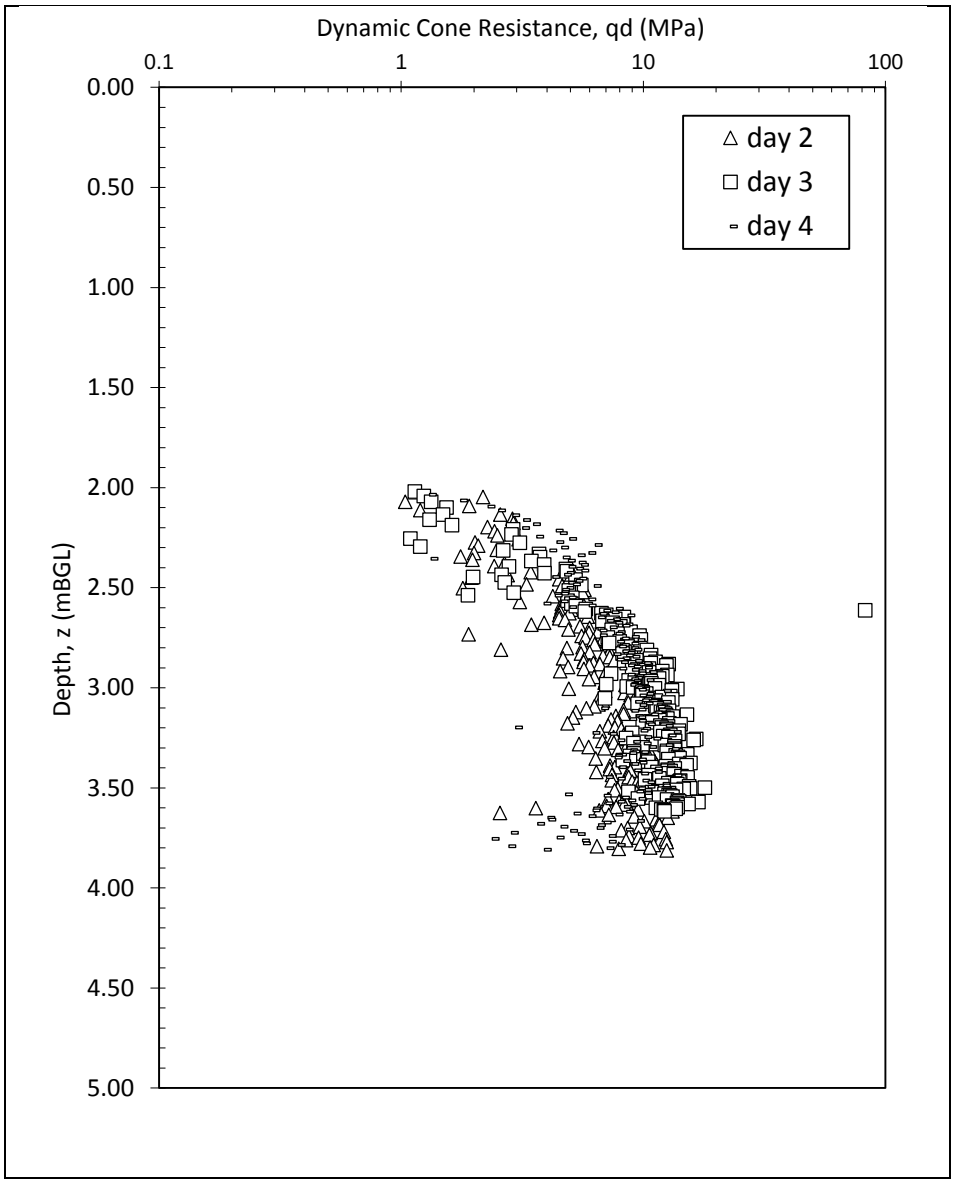

Figure 5-10: Dynamic cone resistance of the soil in situ, qd versus depth, z measured via the Panda test at different days of evaporation

5.6.3 Measurement of soil water content

Figure 5-11 shows the comparison between the water content of the soil in the field before the test and the water content of the soil at 0.3 m from the central borehole BH01 at day 1, day 2, day 3 and day 4 of evaporation. The initial water content of the soil in the field was obtained from the soil specimens that were cut from borehole BH01. The water content of the soil at 0.3m distance from BH01 at day 1, day 2, day 3 and day 4 of evaporation was obtained

from the soil specimen that were cut from borehole 1C, 2C, 3C and 4C, respectively (see Figure 5-8).

The soil water content is plotted approximately every 0.3m from 1mBGL to 5mBGL.

It is possible to see that at day 0, the water content of the soil increases from w=0.22 to w=0.40 between 1mBGL to 3mBGL and remains approximately constant to w=0.4 between 3mBGL and 5mBGL. This trend suggests that the water content of the soil between ground level and 3mBGL is influenced by external weather conditions.

Experimental data referred to day 1, day 2, day 3 and day 4 show that the water content of the soil between ground level and 4mBGL remains approximately equal to the water content of the soil measured on day 0. The water content *w* of the soil between 4mBGL and 5mBGL decreases linearly with depth at day 1 and it reaches w=0.24 at 5mBGL after one day of evaporation. The water content of the soil between 4mBGL and 5mBGL returns equal to the initial water content w=0.40 on days 2 and 3 and it decreases again slightly on day 4. These results suggest that the evaporation was effective on day 1 and essentially stopped working on days 2 to 4. This is not surprising since the site flooded after a heavy rainfall between day 1 and day 2. Probably some water infiltration occurred from ground level through the boreholes drilled the previous days. Following these findings, this paper focuses on the evaporation-induced water flow between 4mBGL and 5mBGL at day 1 of the field test.

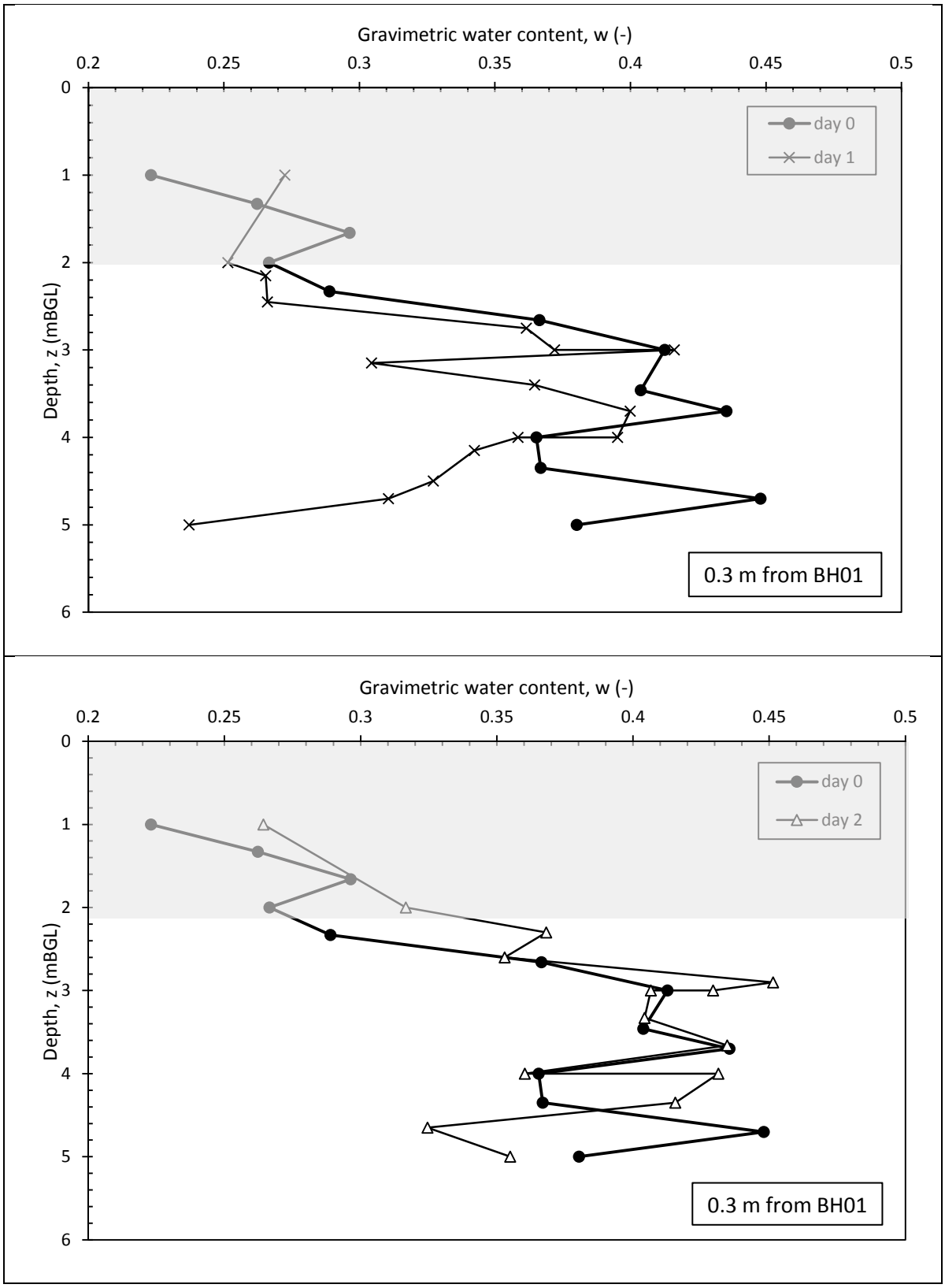
Gravimetric water content, w (-)
0.2
0.25
0.3
0.35
0.4
0.45
0.5
Depth, z (mBGL)
0
1
2
3
4
5
6
day 0
day 1
0.3 m from BH01
Gravimetric water content, w (-)
0.2
0.25
0.3
0.35
0.4
0.45
0.5
Depth, z (mBGL)
0
1
2
3
4
5
6
day 0
day 2
0.3 m from BH01

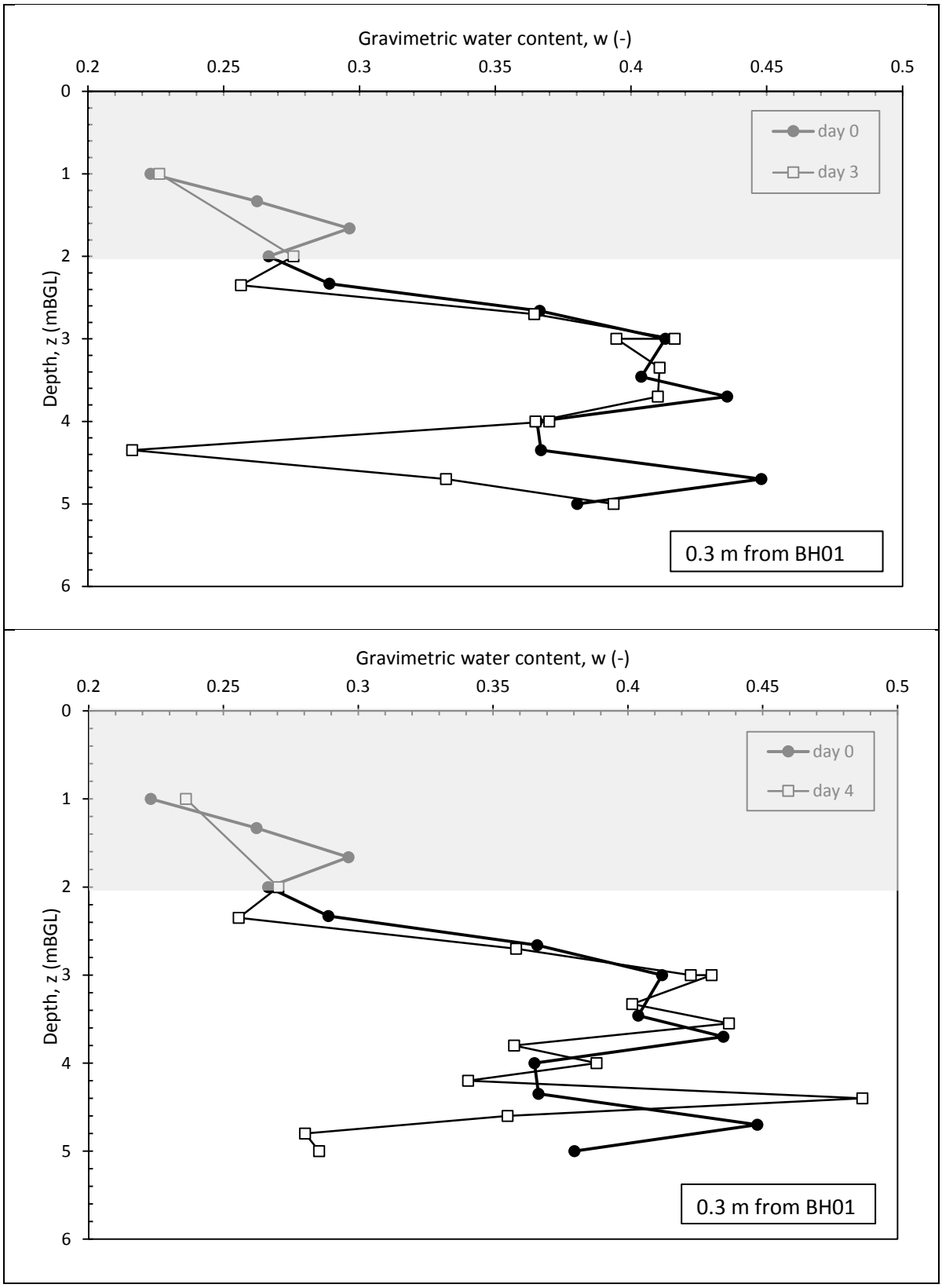

Figure 5-11: Gravimetric water content, w of the soil at 0.3m from the central borehole BH0 versus depth z at different days of evaporation

Figure 5-12 shows the comparison of the gravimetric water content of the soil around the borehole BH01 between 4mBGL and 5mBGL before the evaporation and after 1 day of evaporation. The water content of the soil specimens taken from the central borehole BH01 at day 0 are plotted together with the water content of the soil specimens from boreholes 1C, 1B and 1A at 0.3m, 0.7m and 1.5m, respectively from BH01 after 1 day of evaporation.

The water content of the soil between 4mBGL and 5mBGL after 1 day from the start of the evaporation decreases linearly with depth. No change of water content is measured at 4mBGL. The decrease in water content versus depth was approximately the same for the soil at 0.3 m, 0.7 m and 1.5 m from the central borehole BH01 after 1 day of evaporation. At 5mBGL the water content dropped approximately to w=0.25.

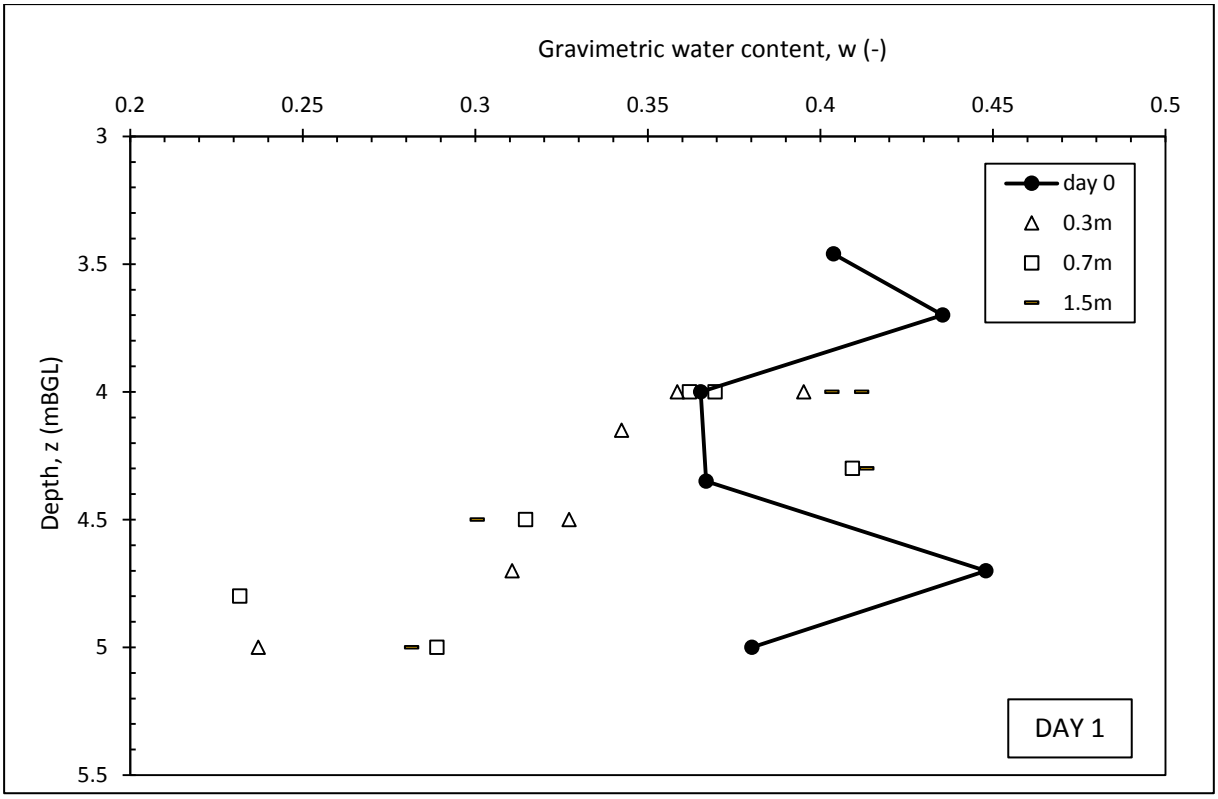

Figure 5-12: Gravimetric water content, w of the soil between 4mBGL and 5mBGL measured at 0.3m, 0.7m and 1.5m from the borehole BH01 at day 1 of evaporation.

5.7 Discussion

The airflow injected into the borehole BH01 removed water successfully from the soil between 4mBGL and 5mBGL after 1 day of evaporation. This section explores the capability of the FEM to reproduce the evaporation-induced water flow that was generated into the soil during the application of the suction drain in the site.

5.7.1 Numerical modelling of the suction drain

A 2D finite element analysis was developed to simulate the evaporation-induced water flow from borehole BH01. The model is based on the assumption that the airflow, which is injected to the end of the borehole, circulates from the end to the entry of the borehole tangentially to the inner surfaces of the borehole. The soil water content after 1 day of evaporation derived numerically will then be compared with the soil water content measured experimentally in the field.

Hydro-mechanical model for the suction drain

The evaporation-induced water flow is a hydro-mechanical coupled process. The hydro-mechanical model that simulates water flow induced by water evaporation is presented in detail in Tarantino et al., (2010). The hydraulic boundary condition associated with tangential air flow in a confined space is discussed in detail in Martini & Tarantino, (2018-submitted). The hydraulic model is based on the water mass balance equation:

$$div(\vec{v}) = \frac{\partial \theta}{\partial t} \tag{5.5}$$

where $\vec{v}$ is the flow velocity, θ is the volumetric water content (volume of water per total volume), and t is the time. In Equation (5.5), the flow velocity is given by the Darcy-Buckingam law (Fredlund et al., 1993; Lu & Likos, 2004):

$$\vec{v} = -\mathrm{k}\,(\mathrm{e}, \mathrm{Sr})\; grad\left(\frac{u_w}{\gamma_w} + z\right) \tag{5.6}$$

where u_w is the pore-water pressure, z is the vertical coordinate increasing upward, γ_w is the specific weight of water, and k is the hydraulic conductivity, which depends on void ratio e and degree of saturation Sr (Mitchell & Soga, 2005). Equation (5.6) neglects diffusive and advective transport of water vapour and this assumption is corroborated by numerical simulation of isothermal drying in low-permeability materials (Baroghel-Bouny, et al., 2001; Coussy, 2004). The volumetric water content can be expressed as a function of Sr and e as follows:

$$\theta = \frac{e(\sigma_{ij}, u_w)}{1 + e(\sigma_{ij}, u_w)} \cdot Sr(u_w) \tag{5.7}$$

where the void ratio e and, hence, the volumetric water content θ, depend on the pore water pressure u_w and on the total stress tensor σ_{ij}. As a first approximation, the volumetric water content θ is considered function of the pore water pressure u_w only (no hydro-mechanical coupling was considered). This simplification allowed developing a simplified model for a first understanding of the evaporation-induced water flow that occurred in the field. In this case Equation (5.5) simplifies to a single-variable as follows:

$$\frac{\partial}{\partial x}\left[k \cdot \frac{\partial}{\partial x}\left(\frac{u_w}{\gamma_w}\right)\right] = \frac{\partial \theta(u_w)}{\partial u_w}\frac{\partial u_w}{\partial t} \tag{5.8}$$

with the following boundary conditions:

$$q\left(\frac{D}{2}, t\right) = \alpha(v_{air}) \cdot p_{v0}(T_{air}) \cdot (RH_{soil} - RH_{air}) \tag{5.9}$$

$$u_w(L, t) = u_{w0} \tag{5.10}$$

and initial conditions:

$$u_w(x,0) = u_{w0} \tag{5.11}$$

where x=D/2 coincides with the evaporating surface of the central borehole of diameter D and x=L coincides with the far field boundary conditions of the model. The term q is the water evaporation rate, α is the vapour transfer coefficient and it is a function of the air velocity that flows tangential to the inner surface of the central borehole, p_{v0} is the saturated vapour pressure which is a function of the temperature of the airflow, $\mathrm{RH_{soil}}$ is the relative humidity at the inner surfaces of the borehole and $\mathrm{RH_{air}}$ is the relative humidity of the airflow. The vapour transfer coefficient $\alpha(\mathrm{v}_{air})$ is derived from Penman equation as demonstrated in Martini & Tarantino, (2018-submitted). The relative humidity at the clay surface $\mathrm{RH_{soil}}$ is related to the soil suction by the psychrometric law:

$$\mathrm{RH_{soil}} = \exp\left[\frac{\mathrm{v_w S}}{\mathrm{RT}}\right] \tag{5.12}$$

where $\mathrm{v_w}$ is the molar volume of liquid water, s is the soil suction, R is the universal constant of gas and T is the absolute temperature. Equation (5.8) together with the boundary conditions and the initial conditions given by Equations (5.9), (5.10) and (5.11) was solved via finite element analysis.

Finite element analysis

The finite element model is represented in Figure 5-13. The analysis is axisymmetric with the vertical axis that is the axis of symmetry of the borehole. Constitutive functions were considered in terms of volumetric water content θ and hydraulic conductivity k. The function $\theta = \theta(u_w)$ was derived from the void ratio e and the degree of saturation Sr, as follows:

$$\theta = \frac{e(u_w)}{1 + e(u_w)}\, Sr\,(u_w) \tag{5.13}$$

where the void ratio $e(u_w)$ is defined by Equation (5.1a) and the degree of saturation $Sr\ (u_w)$ is defined by Equation (5.2).

The hydraulic conductivity k was modelled by using the Kozeny-Carman model (Equation (5.4)) that assumes that the hydraulic conductivity k is a function of the void ratio e and of the degree of saturation Sr as follows:

$$k = f\left(\frac{e^3}{1+e}\ Sr^3\right) \tag{5.14}$$

The saturated hydraulic conductivity that was measured in the laboratory is $k_{sat0} = 2.43\ 10^{-10}\ m/s$ at the reference void ratio $e_0 = 0.89$. Works by Daniel (1984) and Mitchell (1993) show that the hydraulic conductivity of clays in the site is generally found to be 10-1,000 times larger than values obtained from laboratory tests. The main difficulty with laboratory permeability tests is generally related to the problem of obtaining a representative sample of soil for testing.

The water evaporation rate q at the inner surface of the borehole was affected by a certain degree of uncertainty. The air velocity at the inlet of the delivery pipe was measured equal to $v_{air} = 10\ m/s$, however the turbulence of the airflow at the end of the borehole was not controlled. Considering the ratio of the cross-sectional areas of the air delivery tube and the annular gap between the air- delivery tube and the borehole, the air velocity could be considered of the order of 1.3 m/s.

Figure 5-13 illustrates the boundary conditions of the other surfaces of the model. The water evaporation rate $q = 0\ m/s$ was specified at the top and at the bottom surfaces of the model and the constant total head *H* was specified at the surface on the right hand side (outer boundary of the axisymmetric problem). Initial conditions were specified in terms of pore water tension

that enabled to have the soil water content equal to the average water content of the soil between 4mBGL and 5mBGL before the evaporation (w=0.40).

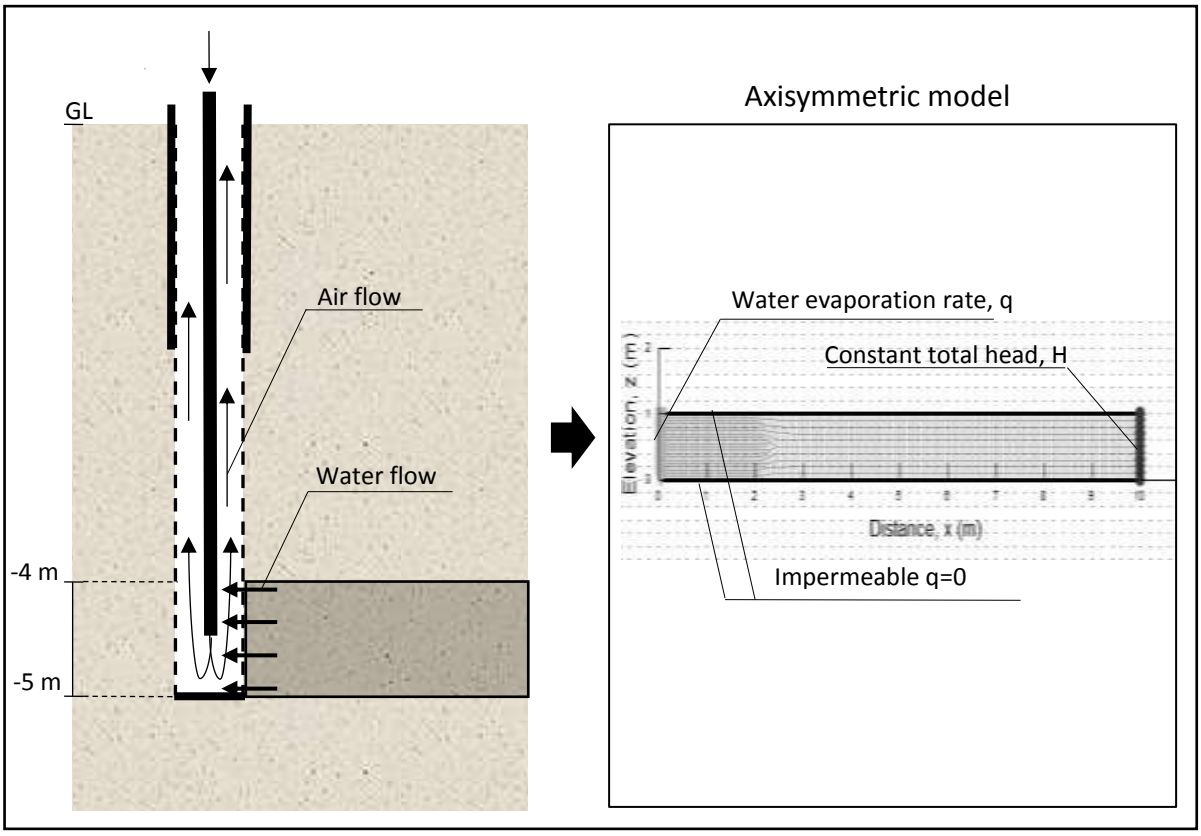

Figure 5-13: The axisymmetric model of the evaporation-induced water flow from borehole BH01

A numerical analysis was initially performed by using the laboratory value of hydraulic conductivity ($2.43\ 10^{-10}\ m/s$) and the ideal air velocity of 1.3 m/s derived by scaling the air flow times area. The values of water content derived numerically dramatically underestimated the values measured in the field. This was attributed to the uncertainty on the field hydraulic conductivity and air flow velocity at the bottom of the borehole.

A different strategy was therefore pursued. The hydraulic conductivity and air flow velocity was first back-calculated by matching experimental and numerical water content data. The back-calculated hydraulic conductivity was then benchmarked against the value derived in

the laboratory to verify whether the discrepancy fell in the range typically observed when comparing laboratory and field data. Similar approach was adopted for the air velocity.

The saturated hydraulic conductivity $k_{sat0} = 1.9x10^{-5} m/s$ and the water flow $q = 9x10^{-4}\ m/s$ were back-calculated. These are the values that provided reasonable matching between numerical and experimental water content at 5mBGL at distances of 0.3 m, 0.7 m and 1.5 m from the borehole BH01 after 1 day of evaporation.

These values are senseless. The hydraulic conductivity of the clay in the site is unlikely to be five orders of magnitude larger than the hydraulic conductivity in the laboratory. The back-calculated water evaporation rate q corresponds to an airflow with air velocity $v_{air} = 33000\ m/s$ if Equation (5.9) is used considering the relative humidity of the airflow RH=0% and the air temperature $T = 15℃$.

In conclusion, this first model was not representative at all of the evaporation-induced water content changes that occurred in the field during the 1 day of test.

5.7.2 Scenario of the horizontal natural suction drain

The cores from the boreholes were reviewed. Lenses of sand were noticed in the clay matrix of the soil samples. The scenario consisting of ‘natural’ horizontal suction drain made of continuous lenses of sands in the clay matrix was then investigated.

The schematic layout and the numerical model for this scenario are shown in Figure 5-14**Error! Reference source not found.**. The scenario of the horizontal natural suction drain assumes that the airflow from the end of the borehole BH01 does not circulate backward to the entry of the borehole. Instead, air flows through the lenses of sand in the clay at 5mBGL generating an effect equivalent to a horizontal suction drain.

This scenario is also supported by the fact that some air was found to flow out at ground level from one of the boreholes at 0.3 m from BH01 during the field. This suggests that the lenses of sand might have acted as channels for the air from borehole BH01, i.e. air flew backwards to the ground level when the lenses of sand were intercepted by the boreholes drilled for the soil sampling.

As a first approximation for the numerical model, it was assumed that only one horizontal lens of sand was present at 5mBGL and that no evaporation occurred from the inner surfaces of the borehole. The finite element model simulates a column of soil that is exposed to the evaporation from the lens of sand at 5mBGL (Figure 5-14). Since water flow generated by the 'infinite' sand lens occurs in vertical direction, the water flow problem reduced to a one-dimensional one.

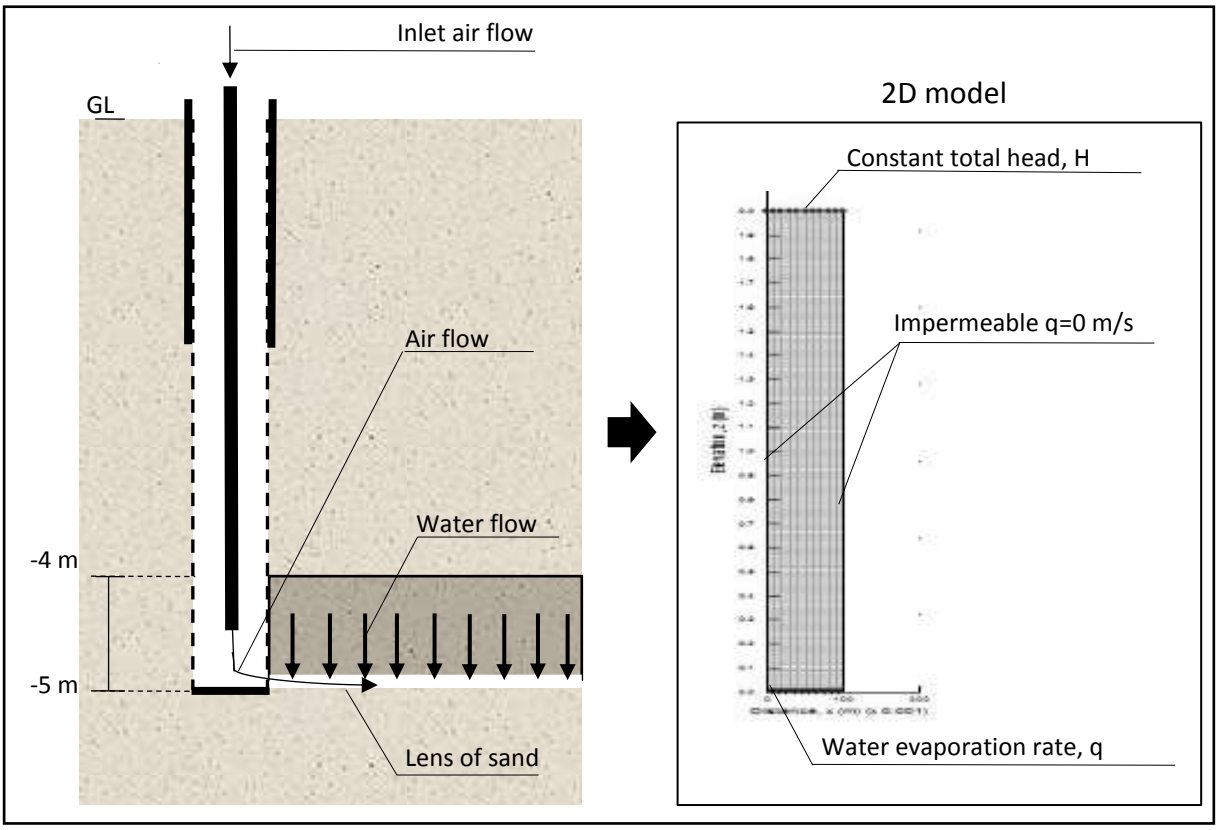

Figure 5-14: Schematic of the plain strain model for the natural horizontal suction drain and its boundary conditions

Constitutive functions were considered in terms of volumetric water content $\theta(u_w)$ and hydraulic conductivity k.

Initial conditions were specified in terms of pore water tension that enabled to have the initial numerical soil water content equal to the experimental soil water content before the evaporation (w=0.40). Boundary conditions included water evaporation rate $q=0\ m/s$ at the lateral surfaces of the model, constant total head H at the top surface of the model and the water evaporation rate q at the bottom surface of the model, as shown in Figure 5-14.

The saturated hydraulic conductivity in the site k_{sat0} and the water flow q at the evaporating surface were back-calculated from the comparison between numerical and experimental data. The saturated hydraulic conductivity in the field k_{sat0} equals to $3.9\text{x}10^{-8}$ m/s and the water flow q equals to $6\text{x}10^{-7}$ m/s allow a good agreement between the experimental and the numerical soil water content after 1 day of evaporation. The experimental and the numerical results are shown in Figure 5-15.

The back-calculated values of saturated hydraulic conductivity k_{sat0} and water evaporation rate q were reasonable. The saturated hydraulic conductivity of the soil in the field is two orders of magnitude larger than the hydraulic conductivity in the laboratory. Also, the water flow at the evaporating surface q corresponds to an airflow with air velocity $v_{air} = 21\ m/s$ considering the relative humidity of the airflow RH=0% and the air temperature $T = 15°\text{C}$ by means of Equation (5.9). This value of the air velocity is reasonable if considered that the air velocity measured at the inlet of the 22mm inner diameter air delivery tube inside the borehole was $\text{v}_{\text{air}} = 10$ m/s.

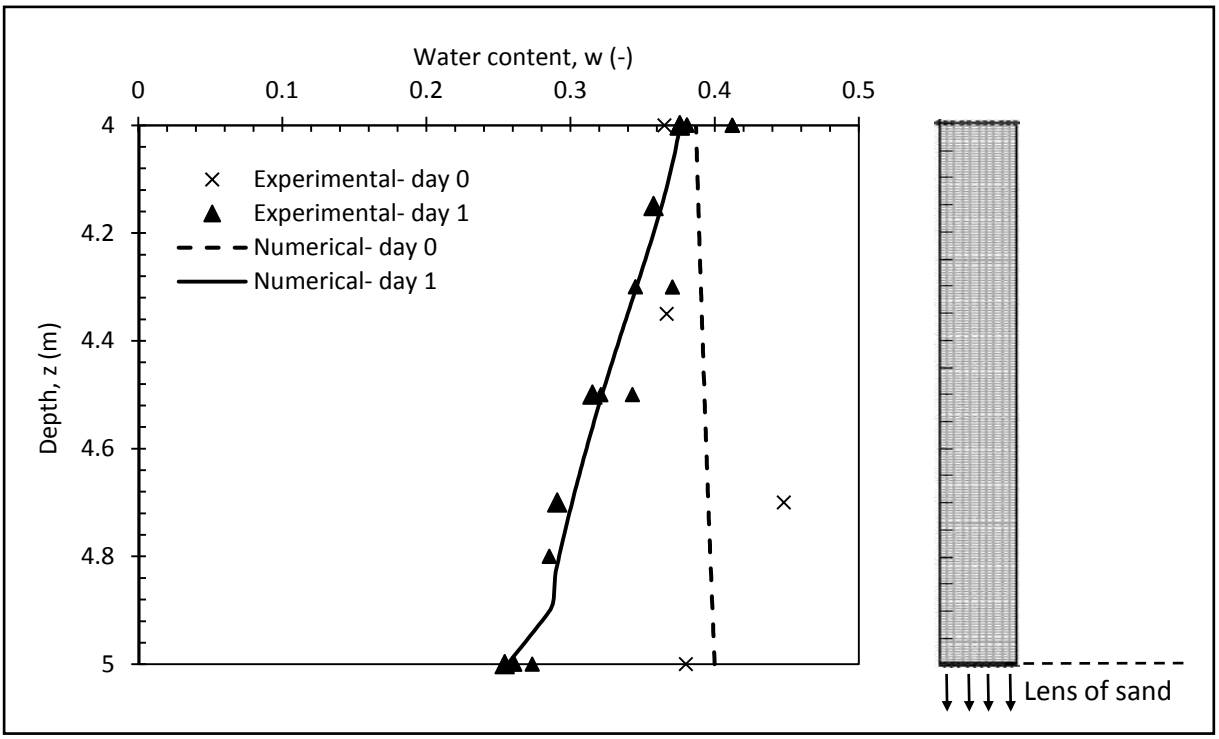

Figure 5-15: Numerical and experimental results in terms of soil water content, w versus depth, z.

5.8 Conclusions

This paper has presented the field trial of the suction drain. Based on the evaporation-induced suction, this innovative technique has been tested for the first time at the field scale. Air was injected to the bottom of a pre-drilled borehole and the water content of the soil around the borehole was measured.

It has been observed that the soil water content decreased significantly around the bottom of the borehole after 1 day of evaporation. No variation of the soil water content was detected at 1m from the bottom of the borehole and above.

The evaporation-induced water flow generated by the suction drain in the field was modelled via finite element analyses to validate the experimental results. The numerical model that considers the air flowing from the bottom to the entry of the borehole tangentially to the inner surface of the borehole failed to reproduce the experimental soil water content around the

borehole. A simplified numerical model that considers the airflow penetrating through lenses of sand at the bottom of the borehole provided a possible explanation to the values of water content measured experimentally.

The experimental results have therefore demonstrated the capability of the suction drain to reduce the soil water content via evaporation and, hence, to enhance soil undrained shear strength. The numerical results have suggested that soil fissures or lenses of sand should be taken into account in the design of the suction drain. The presence of soil fissures into the ground could enhance the potential of this technique in reducing the soil water content through natural horizontal suction drains.

6 CONCLUSION

The goal of this study was to investigate the capability of the suction drain in enhancing the undrained shear strength of clayey soils.

The objectives of this study were:

1. Understanding the evaporation-induced water flow that is generated by a tangential airflow in a confined space;
2. Testing and validating the suction drain at mock-up scale level;
3. Investigating the capability of the suction drain to reduce soil water content in real scale.

In response to the first objective, an apparatus was developed to measure water evaporation from a 3 m long wet surface subjected to a tangential airflow through a confined space. Tests have explored different air velocities (1m/s to 4m/s) and relative humidity at the inlet (RH=0% and RH=30%). Based on experimental result, a simple evaporation model was developed including the assumption that relative humidity and velocity of airflow are uniform in the confined space. The key parameter of the model is the vapour transfer coefficient α, which controls the linear dependency of the evaporation rate on the relative humidity differential between the wet surface and the airflow. The vapour transfer coefficient α was calibrated against the tests with relative humidity at the inlet RH_{inlet}=0% and this allowed probing the model against the tests with relative humidity at the inlet RH_{inlet}=30%. The model was found to perform satisfactorily showing that the simple assumption of uniform relative humidity and velocity does not represent a significant limitation of the model. The values of

vapour transfer coefficient derived from the empirical relationship derived by Penman (1948, 1956) for open water was benchmarked against the values derived experimentally for confined airflow. The good matching between the two sets of values indicates that Penman's relationship can be used successfully for a first estimation of the vapour transfer coefficient for confined airflow.

With reference to the second objective of this study, a mock-up scale test of the suction drain was carried out. A borehole was drilled on a block sample and air was injected to the bottom of the borehole. Airflow circulated from the bottom to the top of the borehole tangentially to the inner surface of the borehole. Experimental results show that the water content of the soil around the borehole decreases significantly. This demonstrates the capacity of the tangential airflow to remove water via evaporation from the soil. The numerical modelling of the mock-up scale test show a good agreement between the numerical and the experimental results. This validates the numerical model as a tool for designing the suction drain. A numerical analysis that simulates the suction drain in an ideal case study of tunnelling demonstrates that the decrease of soil water content detected experimentally provides a relevant enhancement of the undrained shear strength of the soil, hence of the tunnel face stability.

Ultimately, a field trial of the suction drain was carried out in a silty clay deposit in Newton (Scotland). A borehole was drilled into a silty clay deposit and air was injected to the bottom of the borehole. Soil water content was measured around the borehole over time and distance. It has been observed that the soil water content decreased significantly around the bottom of the borehole after 1 day of evaporation. However, no variation of the soil water content has been detected at 1 m from the bottom of the borehole and above. The evaporation-induced water flow generated by the suction drain in the site has been modelled via finite element analyses to validate the experimental results. The numerical model that considers the

air flowing from the bottom to the entry of the borehole tangentially to the inner surface of the borehole has failed to reproduce the experimental soil water content around the borehole. A simplified numerical model that considers the airflow penetrating through the lenses of sand at the bottom of the borehole provides a possible explanation to the experimental results. In conclusion, the experimental results have demonstrated the capability of the suction drain to reduce the soil water content via the evaporation and, hence, to enhance the soil undrained shear strength. However the numerical results have suggested that soil fissures or lenses of sand should be taken into account in the design of the suction drain. The presence of soil fissures into the ground could enhance the potential of this technique in reducing the soil water content through natural horizontal suction drains.

In conclusion, this study allows the suction drain to be a viable technique for ground improvement that enables the enhancement of the undrained shear strength of clayey soils without using expensive equipment and without leaving spoils into the ground after its application.

Future works

Based on the findings of this study, additional experimental investigations of the suction drain in the field should be carried out and the design of the suction should be reviewed. A potential modification of the technology of the suction drain may include the installation of packers at different depths. Packers will have the role to confine the area of the ground that is exposed to the evaporation. In this case airflow will not circulate from the bottom to the top of the borehole, but air will be injected into the ground in a similar way as jet grouting does with cement.

The serviceability of the suction drain has to be verified against the cracking behaviour of cohesive material. In the shrinkage range of the cohesive material, similar condition to the one tested are expected, and hence similar responses. Meanwhile, when value of suction exceeds the air entry value the cracking behaviour of the clayey material might affect the efficiency of the suction drain, thus further research is needed.

Finally, a detailed analysis of the carbon footprint of the suction drain and the comparison with the carbon footprint of the techniques currently used fr ground improvement should be undertaken in further research.

7 REFERENCES

Anagnostou, G., & Kovari, K. (1996). Face Stability Conditions with Earth-Pressure-Balanced Shields. *Tunnelling and Underground Space Technology*, *11*(2), 165–173.

Baroghel-Bouny, V., Mainguy, M. & Coussy, O. (2001). Isothermal drying process in weakly permeable cementitious materials - Assessment of water permeability. Materials Science of Concrete Special Volume: Ion and Mass Transport in Cement-Based Materials, pp. 59-80.

Broms, B. B., & Bennermark, H. (1967). Stability of clay at vertical openings. *Journal of Soil Mechanics & Foundations Div* .

Brutsaert, W. (1982). *Evaporation into the atmosphere: theory, history and applications.* Springer Science & Business Media.

Butcher, A. P., Mcelmeel, K., & Powell, J. J. M. (1995). Dynamic probing and its use in clay soils. In *Proc Int Conf on Advances in Site Investigation Practice. ICE London, March 1995. Thomas Telford. pp 383-395.*

Chandavari, V., & Palekar, S. (2014). Diffuser angle control to avoid flow separation. *Int. J. Tech. Res. Appl, 2(5), 16-21*.

Chapman, D. N., Metje, N., & Stark, A. (2017). *Introduction to tunnel construction* (Crc Press).

Chapuis, R. P., & Aubertin, M. (2003). On the use of the Kozeny – Carman equation to predict the hydraulic conductivity of soils. *Canadian Geotechnical Journal, 40(3), 616-628*.

Chu, C. R., Li, M. H., Chen, Y. Y., & Kuo, Y. H. (2010). A wind tunnel experiment on the evaporation rate of Class A evaporation pan. *Journal of Hydrology, 381(3-4), 221-224.*

Comtebellot, G. (1976). Hot-Wire Anemometry. *Annual Review of Fluid Mechanics*, *8*(Thomas 1920), 209–231.

Coussy, O. (2004). *Poromechanics*. (West Sussex: Wiley, Ed.).

Cristelo, N., Miranda, T., Oliveira, D. V, Rosa, I., Soares, E., Coelho, P., & Fernandes, L. (2015). Assessing the production of jet mix columns using alkali activated waste based on mechanical and fi nancial performance and CO 2 (eq) emissions. *Journal of Cleaner Production*, *102*, 447–460.

Daniel, E. (1984). Predicting hydraulic conductivity of clay liners. *Journal of Geotechnical Engineering, 110(2), 285-300*.

Davis, E., Gunn, M., Mair, R., & Seneviratine, H. (1980). The stability of shallow tunnels and underground openings in cohesive material. *Geotechnique*, (4).

DD Langton. (1999). The Panda lightweight penetrometer for soil investigation and monitoring material compaction. *Ground Engineering*.

de Métrologie Légale, O. I. (1996). The scale of relative humidity of air certified against saturated salt solutions. *International Recommendation, OIML*.

Decagon Devices. (2014). WP4C Dew point Potentiameter-Operator's Manual.

F. A. M. Marinho Æ W. A. Take Æ A. Tarantino. (2008). Tensiometric and axis translation techniques for suction measurement. *Geotechnical and Geological Engineering, 26(6),*

Pp. 615-631.

Fredlund, D. G., Rahardjo, H., & Rahardjo, H. (1993). *Soil mechanics for unsaturated soils*. (John Wiley & Sons, Ed.).

Greenspan, L. (1977). Humidity fixed points of binary saturated aqueous solutions. *Journal of Research of the National Bureau of Standards Section A: Physics and Chemistry*, *81*(1), 89–96.

Leca, E., & Dormieux, L. (1990). Upper and lower bound solutions for the face stability of shallow circular tunnels in frictional material. *Geotechnique, 40(4), 581-606.*

Leca, E., & New, B. (2007). Settlements induced by tunneling in Soft Ground. *Tunnelling and Underground Space Technology*, *22*(2), 119–149.

Leighly, J. (1937). A Note on Evaporation. *Ecology*, *18*(2), 180–198.

Lim, W. H., Roderick, M. L., Hobbins, M. T., Wong, S. C., Groeneveld, P. J., Sun, F., & Farquhar, G. D. (2012). The aerodynamics of pan evaporation. *Agricultural and Forest Meteorology, 152, 31-43.*

Lu, N., & Likos, W. J. (2004). *Unsaturated soil mechanics*. (Wiley, Ed.).

Mair, R. J. (1978). Centrifuge model testing of tunnel construction in soft ground. In *In Proceedings of the Conference on Tunnels and Underground Structures* (p. (pp. 267-310)). Taiwan.

Mair, R. J., & Taylor, R. N. (1997). Theme lecture: Bored tunnelling in the urban environment. In *Theme lecture: Bored tunnelling in the urban environment*. In: Publication Committee

of XIV ICSMFE (Eds.), Proceedings of the 14th International Conference on Soil Mechanics & Foundation Engineering, Taylor and Francis,Hamburg, pp. 2353–2385.

Martini, M., & Tarantino, A. (2019). Evaporation-induced soil water flux to design suction drain for low-carbon ground stabilisation. *Tunnelling and Underground Space Technology.*, (Manuscript submitted for publication-copy on file with author).

Martini, M., Tarantino, A., & Sloan, A. (2019). Suction drain as a low-carbon ground improvement technique: proof-of-concept at the laboratory scale. *(Paper Submitted to Tunnelling and Underground Space Technology).*

Mitchell, J. K. (1993). *Fundamentals of Soil Behavior.* (N. Y. W. Inter-Science, Ed.).

Mitchell, J. K., & Soga, K. (2005). *Fundamentals of soil behavior*. (New York: John Wiley & Sons, Ed.) (Vol. 3).

Monteith, J. L. (1965). Evaporation and environment. In *In Symp. Soc. Exp. Biol (Vol. 19, No. 205-23, p. 4).*

Moseley, M. P., & Kirsch, K. (2004). *Ground improvement*. CRC Press.

Omega Engineering. (2018). User's Guide FMA1000 SERIES.

Peck, R. B. (1969). Deep excavations and tunneling in soft ground. In *Proc. 7th ICSMFE, 1969 , 225- 290.* (p. 1969).

Penman, H. L. (1948). Natural evaporation from open water, bare soil and grass. *Proc. R. Soc. Lond. A, 193(1032), 120-145*.

Penman, H. L. (1956). Estimating Evaporation. *Eos, Transactions American Geophysical*

Union, 37(1), 43-50.

Simpson, L. (2017). *Experimental Study of Induced Evaporation via the Suction Drain in Clayey Soils to Provide Tunnel Face Stability*. University of Strathclyde.

Tarantino, A., Sacchet, A., Dal Maschio, R. & Francescon, F. (2010). A Hydromechanical Approach to Model Shrinkage of Air-Dried Green Bodies. *Journal of the American Ceramic Society, 93, No. 3, 662–670.*

Tarantino, A. (n.d.). Energy limited (potential) and water limited evaporation regimes in unsaturated soils: theoretical approach and strategies for numerical modelling. *Unpublished (in Prep).*

Tarantino, A. (2004). Direct measurement of soil water tension. *Proceedings 3rd International Conference on Unsaturated Soils, Pp. 1005-1017*.

Tarantino, A. (2009). A water retention model for deformable soils. *Géotechnique, 59, No. 9, 751-762.*

Tarantino, A., & Mongiovì, L. (2002). Design and construction of a tensiometer for direct measurement of matric suction. *Proceedings 3rd International Conference on Unsaturated Soils, Pp. 319-324.*

Thom, A. S., & Oliver, H. R. (1977). On Penman's equation for estimating regional evaporation. *Quarterly Journal of the Royal Meteorological Society, 103(436), 345-357*.

Thornthwaite, C. W., & Holzman, B. (1939). The determination of evaporation from land and water surfaces. *Monthly Weather Review, 67*, 4–11.

Trombetti, F., & Tagliazucca, M. (1994). Characteristic scales of atmospheric surface layer. *Technical Paper No. 4, FISBAT-TP-94/1, Istituto FISBAT-C.N.R. Bologna, Italy*, (4), 1994.

Van Genuchten, M. T. (1980). A Closed-form Equation for Predicting the Hydraulic Conductivity of Unsaturated Soils. *Soil Science Society of America Journal, Issue 44, Pp. 892-898*, 892–898.

Whittaker, B. N., & Frith, R. C. (1990). *Tunnelling: design, stability and construction*.

Winston, P. W., & Bates, D. H. (1960). Saturated Solutions For the Control of Humidity in Biological Research. *Ecology, 41(1), 232-237*.

Wood, A. M. (2002). *Tunnelling: management by design* (CRC Press).

Wroth, C. P., & Wood, D. M. (1978). The correlation of index properties with some basic engineering properties of soils. *Canadian Geotechnical Journal, 15(2): 137–145.*

Xanthakos, P. P., Abramson, L. W., & Bruce, D. A. (1994). *Ground control and improvement*. John Wiley & Sons.

Yang, W.; Lunn, R.; Tarantino, A. (2015). MEMS sensor-based monitoring system for engineered geological disposal facilities. *Mineralogical Magazine, November Vol. 79(6), Pp. 1475–1483*.

8 LIST OF CAPTIONS FOR FIGURES

Figure 2-1: Example of divided tunnel face using sprayed concrete linings (Mair & Taylor, 1997) 13
Figure 2-2: Ground treatment and prelining technique (Mair & Taylor, 1997) 14
Figure 2-3: Principle of the slurry shield machine (Mair & Taylor, 1997) 15
Figure 2-4: Principle of the earth pressure balance machine (Mair & Taylor, 1997) 15
Figure 2-5: Ground freezing from within the tunnel (after Chapman et al., 2017) 18
Figure 2-6: Tunnel heading in soft ground (Mair, Taylor 1997) 23
Figure 2-7: Face collapse: basic diagram in cohesive ground soils (Leca & New, 2007) 23
Figure 2-8: Observed failure mechanism based on centrifuge model test (Mair,1978) 24
Figure 2-9: Primary mode: basic transverse cross section (Leca & New, 2007) 25
Figure 2-10: Secondary mode: basic transverse cross section (Leca & New, 2007) 25
Figure 2-11: Three dimension settlement through 26
Figure 2-12: Stability parameters (Leca & New, 2007) 27
Figure 2-13: Critical stability ratio Nc (Mair & Taylor, 1997) 28
Figure 2-14: The plane strain unlined circular tunnel (Davis et al., 1980) 29
Figure 2-15: The plane strain tunnel heading (Davis et al., 1980) 30
Figure 2-16: The circular tunnel heading (Davis et al., 1980) 30
Figure 2-17: Upper bound mechanism for the plane strain heading (Davis et al,1980) 31
Figure 2-18: Upper bound stability solution for plane strain heading (Davis et al., 1980) 32
Figure 2-19: Local collapse for plane strain tunnel heading (Davis et al,1980) 33
Figure 2-20: Schematic of the sublayers of the atmospheric boundary layer ABL (Brutsaert, 1982) 36
Figure 2-21. Logarithmic profile of the air velocity in the proximity of a smooth surface and a rough surface... 39
Figure 2-22: The mass fluxes at the interface soil-atmosphere 46
Figure 2-23: The energy fluxes at the interface soil-atmosphere 47
Figure 2-24. Comparison between different relationships used to estimate the aerodynamic resistance r_a. 54
Figure 3-1: Concept of the suction drain (not in scale) 57
Figure 3-2: Layout of the long evaporation machine (not in scale) 58

Figure 3-3: Layout of the short evaporation machine (not in scale) 60
Figure 3-4: Typical calibration curve of the RH/T sensor 63
Figure 3-5: Calibration curve of the anemometer 65
Figure 3-6: Calibration curves of the balances 67
Figure 3-7: Layout of the air injection system (not in scale) 69
Figure 3-8: Air velocity recorded via the anemometer during the tests 74
Figure 3-9: RH of the airflow at the inlet of the upper air channel recorded by the sensor 'O' during the tests with RH_{inlet}=30% 75
Figure 3-10: Temperature of the airflow at the inlet of the upper air channel recorded by the sensor 'O' during the tests with RH_{inlet}=30% 76
Figure 3-11: Typical reading of the relative humidity of the airflow during the test with RH_{inlet}=30% and v_{air}=1m/s 78
Figure 3-12: Steady state phase of the test with RH_{inlet}=30% and v_{air}=1m/s 79
Figure 3-13: Relative humidity of the airflow measured via the RH/T sensors along the upper air channel-comparison for tests with the airflow at the same RH_{inlet} and different air velocity. 81
Figure 3-14: Relative humidity of the airflow measured via the RH/T sensors along the upper air channel-comparison for tests with the airflow at the same air velocity and different RH_{inlet} 82
Figure 3-15: Temperature of the airflow measured via the RH/T sensors during the tests at varies air velocities and RH_{inlet} =0% and RH_{inlet} =30% 83
Figure 3-16: Experimental evaporation rate of water versus air velocity in the tests with RHinlet=0% and RHinlet=30% 84
Figure 3-17: Loss of mass of water per unit area from the saturated soil sample over time 85
Figure 3-18: Graphical representation of the mass balance in the long evaporation machine for detecting the vapour transfer coefficient α 86
Figure 3-19: Uniform RH and velocity profile of the airflow in the upper air channel assumed in the model 89
Figure 3-20: Comparison of the evaporation rate of water estimated via the model and obtained experimentally92
Figure 3-21: Evaporation rate of water from the saturated soil sample and from the water surface in tests with airflow at v_{air}=4m/s and RH_{inlet}=0% 93
Figure 3-22: Comparison between α-Penman and α-Experimental 96
Figure 3-23: Air velocity profile 97
Figure 3-24: Relative humidity of the airflow measured experimentally, estimated via α-model and estimated via α-Penman for v_{air}=2m/s. 99
Figure 4-1: Concept of the suction drain (not in scale) 105

Figure 4-2: Water retention behaviour of the soil material used for the mock-up scale test 111
Figure 4-3: Hydraulic conductivity model of the soil material used for the mock-up scale test 112
Figure 4-4: Compressibility curve of the soil and indication of the loading steps where the permeability tests were carried out 113
Figure 4-5: Saturated hydraulic conductivity of the soil material used for the mock-up scale test 114
Figure 4-6: Experimental set-up and model for detecting the boundary condition in terms of water flow per unit area and unit time, q (m/s) 115
Figure 4-7: Experimental vapour transfer coefficient, α versus the velocity of the airflow, v_{air} 117
Figure 4-8: Schematic layout of the mock-up scale test 118
Figure 4-9: Schematic layout of the soil sampling in the mock-up scale test for monitoring the soil water content 120
Figure 4-10: Experimental soil water content in the mock-up scale test: a) at 35mm from the central borehole; b) at 70mm from the central borehole 122
Figure 4-11: Numerical modelling for the validation of the mock-up scale test (axisymmetric conditions) 127
Figure 4-12: Comparison between the experimental and the numerical soil water content, w versus time, t 128
Figure 4-13: Numerical model of the suction drain in tunnelling 129
Figure 4-14: 1D finite element mesh and boundary conditions of the numerical model 130
Figure 4-15: Distribution of the suction, s versus distance from the borehole, z at different time steps 132
Figure 4-16: Distribution of the soil water content, w versus distance from the borehole, z at different time steps 132
Figure 4-17: Distribution of the soil undrained shear strength, Cu versus the distance from the borehole, z at different time steps 134
Figure 4-18: Average undrained shear strength of the overburden, Cu_av versus time, t 135
Figure 4-19: Stability factor, N versus the time of evaporation from the suction drain, t 135
Figure 5-1: Application of the suction drain for temporary soil stabilisation in tunnelling 138
Figure 5-2: Particle size distribution of the soil at the site 141
Figure 5-3: Results of one-dimensional compression tests in terms of void ratio e versus vertical effective stress σ'v of the soil in situ 142
Figure 5-4: Water retention behaviour of the soil in situ 148
Figure 5-5: Hydraulic conductivity curve of the soil in the site 149
Figure 5-6: Saturated hydraulic conductivity 151
Figure 5-7: The suction drain cage and its installation in the site 153
Figure 5-8: Mapping of data sampling 156

Figure 5-9: Relative humidity and temperature of the airflow inside the borehole BH01 measured via the RH/T sensors from the start of the evaporation versus the time, t 159
Figure 5-10: Dynamic cone resistance of the soil in situ, qd versus depth, z measured via the Panda test at different days of evaporation 162
Figure 5-11: Gravimetric water content, w of the soil at 0.3m from the central borehole BH0 versus depth z at different days of evaporation 165
Figure 5-12: Gravimetric water content, w of the soil between 4mBGL and 5mBGL measured at 0.3m, 0.7m and 1.5m from the borehole BH01 at day 1 of evaporation. 166
Figure 5-13: The axisymmetric model of the evaporation-induced water flow from borehole BH01 171
Figure 5-14: Schematic of the plain strain model for the natural horizontal suction drain and its boundary conditions 173
Figure 5-15: Numerical and experimental results in terms of soil water content, w versus depth, z. 175
Figure 10-1: Calibration curves of RH sensors 196
Figure 10-2: Relative humidity of the airflow at the inlet of the upper air channel recorded by the sensor 'O' during the tests with RHinlet=0% 196
Figure 10-3: Temperature of the airflow at the inlet of the upper air channel recorded by the sensor 'O' during the tests with RHinlet=0% 197
Figure 10-4: Mass reading from the balances during the tests with RHinlet=0% 198
Figure 10-5: Mass reading from the balances during the tests with RHinlet=30% 200
Figure 10-6: Relative humidity of the airflow measured by each RH/T sensor during the test with RH inlet=30% 201
Figure 10-7: Temperature of the airflow measured by each RH/T sensor during the test with RH inlet=30% .. 203
Figure 10-8: Steady state of the tests with RHinlet=30% (in terms of relative humidity) 204
Figure 10-9: Steady state of the test with RHinlet=30% (in terms of temperature) 206
Figure 10-10: Relative humidity of the airflow measured by each RH/T sensor during the test with RH inlet=0% 208
Figure 10-11: Temperature of the airflow measured by each RH/T sensor during the test with RH inlet=0% .. 210
Figure 10-12: Steady state of the test with RHinlet=0% (in terms of relative humidity) 212
Figure 10-13: Steady state of the test with RHinlet=0% (in terms of temperature) 214
Figure 10-14: Comparison of relative humidity of the airflows with equal air velocity and different RHinlet along the upper air channel 215
Figure 10-15: Comparison of temperature of the airflows with equal air velocity and different RHinlet along the upper air channel. 217

Figure 10-16: Comparison of the relative humidity of the airflow measured experimentally, estimated via α-calibration and estimated via α-Penman for v_air=1m/s 218
Figure 10-17: Comparison of the relative humidity of the airflow measured experimentally, estimated via α-calibration and estimated via α-Penman for v_air=3m/s 219
Figure 10-18: Comparison of the relative humidity of the airflow measured experimentally, estimated via α-model and estimated via α-Penman for v_air=4m/s 220

9 LIST OF CAPTIONS FOR TABLES

Table 2-1:Values of the surface roughness length z0 for different types of surface (after (Trombetti & Tagliazucca, 1994) 40
Table 3-1: Manufacturer's specification of the RH/T sensors 61
Table 3-2: The saturated salt solution and its standard relative humidity value for the calibration of humidity sensors at 20°C 62
Table 3-3: Specification of the anemometer 64
Table 3-4: Specifications of the test procedure in the long evaporation machine 70
Table 3-5: Parameters of the model 90
Table 3-6: Values of the vapour transfer coefficients derived from calibration 91
Table 4-1: Parameters for the water retention behaviour 109
Table 4-2: Specification of the anemometer 119
Table 4-3: Parameters for Psychrometric Law 126
Table 5-1: Parameters for the water retention behaviour 146
Table 5-2: Manufacturer's specification of the RH/T sensors 152
Table 5-3: Specification of the anemometer 154

10 APPENDIX A.1- EXPERIMENTAL INVESTIGATION OF THE EVAPORATION-INDUCED SOIL WATER FLUX

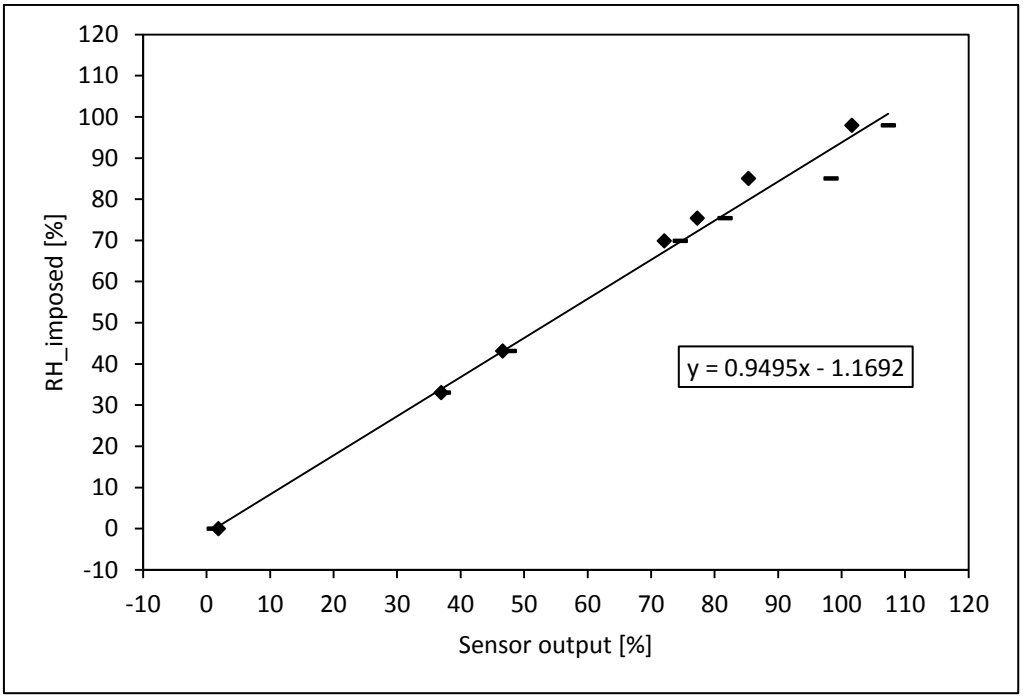

Sensor O

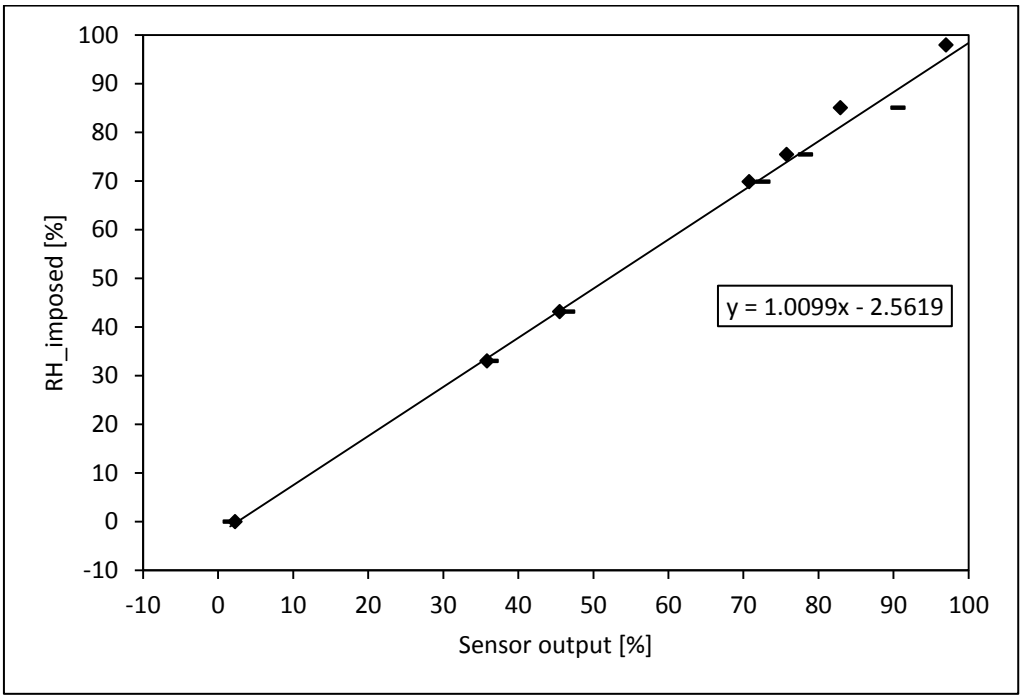

Sensor S

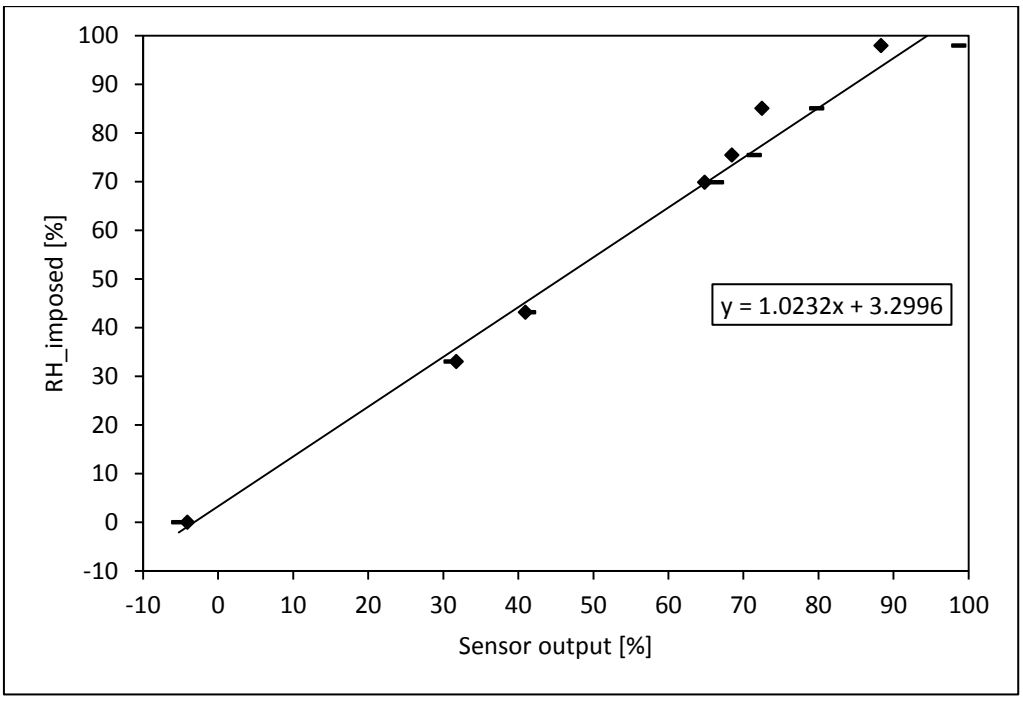

Sensor D

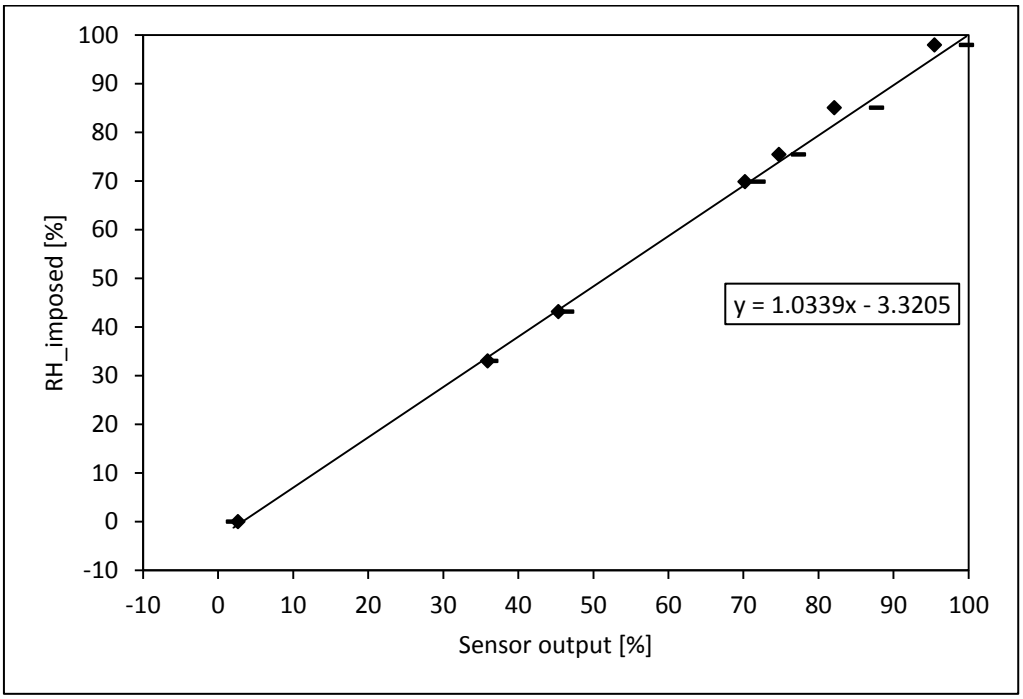

Sensor Q

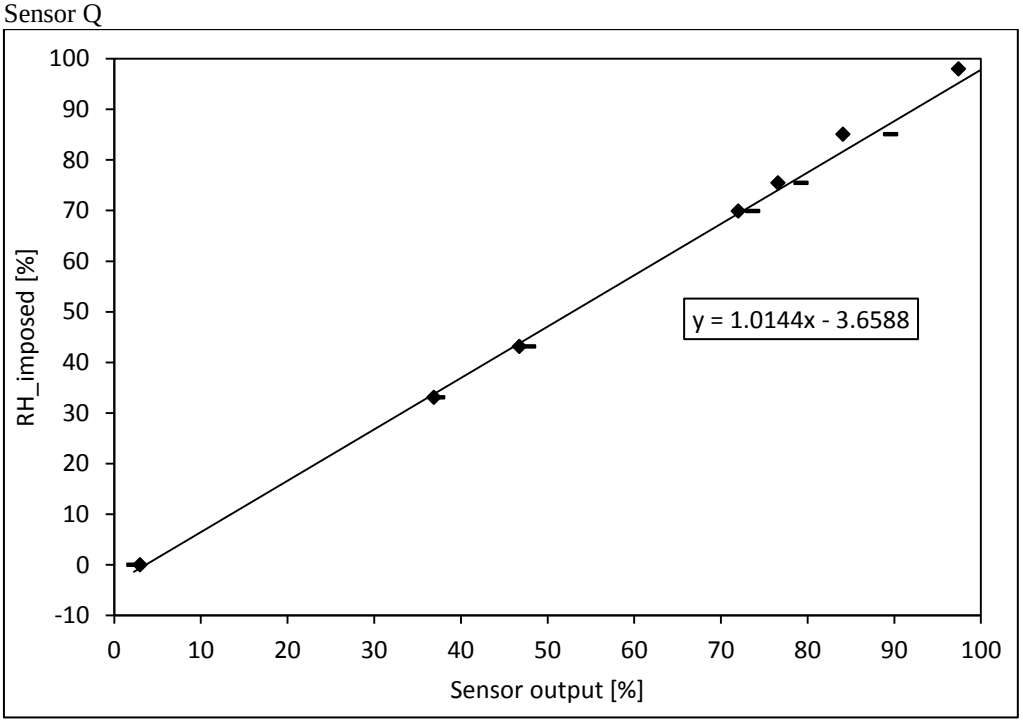

Sensor T

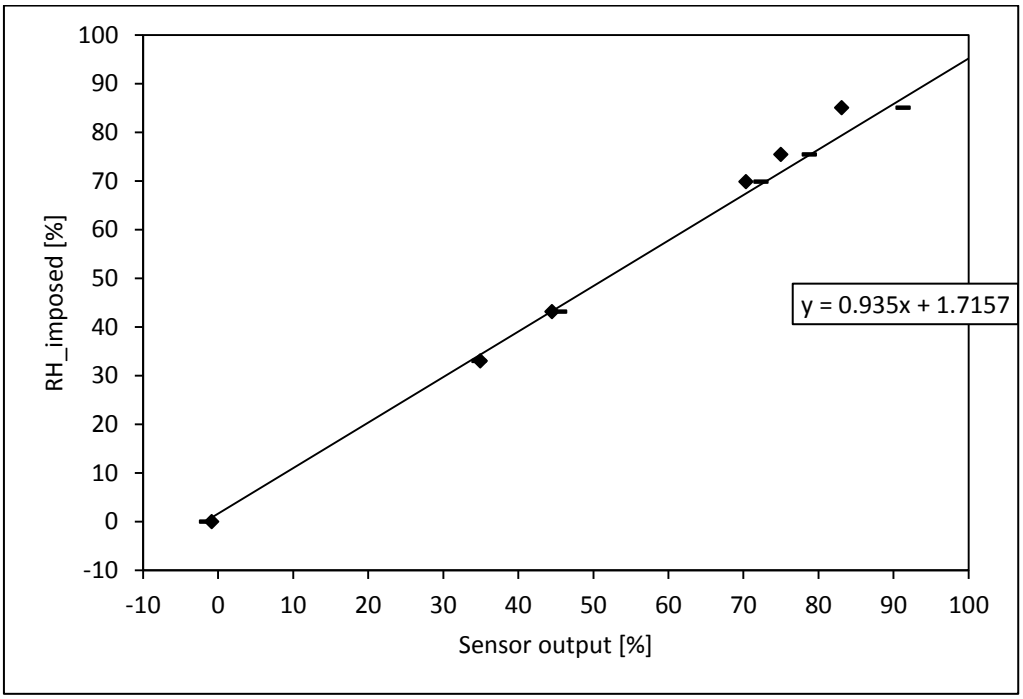

Sensor P

Figure 10-1: Calibration curves of RH sensors

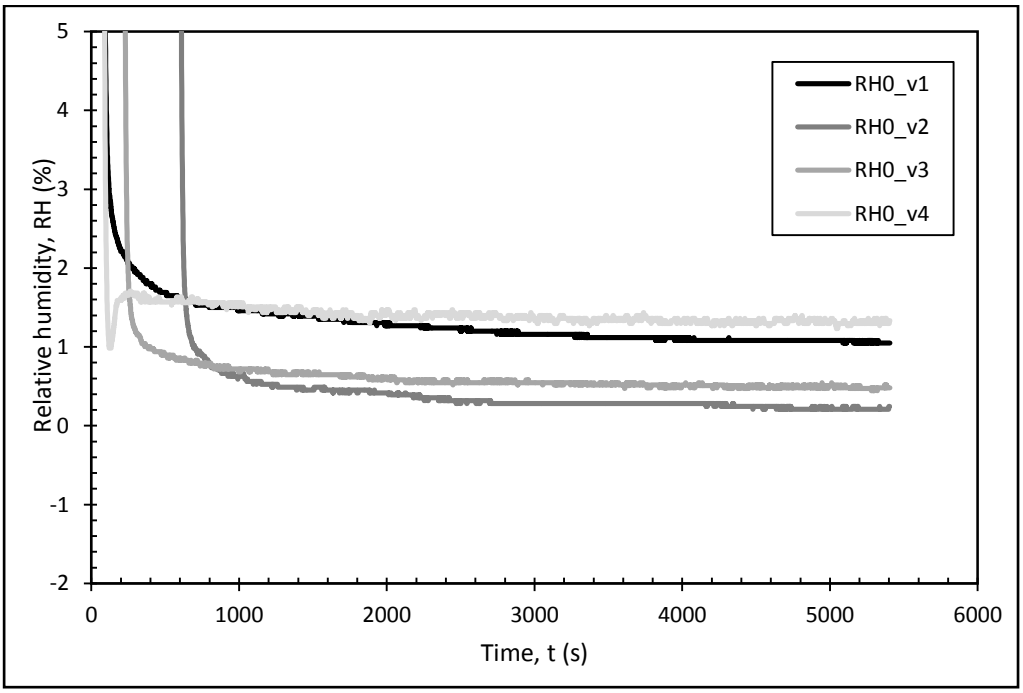

Figure 10-2: Relative humidity of the airflow at the inlet of the upper air channel recorded by the sensor 'O' during the tests with RHinlet=0%

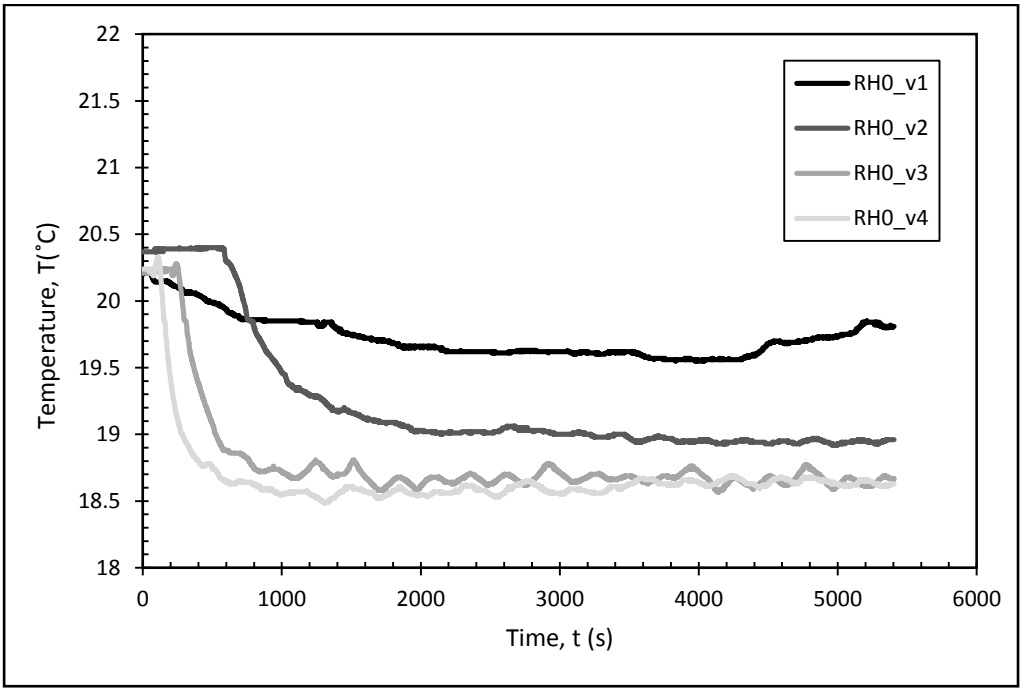

Figure 10-3: Temperature of the airflow at the inlet of the upper air channel recorded by the sensor 'O' during the tests with RHinlet=0%

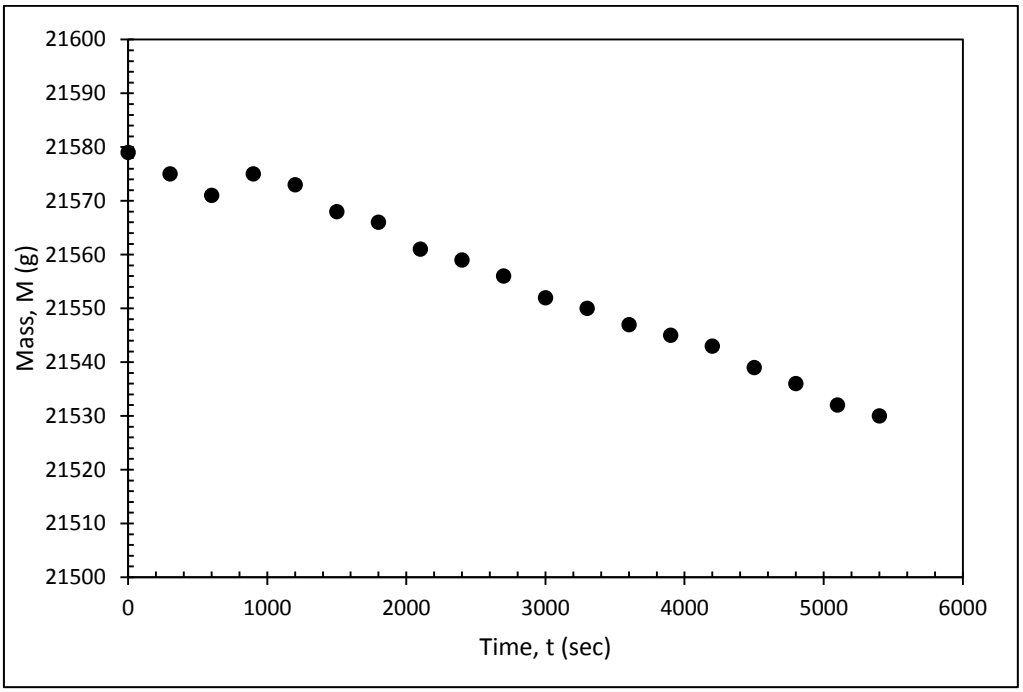

RH0 _v2

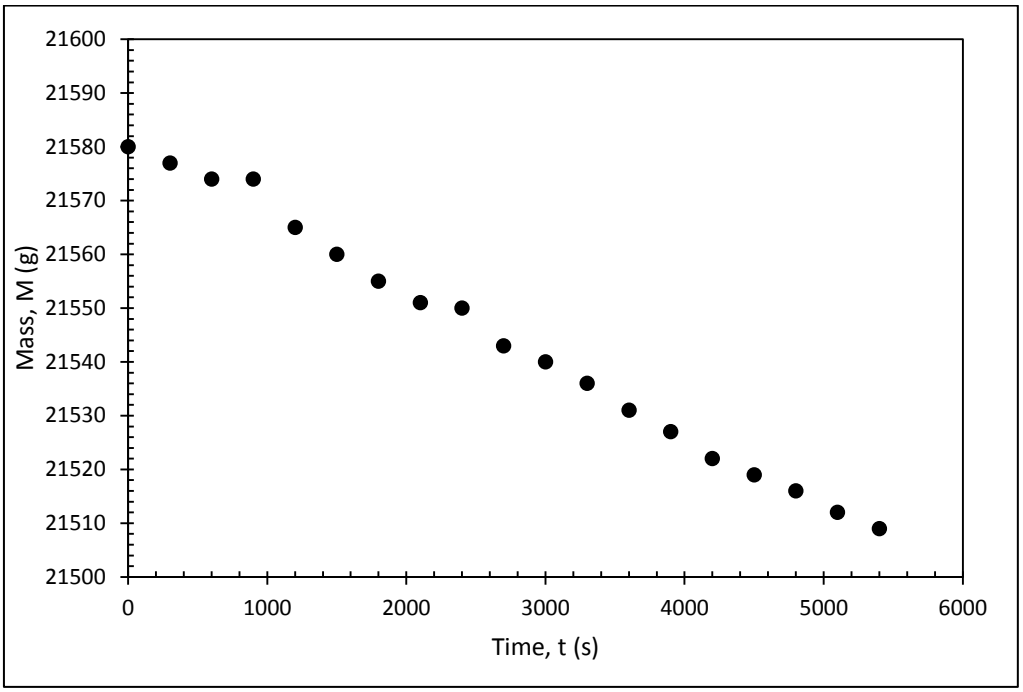

RH0_v3

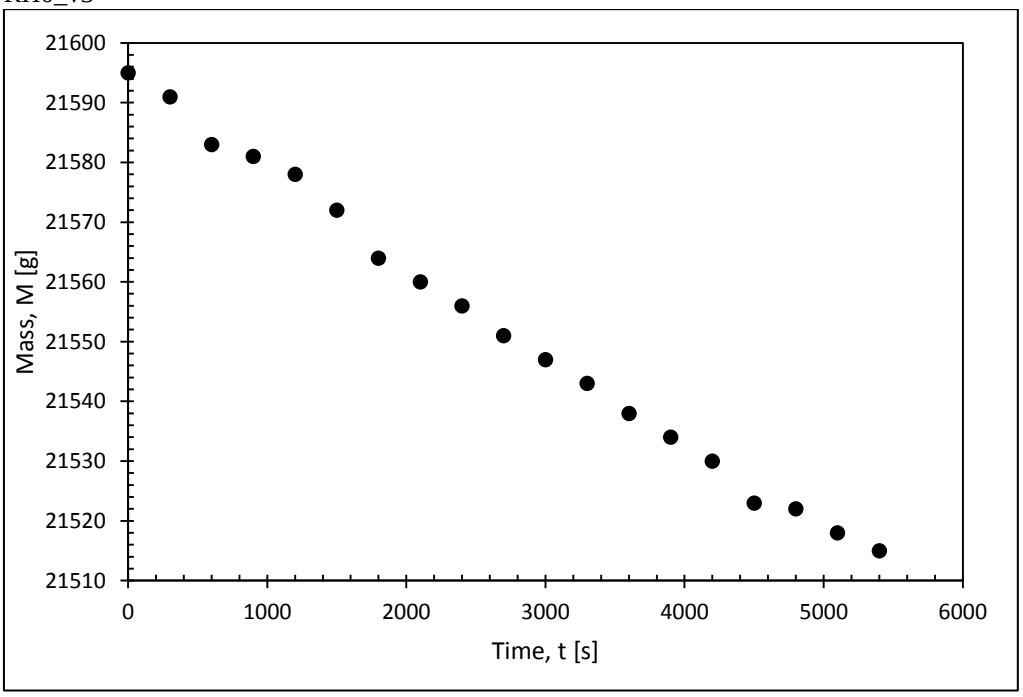

RH0_v4

Figure 10-4: Mass reading from the balances during the tests with RHinlet=0%

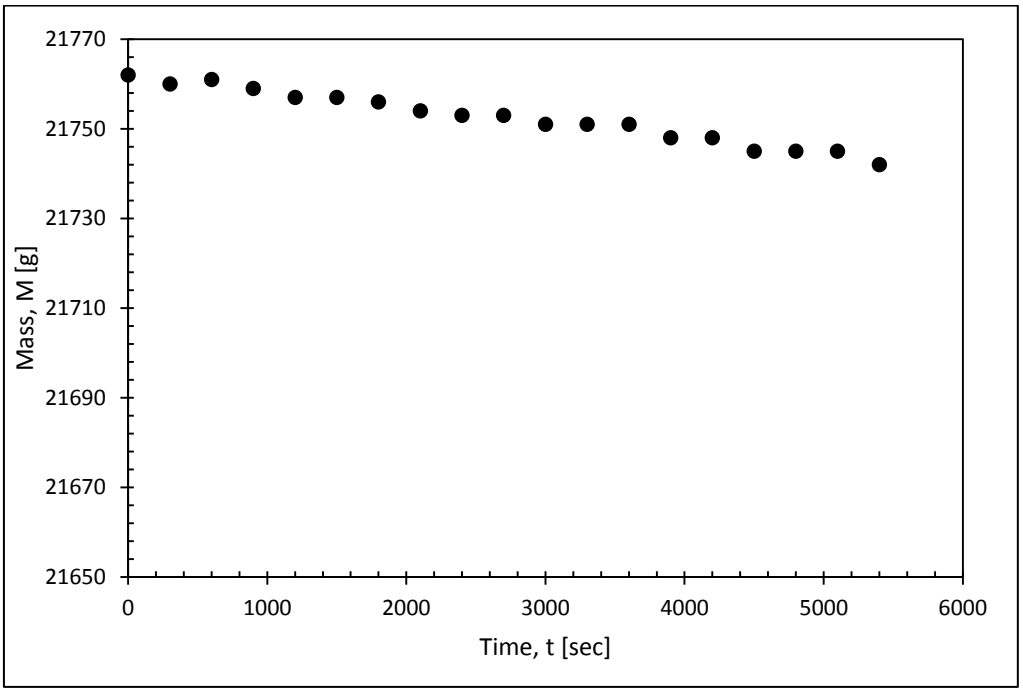

RH30_v2

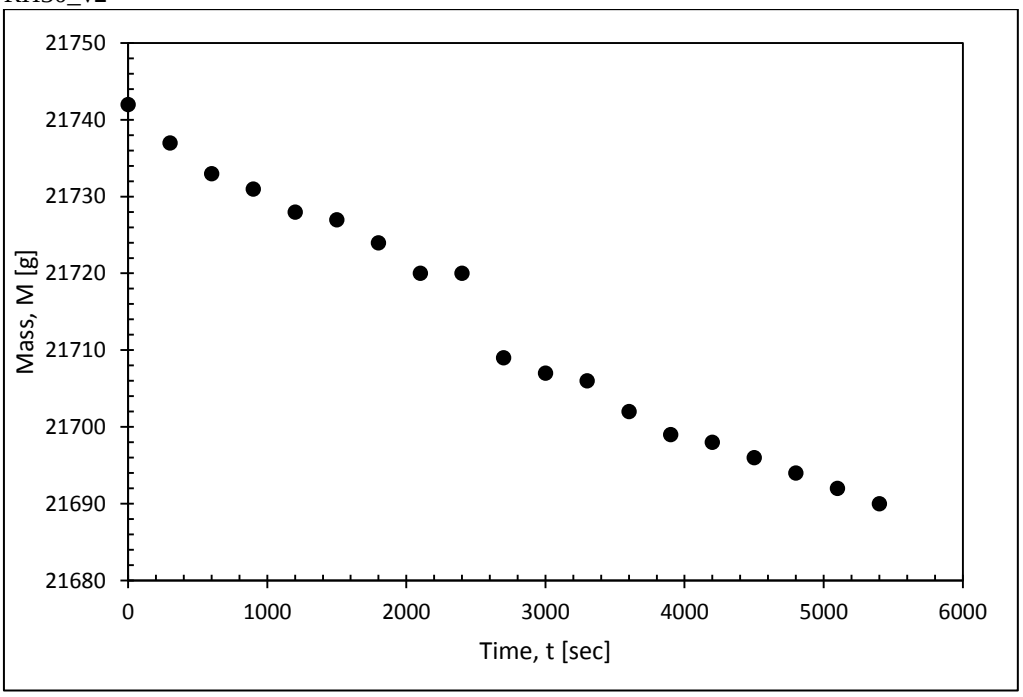

RH30_v3

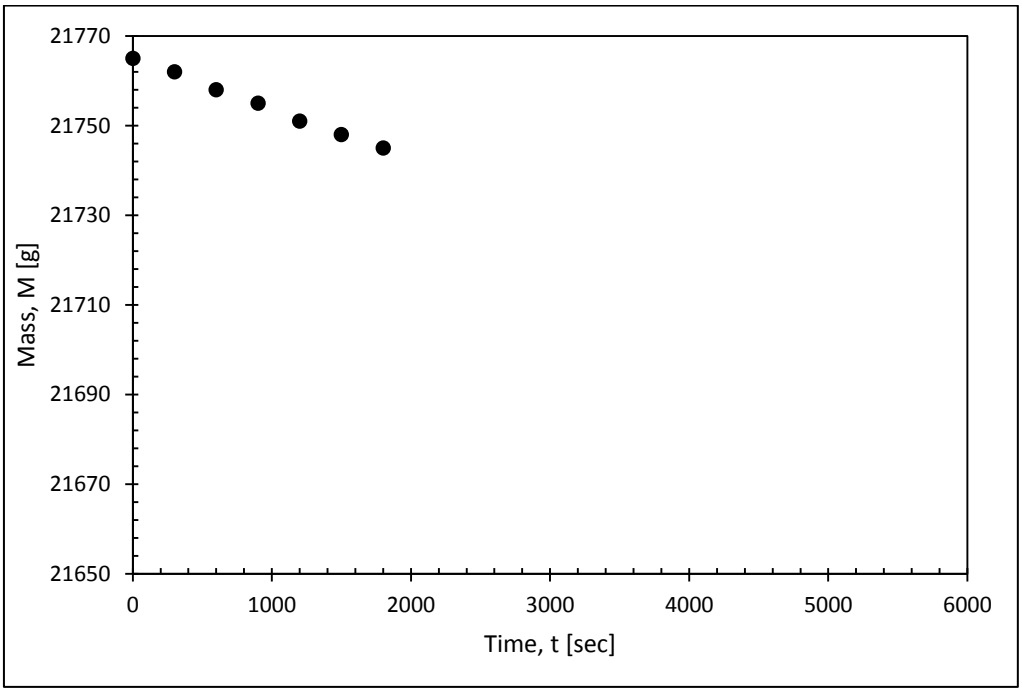

RH30_v4

Figure 10-5: Mass reading from the balances during the tests with RHinlet=30%

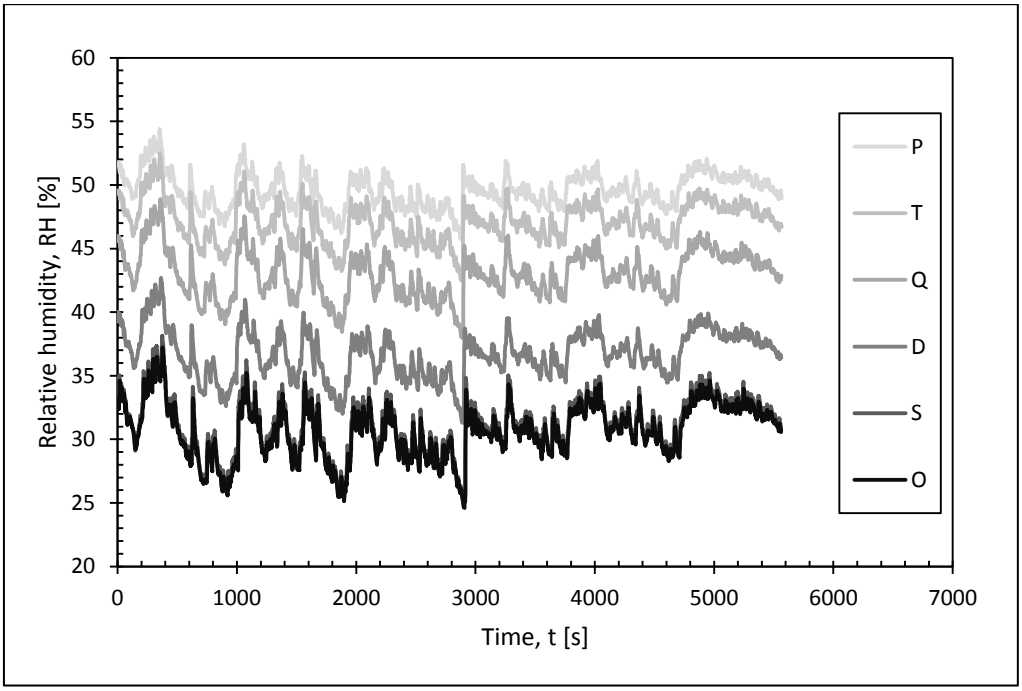

RH30_v2

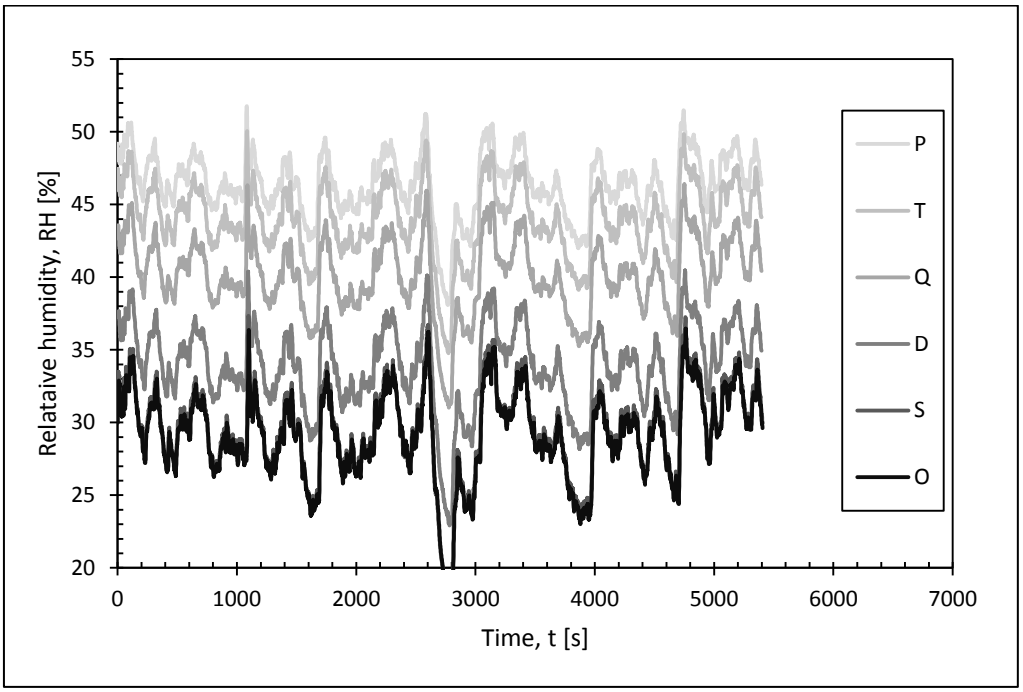

RH30_v3

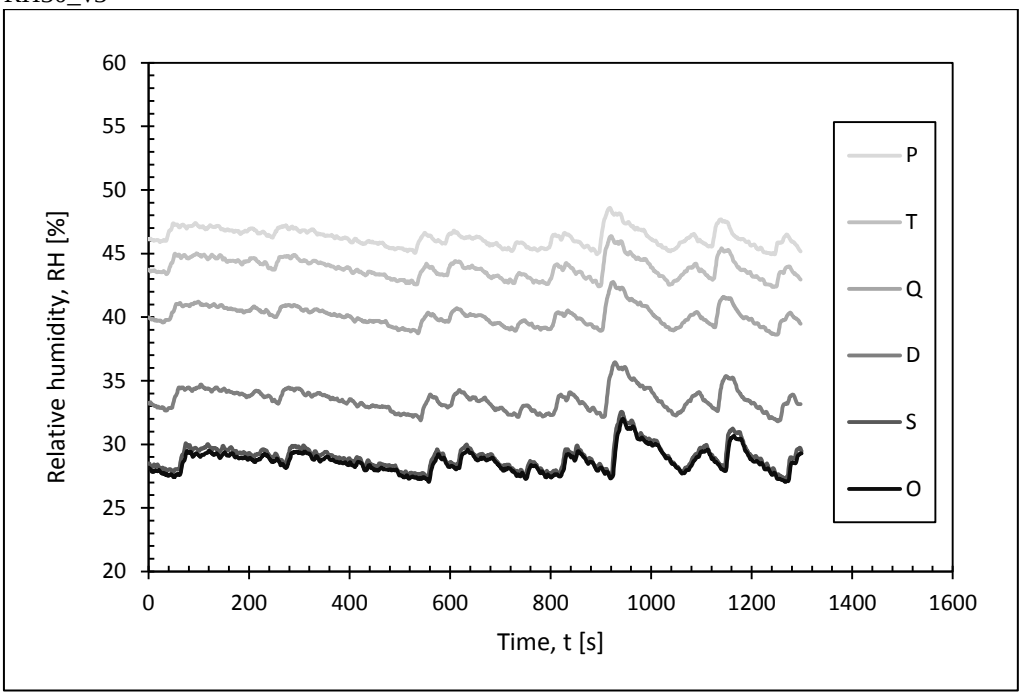

RH30_v4

Figure 10-6: Relative humidity of the airflow measured by each RH/T sensor during the test with RH inlet=30%

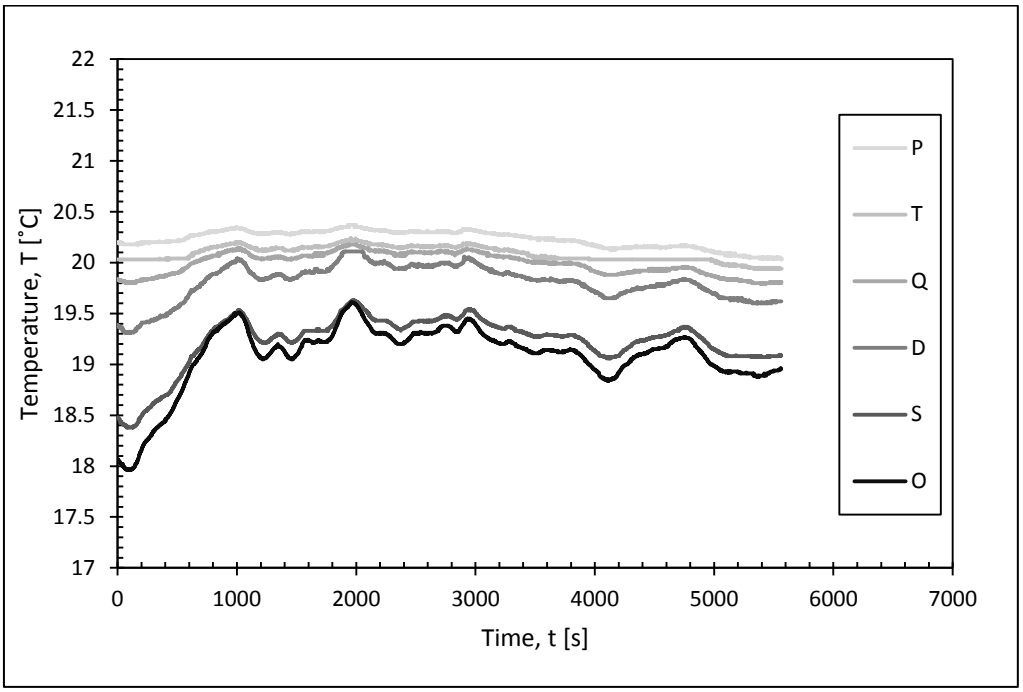

RH30_v2

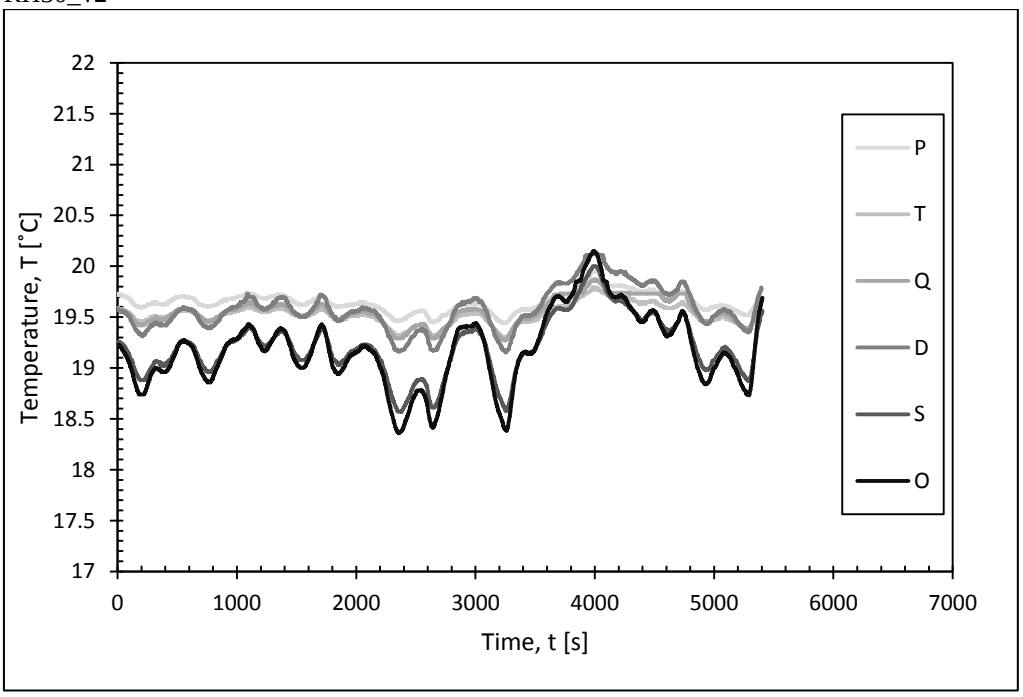

RH30_v3

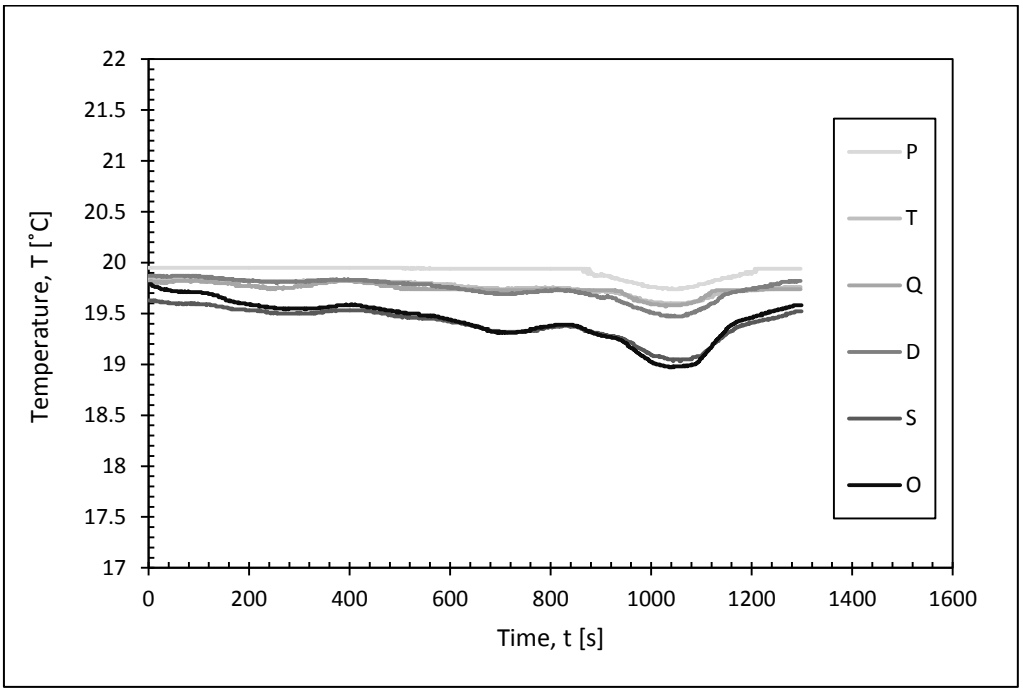

RH30_v4

Figure 10-7: Temperature of the airflow measured by each RH/T sensor during the test with RH inlet=30%

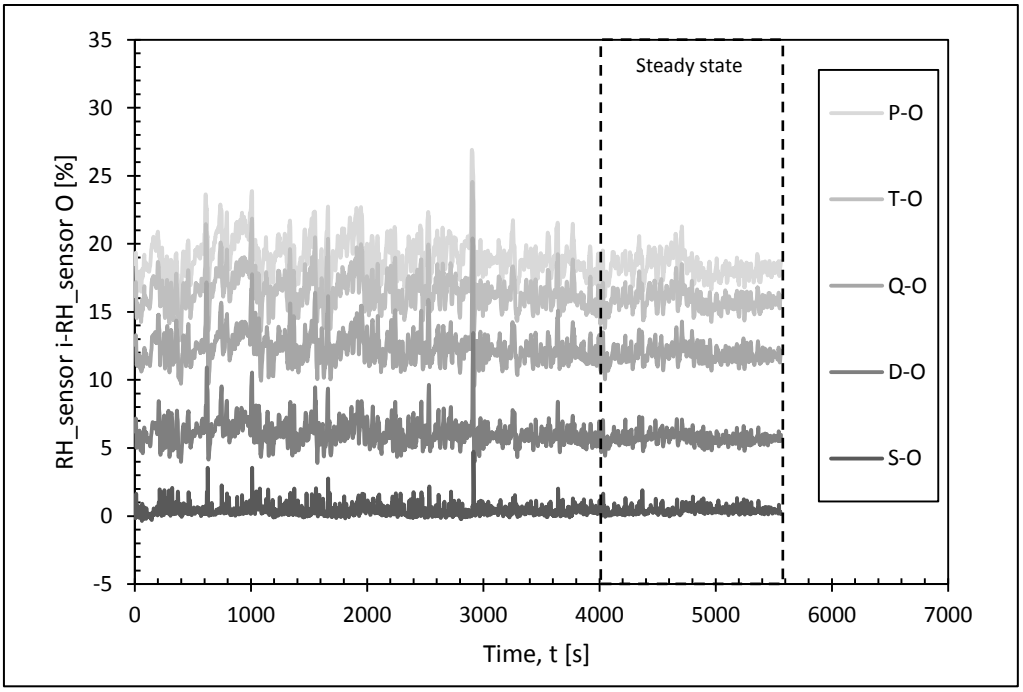

RH30_v2

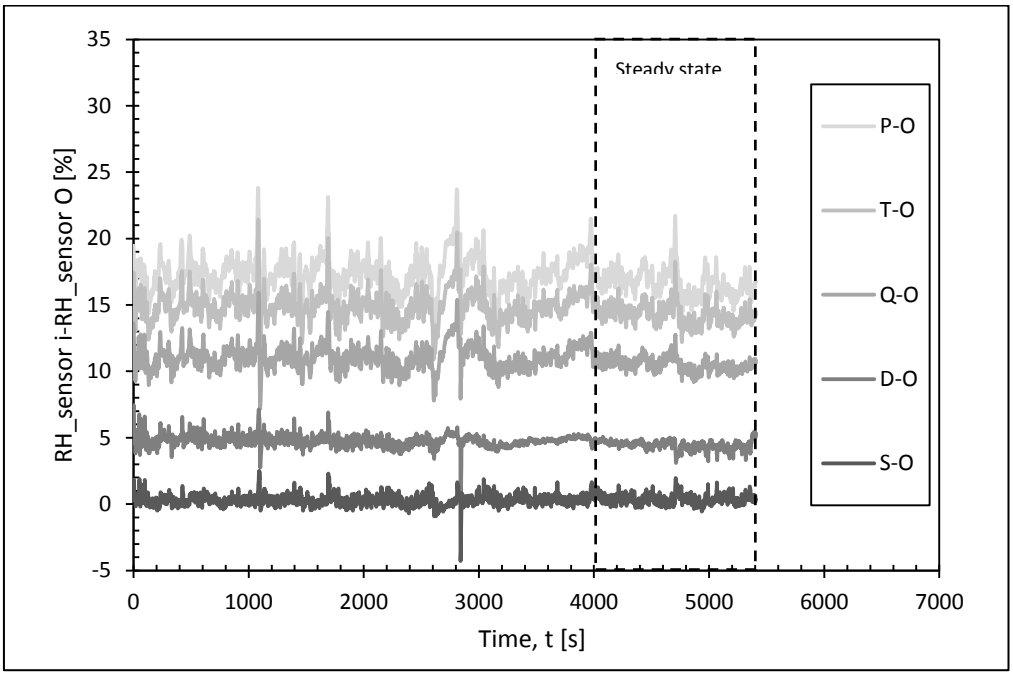

RH30_v3

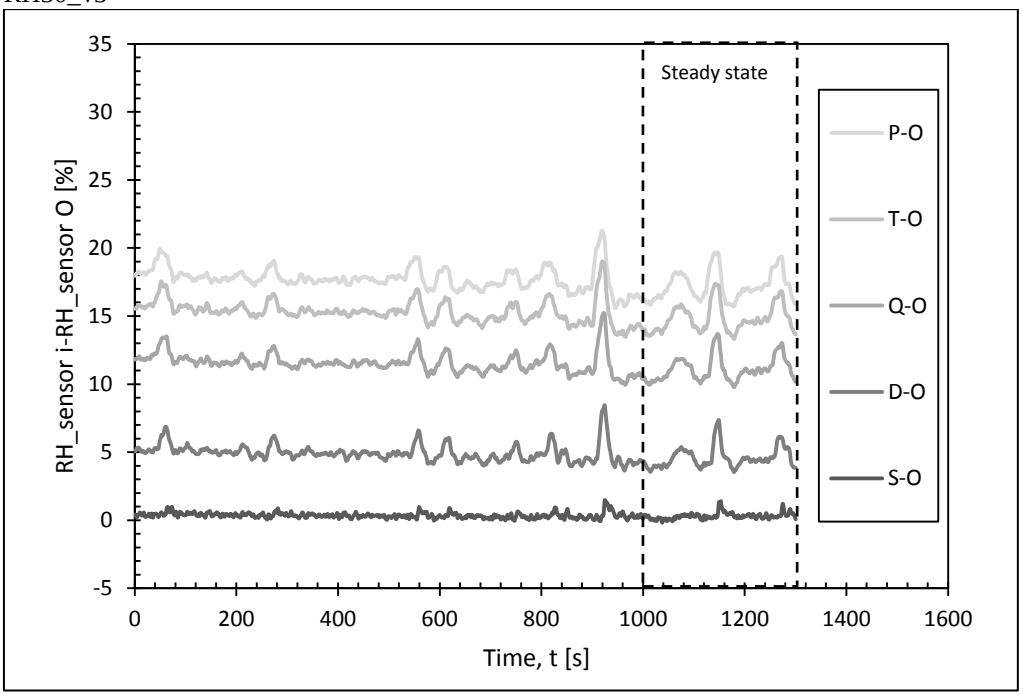

RH30_v4

Figure 10-8: Steady state of the tests with RHinlet=30% (in terms of relative humidity)

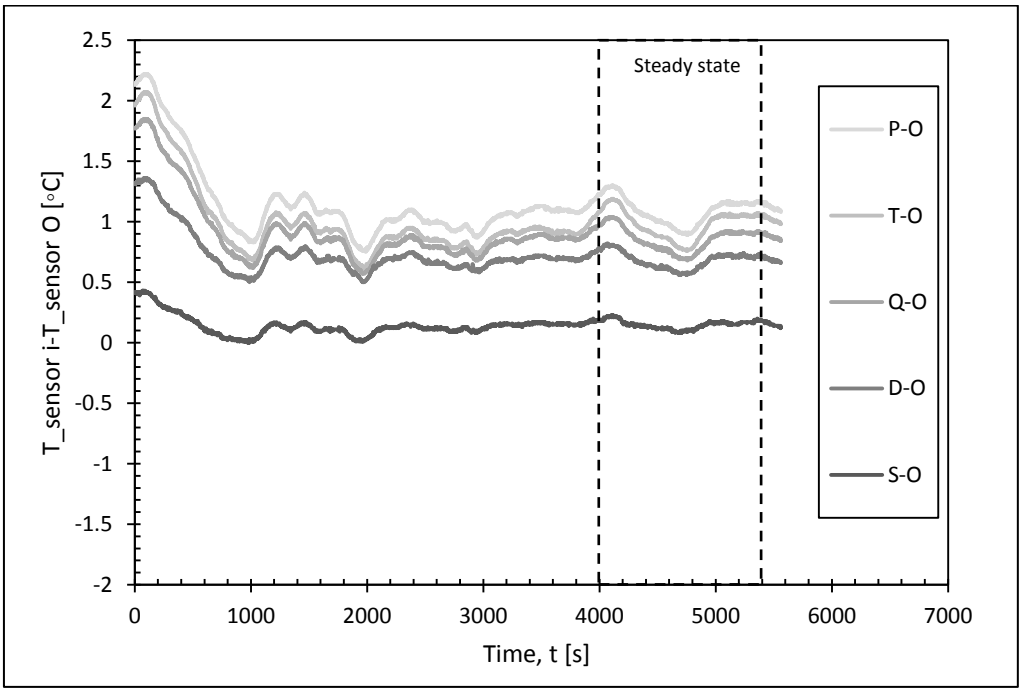

RH30_v2

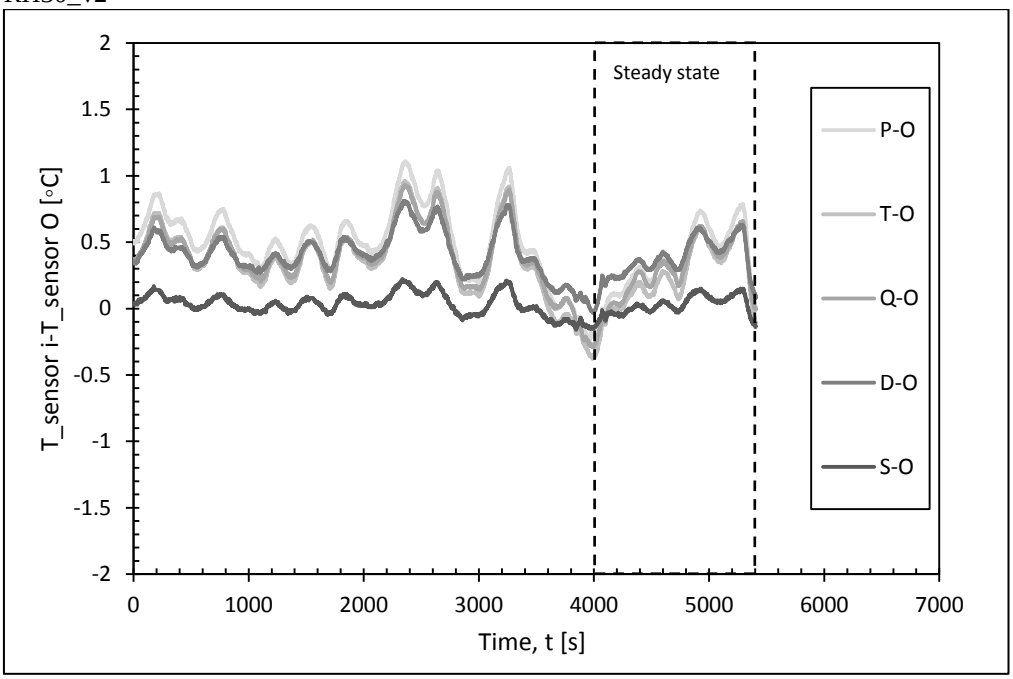

RH30_v3

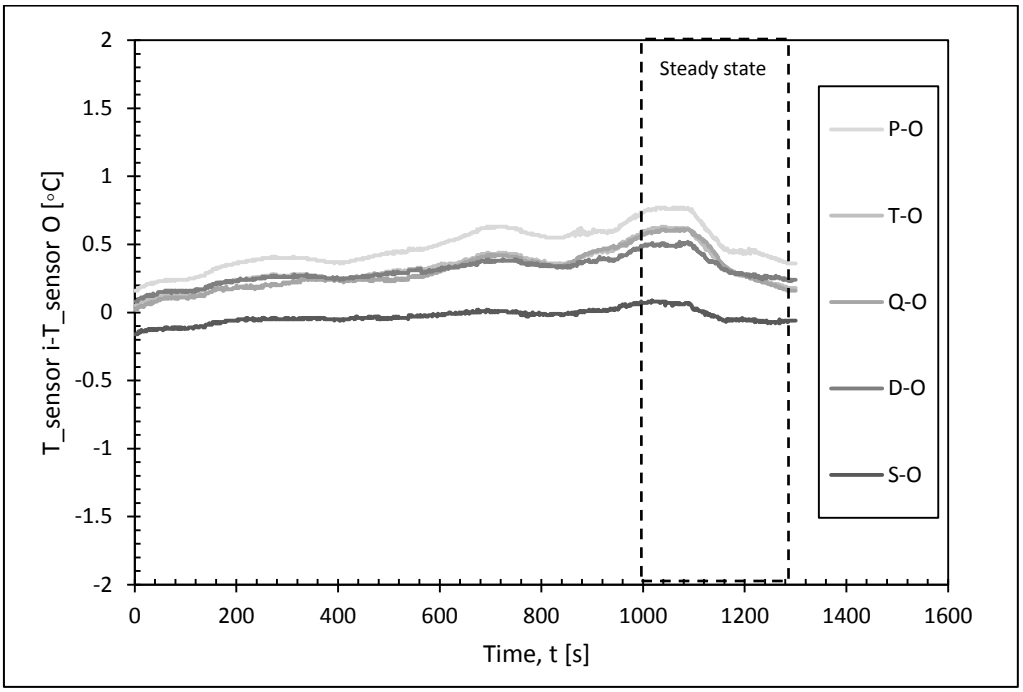

RH30_v4

Figure 10-9: Steady state of the test with RHinlet=30% (in terms of temperature)

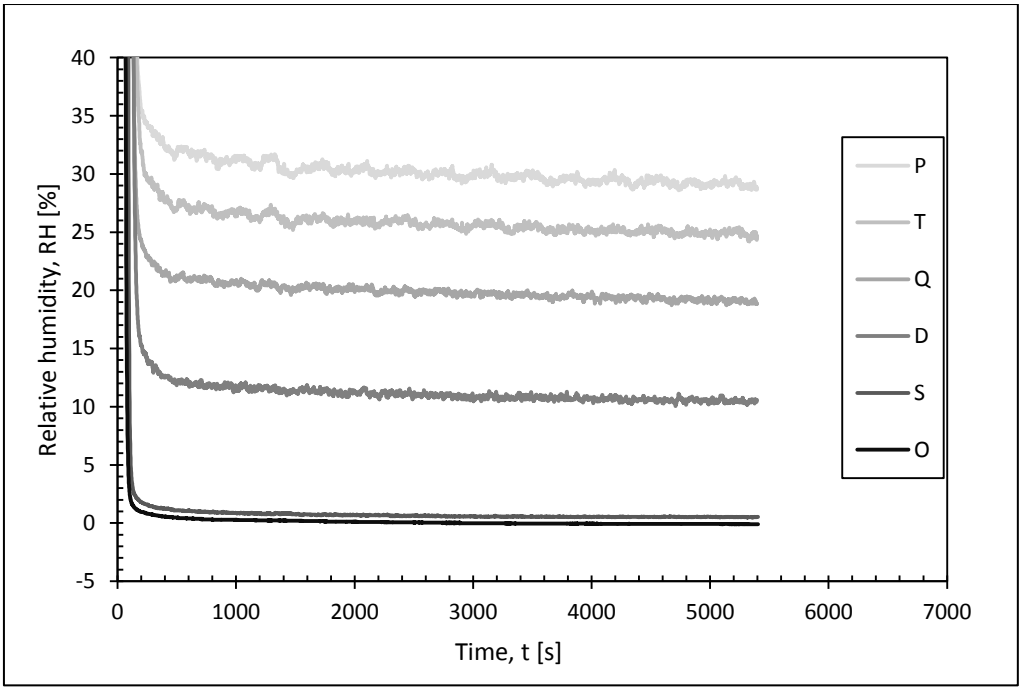

RH0_v1

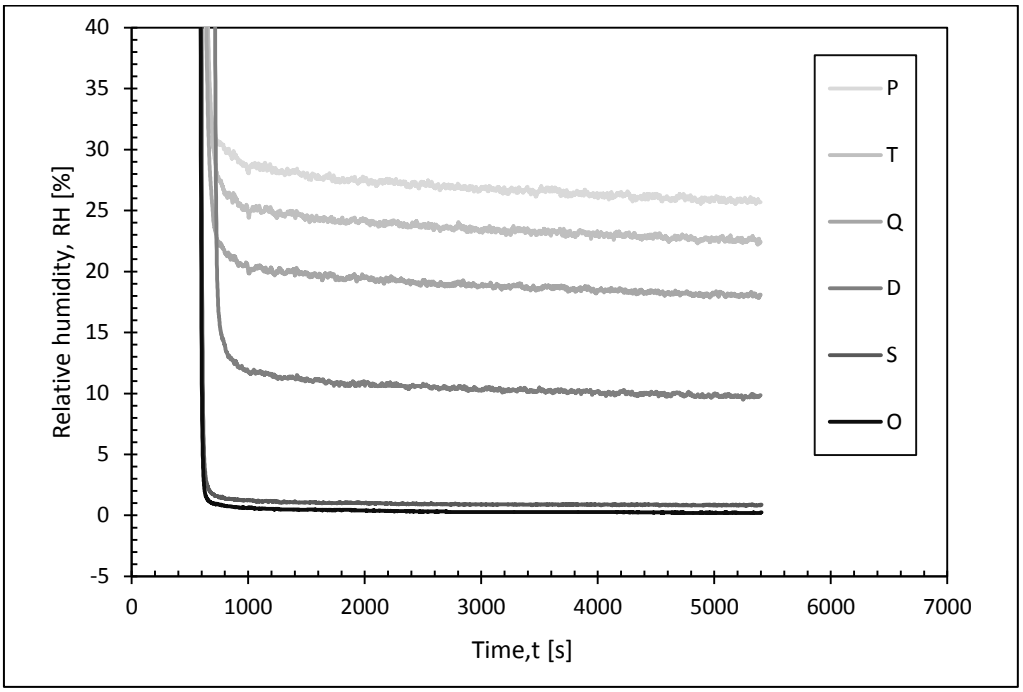
Relative humidity, RH [%]
Time,t [s]
P
T
Q
D
S
O

RH0_v2

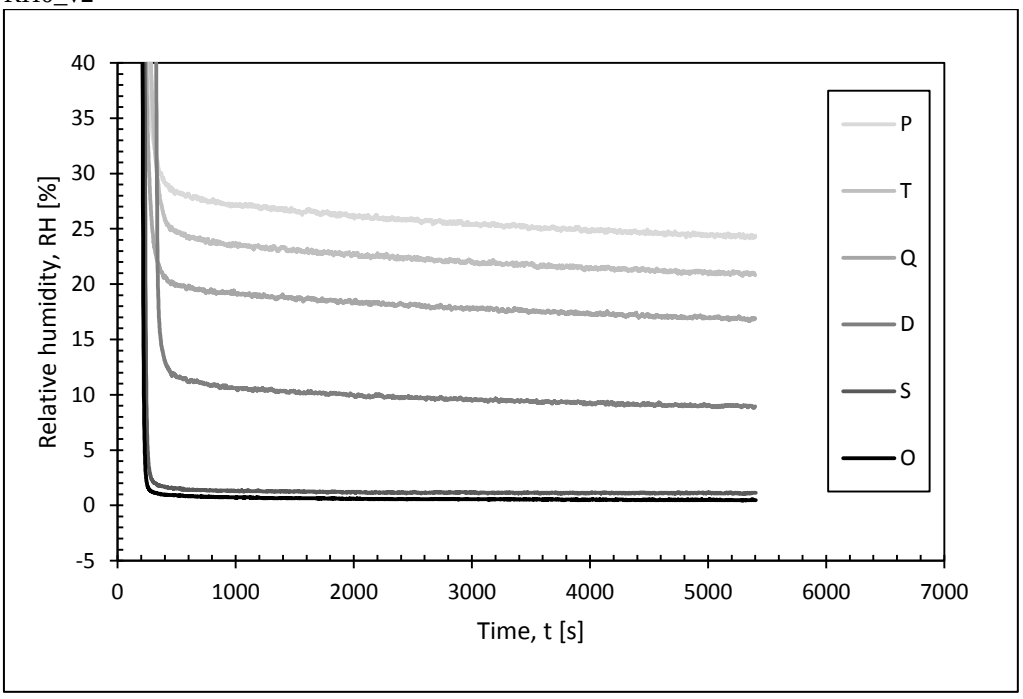
Relative humidity, RH [%]
Time, t [s]
P
T
Q
D
S
O

RH0_v3

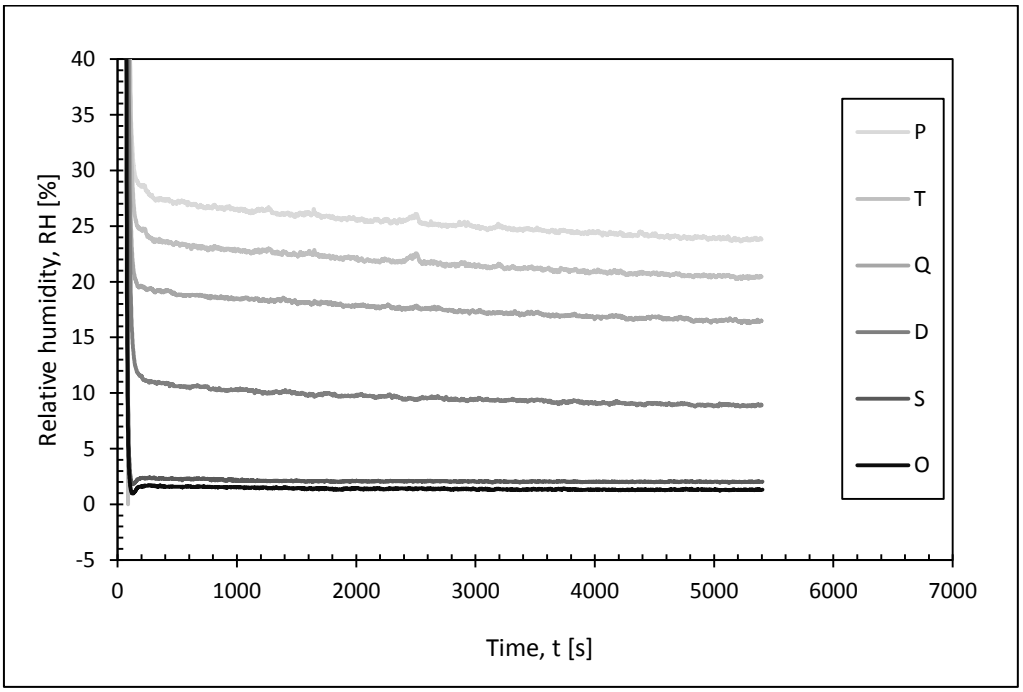

RH0_v4

Figure 10-10: Relative humidity of the airflow measured by each RH/T sensor during the test with RH inlet=0%

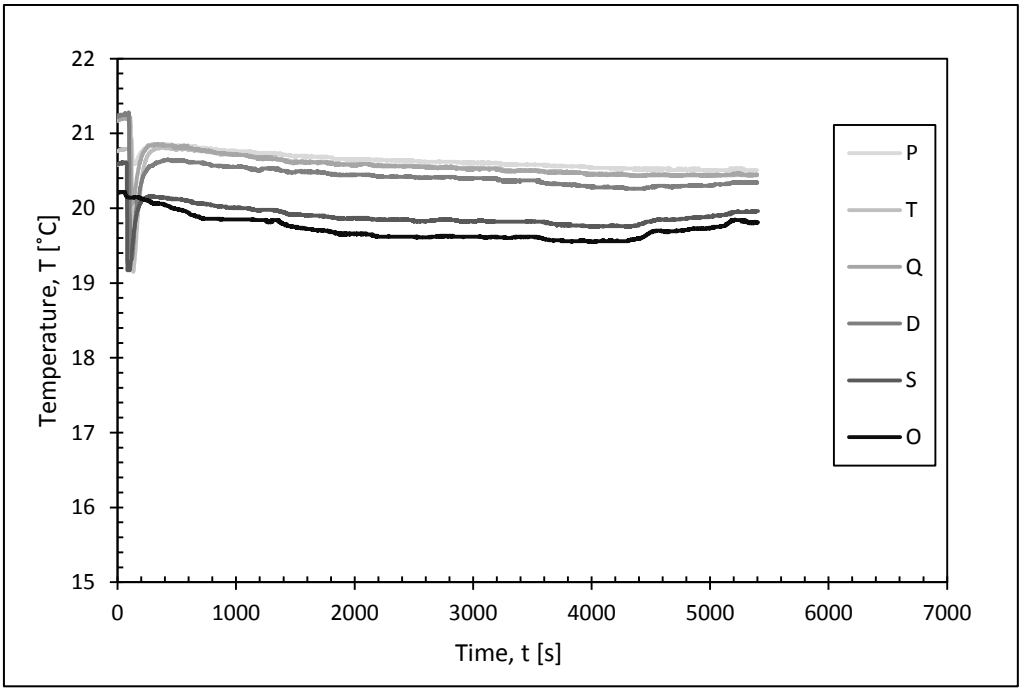

RH0_v1

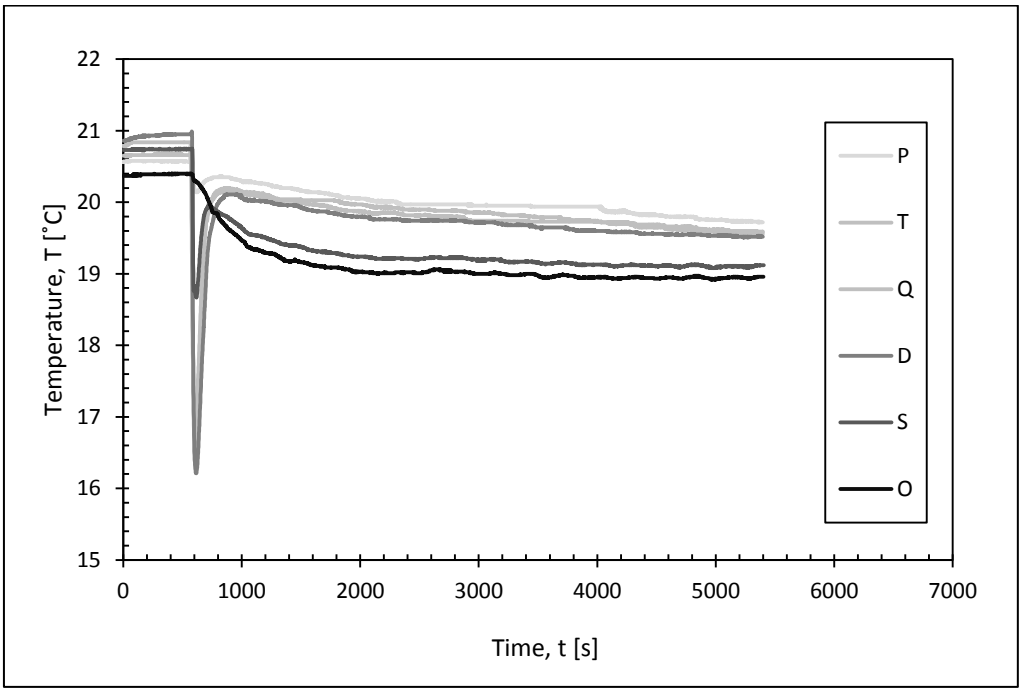
22
21
20
19
18
17
16
15
Temperature, T [°C]
0
1000
2000
3000
4000
5000
6000
7000
Time, t [s]
P
T
Q
D
S
O

RH0_v2

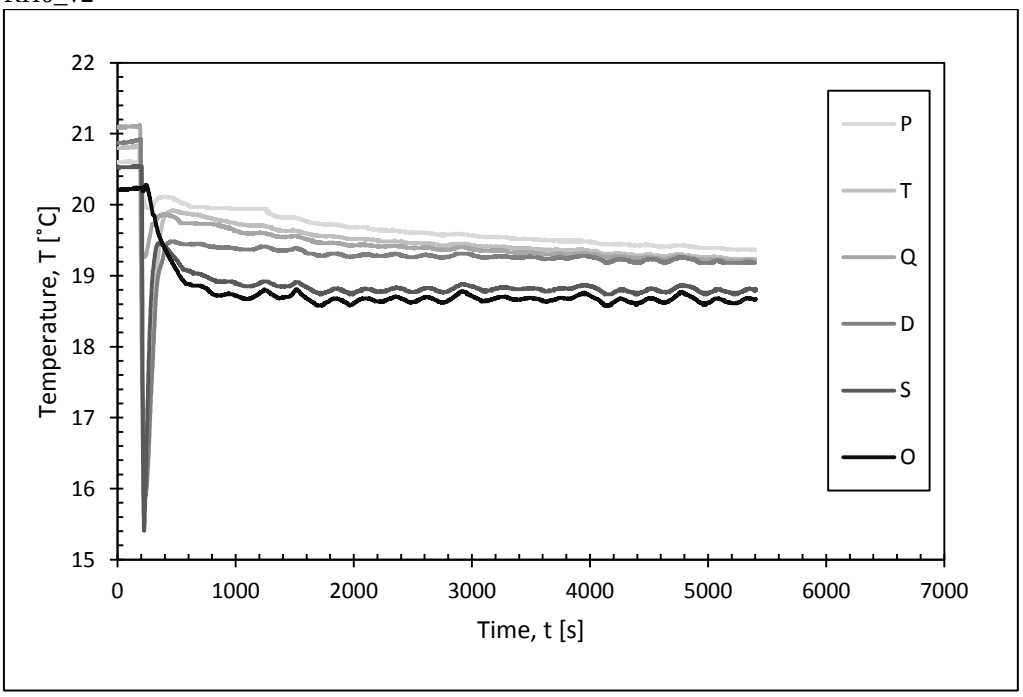
22
21
20
19
18
17
16
15
Temperature, T [°C]
0
1000
2000
3000
4000
5000
6000
7000
Time, t [s]
P
T
Q
D
S
O

RH0_v3

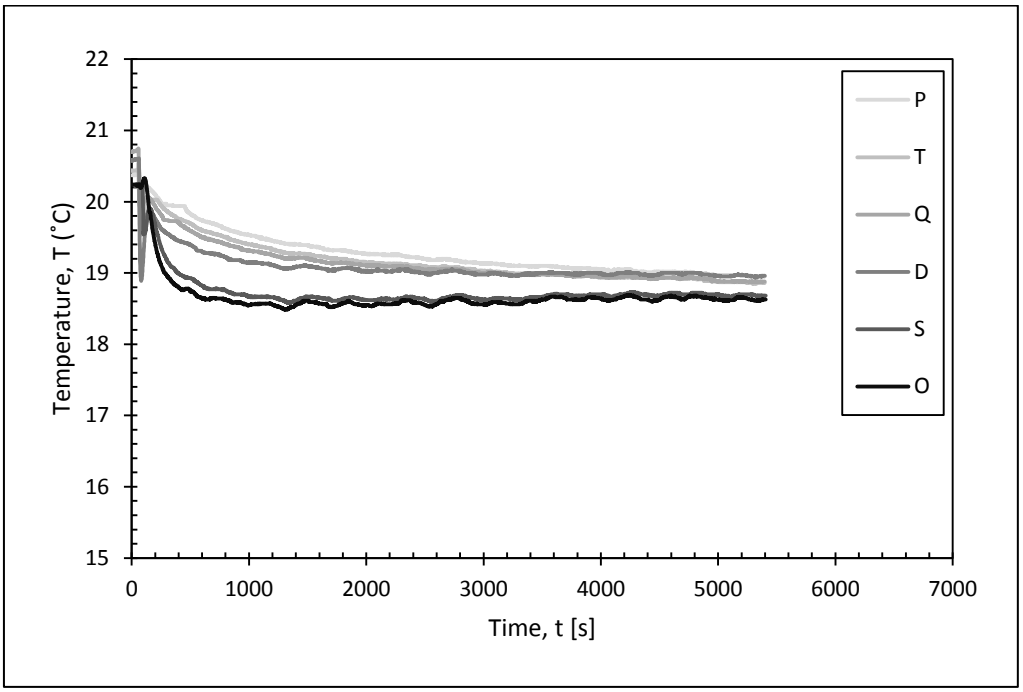

RH0_v4

Figure 10-11: Temperature of the airflow measured by each RH/T sensor during the test with RH inlet=0%

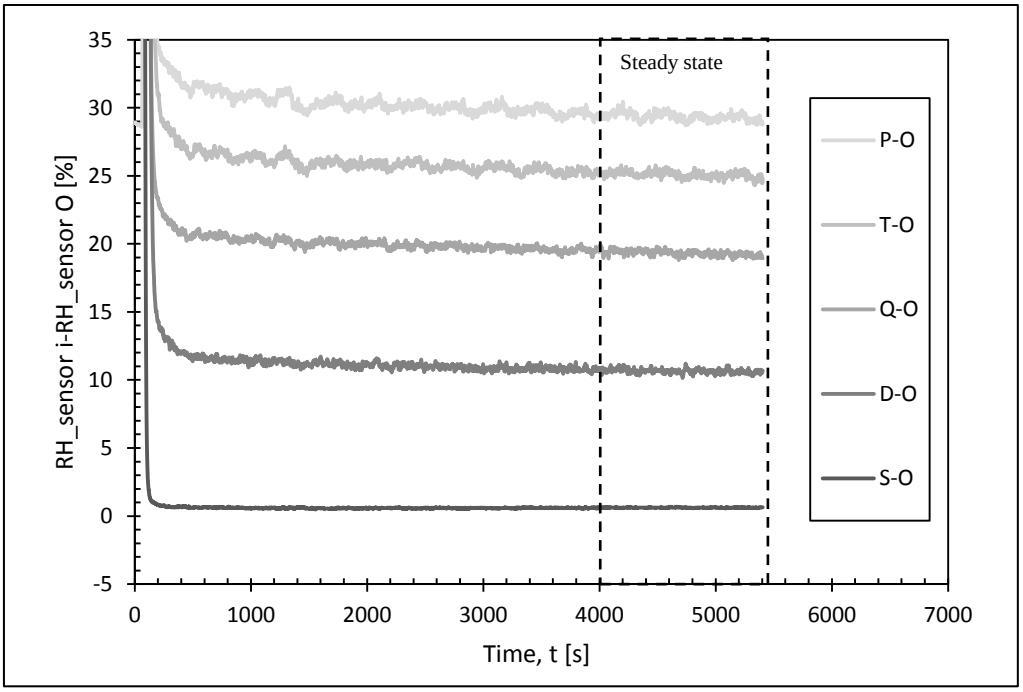

RH0_v1

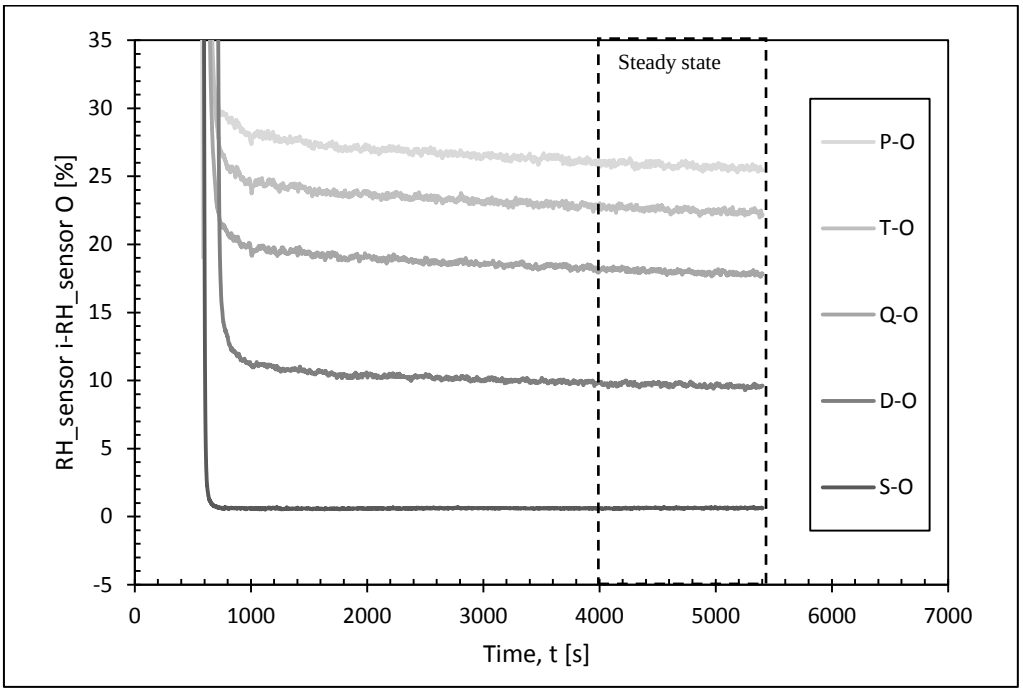
Steady state
P-O
T-O
Q-O
D-O
S-O
RH_sensor i-RH_sensor O [%]
Time, t [s]
35
30
25
20
15
10
5
0
-5
0
1000
2000
3000
4000
5000
6000
7000

RH0_v2

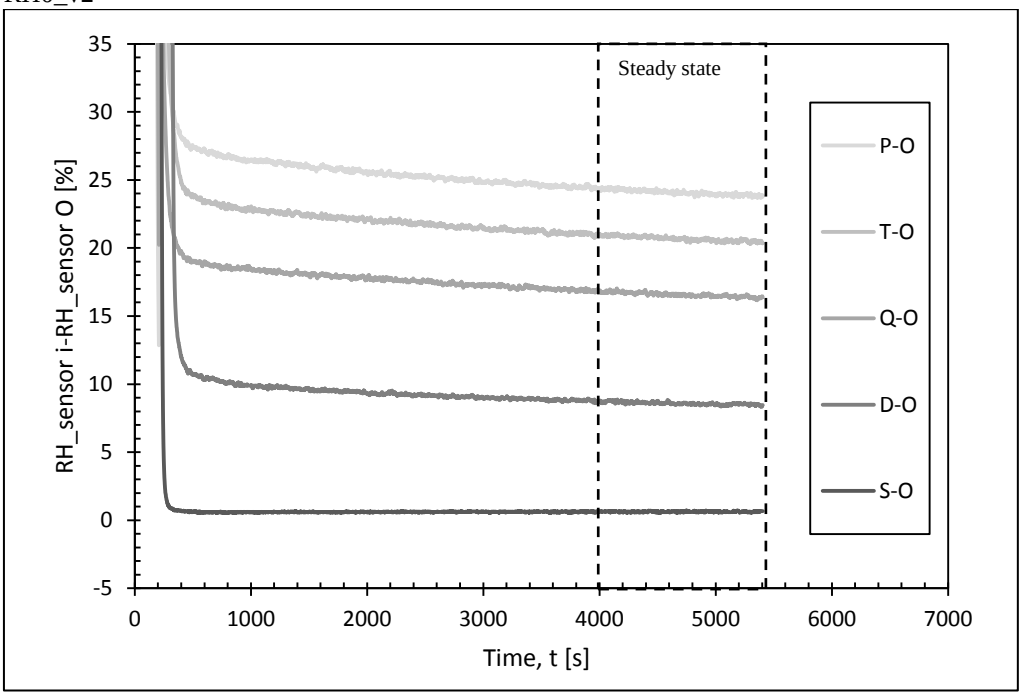
Steady state
P-O
T-O
Q-O
D-O
S-O
RH_sensor i-RH_sensor O [%]
Time, t [s]
35
30
25
20
15
10
5
0
-5
0
1000
2000
3000
4000
5000
6000
7000

RH0_v3

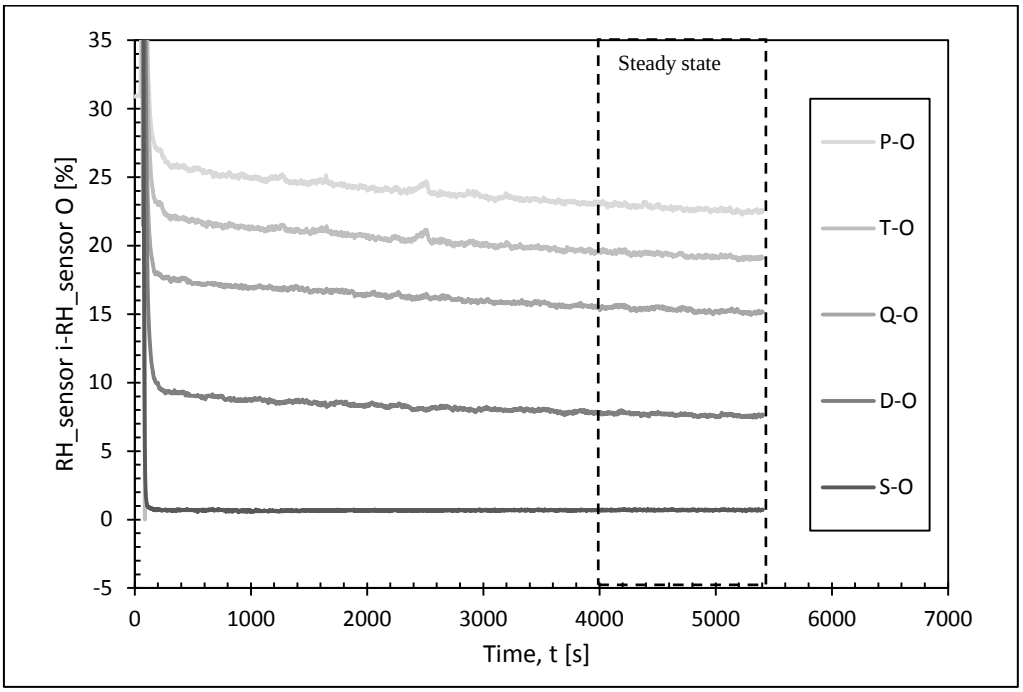

RH0_v4

Figure 10-12: Steady state of the test with RHinlet=0% (in terms of relative humidity)

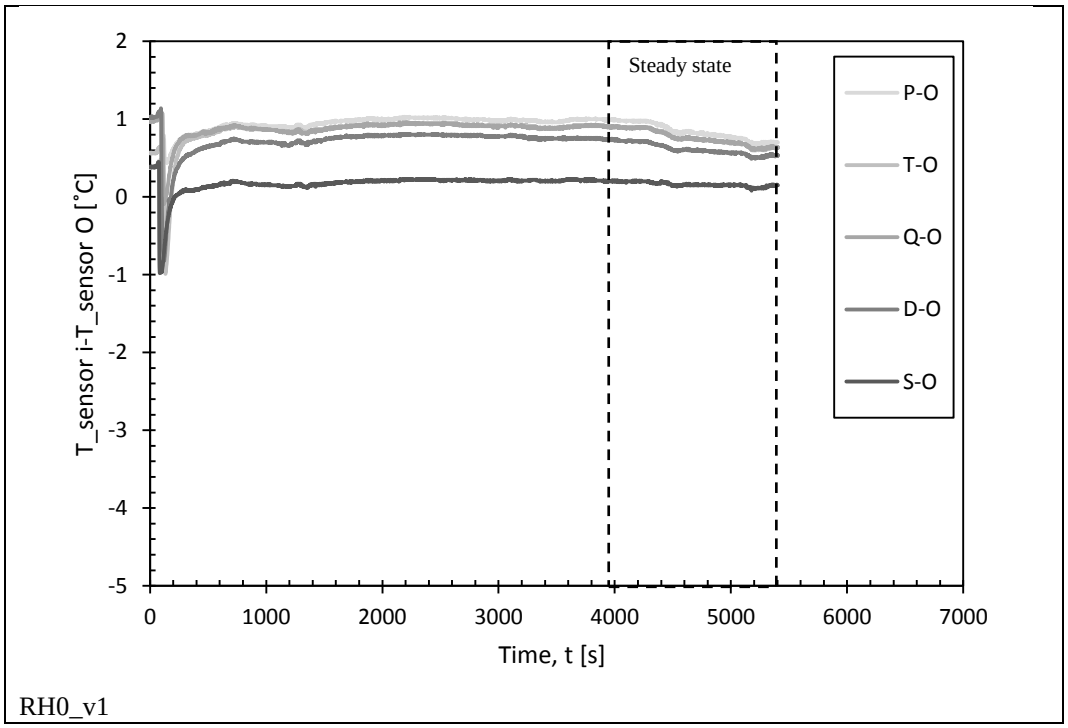

RH0_v1

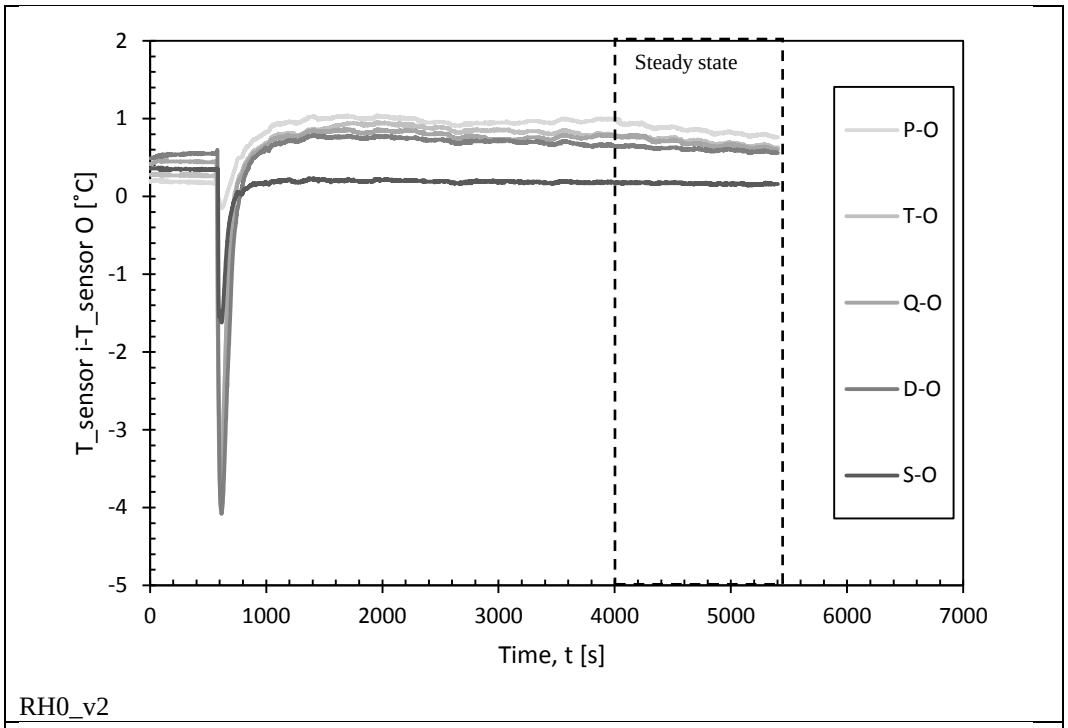
Steady state
P-O
T-O
Q-O
D-O
S-O
T_sensor i-T_sensor O [°C]
Time, t [s]
2
1
0
-1
-2
-3
-4
-5
0
1000
2000
3000
4000
5000
6000
7000

RH0_v2

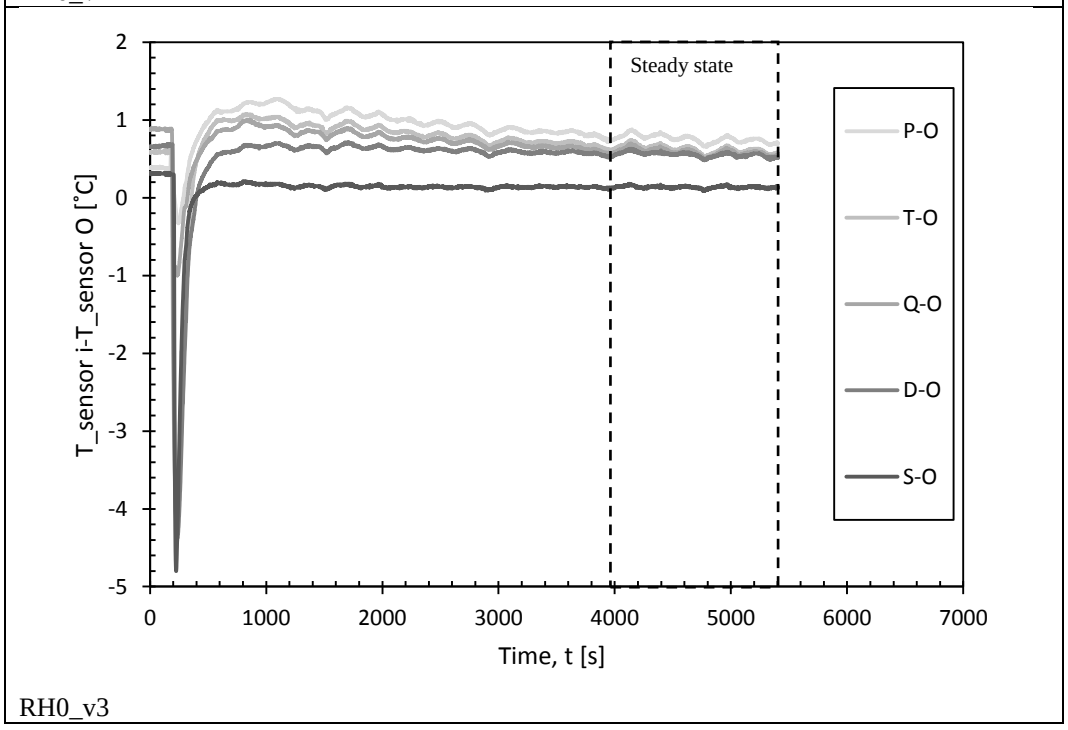
Steady state
P-O
T-O
Q-O
D-O
S-O
T_sensor i-T_sensor O [°C]
Time, t [s]
2
1
0
-1
-2
-3
-4
-5
0
1000
2000
3000
4000
5000
6000
7000

RH0_v3

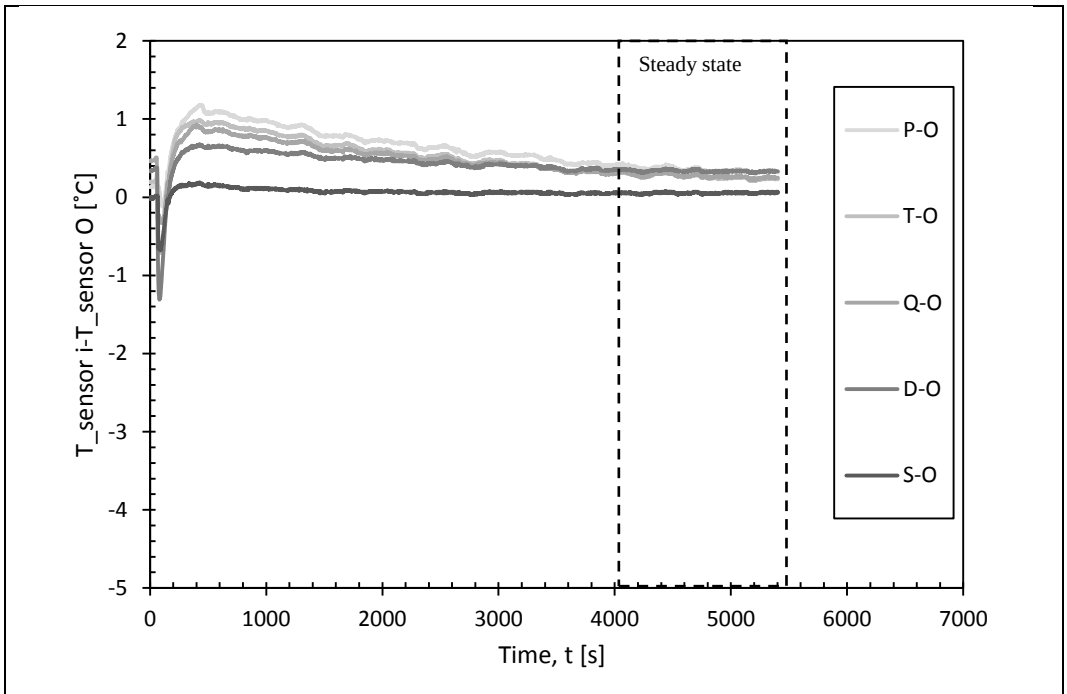

RH0_v4

Figure 10-13: Steady state of the test with RHinlet=0% (in terms of temperature)

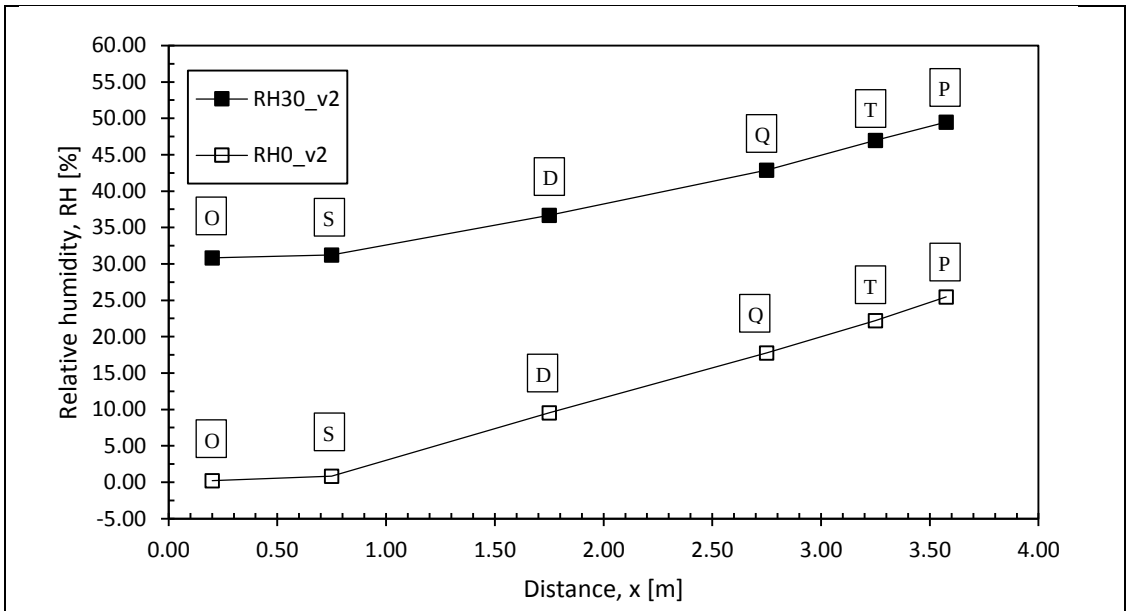

a) v2

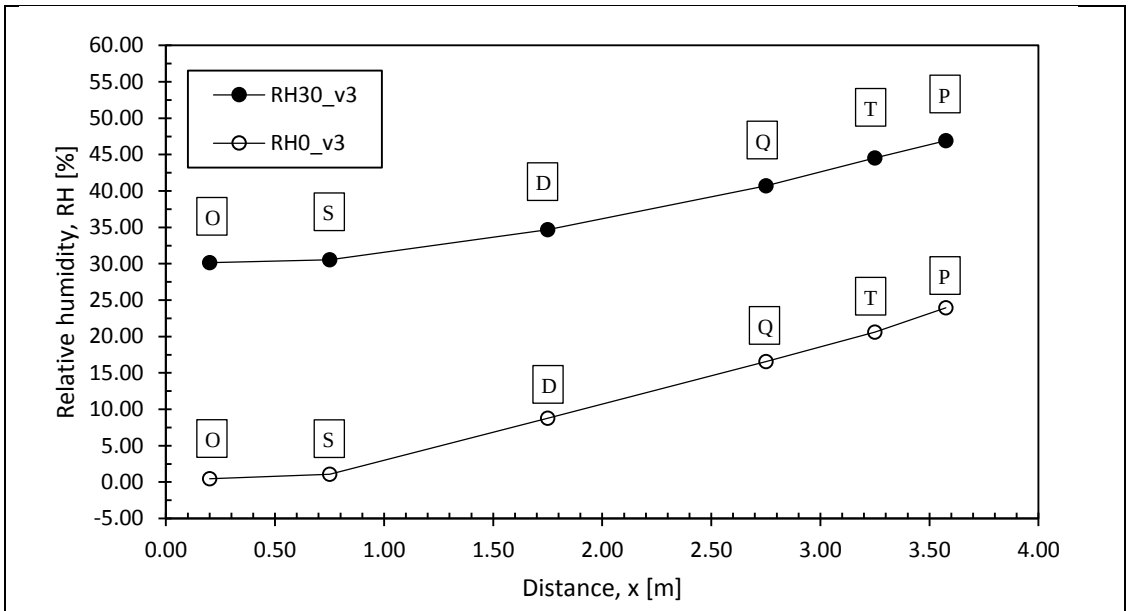

b) v3

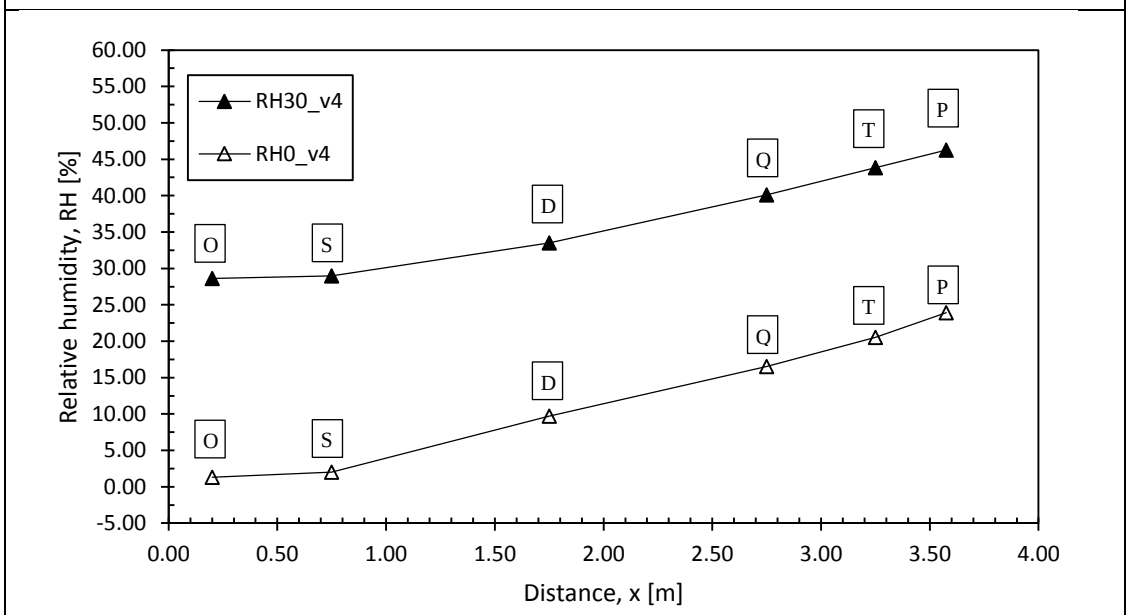

c) v4

Figure 10-14: Comparison of relative humidity of the airflows with equal air velocity and different RHinlet along the upper air channel

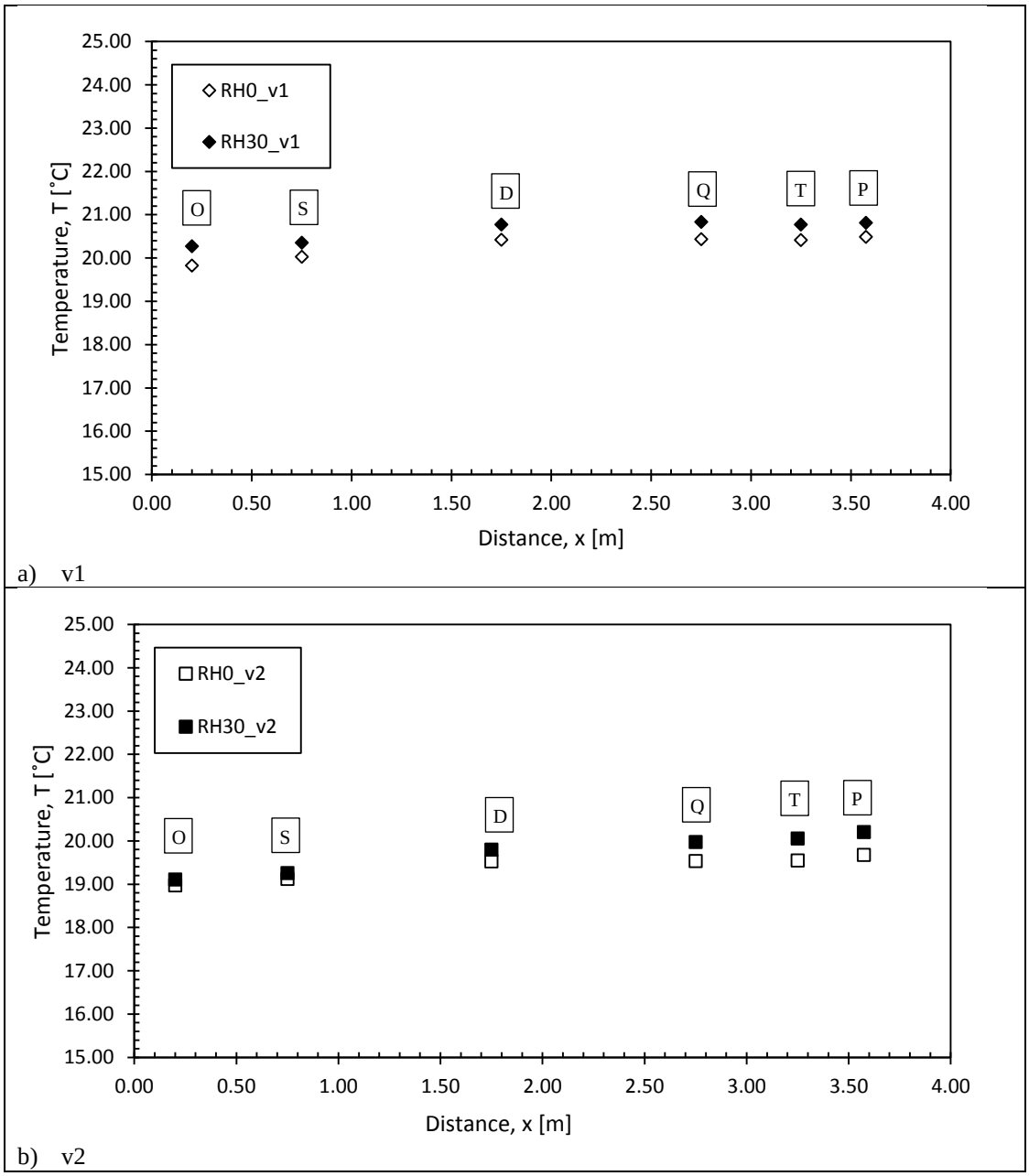
25.00
24.00
23.00
22.00
21.00
20.00
19.00
18.00
17.00
16.00
15.00
Temperature, T [°C]
RH0_v1
RH30_v1
O
S
D
Q
T
P
0.00
0.50
1.00
1.50
2.00
2.50
3.00
3.50
4.00
Distance, x [m]

a) v1

25.00
24.00
23.00
22.00
21.00
20.00
19.00
18.00
17.00
16.00
15.00
Temperature, T [°C]
RH0_v2
RH30_v2
O
S
D
Q
T
P
0.00
0.50
1.00
1.50
2.00
2.50
3.00
3.50
4.00
Distance, x [m]

b) v2

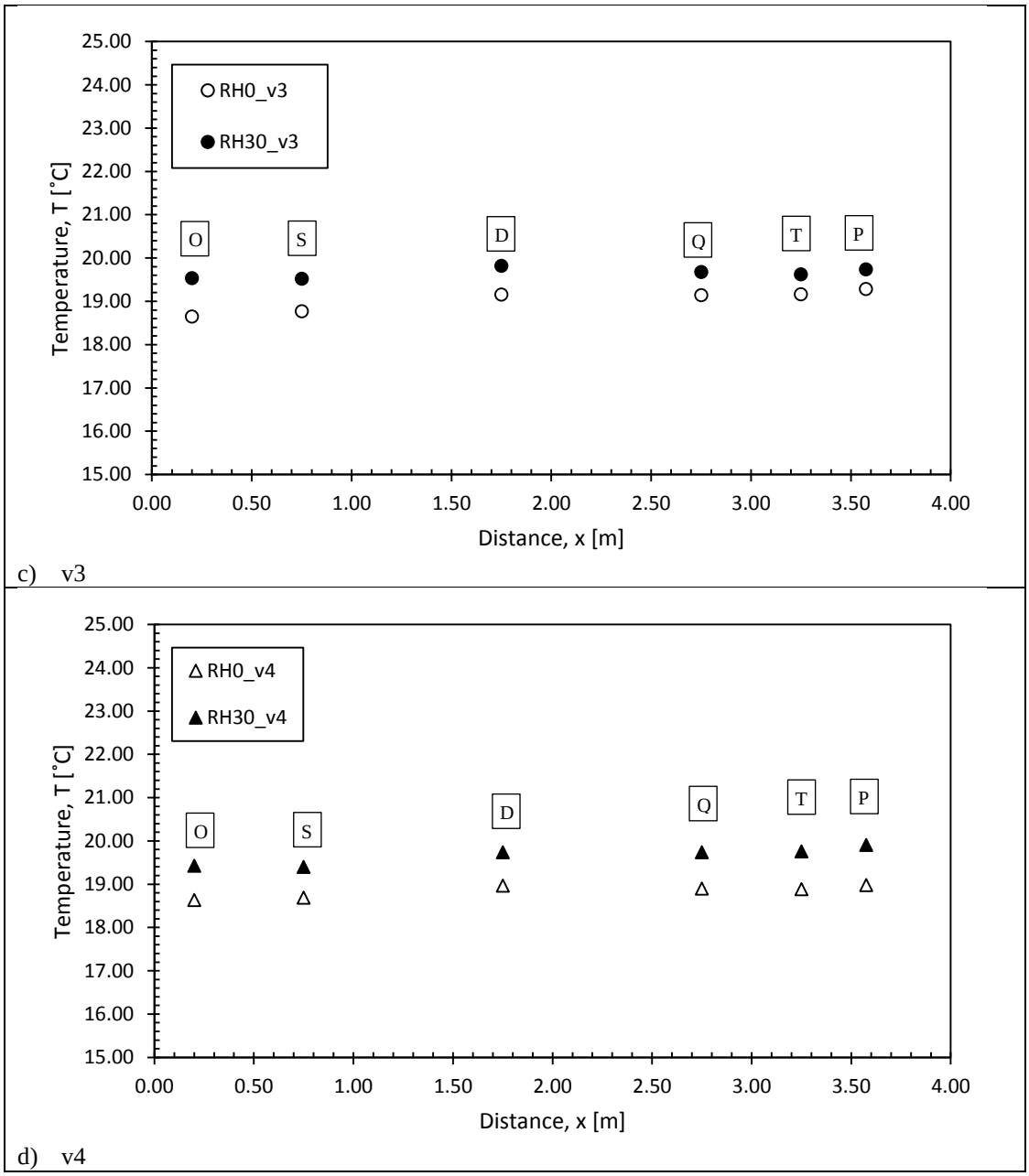

Figure 10-15: Comparison of temperature of the airflows with equal air velocity and different RHinlet along the upper air channel.

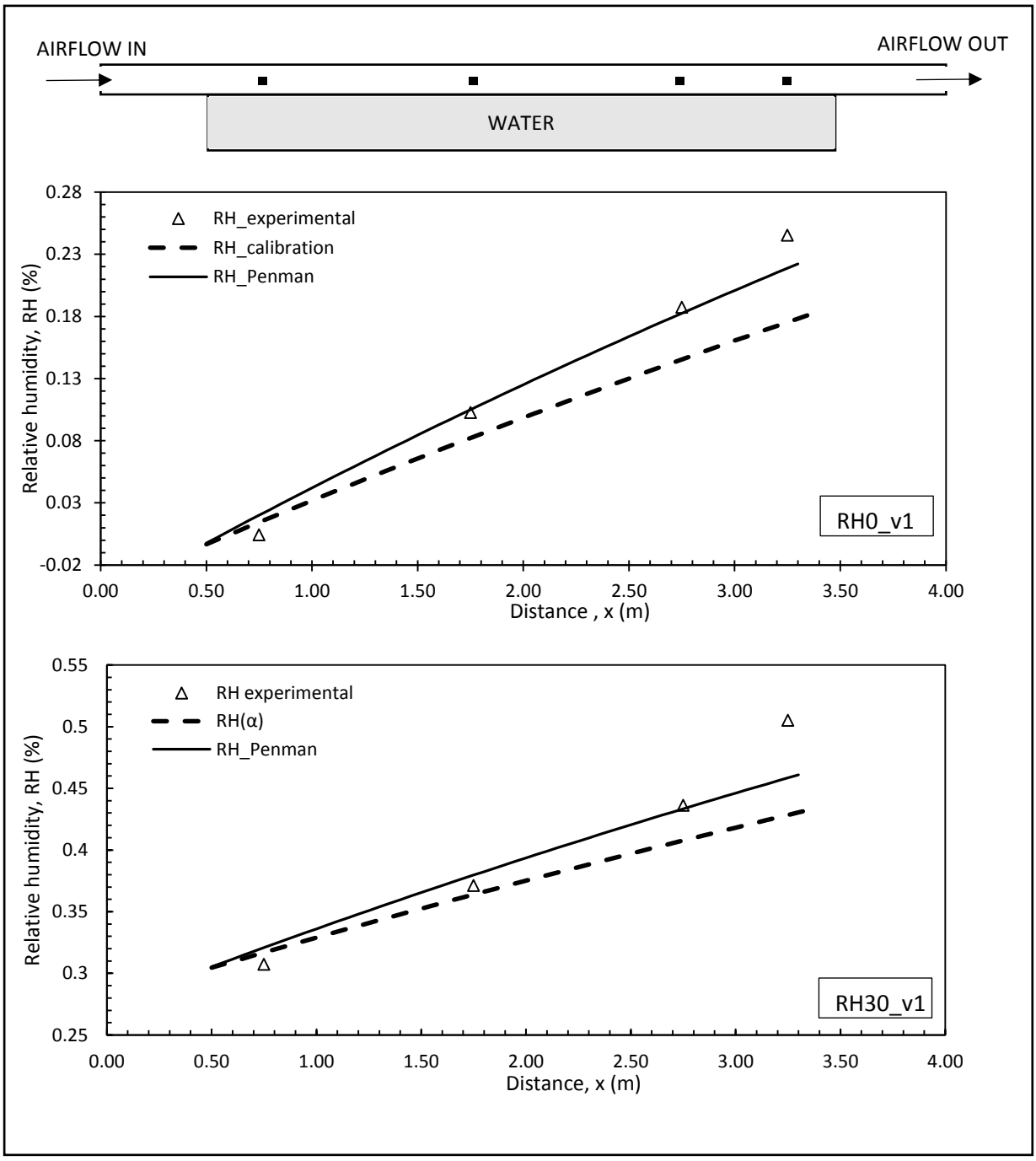

Figure 10-16: Comparison of the relative humidity of the airflow measured experimentally, estimated via α-calibration and estimated via α-Penman for v_air=1m/s

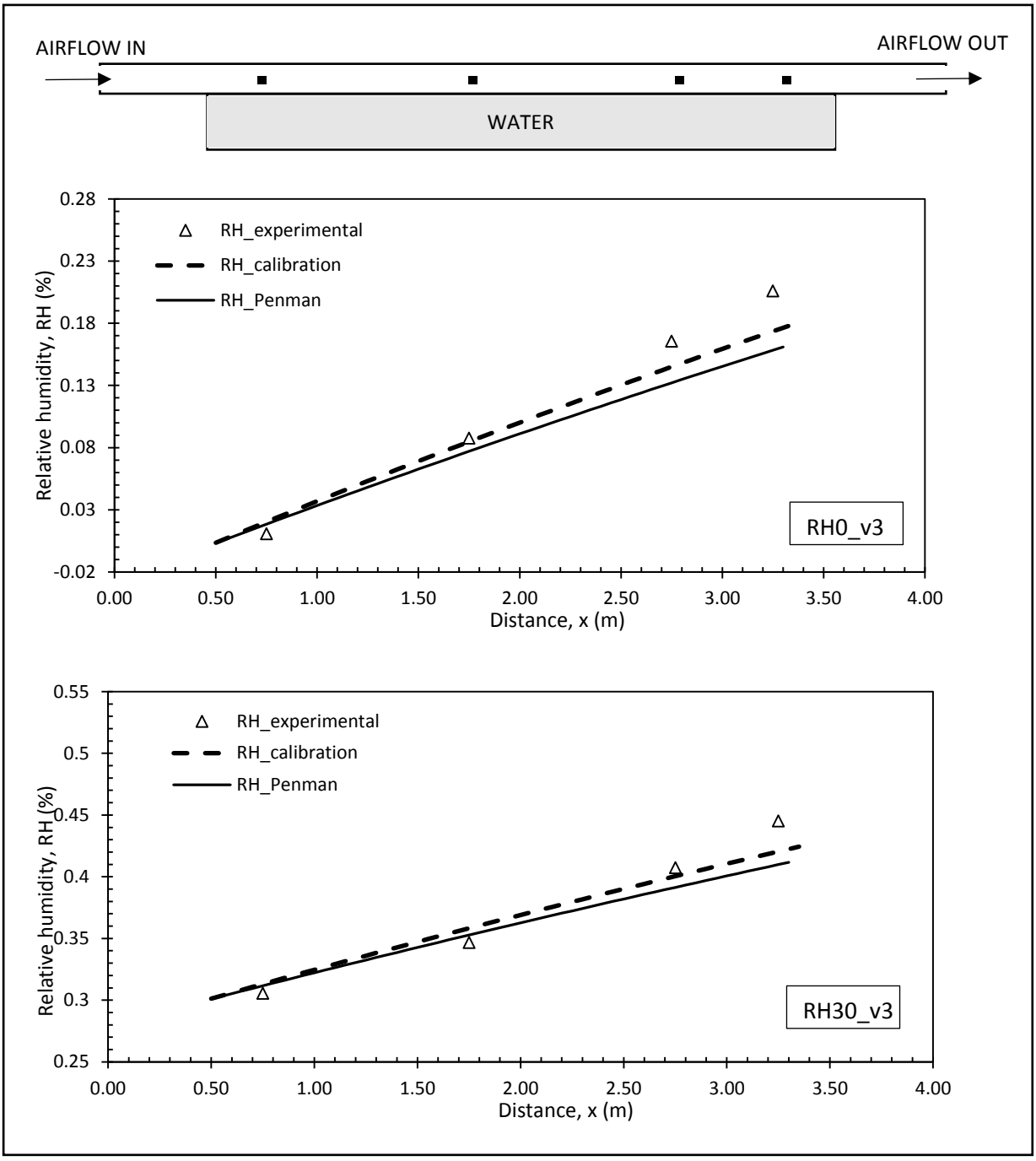

Figure 10-17: Comparison of the relative humidity of the airflow measured experimentally, estimated via α-calibration and estimated via α-Penman for v_air=3m/s

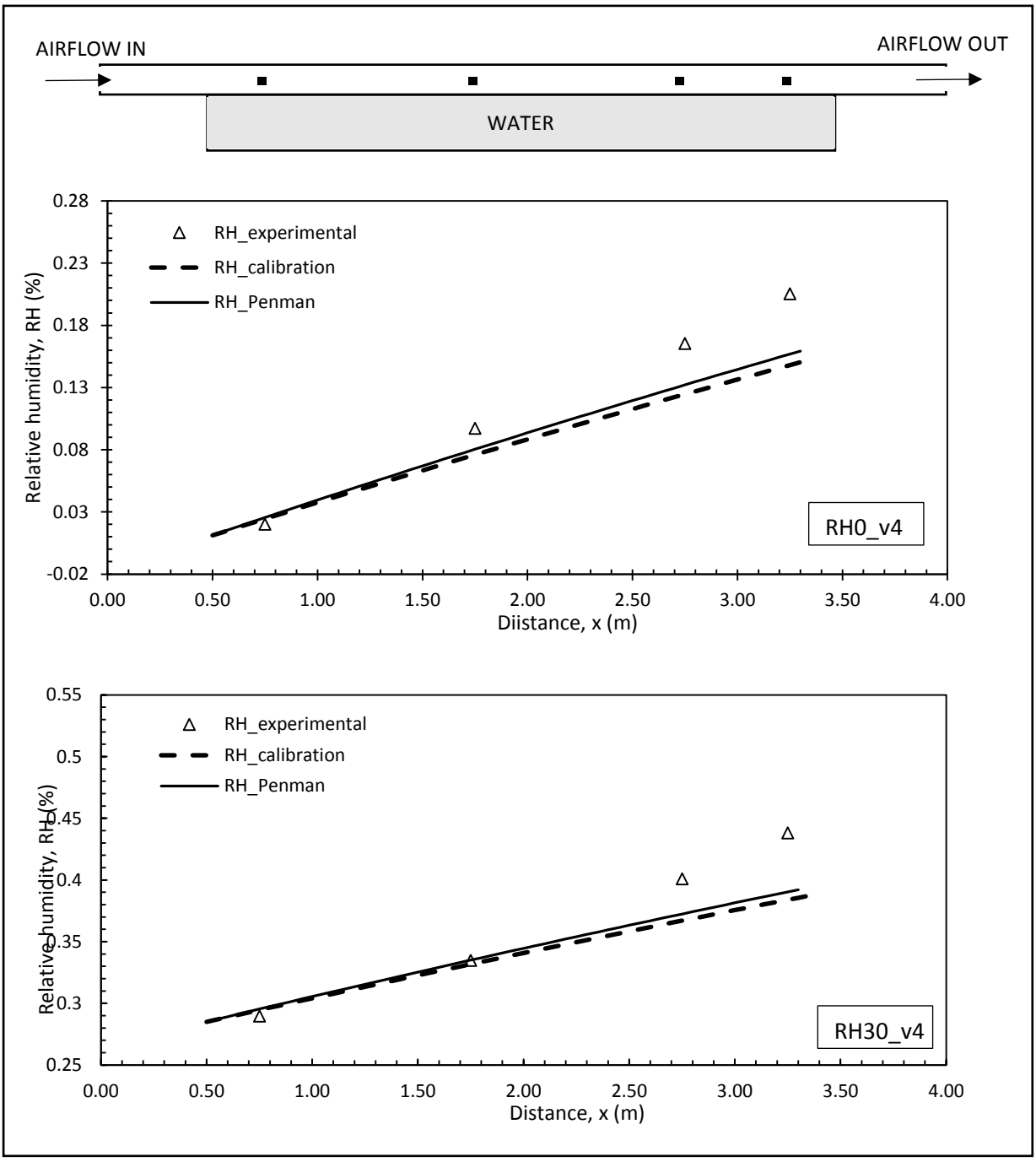

Figure 10-18: Comparison of the relative humidity of the airflow measured experimentally, estimated via α-model and estimated via α-Penman for v_air=4m/s